



**HAL**  
open science

# The meridional overturning circulation variability and heat content changes in the North Atlantic subpolar gyre

Damien Desbruyères

► **To cite this version:**

Damien Desbruyères. The meridional overturning circulation variability and heat content changes in the North Atlantic subpolar gyre. Earth Sciences. Université de Bretagne occidentale - Brest, 2013. English. NNT : 2013BRES0074 . tel-01362211

**HAL Id: tel-01362211**

**<https://theses.hal.science/tel-01362211>**

Submitted on 8 Sep 2016

**HAL** is a multi-disciplinary open access archive for the deposit and dissemination of scientific research documents, whether they are published or not. The documents may come from teaching and research institutions in France or abroad, or from public or private research centers.

L'archive ouverte pluridisciplinaire **HAL**, est destinée au dépôt et à la diffusion de documents scientifiques de niveau recherche, publiés ou non, émanant des établissements d'enseignement et de recherche français ou étrangers, des laboratoires publics ou privés.



université de bretagne  
occidentale



**THÈSE / UNIVERSITÉ DE BRETAGNE  
OCCIDENTALE**

*sous le sceau de l'Université européenne de Bretagne*

pour obtenir le titre de

**DOCTEUR DE L'UNIVERSITÉ DE BRETAGNE  
OCCIDENTALE**

*Mention : Océanographie Physique*

**École Doctorale des Sciences de la Mer**

présentée par

**Damien Desbruyères**

Préparée à l'Unité Mixte de Recherche n°6523

CNRS – IFREMER – UBO – IRD

Laboratoire de Physique des Océans

**Soutenance prévue le 22 janvier 2013**

devant le jury composé de :

**Sabrina SPEICH**

Professeur des Universités, UBO, LPO Brest / *Présidente*

**Gilles REVERDIN**

Directeur de recherche CNRS, LOCEAN Paris / *rapporteur*

**Robert MARSH**

Reader, University of Southampton / *rapporteur*

**Christophe HERBAUT**

Chargé de recherche CNRS, LOCEAN Paris / *examineur*

**Herlé MERCIER**

Directeur de recherche CNRS, LPO Brest / *Directeur de Thèse*

**Virginie THIERRY**

Chercheur IFREMER, LPO Brest / *Co-encadrante de thèse*

# The Meridional Overturning Circulation Variability and Heat Content Changes in the North Atlantic Subpolar Gyre



THE MERIDIONAL OVERTURNING CIRCULATION  
VARIABILITY AND HEAT CONTENT CHANGES IN  
THE NORTH ATLANTIC SUBPOLAR  
GYRE

VARIABILITE DE LA CIRCULATION MERIDIENNE  
DE RETOURNEMENT ET DU CONTENU DE  
CHALEUR DANS LE GYRE SUBPOLAIRE DE  
L'ATLANTIQUE NORD

*Author*

**Damien Desbruyères**

*ABSTRACT*

The Meridional Overturning Circulation (MOC) of the North Atlantic ocean is a key component of the global climate system, through its role in redistributing heat, freshwater and chemical properties between low and high latitude regions. In mid-high latitude regions, the North Atlantic Current (NAC) forms the upper limb of the MOC. It flows northeastward at the subtropical/subpolar boundary, and splits into two main branches in the eastern subpolar gyre: a northern branch that recirculates within the subpolar region and a southern branch that feed the Nordic Seas.

A realistic eddy-permitting simulation (ORCA025-G70, 1/4°) is combined with a Lagrangian analysis tool (ARIANE) to investigate the MOC variability (1965-2004) across the A25-Ovide line, which joins Greenland to Portugal. Two vertical overturning cells are identified: a subtropical cell connecting low and high latitudes (12 Sv) and a cell internal to the subpolar gyre (4 Sv). The decadal MOC variability is associated with synchronized transport changes of the subtropical and subpolar inflow within the NAC. The latter undergoes important horizontal restructuring with opposed transport changes of its northern and southern branches. Those horizontal transport changes are largely induced by the horizontal variability of the subtropical inflow.

Changes in oceanic heat transport across A25-Ovide are largely responsible for the observed heat content changes in the eastern subpolar gyre (1965-2004). Heat transport variability at A25-Ovide results from an imbalance between opposed changes in its velocity and temperature components. Both temperature and velocity anomalies are partly reflected in large scale heaves of isopycnals, and potentially relate to the varying proportion of warm subtropical waters and cold subpolar waters advected within the northern NAC branch.

A 2000's mean full-depth circulation computed along the merged AR7W/A25-Ovide line from repeated hydrographic profile and altimetry data indicates a minor contribution of the Labrador Sea to the basin wide mean MOC. However, the strength of the diapycnal overturning at AR7W has almost halved between the 1990's and the 2000's, confirming the importance of the region for the low-frequency MOC variability.

**KEY-WORDS**

Ovide - Subpolar Gyre - Subtropical Gyre - North Atlantic - Variability - Meridional Overturning Circulation - North Atlantic Current - ORCA025 - ARIANE - Altimetry

*Auteur*

**Damien Desbruyères**

*RESUME*

La circulation méridienne de retournement (MOC) de l'Atlantique Nord est une composante clé du système climatique global, via son rôle dans la redistribution de chaleur, d'eau douce et de propriétés chimiques entre hautes et basses latitudes. Aux moyennes et hautes latitudes, le Courant Nord-Atlantique (NAC) forme la branche haute de la MOC. Il s'écoule vers le nord-est à la frontière des gyres subpolaire et subtropical, et se divise en deux branches principales dans l'Est du gyre subpolaire: une branche nord qui recircule vers l'ouest dans le gyre subpolaire et une branche sud qui alimente les mers Nordiques.

Une simulation réaliste haute résolution (ORCA025-G70, 1/4°) est combinée à un outil d'analyse Lagrangienne pour étudier la variabilité de la MOC (1965-2004) à travers la section A25-Ovide qui joint le Portugal au Groenland. Deux cellules de retournement vertical sont identifiées: une cellule subtropicale connectant les hautes et basses latitude, et une cellule interne au régions subpolaire. La variabilité décennale de la MOC est associée à des changements synchronisés des apports subtropical et subpolaire dans le NAC. Ce dernier subit d'importantes restructurations horizontales caractérisées par la variabilité opposée de ses deux branches. Ces modifications de la distribution horizontal du transport sont principalement régies par la variabilité de l'afflux subtropical.

Les variations du transport de chaleur à travers A25-Ovide sont la cause principale de la variabilité du contenu de chaleur observée dans l'est du gyre subpolaire (1965-2004). La variabilité du transport de chaleur résulte d'un déséquilibre entre des changements opposés de ses composantes "vitesse" et "température". Les anomalies de vitesse et température sont en partie reflétées dans des déplacements verticaux d'isopycnes, potentiellement associés à la proportion changeante de masses d'eau subtropicales et subpolaires transportées par la branche nord du NAC.

Une circulation surface-fond moyenne calculée depuis des mesures hydrographiques répétées et des mesures altimétriques indique une contribution mineure de la mer du Labrador pour la MOC global. Cependant, l'intensité du retournement diapycnal à AR7W a presque diminué de moitié entre les 1990's et les 2000's, confirmant l'importance de la région pour la variabilité basse-fréquence de la MOC.

**MOTS-CLES**

Ovide - Gyre Subpolaire - Gyre Subtropical - Atlantique Nord - Variabilité - Circulation Méridienne de retournement - Courant Nord Atlantique - ORCA025 - ARIANE - Altimétrie



# Contents

<b>1</b>	<b>Introduction</b>	<b>4</b>
1.1	General Oceanic Circulation and Climate . . . . .	4
1.2	The mean circulation in the North Atlantic: some key elements . . . . .	7
1.2.1	Context . . . . .	7
1.2.2	The subpolar gyre circulation . . . . .	9
1.3	Decomposing the three-dimensional circulation . . . . .	18
1.4	Interannual to decadal oceanic variability in the North Atlantic . . . . .	21
1.4.1	The North Atlantic Oscillation . . . . .	21
1.4.2	The oceanic response to the NAO: some key studies . . . . .	23
1.5	Aims of the PhD . . . . .	32
<b>2</b>	<b>Observational and Modeling Tools</b>	<b>36</b>
2.1	Observational Datasets . . . . .	36
2.1.1	Ovide cruises . . . . .	36
2.1.2	AR7W cruises . . . . .	37
2.1.3	Satellite altimetry: the AVISO record . . . . .	38
2.1.4	The World Ocean Atlas 2009 . . . . .	38
2.2	The ORCA025-G70 simulation . . . . .	39
2.2.1	Global configuration . . . . .	39
2.2.2	Evaluation of the ORCA025-G70 simulation . . . . .	40
2.2.3	The Lagrangian analysis tool: ARIANE . . . . .	52

<b>3</b>	<b>Decadal variability of the <math>\text{MOC}_\sigma</math> across the A25-Ovide section</b>	<b>54</b>
3.1	Introduction . . . . .	55
3.2	The mean $\text{MOC}_\sigma$ across the A25-Ovide section: spatial structure and composition	59
3.2.1	The Eulerian view . . . . .	60
3.2.2	The Lagrangian analysis . . . . .	62
3.3	Variability of $\text{MOC}_\sigma$ . . . . .	70
3.3.1	The Eulerian view . . . . .	70
3.3.2	The Lagrangian analysis . . . . .	73
3.4	On the link between the intensity and the spatial extent of the subtropical inflow	77
3.5	Discussion . . . . .	81
3.6	Conclusion . . . . .	82
<b>4</b>	<b>Decadal heat content variability in the eastern Subpolar Gyre</b>	<b>85</b>
4.1	Introduction . . . . .	86
4.2	Validation of simulated heat content variability in the eastern SPG . . . . .	89
4.3	Heat budget in the eastern SPG . . . . .	91
4.4	Full-depth heat transport variability at A25-Ovide . . . . .	95
4.4.1	Spatial decomposition of $\text{HT}_{A25}$ : vertical and horizontal cell contributions	95
4.4.2	Temporal decomposition of $\text{HT}_{A25}$ : temperature and velocity contributions	98
4.5	On the link with the Meridional Overturning Circulation variability . . . . .	105
4.6	A Lagrangian approach for investigating temperature and associated heat transport anomalies . . . . .	116
4.6.1	Reconstructing the $\text{HT}_\theta$ signal in ARIANE . . . . .	116
4.6.2	Decomposition of $\text{HT}_\theta^{\text{Lag}}$ . . . . .	117
4.7	Conclusion . . . . .	124
<b>5</b>	<b>The mean 2002-2010 circulation state along the merged AR7W/A25-Ovide line</b>	<b>127</b>
5.1	Introduction . . . . .	128

5.2	Schematic circulation in the Labrador Sea . . . . .	131
5.3	Mean summer hydrography at AR7W in the 2000's . . . . .	132
5.4	Mean summer velocity field across AR7W in the 2000's . . . . .	136
5.4.1	Some basic theory for absolute velocity calculations . . . . .	136
5.4.2	Application to the AR7W section . . . . .	137
5.5	Merging the AR7W and A25-Ovide lines: the basin wide picture . . . . .	144
5.5.1	Methodology applied to the Ovide data set . . . . .	144
5.5.2	Volume transport . . . . .	145
5.5.3	Heat transport . . . . .	148
5.6	A preliminary inter-comparison of the 1990's and 2000's circulation at AR7W .	149
5.7	Conclusion . . . . .	152
<b>6</b>	<b>Conclusion</b>	<b>155</b>
6.1	Decadal variability in the eastern subpolar gyre: $MOC_{\sigma}$ , heat transport and heat content . . . . .	157
6.1.1	Summary . . . . .	157
6.1.2	Related perspectives . . . . .	159
6.2	The 2000's mean circulation along AR7W/A25-Ovide from observational datasets	161
6.2.1	Summary . . . . .	161
6.2.2	Related perspectives . . . . .	163
<b>7</b>	<b>Appendix</b>	<b>165</b>
7.1	Appendix A: Alphabetic list of acronyms . . . . .	165
7.2	Appendix B: Merged fields of temperature, salinity and velocity along the AR7W/A25-Ovide line . . . . .	168
7.3	Appendix C: Chapter summaries in French . . . . .	175
7.3.1	Chapitre 3: La variabilité décennale de la $MOC_{\sigma}$ à travers la section A25-Ovide . . . . .	175

7.3.2	Chapitre 4: La variabilité décennale du contenu de chaleur dans l'Est du gyre subpolaire . . . . .	177
7.3.3	Chapitre 5: La circulation moyenne observée le long de la section AR7W/A25-Ovide . . . . .	179

# Chapter 1

## Introduction

### 1.1 General Oceanic Circulation and Climate

Recent decades were marked by a growing interest in Earth climate change and its potential social and environmental impacts. It has become crucial to reconstruct and understand past climate variability on a wide variety of timescales thereby providing clues to predict its future evolution. The global ocean is an essential climate component through its role in storing and redistributing heat, freshwater, carbon and other properties across the Earth regions. It is, for instance, responsible for a significant fraction of the total meridional heat transport, a key variable for monitoring climate fluctuations (Figure 1.1). Its contribution may even overcome that of the atmosphere in the tropical northern hemisphere (*Trenberth and Caron, 2001*). The Thermohaline Circulation (THC), often sketched as the *Great Conveyor Belt* (Figure 1.2), is a critical component of the global oceanic system. It is driven by spatial inhomogeneities in the density oceanic field and its long-term variability is associated with a variety of processes including air-sea buoyancy exchanges (heat and freshwater), ice melting and horizontal oceanic advection. As hypothesized in several climatic studies, a modification of the Earth hydrological cycle under global warming scenarios would alter the strength of the THC and associated heat transport with substantial climatic implications (e.g. *Rahmstorf, 1999; Gregory et al., 2005*). Simulate the future behavior of the THC is a complex task yet, as illustrated by the sparsity

of climate model results published in the last *IPPC* report (Figure 1.3). It requires a precise understanding of the complex and various processes involved and thus partly relies on modeling and observational studies of its past variability.

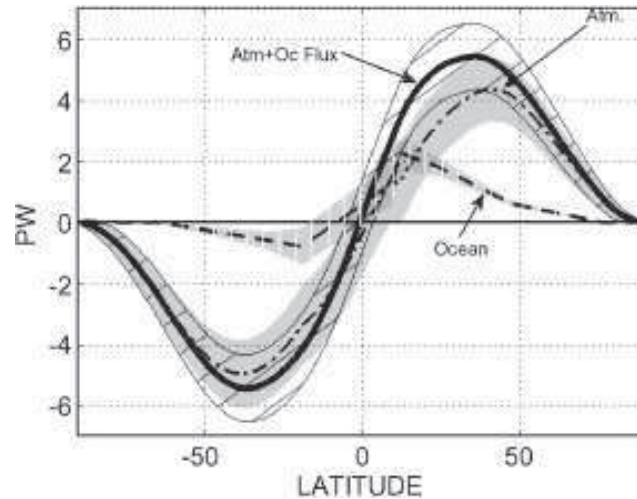


**Figure 1.1:** Total meridional heat transport of the combined ocean/atmosphere system estimated from the *Earth Radiation Budget Experiment* (solid), direct ocean measurements (dashed) and atmospheric contribution as residual (dashed-dotted). Taken from Wunsch (2005).

An important component of the global THC occurs in high latitude regions of the North Atlantic ocean. There, buoyancy exchanges with the overlying atmosphere produce dense water masses that spread equatorward in the deep and abyssal ocean, balanced in the upper layers by a returning northward flow of warm and salty waters. The subpolar North Atlantic has thus received much attention in climate-relevant studies, as seen by the high data-coverage of the region and the large amount of diverse analysis performed in this sector. Although the basic features of its mean large scale circulation are relatively well-known, much remains to be done to identify and assess the main drivers and actors of its low-frequency variability.

The present chapter starts by a broad description of the North Atlantic Ocean circulation, with a focus on the subpolar region. We then provide some basic conceptual definitions frequently used in the literature to study this complex, three-dimensional flow field. Finally, some spatio-temporal index of the interannual to decadal North Atlantic variability will be briefly reviewed and used to introduce the main questions raised in the following chapters. This short



**Figure 1.2:** Simplified representation of the global Thermohaline Circulation. Arrows indicate the direction of the flow. Warm and salty surface pathways are shown in orange; Cold deep branches are shown in blue. Taken from Lozier (2010). Credit: Joe LeMonnier.

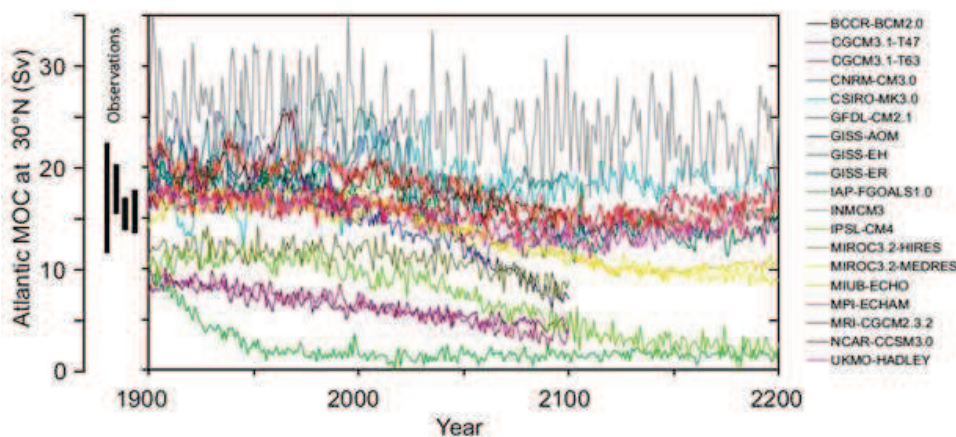


**Figure 1.3:** Climate Change 2007: Working Group I: The Physical Science Basis. Evolution of the Atlantic meridional overturning circulation (MOC) at 30N in simulations with the suite of comprehensive coupled climate models from 1850 to 2100 using 20th Century Climate in Coupled Models (20C3M) simulations for 1850 to 1999 and the SRES A1B emissions scenario for 1999 to 2100. Units are in Sv ( $1 \text{ Sv} = 10^6 \text{ m}^3 \cdot \text{s}^{-1}$ ).

literature review will notably serve as a benchmark for the validation of the ORCA025-G70 simulation presented in chapter 2.

## 1.2 The mean circulation in the North Atlantic: some key elements

### 1.2.1 Context

The structure of the large scale oceanic circulation is evidently much more complicated than the simple *conveyor belt* representation of the buoyancy-forced circulation. In reality, both limbs of the North Atlantic THC are embedded in basin wide wind-driven horizontal circulations: the anticyclonic subtropical gyre and the cyclonic subpolar gyre. They approximately occupy the 20°N-45°N and 45°N-65°N latitudinal bands and have centers of action located near Bermudas and in the Labrador Sea, respectively. Hence, the current systems of the North Atlantic Ocean are maintained through both air-sea fluxes of buoyancy and momentum. The climatological pattern of heat flux, freshwater flux, and windstress curl are shown in Figure 1.4a, 1.4b and 1.4c, respectively.

Overall, subpolar regions lose heat to the atmosphere, most strongly over the northeastward extension of the Gulf Stream where heat flux reaches  $150 \text{ W m}^{-2}$ , but also in the Labrador Sea and in the eastern subpolar gyre (about 50 to  $100 \text{ W m}^{-2}$ ). Ocean heat gain occurs in the vicinity of Newfoundland and in the eastern subtropical Atlantic. The spatial distribution of air-sea freshwater fluxes shows a transition from net evaporation south of 40°N - 45°N to net precipitation north of it. Evaporation is strong off Cape Haterras and in the eastern subtropical area, while precipitation is strong along the eastern Greenland margin and in the vicinity of Flemish Cap. The mean pattern of windstress curl is characterized by negative (resp. positive) values south (resp. north) of a line joining Cap Haterras and Scotland. Negative (resp. positive) windstress curl is associated with a downward (resp. upward) Ekman pumping and an anticyclonic (resp. cyclonic) circulation. Thus, the line of zero wind-stress curl is often

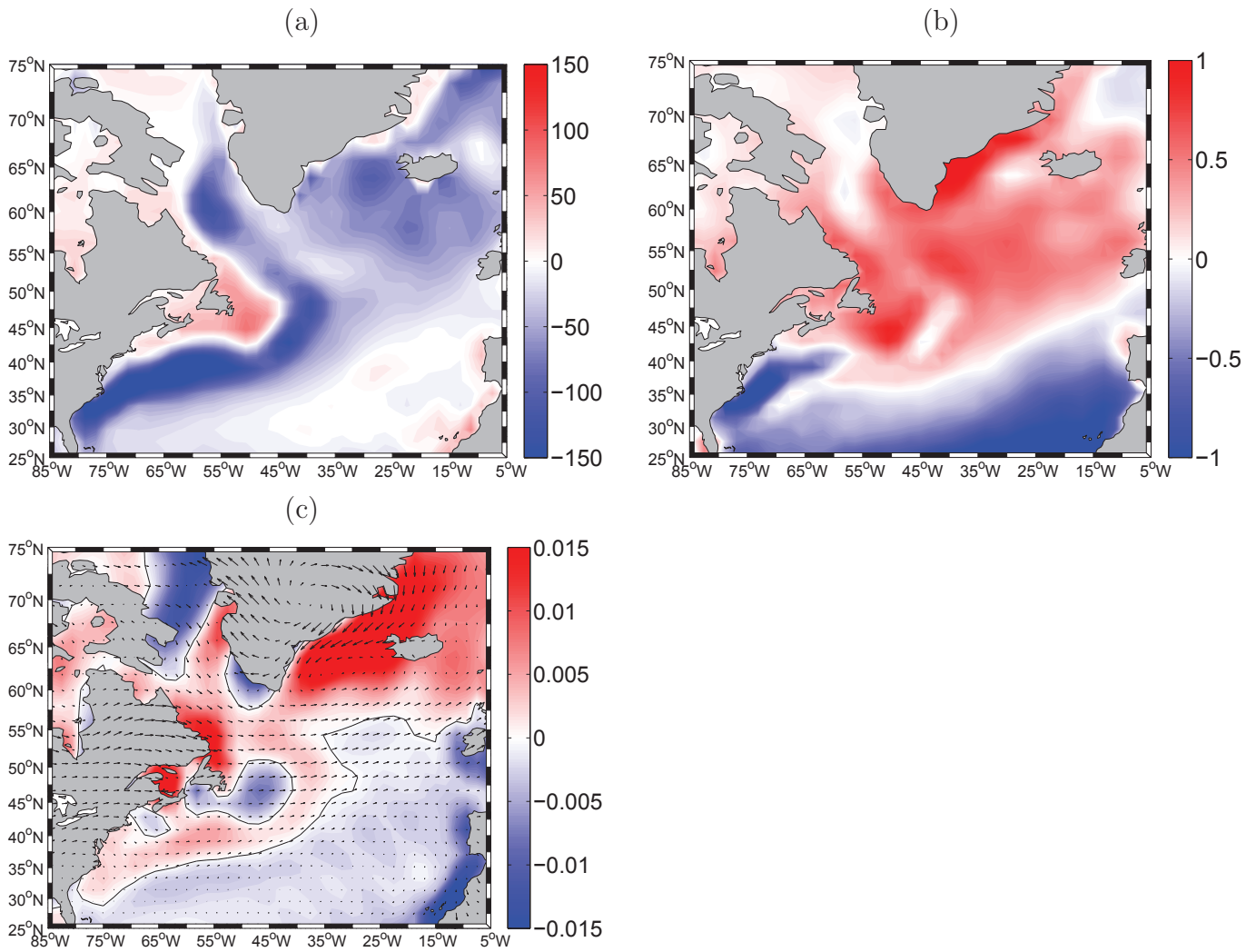


**Figure 1.4:** Climatological field of (a) air-sea heat flux ( $W m^{-2}$ , positive downward), (b) air-sea freshwater flux ( $m year^{-1}$ , positive upward) and (c) windstress curl ( $N m^{-3}$ ) from the NCEP climatology (1981-2010). The black line in (c) indicates the zero windstress curl line.

considered as a climatological boundary between the subtropical and subpolar gyre circulation.

Below, we present simple observational diagnostics and build on previous studies based on assimilated model simulations to provide a description of water masses and circulation in the subpolar North Atlantic. As the description goes on, the reader can refer to Figure 1.5 which shows a schematic representation of the upper, intermediate and deep current systems in the subpolar gyre.



**Figure 1.5:** Schematic representation of the upper (red), intermediate (purple) and deep (blue) circulation in the northern North Atlantic. Courtesy of Pascale Lherminier.

## 1.2.2 The subpolar gyre circulation

### The upper layers

The surface temperature and circulation can now be easily mapped thanks to the advance of satellite measurements and the dense coverage of surface drifter floats. The mean sea-surface temperature (SST) from the World Ocean Atlas (WOA) 2009 and surface geostrophic currents from AVISO in the North Atlantic for the period 1992-2008 are shown in Figure 1.6 (see Chapter 2 for details about these data sets). The main regions and topographic features of the northern North Atlantic discussed in the text are indicated.

The strongest surface velocities and associated eddy kinetic energy are seen in the Gulf Stream extension ( $\sim 0.9 \text{ m s}^{-1}$ ) and along the northern and western boundaries of the subpolar gyre ( $\sim 0.4 \text{ m s}^{-1}$ ). Both flows meet in the vicinity of Flemish Cap ( $45^\circ\text{N} - 45^\circ\text{W}$ ) and the resulting mixture of cold/fresh subpolar and warm/salty subtropical waters forms the so-called

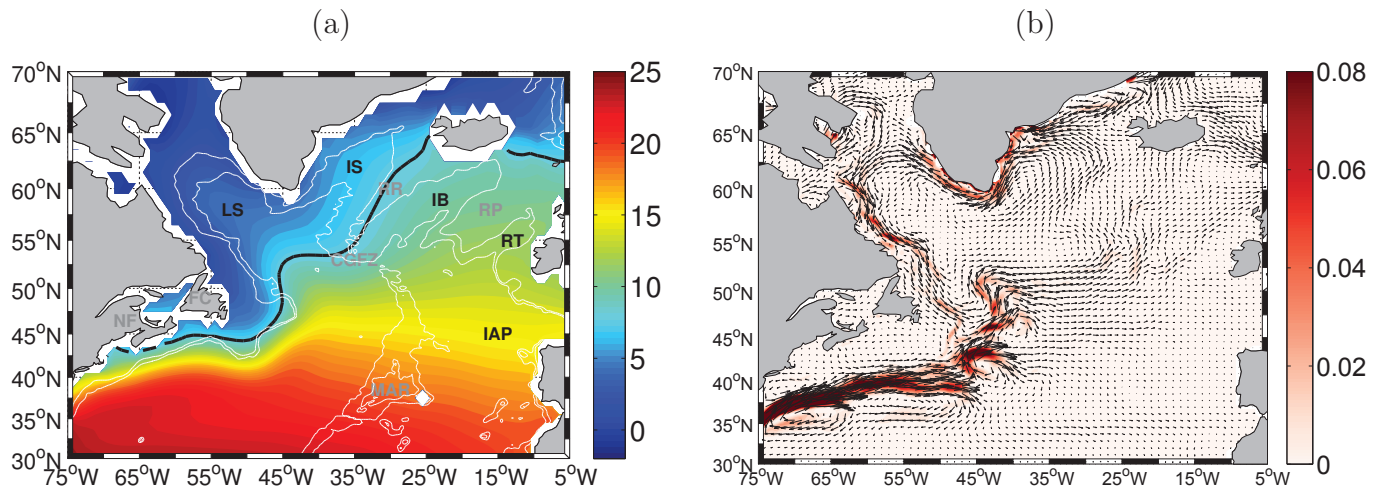


**Figure 1.6:** Maps of time-averaged (a) sea surface temperature from the World Ocean Atlas climatology ( $^{\circ}\text{C}$ ) and (b) absolute surface geostrophic currents from AVISO ( $\text{m s}^{-1}$ ) superimposed on the corresponding EKE field ( $\text{m}^2 \text{s}^{-2}$ , red colorscale), for the period 1992-2008. The thin white lines in (a) refer to the 2000m and 3000m isobaths. The thick black line indicates the  $8^{\circ}\text{C}$  isotherm, a proxy for the subpolar front position. The topographic features and major basins are labeled as follow: LS (Labrador Sea), IS (Irminger Sea), IB (Iceland Basin), RT (Rockall Trough), IAP (Iberian Abyssal Plain), MAR (Mid-Atlantic Ridge), RR (Reykjanes ridge), CGFZ (Charlie Gibbs Fracture Zone), RP (Rockall Plateau), NF (Newfoundland) and FC (Flemish Cap).

North Atlantic Current (NAC). The contrasted properties of the involved water masses induce a sharp hydrographic front, often referred to as the *subpolar* or *subarctic* front, which marks the northern limit of the subtropical gyre system. There is no unique definition of the subpolar front in the literature. Here, it is defined as the  $8^{\circ}\text{C}$  sea-surface isotherm (black line in Figure 1.6a). At about  $50^{\circ}\text{N} - 43^{\circ}\text{W}$ , the NAC recirculates around the so-called "Northwest Corner" (Worthington, 1976) and continues its routes eastward as a broader and weaker flow toward the Mid-Atlantic Ridge (MAR). The strong topographic features of the MAR constrain the NAC to split into distinct branches above the Charlie Gibbs (CGFZ,  $53^{\circ}\text{N}$ ), Faraday (FFZ,  $50^{\circ}\text{N}$ ) and Maxwell (MFZ,  $48^{\circ}\text{N}$ ) fracture zones (e.g. Sy *et al.*, 1992; Schott *et al.*, 1999; Belkin and Levitus, 1996; Bower and von Appen, 2007). This is illustrated in Figure 1.7, which shows the spatial distribution of isopycnal drifting floats above the MAR in the 1990's (taken from Bower and von Appen (2007)). The volume transport of the NAC in the vicinity of the MAR was estimated as  $20 \pm 5 \text{ Sv}$  ( $1 \text{ Sv} = 10^6 \text{ m}^3 \text{ s}^{-1}$ ) using different tools and approaches (e.g. Sy, 1988; Krauss, 1995; Perez-Brunius *et al.*, 2004).

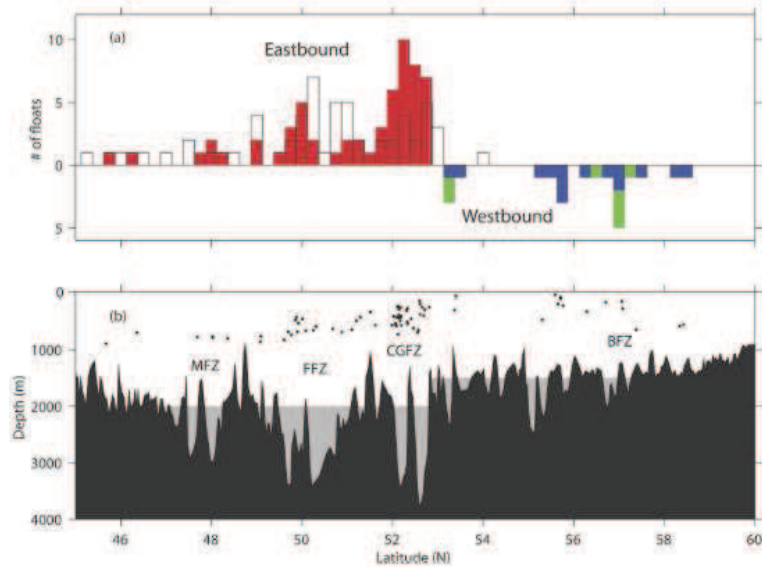


**Figure 1.7:** Latitudinal distribution of drifting floats launched in the northern North Atlantic as they cross the MAR in the 1990's. The crossing (resp. launch) latitudes of floats are shown with filled (resp. unfilled) bars. The bottom panel shows the ridge crest (averaged over a longitudinal band that includes the eastern and western margin of the ridge), along with the spatial positions of the floats. Taken from Bower and von Appen (2007)

In the northeastern Atlantic, the NAC follows three main paths. Surface velocities east of the MAR ( $\sim 0.1 \text{ m s}^{-1}$ ) are much weaker than in the western basin. A recirculating branch feeding the eastern limb of the subtropical gyre is observed in the Iberian abyssal plain (Paillet and Mercier, 1997). The remaining water masses are advected within the eastern subpolar gyre as two main branches located on each sides of the Rockall Plateau: in the Iceland Basin and in Rockall Trough (e.g. Fratantoni, 2001; Bower et al., 2002; Flatau et al., 2003). In the present manuscript, those two branches will be referred to as the northern and southern NAC branch, respectively. The latter flows into Rockall Trough and crosses the Feroe-Scotland sill to feed the Norwegian Current in the Nordic Seas. The northern branch flows cyclonically around the Iceland basin and constitutes the eastern limb of the subpolar gyre. While some of its water bifurcates northeastward across the Iceland-Feroe sill, the remaining circulates around and over Reykjanes Ridge and continues its route as the Irminger Current. Interestingly, the southwestward flow along the eastern flank of Reykjanes Ridge is somewhat weak in the surface record (Reverdin et al., 2003; Flatau et al., 2003) but is clearly visible at subsurface

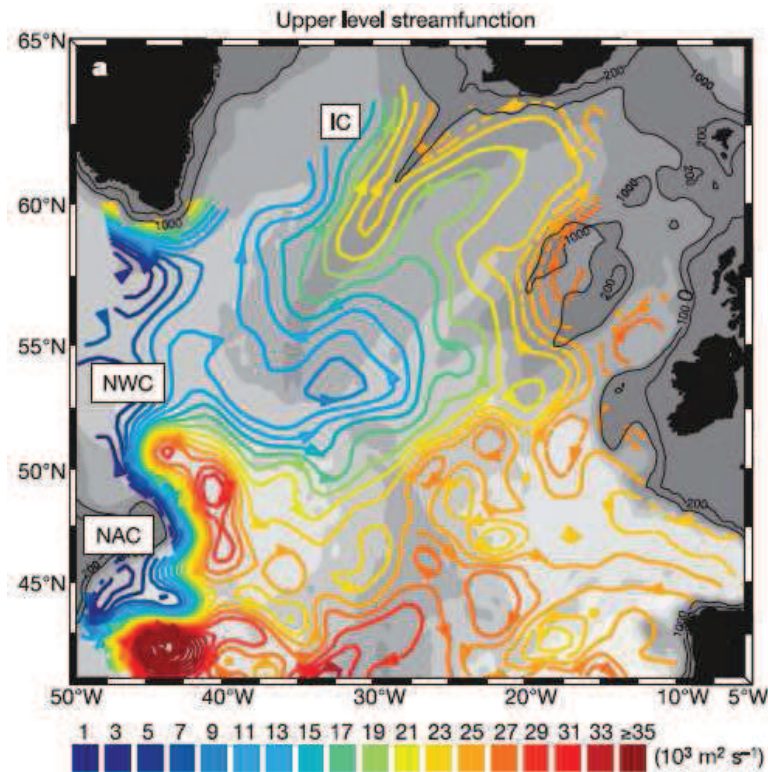


**Figure 1.8:** Mean streamfunction on the  $\sigma_0 = 27.5$  isopycnal surface in the subpolar North Atlantic, deduced from subsurface float data. Taken from Bower *et al.* (2002)

levels (Lavender *et al.*, 2000; Bower *et al.*, 2002). This is illustrated in Figure 1.8, which shows a time-averaged picture of the circulation on the  $\sigma_0 = 27.5$  isopycnal surface, a lower bound for thermocline waters in this region.

The total transport from the Iceland Basin to the Irminger Sea is estimated as  $\sim 13$  Sv (Schott *et al.*, 2004). Note from Figure 1.6a and Figure 1.8 that the Irminger Current is also directly fed by NAC waters from the CGFZ. It then flows cyclonically in the basin and reaches relatively high velocities along the eastern margin of Greenland. There, the Irminger current is often dissociated from the East Greenland Current transporting fresh waters from the Nordic Seas and the Greenland shelfbreak. A third component of this boundary current was evidenced by Bacon *et al.* (2002): the East Greenland Coastal Current above the Greenland plateau, which plays a critical role in transferring freshwater from the Nordic Sea to the Atlantic ocean. The resulting (upper) boundary current follows its cyclonic journey in the Labrador Sea before

exiting the subpolar basin along the American continental slope as the Labrador Current.

### The intermediate and deep layers

Along their cyclonic paths around the gyre periphery and in the Nordic Seas, the NAC waters are actively transferred to higher density classes through mixing processes (both atmospherically-driven and internally-driven), and subsequently feed the lower limb of the THC. Two major sites for deep water formation are frequently discussed in the literature: the Labrador Sea and the Nordic Seas. In the Labrador Sea, strong buoyancy loss to the atmosphere during winter and intense cyclonic circulation trigger deep convective events that produce an homogenous body of relatively cold and fresh water: the Labrador Sea Water (LSW) [hydrography and circulation in the Labrador Sea will be further examined in Chapter 6]. Note that the western Irminger Sea has been suggested as a second site of upper LSW formation in the North Atlantic (e.g. *Pickart et al.*, 2003b,a). Those main regions where deep convection potentially takes place in the North Atlantic are easily observed in Figure 1.9, which shows a time-averaged picture of winter mixed layer depth in the North Atlantic derived from the Simple Ocean Data Assimilation (SODA) (taken from *Schott et al.* (2009)). Mixed layer depths exceeds 1000 m in the central Labrador Sea and Irminger Sea. Relatively deep mixed layers are also reached in the vicinity of the Fereo-Scotland sills but they reside in a lighter density range (*Schott et al.*, 2009). The LSW then spreads at intermediate depth, southward toward the subtropics (e.g. ?) and eastward toward the Irminger and Iceland basins (e.g. *Talley and McCartney*, 1982; *Yashayaev et al.*, 2007). The magnitude of LSW formation rate is still uncertain. Data-based studies provide an average estimate of  $4.4 \pm 2.4$  Sv (*Pickart and Spall*, 2007). The physical properties of LSW (volume, temperature, salinity) stands as crucial indicators for monitoring the state of the North Atlantic circulation and its response to atmospheric forcing variability (see Section 1.4).

The bottom layers of the lower THC limb are mainly composed of dense water masses originating in the Nordic Seas and cascading down the shallow sills between Greenland and Scotland (*Smethie and Swift*, 1989). This dense water export from the Arctic Ocean is compensated by

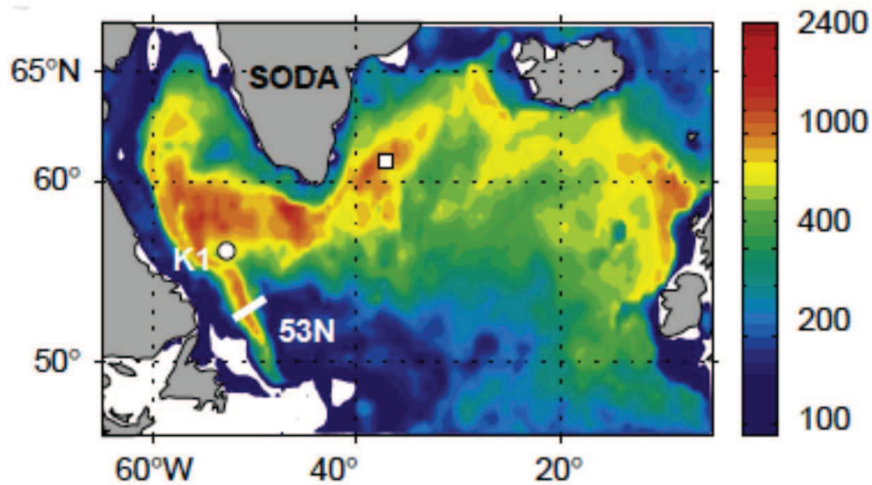


**Figure 1.9:** Mean March mixed layer depth derived from monthly SODA distribution for 1993-2001 and defined as the depth at which the density exceeds the surface density by  $0.1 \text{ kg m}^{-3}$ . Taken from Schott *et al.* (2009)

distinct inflows of Atlantic waters at upper levels, mainly from the northern and southern NAC branches east of Reykjanes Ridge. A simple mass budget for the region is shown in Figure 1.10 (taken from Hansen *et al.* (2008)). Two main classes of overflow waters can be identified: the Iceland-Scotland Overflow Water (ISOW) that recirculates around Reykjanes Ridge through CGFZ before entering the Irminger basin, and the denser Denmark Strait Overflow Water (DSOW) that occupies the bottommost layers of the Western Boundary Current along Greenland.

While LSW, ISOW and DSOW are presumably formed through air-sea interactions in their source regions, internal oceanic processes also contribute to the transport of the lower THC limb, mainly through entrainment of thermocline waters into the dense overflow in the vicinity of the Greenland-Scotland sills. Entrainment is believed to roughly double the volume transport of the overflow waters (e.g. Price and Baringer, 1994; Mauritzen and Häkkinen, 1999). The overall product of deep water masses (LSW, ISOW and DSOW) form altogether the so-called North Atlantic Deep Water (NADW), which flows cyclonically in the subpolar gyre before being exported equatorward within a deep western boundary current (DWBC). According to

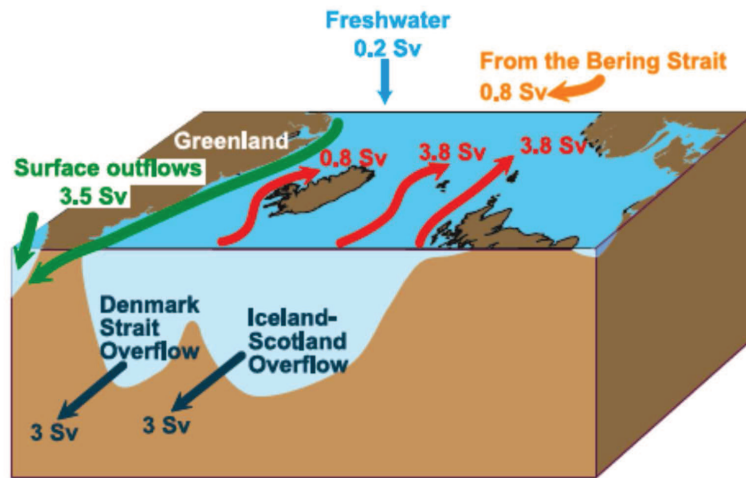


**Figure 1.10:** Schematic representation of the main exchanges of mass across the Greenland-Scotland sills. The value for the volume flux of the surface outflow has been chosen to acquire balance. Taken from Hansen et al. (2008)

the above description, its average transport should reach  $\sim 16$  Sv (LSW (4 Sv) + DSOW (3 Sv) + ISOW (3 Sv) + entrainment (6 Sv)).

### A focus at the A25-Ovide line

In the following studies, the circulation and hydrography of the eastern subpolar gyre will receive much attention. The A25-Ovide line joining Cap Farewell (Greenland) and Portugal will be used as a reference section for studying their decadal variability (see Figure 1.5 for the section position and chapter 2 for details about the Ovide project and associated data set). Time-averaged sections of temperature, salinity and velocity at A25-Ovide from five summer cruises in the 2000's were computed by N.Daniault (LPO). They are shown in Figure 1.11. In chapter 6, those fields will be merged with concomitant estimates along the A7RW line in the Labrador Sea to provide a picture of the mean basin wide hydrography and circulation in the 2000's. Here, we just concentrate on a broad qualitative description at A25-Ovide.

The strong downward sloping of isotherms from Greenland to Portugal reveals the substantial densification of surface and subsurface waters as they move cyclonically along the eastern boundary of the subpolar gyre. The main water masses encountered along the A25-Ovide line

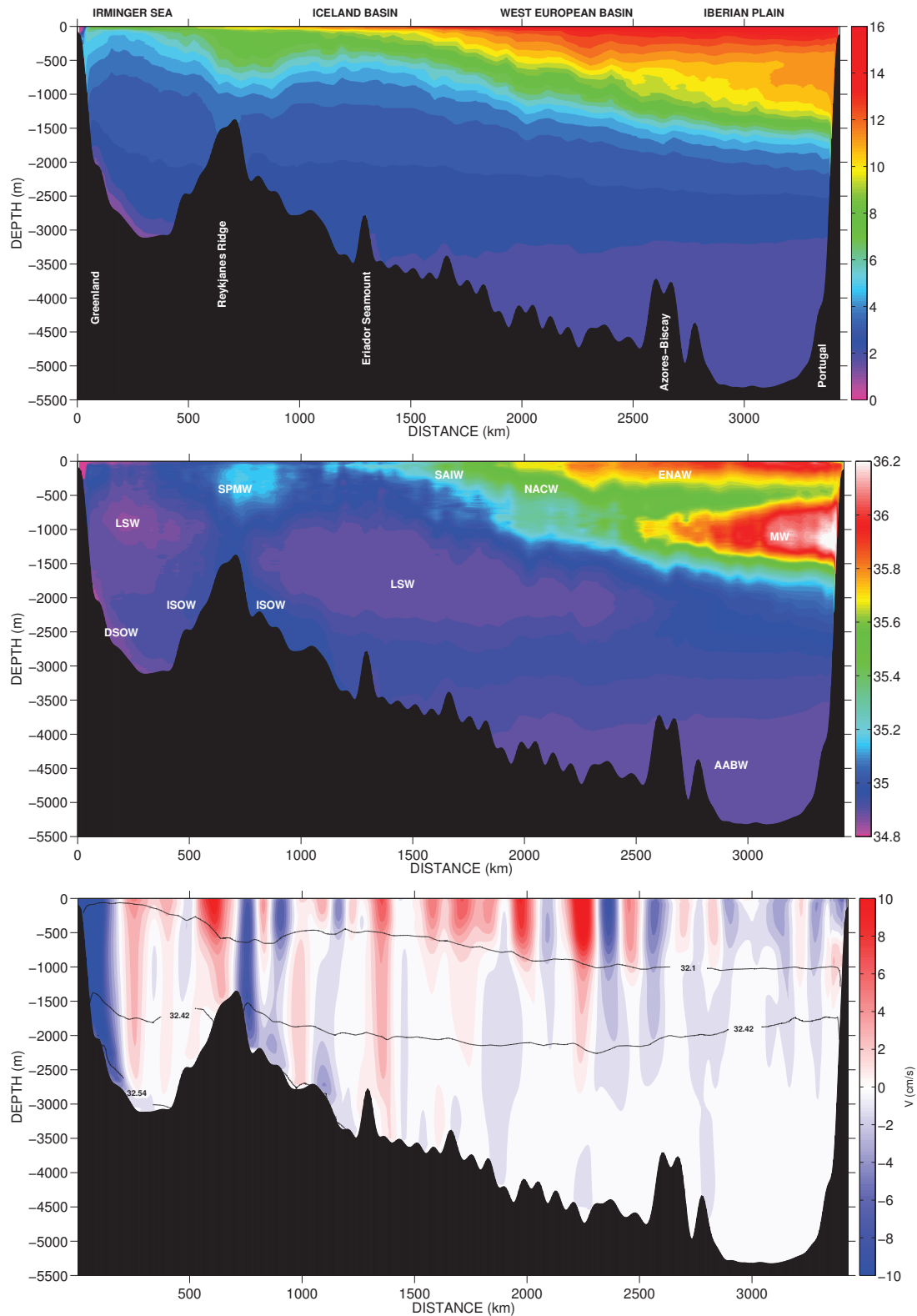


**Figure 1.11:** Time-averaged section of temperature (top, °C), salinity (middle) and velocity (bottom,  $\text{cm}\cdot\text{s}^{-1}$ ) at the A25-Ovide line, deduced with a gridding-then-averaging method performed from five summer hydrographic surveys in the 2000's (Credits of N. Daniault). Details about the inverse method used to compute the absolute velocity field are provided by Lherminier et al. (2010). The major basins and topographic features are indicated. Water masses are labeled as follow: NACW (North Atlantic Central Water), ENAW (Eastern North Atlantic Water), SAIW (Subarctic Intermediate Water), MW (Mediterranean Water), SPMW (Subpolar Mode Water), LSW (Labrador Sea Water), AABW (Antarctic Bottom Water), DSOW (Denmark Strait Overflow Water) and ISOW (Iceland Scotland Overflow Water).

are indicated on the salinity field. Warm and relatively salty North Atlantic Central Waters (NACW) are observed within the upper layers of the West European Basin. NACW is often decomposed into two distinct water masses: the Eastern North Atlantic Water (ENAW) and the Subarctic Intermediate waters (SAIW) (e.g. *Harvey*, 1982). They primarily consist of a mixture of subpolar (from the Labrador Current) and subtropical waters (from the Gulf Stream) advected from the western Atlantic by the NAC. In the Iberian abyssal plain, the Mediterranean Water (MW) lies at about 1000m depth and is characterized by very high salinities. The homogenous body of water surmounting Reykjanes Ridge is a variety of the Subpolar Mode Waters (SPMW) that are formed during winter through air-sea interactions along the rim of the subpolar gyre (e.g. *Brambilla and Talley*, 2008; *Brambilla et al.*, 2008; *de Boisséson et al.*, 2012). The formation of SPMW is an important preconditioning of the upper layers for subsequent convection in the Irminger and Labrador Sea and associated formation of LSW. The latter is identified at A25-Ovide as a fresh and cold water mass lying in the middle of the section around 1500m depth. It is also observed in the Irminger Sea at about 1000m depth. Within the bottom layers, the Antarctic Bottom Water (AABW) is visible in the Iberian abyssal plain, while ISOW and DSOW are observed adjacent to the eastern flank of Reykjanes Ridge and Greenland, respectively.

The mean velocity field at A25-Ovide (Figure 1.11) contains the various components of the circulation described above. The circulation in the Irminger Sea is characterized by the strong barotropic Western Boundary Current (WBC) along Greenland and a weaker northward flow in the basin interior. The anticyclonic recirculation around Reykjanes Ridge revealed in the subsurface current record (see Figure 1.8) is shown to extend down to the ocean floor. To the east, the circulation is more baroclinic and encompasses distinct branches of the NAC. In the Iberian abyssal plain, the southward recirculation feeding the eastern limb of the subtropical gyre is visible, while the ocean interior is relatively quiescent. The isopycnal surface  $\sigma_1 = 32.1$ ,  $\sigma_1 = 32.42$  and  $\sigma_1 = 32.54$  delimit the upper, intermediate, deep and bottom layers of the eastern subpolar gyre (*Lherminier et al.*, 2010).

### 1.3 Decomposing the three-dimensional circulation

Although there exists no fundamental decomposition of the inherently coupled buoyancy and wind-driven circulations, the three-dimensional flow field is often partitioned into a variety of vertical and horizontal two-dimensional cells. The wind-driven circulation in the horizontal plane is often represented by a barotropic streamfunction ( $\psi_{BT}$ ) of the vertically-integrated flow. The shape of  $\psi_{BT}$ , as obtained from a "time-mean state nudging" assimilation method is shown in Figure 1.12 (taken from *Lu et al. (2007)*). The subtropical and subpolar gyres previously presented are well-visible and their maximum intensities reach 40 Sv and 45 Sv, respectively. The overall structure of the circulation is similar to that depicted in Figure 1.6b using altimetry data, denoting the strong surface signature of the depth-independent flow in mid-high latitude regions. Note the presence of several recirculating cell south of the Gulf Stream path, and in the Labrador and Irminger Sea (e.g. *Lavender et al., 2000*).

Deep water formation in high latitude regions and the subsequent circulation in the meridional-vertical plane are usually represented by an overturning streamfunction of the zonally-integrated flow, the so-called Meridional Overturning Circulation (MOC). Importantly, the term "MOC" refers to a geographical or conceptual representation of the circulation. It includes wind-driven currents and should not be confused with the "THC" appellation that involves a precise forcing mechanism (i.e. buoyancy fluxes). In the literature, the MOC is often computed in the depth ( $z$ ) framework and its intensity is thus representative of a net downwelling or sinking of surface waters. The shape of the  $MOC_z$  in the North Atlantic from SODA is shown in Figure 1.13a (taken from *Schott et al. (2009)*). The major feature is a northward transport of surface waters within the 0-1000m layer, a relatively confined downwelling north of  $\sim 50^\circ\text{N}$ , and a deep southward flow between 2000m and 3000m depth. According to the above description of the subpolar circulation, those three components of the  $MOC_z$  approximate the Gulf Stream/NAC flow, deep convection in high latitude regions, and the southward export of NADW. In agreement with the estimation of the mean NADW transport (see above), a maximum overturning

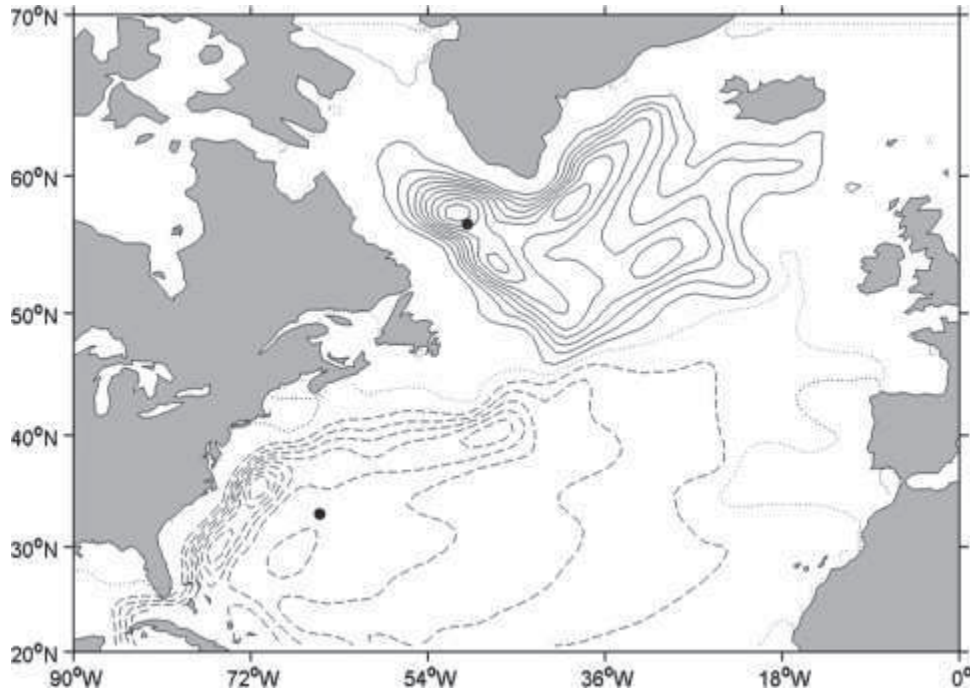


**Figure 1.12:** Time-averaged barotropic streamfunction ( $\psi_{BT}$ ) from the benchmark nudged simulation described in Lu et al. (2007). Contour intervals is 5 Sv, with solid (resp. dashed) contours denoting an anti-clockwise (resp. clockwise) circulation. Dotted contours indicate the  $\psi_{BT} = 0$  line, often used as a boundary between the subtropical and subpolar gyres.

of 16 Sv occurs at about 1000m depth and around 35°N. It amounts to 14 Sv near 43°N at the exit of the subpolar gyre. These are typical values for the mean strength of the  $MOC_z$  in the North Atlantic (e.g. Marsh et al., 2005). A weaker and counter-clockwise cell is visible in the bottommost layer, reflecting the northward spreading of Antarctic Bottom Water (AABW).

Another common representation of the meridional circulation involves potential density ( $\sigma$ ) as a vertical coordinate. The  $MOC_\sigma$  is thus representative of a diapycnal mass flux, which takes into account transformation processes occurring in the horizontal plane. The shape of the  $MOC_\sigma$  from SODA is shown in Figure 1.13b (taken from Häkkinen et al. (2011a)). The northward flow of thermocline waters is associated with a progressive densification as one moves to high latitude regions, while the dense return flow is confined to a relatively small density range. Two regions of maximum overturning emerge near  $\sigma_0 = 27.6$  in the subtropics around 35°N and in the subpolar gyre around 55°N. The latter signal was not present in the depth

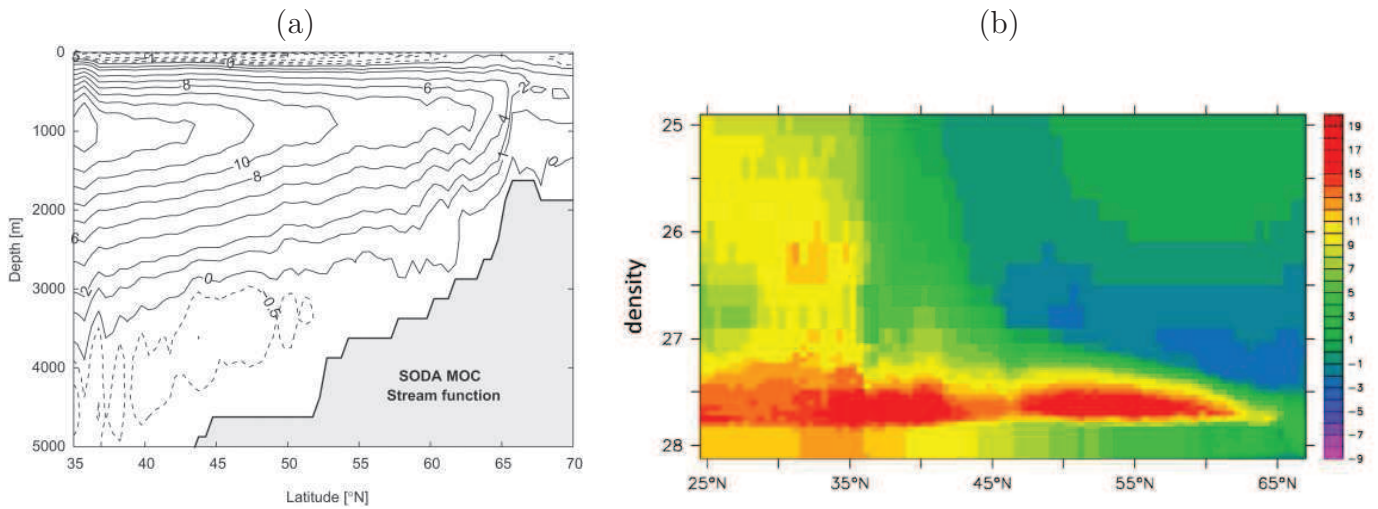


**Figure 1.13:** (a) Time-averaged (1958-2007) Meridional Overturning Circulation in the latitude-depth plane ( $MOC_z$ ) of the northern North Atlantic sector from SODA. Positive values with contour intervals of 2 Sv, negative contours in 0.5 Sv intervals. Taken from Schott et al. (2009). (b) Same as (a) but in the latitude-density plane ( $MOC_\sigma$ ). Taken from Häkkinen et al. (2011a).

framework and thereby reflect a diapycnal flux in the horizontal plane.

Those spatial decompositions of the three-dimensional flow field can be applied for the transport of any properties across a given basin wide section. For instance, the total meridional heat transport is primarily carried out by the  $MOC_z$  in subtropical regions, while the horizontal  $\psi_{BT}$  dominates in subpolar regions (e.g. Marsh et al., 2008). This will be further addressed in chapter 5 through a study of heat transport variability across the A25-Ovide section.

Having establish a time-averaged picture of the North Atlantic circulation, we can now focus on its variability. In a climatic perspective, it is of particular interest to understand the low-frequency response of this complex oceanic system to changes in large scale atmospheric forcing, as well as potential feedbacks between both compartments. The following section briefly reviews some indexes of the interannual/decadal oceanic variability derived from observational and modeling studies, and outline their relationship with the dominant mode of low-frequency atmospheric variability in the North Atlantic: the North Atlantic Oscillation (NAO).

## 1.4 Interannual to decadal oceanic variability in the North Atlantic

### 1.4.1 The North Atlantic Oscillation

The NAO is associated with an atmospheric redistribution of mass between subtropical and subpolar regions in the North Atlantic. It was initially defined as the surface pressure difference between the Iceland-low and the Azores-high pressure centers (*Hurrell, 1995*). In broad terms, a positive (resp. negative) phase of the NAO reflects enhanced (resp. weakened) westerlies and a northward (resp. southward) shift of the storm tracks toward Europe (Figure 1.14). Those basin wide variations of the wind field imply substantial changes in heat, freshwater and momentum fluxes at the air-sea interface that affect the ocean locally (mixed-layer response) and on large spatial scales (global oceanic circulation response).

In the present study, the NAO index is defined as the first principal component of winter sea-level pressure in the North Atlantic (based on the NCEP data set). It is shown in Figure 1.15 for the period 1958-2008. On interannual timescales, the NAO index describes a succession of positive and negative phases of variable durations. On decadal timescales, it is characterized by a gradual positive trend from low values in the 1960's to strong values in the early 1990's, and a subsequent decrease in the late 1990's and 2000's.

To briefly document the spatial and temporal characteristics of the NAO forcing, the first Empirical Orthogonal Function (EOF) of wind stress curl and air-sea heat flux in the northern North Atlantic are displayed in Figure 1.16 and Figure 1.17, respectively. The diagnostic is performed for the winter season only (December to March), that is when the NAO pattern is best defined (*Hurrell, 1995*). The principal components (PC) of both heat and momentum fluxes are well correlated with the NAO index ( $R = 0.8$  and  $R = 0.7$  significant at the 95% level<sup>1</sup>, respectively). We will restrict the description of both spatial patterns for the case of a positive

---

<sup>1</sup>In the remainder of the manuscript, all given correlations are significant within the 95% interval

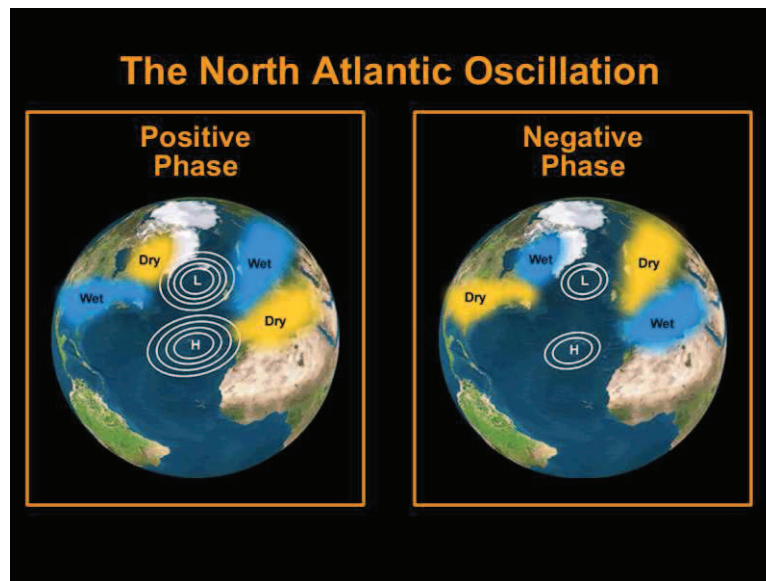


**Figure 1.14:** Schematic representation of a positive (left) and negative (right) phase of the North Atlantic Oscillation. During a positive (resp. negative) phase, the meridional pressure gradient between Iceland and Azores is large (resp. weak). The resulting westerlies are consequently stronger (resp. weaker) than usual and the storm track is shifted northward (resp. southward), providing wet and mild (resp. dry and cold) winter in northern Europe. Courtesy of UCAR.

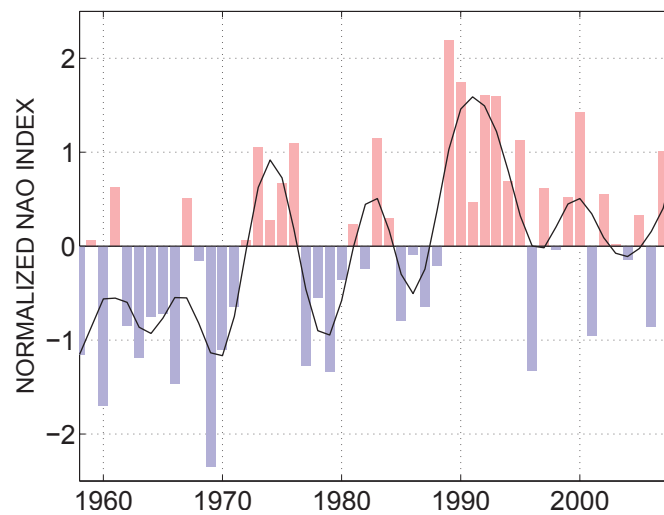


**Figure 1.15:** Normalized NAO index calculated as the first principal component of winter sea-level pressure in the North Atlantic. Annual values are shown in bars. A 3-year low-pass filtered time series is shown with the thin black line.

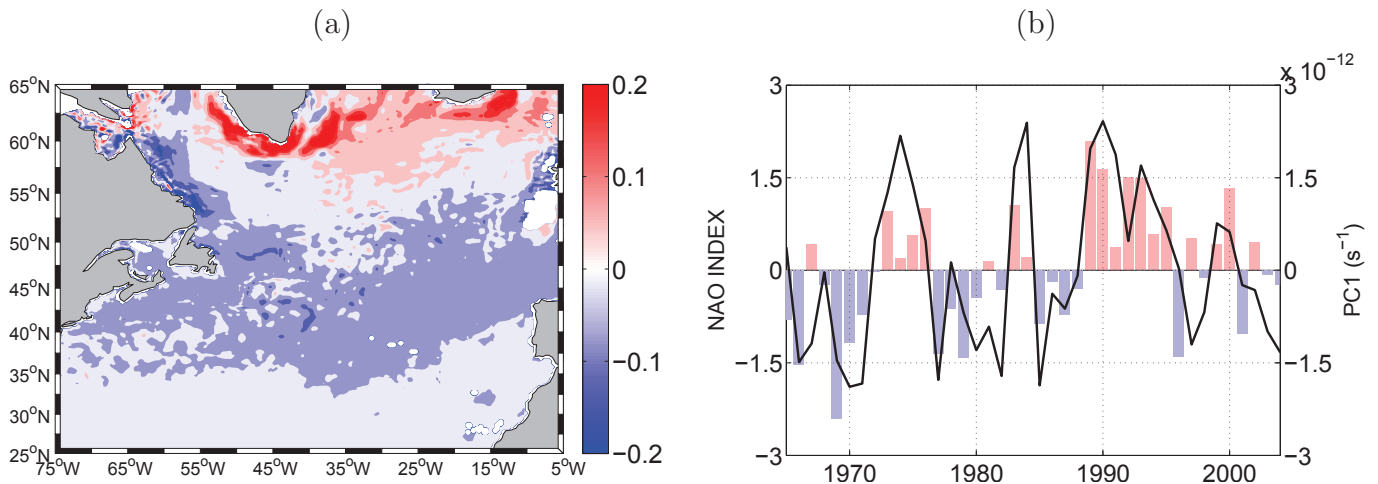


**Figure 1.16:** (a) Spatial pattern of the first EOF of winter (December - March) wind stress curl in the North Atlantic accounting for 15% of the total variance (unitless). (b) The associated principal component (black,  $s^{-1}$ ) along with the normalized NAO index.

NAO phase (that is positive PC's anomalies), keeping in mind that the inverse situation holds for a negative NAO phase.

The first mode of wind stress curl variability (15 % of variance explained) is characterized by strong positive anomalies around Greenland and Iceland north of 60°N, and a large band of weaker negative anomalies in the intergyre region between 35°N and 50°N. This dominant mode of wind stress curl changes can be understood as a meridional shift of the zero wind-stress curl line (*Marshall et al.*, 2001). The spatial structure of heat flux variability (28 % of variance explained) is characterized by two opposed poles of variability located in the center of both gyres: anomalous heat loss is observed in the Labrador Sea while anomalous heat gain characterized the western subtropics.

### 1.4.2 The oceanic response to the NAO: some key studies

Great efforts have been made to understand the various processes by which NAO-related changes in air-sea heat and momentum fluxes influences the hydrography and circulation of the North Atlantic. Those efforts were based on various approaches, using both observations (hydrographic sections, satellite altimetry, surface and subsurface floats) and models of different

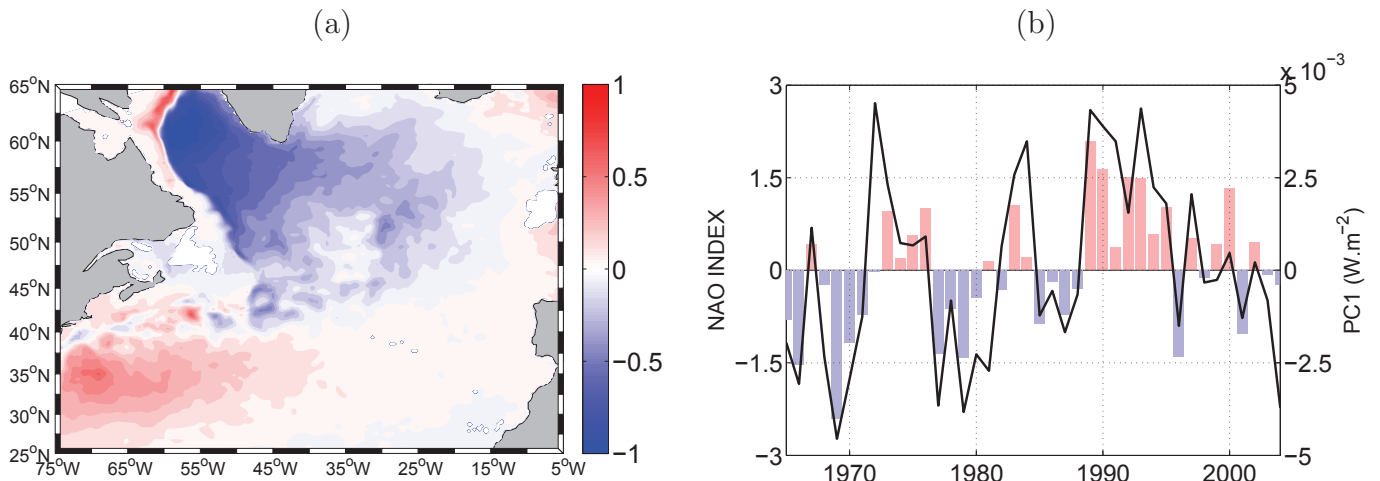


**Figure 1.17:** (a) Spatial pattern of the first EOF of winter (December - March) air-sea heat flux in the North Atlantic accounting for 28% of the total variance (unitless). (b) The associated principal component (black,  $W m^{-2}$ ) along with the normalized NAO index.

complexities (from simple box-models to "realistic" simulations at very high resolution). The use of sensitivity forcing experiments notably provided crucial information about the various mechanisms at play, whether wind or buoyancy-driven.

A first insight into the impact of the NAO in the North Atlantic can be obtained by focusing on the Labrador Sea sector. This area was effectively sampled since the late 1980's, mainly through hydrographic surveys along the AR7W line. Building on the resulting data set, *Yashayaev et al.* (2007) provided an original picture of changes in LSW production in the Labrador Sea between the late 1980's and the 2000's (Figure 1.18). Strong buoyancy loss associated with a persistent positive phase of the NAO during 1989-1995 led to the formation of dense and deep LSW, often referred to as the "classical" LSW (e.g. *Kieke et al.*, 2006; *Rhein et al.*, 2007). As shown in Figure 1.15, the NAO index turned to negative values in the winter 1995/96 and remained relatively weak afterwards (except in 2000), leading to a shallower and lighter LSW product, the "upper" LSW. A decadal view of this NAO-convection relationship in the Labrador Sea was recently provided by *Lu et al.* (2007) using an assimilated model spanning the period 1949-2001. Monthly density profiles at station Bravo in the central basin were used to construct a continuous index of deep convection (Figure 1.19). The three main periods of active convection (the early 1970's, the mid-1980's and the first half of the 1990's)

are consistently occurring during positive phases of the NAO.

A potential direct link between deep wintertime convection in the Labrador Sea and multi-decadal trends in the  $\text{MOC}_z$  (or  $\text{MOC}_\sigma$ ) is suggested by many numerical models. The occurrence of deep convective events in the Labrador Sea was shown to reverberate within a few years into the strength of the DWBC and associated  $\text{MOC}_z$  at the exit of the subpolar gyre (e.g. *Eden and Willebrand, 2001; Böning et al., 2006*). The equatorward propagation of these  $\text{MOC}_z$  anomalies accelerates in subtropical region, via fast boundary wave processes (e.g. *Getzlaff et al., 2005*). A typical  $\text{MOC}_z$  signal in hindcast simulations is a positive trend from low values in the 1960's to strong values in the mid-1990's and a subsequent decrease until the mid-2000's (e.g. *Häkkinen, 1999; Marsh et al., 2005; Biastoch et al., 2008*). Note that those changes are relatively weak in amplitude ( $\sim 2\text{-}3$  Sv) and are effectively masked by higher-frequency wind-driven anomalies (i.e. Ekman-induced overturning) or mesoscale eddy signals, most notably in low-mid latitude regions (*Baehr et al., 2004; Cunningham et al., 2007; Biastoch et al., 2008*). This prevent such long-term signals in the MOC intensity to be detected from relatively sparse basin wide and full-depth observations.

Finding observational and continuous proxy of the MOC is hence of primary importance. *Curry and McCartney (2001)* provided a detailed study of stratification changes in both the subpolar and subtropical gyre. Using hydrographic data in the upper 2000m of the water column in the central Labrador Sea and at Bermudas, they showed that their respective potential energy histories were interestingly similar in amplitude, and characterized by an out-of-phase relationship (top panels in Figure 1.20). Yet, the physical processes involved differ at both location. In the subpolar gyre, diabatic mixed layer dynamics dominates, whereas adiabatic displacements of the main pycnocline via baroclinic wave propagation are predominant in the western subtropical gyre. A simple difference between both time series (weighted by  $\frac{1}{f}$ , with  $f$  the Coriolis parameter) yields an original index of the intergyre flow intensity, namely the NAC (bottom panel in Figure 1.20). Note that this transport index assumes a level of no motion at depth, and thus only pertains for the baroclinic component of the flow. The decadal signal is characterized by a transport decline in the 1960's and a gradual intensification until the

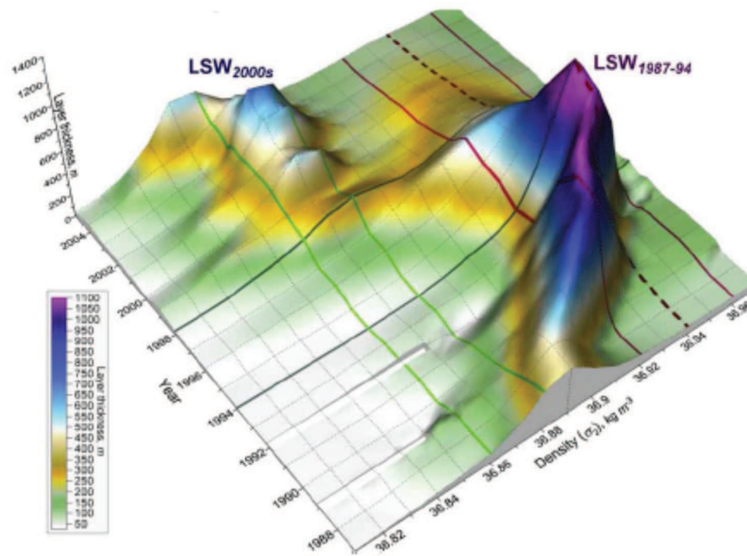


**Figure 1.18:** Volume and density properties of the Labrador Sea Water between 1988 and 2005. Taken from Yashayaev *et al.* (2007).

mid-1990's, and is thought to reflect a time integration of NAO-like buoyancy and wind forcing.

The transport index of Curry and McCartney (2001) was recently prolonged by Kieke *et al.* (2007) until 2003 to show a sharp slowing of the circulation since the NAO drop in the winter 1995/96. This was consistent with the famous study of Häkkinen and Rhines (2004) who revealed substantial sea-level changes in the North Atlantic during that period, as shown in the first EOF of (altimetry) SSH anomalies: the so-called *gyre index* (Figure 1.21). Its spatial structure shows a dipole pattern spanning the northern North Atlantic: while sea-level rose within the whole subpolar gyre from the early 1990's (indicative of a weakening circulation), it dropped in a region spanning the climatological position of the Gulf Stream/NAC system (indicative of an anomalous cyclonic circulation). As previously noted, the decay of the isopycnal dome induced by NAO-related buoyancy forcing was invoked to explain the subpolar gyre weakening, while the concomitant southward displacement of the zero windstress curl line

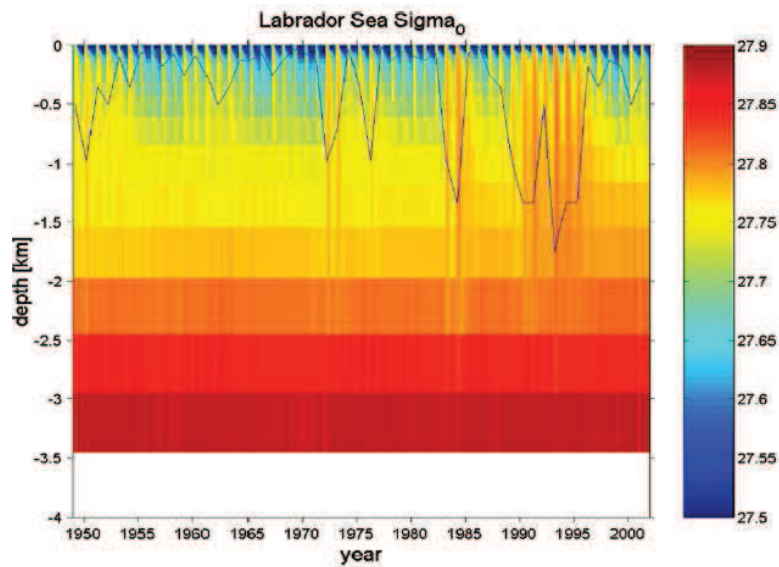


**Figure 1.19:** Changes in potential density ( $\text{kg m}^{-3}$ ) and associated depth of deep convection (km) at station Bravo (see Figure 1.13 for the station location) from a benchmark nudged simulation. Taken from Lu et al. (2007).

is potentially responsible for the setup of the cyclonic "intergyre gyre" (e.g. Marshall et al., 2001). In numerical hindcast simulations, the decreasing gyre index of the 1990's was shown to be preceded by a gradual positive trend from the late 1960's (Hátún et al., 2005; Böning et al., 2006), in good agreement with the aforescribed transport index of Curry and McCartney (2001). Overall, the link between large scale changes of the horizontal circulation depicted in the gyre index and the vertical MOC variability has not been fully examined.

Altimetry data combined with surface drifter floats were also used to document regional changes in the spatial structure of the NAC. Bower and von Appen (2007) showed the occurrence of distinct modes of the surface circulation in the vicinity of the MAR, characterized by the varying intensity and position of the main NAC branches. The authors suggested a link between those shifts in the surface circulation and interannual fluctuations of the NAO, with high (resp. low) NAO conditions preferably associated with a northerly (resp. southerly) position of the NAC, in line with other studies (e.g. Curry and McCartney, 2001). Combining drifters and altimetry data, Häkkinen and Rhines (2009) evidenced shifting pathways of the NAC southern branch in the early 2000's (Figure 1.22). The warm waters originating in the

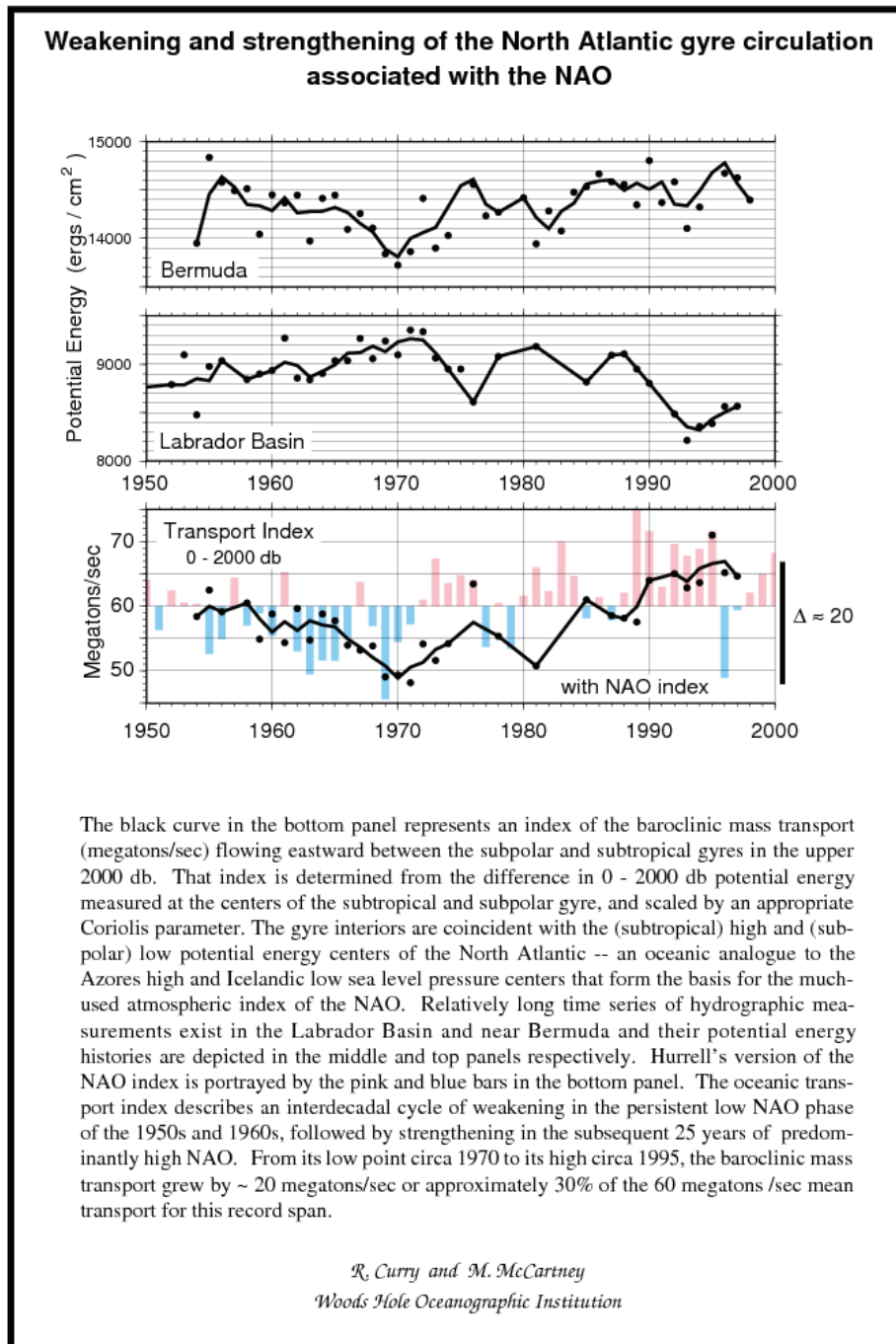


**Figure 1.20:** Index of the intergyre baroclinic transport (bottom) based on Available Potential Energy histories of the subtropical (top) and subpolar (middle) gyres. See panel for details. Taken from Curry and McCartney (2001).

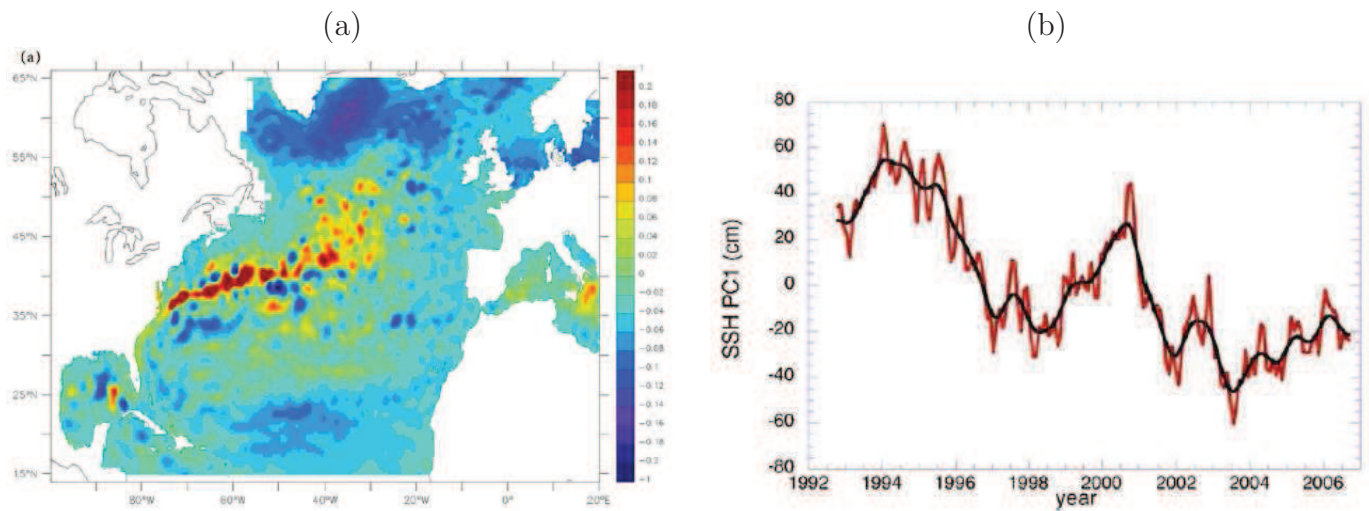


**Figure 1.21:** (a) Spatial pattern of the first EOF of sea-surface height from AVISO altimeter data in the North Atlantic (unitless). (b) The associated principal component (cm). Taken from Häkkinen and Rhines (2009).

subtropics increased their penetration toward Rockall Trough instead of turning southeastward in the eastern North Atlantic. Note that such an increased connection between the subtropical and subpolar basins may have also occurred in the late 1960's and mid-1980's, as seen in the numerical tracer experiments of Häkkinen *et al.* (2011a). Interestingly, the authors rejected the predominant role of the NAO (see Figure 1.16 and Figure 1.17) as a driving mechanism. Instead, the events of increased connections were shown to be associated with relatively weak gyre circulations induced by anomalously weak climatological wind forcing (captured by the second EOF of wind stress curl). As suggested by Chaudhuri *et al.* (2011), the link between these shifting pathways of the subtropical waters towards the eastern subpolar basin and the actual strength of the intergyre volume transport (and associated MOC) is still unclear and requires more investigations.

The shifting pathway of NAC waters observed during the 2000's stands as a potential cause for the concomitant warming and increase in salinity of the eastern subpolar gyre. Many observational studies have indeed showed a sharp reversal of the 1960's to 1990's freshening/cooling trend in the northeastern Atlantic (e.g. Holliday *et al.*, 2008), with salinity and temperature

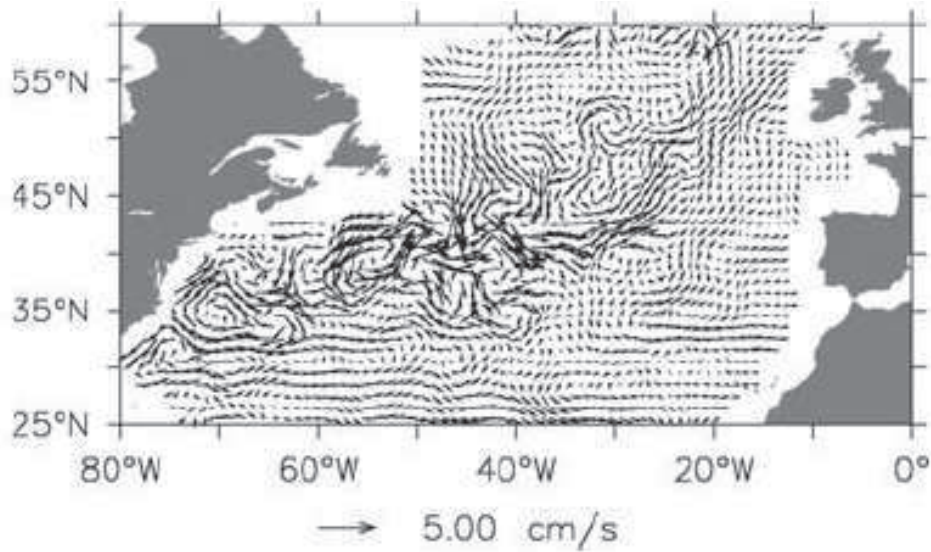
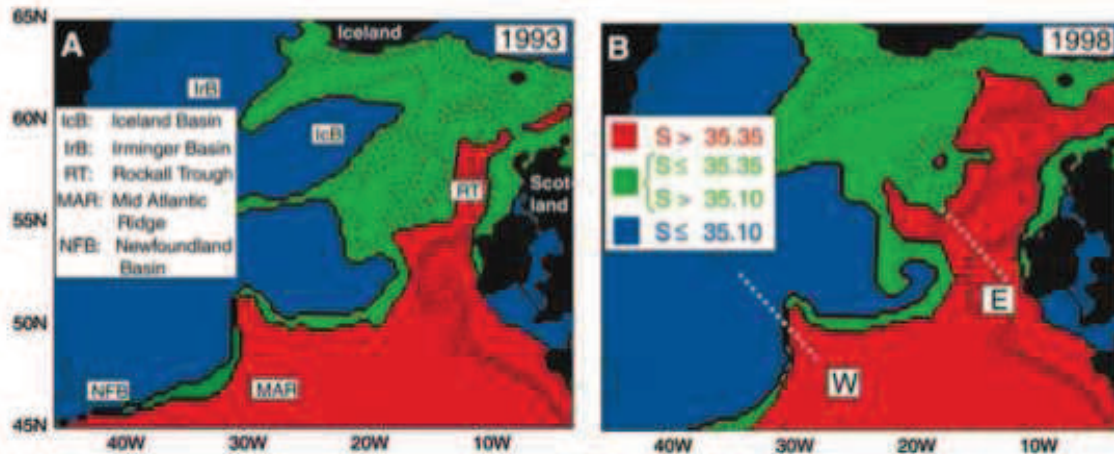


**Figure 1.22:** Difference of ocean surface current for the period [2001-2005] minus [1996-2000] deduced from real time OSCAR surface current fields. Taken from Häkkinen and Rhines (2009).

values not seen since the 1960's. Air-sea fluxes of heat and freshwater cannot account on their own for the observed changes, pointing out ocean dynamics as an important contributor. Using hydrographic data from repeated cruises along the A1E line joining Greenland and Ireland in the 1990's, *Bersh* (2002) highlighted a westward retreat of the subpolar front in the Irminger and Iceland basins after the abrupt NAO changes in 1995. This "contraction" of the subpolar gyre in the northeastern Atlantic was attributed to a reduced eastward transport of subarctic waters within the NAC. Consistently, *Holliday* (2003) studied interannual/decadal salinity and temperature variation at the Rockall Trough entrance from hydrographic surveys. They proposed a causal relationship between the warming/salinization post 1995 and changes in horizontal advection affecting the composition of the inflowing NAC waters. Likewise, *Thierry et al.* (2008) (from ARGO data) and *De Boisséson* (2010) (from an eddy-permitting model) suggested a link between the changing properties of the subpolar mode water above Reykjanes ridge and changes in ocean dynamics driven by the NAO.

The modeling results of *Hátún et al.* (2005) are of particular interest for the analysis presented in chapter 3 and 4. The authors showed a clear correspondence between the gyre index

(a)



(b)

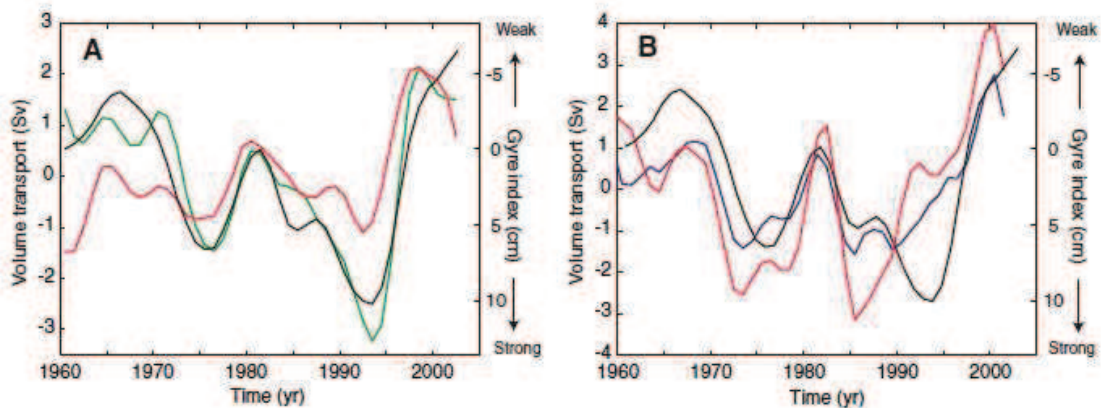


**Figure 1.23:** (a) Simulated spatial distribution of the upper salinity field in 1993 (left) and 1998 (right). Salinity criterion is applied to extract the signature of typical SPG water (blue), STG water (red), and a mixture of both source waters (green). (b) Simulated anomalies (3-year running mean) of upper-layer volume transport across the E (left) and the W section shown in (a), with the corresponding colors. Positive values of transport anomalies for the red lines on (A) and (B) indicate anomalous transport toward the northeast. Positive values of transport anomalies for the green line on (A) and the blue line in (B) indicate anomalous transport toward the southwest. The gyre index is shown in black. Taken from Hátún et al. (2005).

decadal fluctuations and the salinity content of the eastern subpolar gyre (Figure 1.23). By decomposing the NAC transport hydrographically into a fresh subpolar and a salty subtropical component, they highlighted an opposed behavior of both source waters on interannual/decadal timescales: when the gyre index is high the transport of cold subpolar (resp. warm subtropical) waters is strong (resp. weak) and the subpolar front shift eastward, and vice versa for a low gyre index phase. They concluded that the subpolar gyre dynamics was the main driver for salinity changes in the Atlantic inflow toward the Nordic Seas. Care should be taken, however, when interpreting transport indexes computed from hydrographic criterion. As was suggested by *Chaudhuri et al.* (2011), the northeastward transport of warm and salty water toward the eastern subpolar gyre may not be representative of the actual subtropical intergyre inflow. Likewise, an increasing transport of cold/fresh waters within the NAC does not necessarily imply a spin up of the subpolar gyre. Interestingly, *Herbaut and Houssais* (2009) pointed out the potential role of the wind-driven intergyre gyre in driving salinity anomalies in the eastern subpolar gyre, and consequently suggested no causal relationship between concomitant changes in the strength and the shape of the subpolar gyre. Hence, the validity of using hydrographic criterion to study the changing composition of the NAC (in terms of source waters) should be tested from alternative methods.

## 1.5 Aims of the PhD

The aforementioned studies have revealed recent and significant changes in the North Atlantic hydrography and circulation. The NAO was shown to modify large scale current systems in both the vertical (convective mixing) and horizontal plane (structure and intensity of the upper circulation), which lead to significant basin wide changes in temperature and salinity. Yet, the underlying mechanisms are not fully understood, and some more regional studies are needed. Most particularly, the low-frequency signals in the northeastern Atlantic (MOC, horizontal circulation, heat content) have not received so much attention and some important issues are still unanswered:

- What is the decadal variability of the MOC in the eastern subpolar gyre and how does it relate to the larger scale gyre circulation?
- Is there a link between the MOC variability and the changing structure of the North Atlantic Current (branches, recirculations)?
- What are the respective contributions of the subpolar (Labrador Current) and subtropical (Gulf Stream) circulations to the mean and anomalous NAC transport? Can we effectively isolate both inflows from hydrographic properties?
- How the spreading of subtropical water masses toward the eastern subpolar gyre relates to the actual intergyre volume transport?
- What are the main mechanisms behind heat transport variability in this particular region (temperature vs. velocity anomaly) and how they relate to the MOC variability? where do these changes preferentially take place? How do they compete with air-sea heat fluxes in driving heat content changes?
- Can we quantify the respective contribution of the western and eastern basins to the basin wide MOC/HT from observations?

The present PhD work attempts to answer those questions, using the A25-Ovide section as a reference line for various Eulerian and Lagrangian diagnosis. Since there exist no appropriate observational data sets for investigating such questions on the decadal timescale, we will use a numerical simulation (ORCA025-G70) forced with reanalysis products, which provides a realistic representation of the mean and anomalous circulation of the North Atlantic Ocean. Below, we briefly detail the goal of each following chapters.

- **Chapter 2** presents the observational and modelling tools used during the PhD. Building on the above literature review, the ability of the eddy-permitting ORCA025-G70 simulation to reproduce consistent circulation patterns in the North Atlantic (mean and variability) will be tested.

- **Chapter 3** is dedicated to a study of the decadal  $\text{MOC}_\sigma$  variability across the A25-Ovide section, with a focus on its upper limb. Investigating meridional volume exchanges in the density space appears more suitable in high latitude regions, due to the strong zonal inhomogeneity of hydrographic properties at constant depth. Hence, the  $\text{MOC}_\sigma$  is in our case a better proxy for water mass transformation processes than its  $\text{MOC}_z$  companion. By focusing on the upper  $\text{MOC}_\sigma$  limb at A25-Ovide, the overturning variability will be linked with spatio-temporal changes of the NAC current system, and most notably with the respective variability of its distinct branches in the eastern subpolar gyre. Emphasis will be made on the sources of the NAC transport and the respective contribution of the subpolar and subtropical inflows will be extracted. To overcome the issue of defining both source waters with distinct hydrographic properties, the ORCA025-G70 simulation will be combined with a Lagrangian analysis tool (ARIANE), thereby providing a complementary view of the NAC/ $\text{MOC}_\sigma$  mean structure and variability (pathways, amplitude) in the Lagrangian framework. This chapter is based on an article submitted in *Journal of Geophysical Research*.
- **Chapter 4** is dedicated to a study of decadal heat content changes in the eastern subpolar gyre. Understand temperature (and salinity) changes in this region, such as the sharp warming trend observed since the mid-1990's, is crucial since they may act as positive/negative feedbacks onto the MOC strength. Yet, modeling tools have rarely been used to study this significant regional variability, and the link between the basin wide heat transport variability, and related changes in the  $\text{MOC}_\sigma$  and NAC structure and intensity is still lacking. Most notably, the respective impacts of velocity and temperature anomalies on heat transport in the eastern subpolar gyre have not been precisely assessed so far. A heat budget calculation within a box bounded by the A25-Ovide section and the Greenland-Scotland sills will be performed, and spatio-temporal decompositions of the heat transport across A25-Ovide will be carried out to highlight the dominant mechanisms at play. ARIANE will be used to complement the Eulerian analysis. The content of

this chapter is in preparation for submission in *Progress in Oceanography*.

- **Chapter 5** provides a quantitative description of the mean basin wide oceanic state along the merged AR7W/A25-Ovide line, from repeated hydrographic measurements and satellite altimetry. To investigate the MOC variability from sparse full-depth hydrographic observations is a challenging task. Yet, when repeated over a certain time period, these surveys can help in characterizing the time-averaged circulation state. Of particular interest for the study of the MOC in the subpolar gyre is the respective contribution of the western (the Labrador Sea) and eastern (Irminger, Iceland and Nordic Seas) basins to the total transformation rates and basin wide heat transport. This issue will here be addressed for the 2000's time span. Some preliminary comparisons of changes in the Labrador Sea MOC between the 1990's and the 2000's will be presented.
- **Chapter 6** summarizes the main results and provides some hints for future work.

# Chapter 2

## Observational and Modeling Tools

The present chapter aims to present the different tools and datasets that will be used in the following analysis of the North Atlantic circulation. The first section is dedicated to a presentation of four observational datasets: hydrographic data from repeated cruises along the A25-Ovide and the AR7W lines, sea-surface height records from satellite altimeter, and the World Ocean Database 2009. The second section presents the ORCA025-G70 simulation and evaluates its ability to simulate the North Atlantic ocean circulation and variability. Finally, a third section will provide information about the Lagrangian analysis tool ARIANE, used in Chapter 3 and Chapter 4 to complement the Eulerian study of the  $MOC_\sigma$  and associated heat content changes in the eastern subpolar gyre.

### 2.1 Observational Datasets

#### 2.1.1 Ovide cruises

This PhD is a contribution to the OVIDE project (Observatoire de la Variabilité Interannuelle à DEcennale), primarily aimed to provide an observation-based picture of water mass properties and circulation variability in the eastern subpolar gyre, through the analysis of hydrographic data collected along a transoceanic section joining Cap Farewell (Greenland) and Portugal (see Figure 2.1 for the section location). Ovide is involved in the international CLIVAR

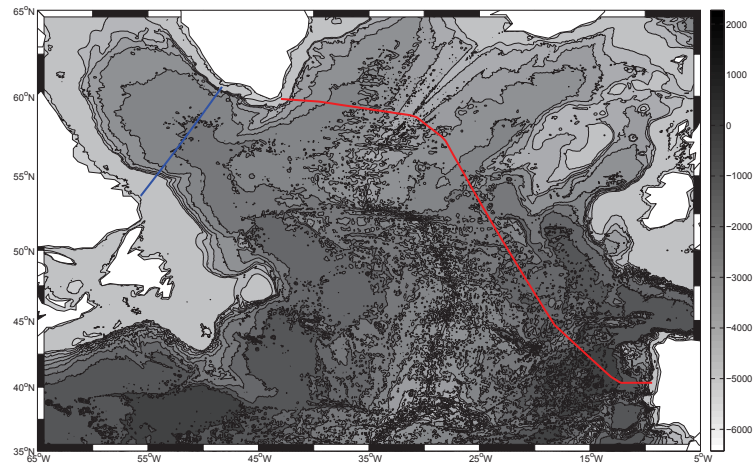


**Figure 2.1:** Bathymetry of the northern North Atlantic (m) and position of the A25-Ovide (red) and AR7W (blue) hydrographic lines.

project, dedicated to the observation and understanding of climate variability. Five summer cruises were carried out every two other year between 2002 and 2010, consisting of about 100 CTD (Conductivity Temperature Depth) profiles distributed along the 3500 km of the section, ADCP (Acoustic Doppler Current Profiler) and XBT (EXpendable BathyThermograph) measurements, as well as surface buoys and ARGO float deployments. Time-averaged sections of temperature, salinity, and velocity have already been shown in Chapter 1. In Chapter 5, they will be merged with corresponding fields from concomitant cruises carried out along the AR7W line in the Labrador Sea, thereby providing an average picture of the basin wide circulation in the northern North Atlantic during the 2000's.

### 2.1.2 AR7W cruises

As just mentioned, another set of hydrographic data will be used in Chapter 5. It consists of full-depth temperature, salinity and pressure data obtained along the AR7W transect in the Labrador Sea. The data were provided by Ygor Yashayaev from the *Bedford institute of Oceanography*, Canada. Many cruises were carried out since the late 1980's across the Labrador Sea (*The Labrador Sea Group*, 2008) and we will here use five of them that are concomitant

with the A25-Ovide surveys: summer 2002, 2004, 2006, 2008 and 2010 (see Figure 2.1 for the section location). Data from five 1990's cruises (1990, 1992, 1993, 1994, 1996) will also be used.

### 2.1.3 Satellite altimetry: the AVISO record

One of the major tool in modern physical oceanography is the sea-surface height record of satellite altimeters. Since 1992, the AVISO team provides along-track and gridded products of anomalous sea level and surface geostrophic currents over the global ocean with a  $\frac{1}{3}^\circ$  horizontal resolution. Altimetry cannot provide the absolute sea-level (ADT, for absolute dynamic topography) but gives acces to its anomalous component (*SLA* for sea-level anomaly). During the PhD, the mean dynamic topography (MDT) of *Rio and Hernandez (2004)* based on assimilated models of the geoid was chosen to compute maps of absolute sea-surface height (ADT = MDT + SLA). Altimetry data were used in Chapter 1 to describe the main characteristics (mean and variability) of the large scale surface circulation. In Chapter 5, they will be used to obtain a reference velocity level for absolute velocity calculation along the AR7W line.

### 2.1.4 The World Ocean Atlas 2009

The World Ocean Database 2009 (WOA09) provides climatological and annual fields of temperature and salinity since 1955. It is an update of the former WOA2005 with additional historical and modern data, including Argo float data that have been corrected for systematic errors. Those objectively analyzed fields have a  $1^\circ$  horizontal resolution and cover the 0-700m layer. A complete description of the WOA09 data set is available in *Levitus et al. (2009)*. In the present manuscript, WOA09 will be used to evalute heat content changes in the eastern subpolar gyre, and prove the suitability of the ORCA025-G70 for investigating the underlying mechanisms.

## 2.2 The ORCA025-G70 simulation

### 2.2.1 Global configuration

The study utilizes the ORCA025-G70 simulation from the global configuration ORCA025 of the Nucleus for European Modeling of the Ocean (NEMO, (*Madec*, 2008)) coupled with the Louvain-la-Neuve Ice model version 2 (LIM2, (*Fichefet and Maqueda*, 1999)). The ORCA025 numerical characteristics are fully detailed in *Barnier et al.* (2006). The domain is global and is configured using a tripolar grid with 1442 x 1021 grid points and a horizontal resolution that increases with latitude (from 27.75 km at equator to 13.8 km at 60°N). The vertical grid consists of 46  $z$ -levels with vertical spacing that increases with depth (6 m near the surface, 250 m at the bottom). The ORCA025 parameterizations comprise a Laplacian mixing of temperature and salinity along isopycnals, a horizontal biharmonic viscosity, and a turbulence closure scheme (TKE) for vertical mixing.

A complete description of the ORCA025-G70 simulation is provided by *Molines et al.* (2006) and *Treguier et al.* (2007). It was initialized with the Polar Science Center Hydrographic T/S Climatology (PHC 3.0, *Steele et al.* (2001)), which consists of the Levitus 1998 climatology (*Levitus et al.*, 1998) everywhere except in the Arctic domain where a blend of the Arctic Ocean Atlas and additional data from the Bedford Institute of Oceanography was added to produce a more realistic Arctic hydrography. The simulation was run from 1958 to 2004 with no spin-up. The forcing dataset (referenced as DFS3 by *Brodeau et al.* (2009)) was built using data from various origins at different frequencies. Air temperature, wind and air humidity data originate from the European Centre for Medium-Range Weather Forecast (ECMWF) ERA40 reanalysis for the period 1958-2001 and from the ECMWF analysis for the period 2002-2004. Daily radiative flux and monthly precipitation fields came from the Coordinated Ocean-ice Experiment (CORE) (*Griffies et al.*, 2009) database and turbulent fluxes (wind stress, latent and sensible heat fluxes) were calculated from the CORE bulk formulae (*Large and Yeager*, 2004). To minimize the model drift, a global surface salinity restoring (300 days over 50 m)

to the PHC climatology was incorporated. A surface salinity restoring under the ice cover was maintained with a 5-time enhanced coefficient (60 days over 50 m). An additional restoring was also applied at the exit of the Red Sea (60 days over 50 m) and the Mediterranean Sea (100 days over 50 m) for a better representation of the overflows. *Rattan et al.* (2010) showed a strong drift in the freshwater content of the Labrador Sea during the first decade of integration in ORCA025-G70. For our present purpose, we believe the degree of equilibrium achieved by the late 1960's is adequate and that the subsequent signal presumably relates to the prescribed interannual forcing. Additionally, *Huck et al.* (2008) reconstructed a MOC signal in the subpolar North Atlantic from hydrographic data for the period 1955-1998 and showed a close correspondence with the ORCA025-G70 variability. We verified that a twin simulation without any restoring to the surface salinity climatology (ORCA025-KNMI01) yields a very similar North Atlantic MOC signal. The tendencies in our transport time series were therefore not removed. All the results presented are obtained with monthly model outputs and all time series presented thereafter are annual averages of the monthly time series. Although this relatively low temporal sampling could under-estimate the influence of eddies, the use of 5-day model outputs yields similar results when considering the MOC variability. Accordingly, *Treguier et al.* (2006) showed in the Clipper ATL6 model ( $\frac{1}{6}^\circ$  resolution) a small impact of eddy fluxes on the overturning variability at A25-Ovide.

### 2.2.2 Evaluation of the ORCA025-G70 simulation

This simulation has been extensively used to study circulation and water masses in several regions of the global ocean (e.g. *Lique et al.*, 2010; *Jouanno et al.*, 2011; *Treguier et al.*, 2012). Of particular interest for the present PhD, *de Boisséson et al.* (2012) used the ORCA025-G70 simulation for a complete study of the subpolar mode waters in the eastern subpolar gyre, and the authors already proved its consistency in this particular region. Here, we build on the literature review presented in Chapter 1 to briefly evaluate the ability of ORCA025-G70 in reproducing some important features of the North Atlantic circulation and hydrography (mean

and variability). More specific data-model comparisons in the eastern subpolar region will also be provided in Chapter 3 and 4.

### The mean state of the North Atlantic circulation

The mean SST and surface geostrophic currents from ORCA025-G70 for the period 1992-2008 are shown in Figure 2.2 (see Figure 1.6 for model-data comparison). The location of the 8°C isotherm (i.e. a subpolar front proxy) compares nicely with observations in both the western and eastern basins. The global picture of surface currents is also in line with altimetry observations (see Figure 1.6b) or surface drifter analysis (*Reverdin et al., 2003; Niiler et al., 2003*), and depicts the major current systems of the northern North Atlantic mentioned in Chapter 1. The intensity of the southern (resp. northern) branch in the western and mid basin is somewhat overestimated (resp. underestimated) in ORCA025-G70, possibly due to the misrepresentation of the Gulf Stream separation at Cape Haterras and/or the unrealistic weak Northwest Corner recirculation. According to *Böning et al. (1996)*, the position of the NAC is a common weakness of such eddy-permitting simulation and may depend on a number of model factors. Increasing the horizontal resolution of the model to efficiently resolve eddies in the western North Atlantic led to a northward shift of the current and more realistic sea surface temperature in the Newfoundland area. Additionally, the strength of the western boundary current in the subpolar gyre seems slightly overestimated in the model. Note however that the overall distribution of eddy kinetic energy compares relatively well with the corresponding field deduced from altimetry (Figure 1.6b) or surface drifter data (*Reverdin et al., 2003*), considering the medium resolution of the model ( $\frac{1}{4}^\circ$ ).

The surface temperature distributions at 29°W (i.e. above the MAR) in WOA09 and ORCA025-G70 are compared in Figure 2.3a. The two meridional profiles match well south of 40°N, whereas ORCA025-G70 presents a slight warm bias in the NAC core between 40°N and 55°N, possibly due to the too southerly path of the current from the Newfoundland basin. A slight cold bias is also observed at higher latitudes. The surface velocity distributions along 29°W in AVISO and ORCA025-G70 are compared in Figure 2.3b. Despite some local discrep-

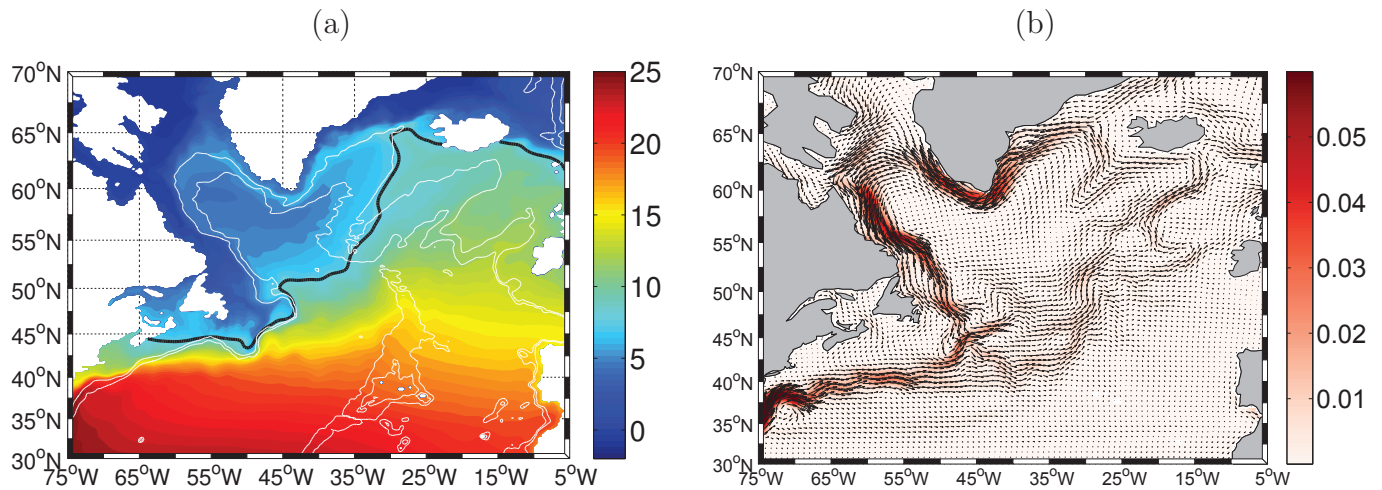


**Figure 2.2:** Maps of time-averaged (a) sea surface temperature ( $^{\circ}\text{C}$ ) for the period 1965-2004 and (b) absolute surface geostrophic currents ( $\text{m}\cdot\text{s}^{-1}$ ) superimposed on the corresponding eddy kinetic energy field ( $\text{m}^2 \text{s}^{-2}$ ) for the period 1992-2008, in ORCA025-G70. The thin white lines in (a) refer to the 2000m and 3000m isobaths. The thick black line indicates the  $8^{\circ}\text{C}$  isotherm.

ancies, the position and amplitude of the major currents are satisfactorily represented in the model: the Azores Current between  $32^{\circ}\text{N}$  and  $35^{\circ}\text{N}$ , the NAC between  $40^{\circ}\text{N}$  and  $57^{\circ}\text{N}$ , and the anticyclonic recirculation around Reykjanes Ridge between  $57^{\circ}\text{N}$  and  $62^{\circ}\text{N}$ . Of particular importance for our purpose, the two main branches of the NAC respectively centered at  $52^{\circ}\text{N}$  above CGFZ (the northern NAC branch) and  $45^{\circ}\text{N}$  above MFZ (the southern NAC branch) are well visible.

The total NAC transport within the 0-1000m layer amounts to 30 Sv, that is within the upper range of observational estimates (*Perez-Brunius et al.*, 2004). In the eastern subpolar gyre, the main path of the NAC on each sides of Rockall Plateau are consistent with the altimetric data (see Figure 1.6b). Two main differences between the model and altimetry fields emerged. The intensity of the northern "Iceland Basin" branch and of its downstream extension along the eastern flank of Reykjanes Ridge seem overestimated in the model. According to *Treguier et al.* (2005), this might reflect a too strong topographic constrain due to the lack of small-scale processes capable of destabilizing and diverting the flow into the Iceland Basin interior. Additionally, very few connections between the MAR and the Irminger Sea occur in the model, whereas observations indicate that a fraction of the NAC directly reaches the

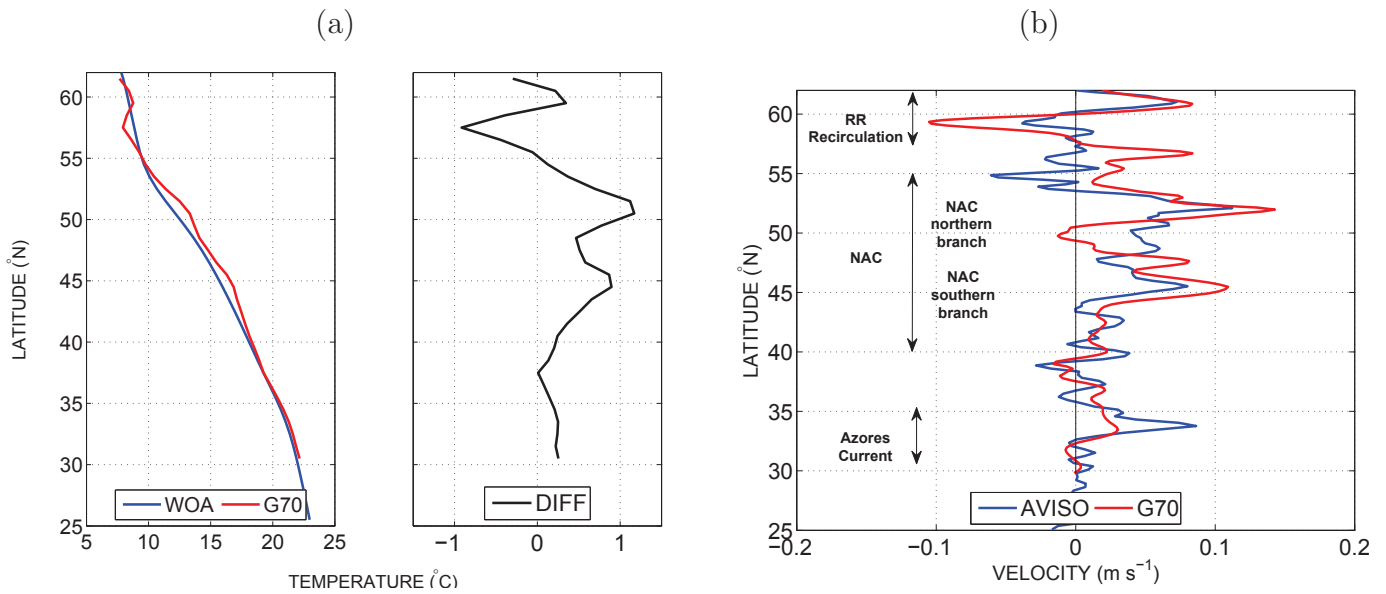


**Figure 2.3:** (a, left) Mean (1965-2004) temperature ( $^{\circ}\text{C}$ ) distribution at  $29^{\circ}\text{W}$  in WOA (blue) and ORCA025-G70 (red), and (a, right) difference between the two profiles (G70 minus WOA). (b) Mean (1992-2004) distribution of surface velocity ( $\text{m s}^{-1}$ ) at  $29^{\circ}\text{W}$  in AVISO (blue) and ORCA025-G70 (red).

Irminger Sea after crossing the MAR without entering the Iceland Basin. Yet, despite the aforementioned slight discrepancies between observed and simulated surface circulations, they are overall in good agreement.

Figure 2.4 shows a time-averaged map of winter mixed-layer depth in ORCA025-G70, one of the most sensitive features of ocean models (Treguier *et al.*, 2005). The overall spatial pattern is in good agreement with SODA (see Figure 1.9) and depicts the Labrador Sea as the main region for deep convection. Relatively deep mixed layers are consistently simulated in the southern Irminger Sea and in the vicinity of the Feroe-Scotland sills. Overall, mixed layer depths are somewhat overestimated in the model, most notably in the central Labrador where convection reaches down to  $\sim 2300\text{m}$  (as compared to  $\sim 1500\text{m}$  in SODA).

The mean fields of temperature and salinity along the A25-Ovide section from ORCA025-G70 for the period 1965-2004 are shown in figure 2.5. The global distribution of hydrographic properties agrees relatively well with the observational time-averaged estimate presented in Figure 1.11. The mean spatial structure and amplitude of the velocity field along A25-Ovide from ORCA025-G70 appears also in good agreement with data-based picture, as well as the

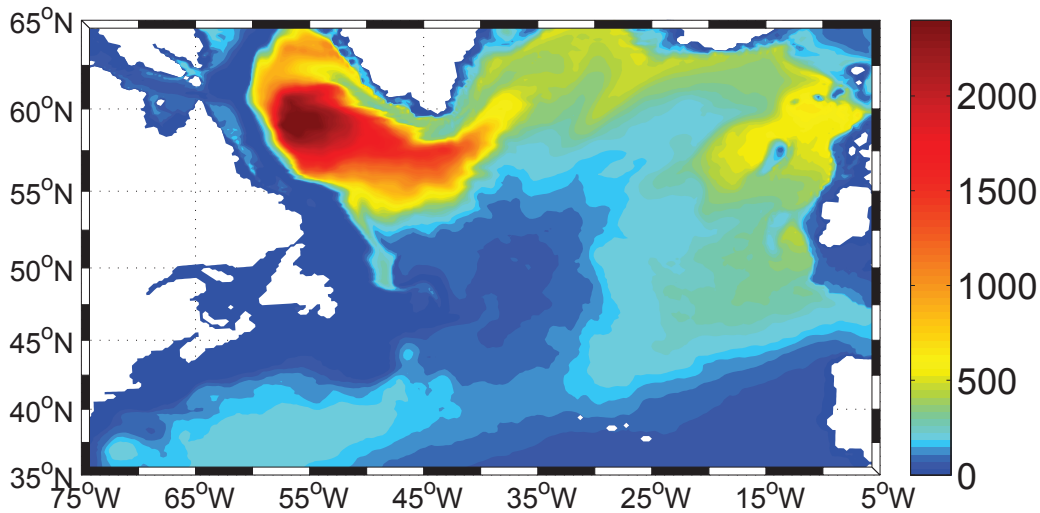


**Figure 2.4:** Mean march mixed layer depth in ORCA025-G70 for the period 1965-2004, defined as the depth at which the density exceeds the surface density by  $0.1 \text{ kg m}^{-3}$ .

depth of the  $\sigma_1 = 32.1$  (lower bound for thermocline waters) and  $\sigma_1 = 32.42$  (upper bound for deep waters) isopycnal surfaces. The mean (1965-2004)  $\text{MOC}_\sigma$  and heat transport across the section amounts to 16 Sv and 0.38 PW, in line with observational estimates. In the next chapters, a more detailed and quantitative model-data comparison of the eastern subpolar gyre circulation at A25-Ovide will be carried out.

The mean  $\psi_{bt}$  for the period 1965-2004 in ORCA025-G70 is shown in Figure 2.6 and should be compared with the SODA estimation previously described (see Figure 1.12). The green contour indicates the separation between the anticyclonic subtropical gyre and the cyclonic subpolar gyre. As discussed in *Barnier et al. (2006)*, their spatial structure and intensities ( $\sim 40$  Sv) agree with several and various model results (e.g. *Eden and Willebrand, 2001*). As already noted from the mean surface current map, the main deficiency of the present simulation is the too weak northwest corner recirculation associated with a southerly path of the NAC between Newfoundland and the MAR.

The mean  $\text{MOC}_z$  for the period 1965-2004 in ORCA025-G70 is shown in Figure 2.7a and can be compared with the SODA estimation previously described (see Figure 1.13a). Maximum overturning ( $\sim 16$  Sv) consistently occurs near  $30^\circ\text{N}$  at about 1000m depth and subsequently

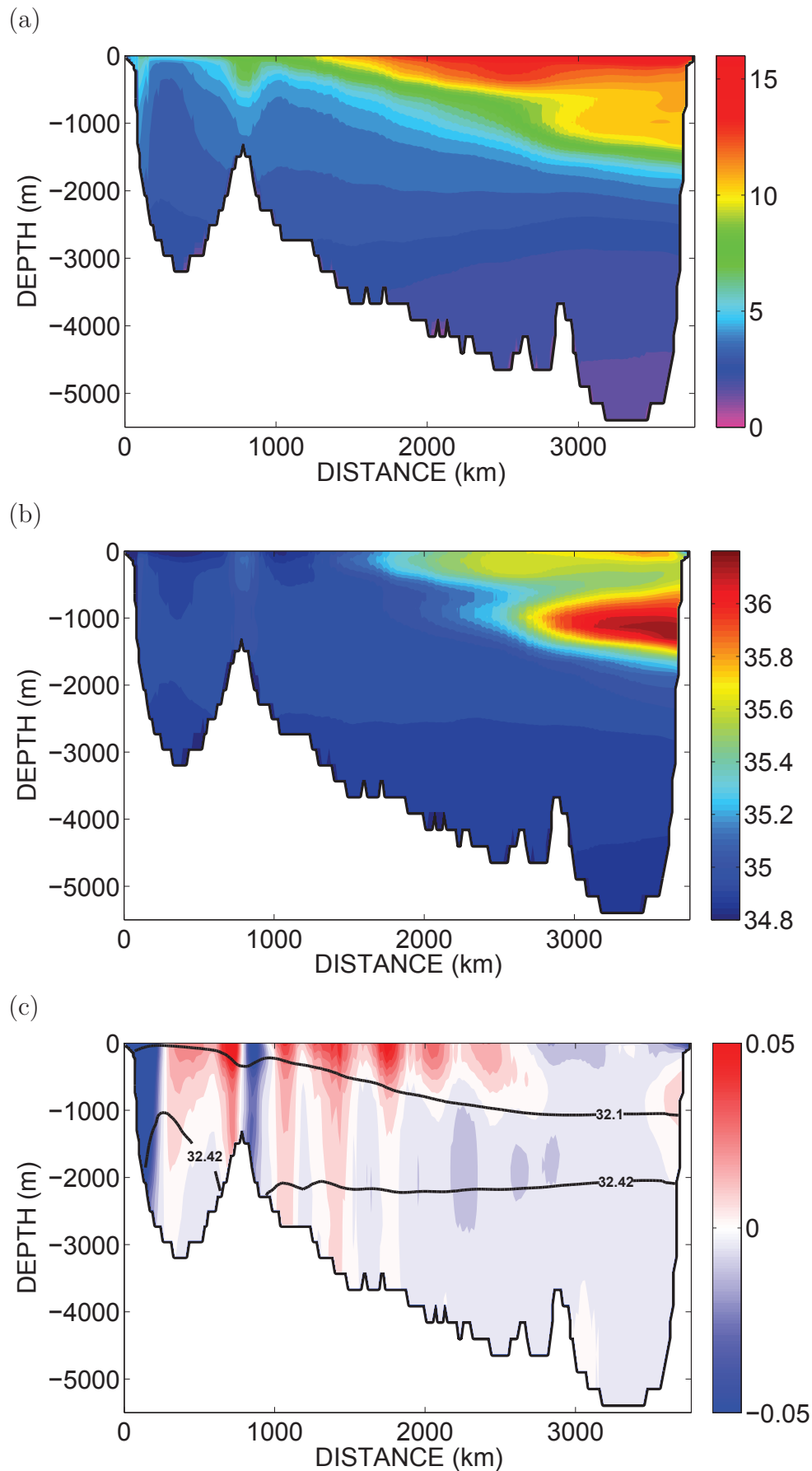


**Figure 2.5:** Mean fields of (a) temperature ( $^{\circ}\text{C}$ ) (b) salinity and (c) velocity ( $\text{m s}^{-1}$ ) along the A25-Ovide section for the period 1965-2004, in ORCA025-G70. The black lines in (c) indicate the  $\sigma_1 = 32.1$  and  $\sigma_1 = 32.42$  isopycnal surfaces.

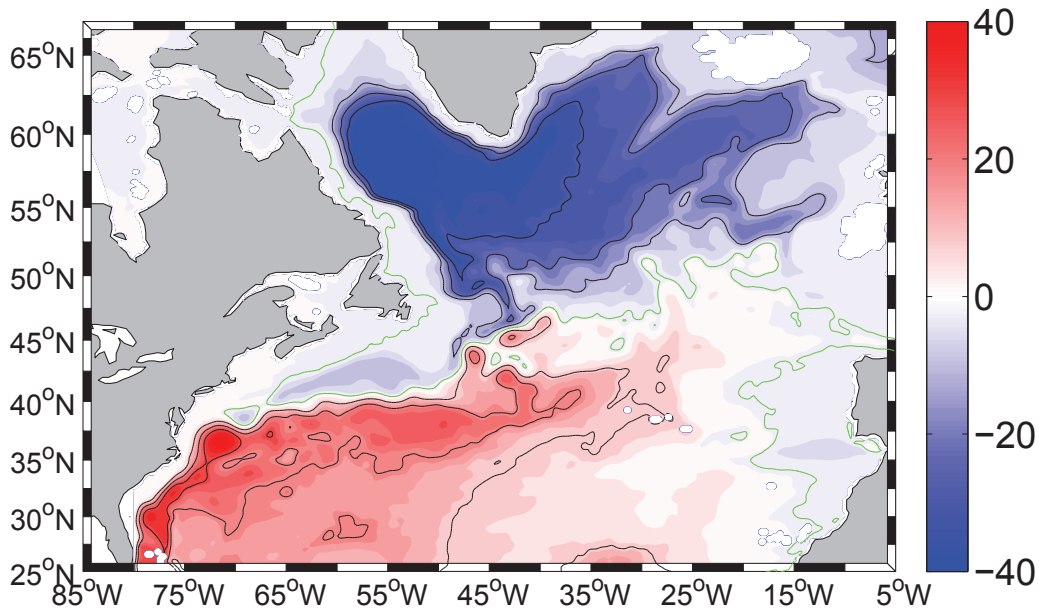


**Figure 2.6:** Mean barotropic streamfunction ( $Sv$ ) for the period 1965-2004, in ORCA025-G70. The green line indicates the zero contour.

decreases as one moves toward higher latitudes. The deep return flow lies around 2500m, that is slightly shallower than in SODA or in the estimation of *Forget et al.* (2008). This potentially reflects unrealistic properties of the DSOw and ISOW overflow waters in ORCA025-G70. The mean  $MOC_{\sigma}$  is also fairly consistent with the SODA estimation (Figure 2.7b). The maximum subtropical (35°N) and subpolar (55°N) overturning are satisfactorily reproduced around  $\sigma_1 = 32.1$  (i.e.  $\sigma_0 \approx 27.5$ ). The discontinuity at about 37°N visible in both representations is due to a non-zero mass flux from the Mediterranean Sea.

As mentioned in Chapter 1, both  $\psi_{bt}$  and  $MOC_z$  are effective components of the climate-relevant meridional heat transport (MHT) (note that the  $\psi_{bt}$  component also includes heat fluxes from the eddy field, not only the large scale gyres). In ORCA025-G70, the total MHT reaches highest values in subtropical regions ( $\sim 1$  PW) and gradually decreases as one moves toward higher latitudes (Figure 2.8). A second MHT peak is visible around 50°N ( $\sim 0.6$  PW). This meridional structure and the amplitude of MHT are in line with the range of observational estimates reported in *Ganachaud and Wunsch* (2003) and in others modeling studies (e.g. *Wunsch and Heimbach*, 2006; *Marsh et al.*, 2008). The contributions of the vertical and horizontal

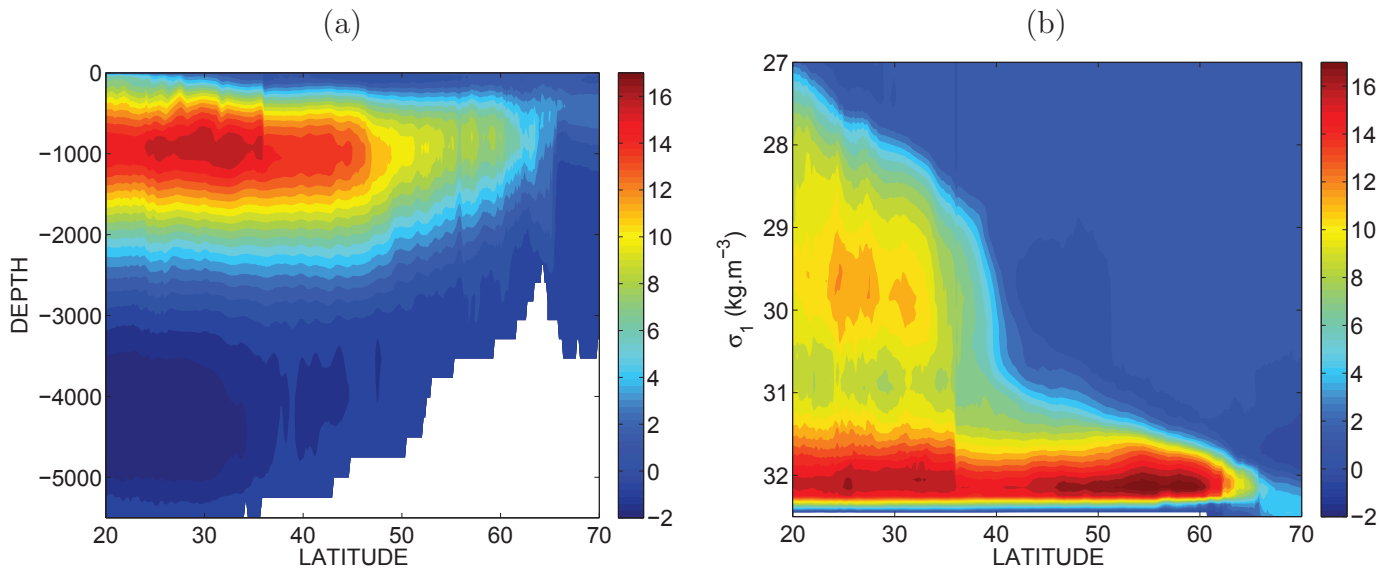


**Figure 2.7:** (a) Mean Meridional Overturning Circulation ( $Sv$ ) in the latitude-depth plane ( $MOC_z$ ) of the northern North Atlantic sector for the period 1965-2004, in ORCA025-G70. (b) Same as (a) but in the latitude-density plane ( $MOC_\sigma$ ).

circulating cells are shown with red and blue lines, respectively (the underlying method of calculation will be detailed in Chapter 4). While  $MOC_z$  dominates in subtropical regions, the contribution of the gyre circulation increases as latitude goes up and largely overcome  $MOC_z$  in subpolar regions.

### Index of variability

In Chapter 1, we reviewed some observational and modeling indexes of the global North Atlantic variability. Before investigating in details decadal changes in volume and heat transports across A25-Ovide in the next chapters, we wish to emphasize the suitability of ORCA025-G70 in simulating those well-known large scale signals. We start by an index of deep convection for the period 1965-2004, as obtained by the first EOF of winter mixed layer depth (Figure 2.9). The first mode explains 73% of the total variance and its spatial pattern has a clear center of action in the central and eastern Labrador Sea, which extends toward the Irminger Sea. Variability in the rest of the domain is almost inexistent. The associated principal component is fairly consistent with that presented in Figure 1.19 and depicts three main periods of intense convection: the

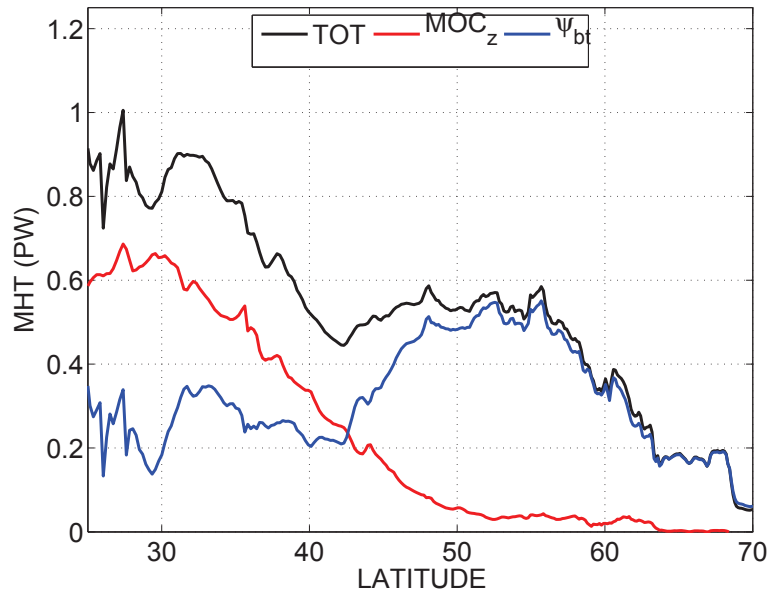


**Figure 2.8:** Mean meridional heat transport in the North Atlantic (PW, black) as a function of latitude for the period 1965-2004, in ORCA025-G70. The total signal is decomposed into a vertical (red) and a horizontal (blue) contribution. See Chapter 4 for details about the calculation.

early 1970's, the mid-1980's and the early 1990's. Those episodes are consistently associated with positive phases of the NAO, both index being significantly correlated at the 95% level ( $R = 0.6$ ). The strong change in deep convection between the early 1990's and the late 1990's/2000's is, for instance, in good agreement with the observational diagnosis of *Yashayaev et al.* (2007) (see Figure 1.18).

Secondly, the intergyre transport index of *Curry and McCartney* (2001) (see Figure 1.20) was reproduced in ORCA025-G70 (Figure 2.10). The available potential energy within the 0-2000m layer was spatially averaged within two boxes located at the center of the subtropical and subpolar gyre. The subpolar PEA anomalies ( $\text{std} = 6.10^5$ ) have stronger amplitudes than the subtropical one ( $\text{std} = 3.5.10^5$ ), but the out-of-phase relationship is well reproduced. The difference between both indexes (weighted by  $\frac{1}{f}$ ) yields a baroclinic transport index in close agreement with the observational one: a gradual positive trend from the late 1960's to the mid-1990's and a sharp weakening afterwards.

Consistently, the *gyre index* of *Häkkinen and Rhines* (2004) (i.e. the first EOF of SSH in the North Atlantic) is satisfactorily simulated in ORCA025-G70 (Figure 2.11). Its horizontal

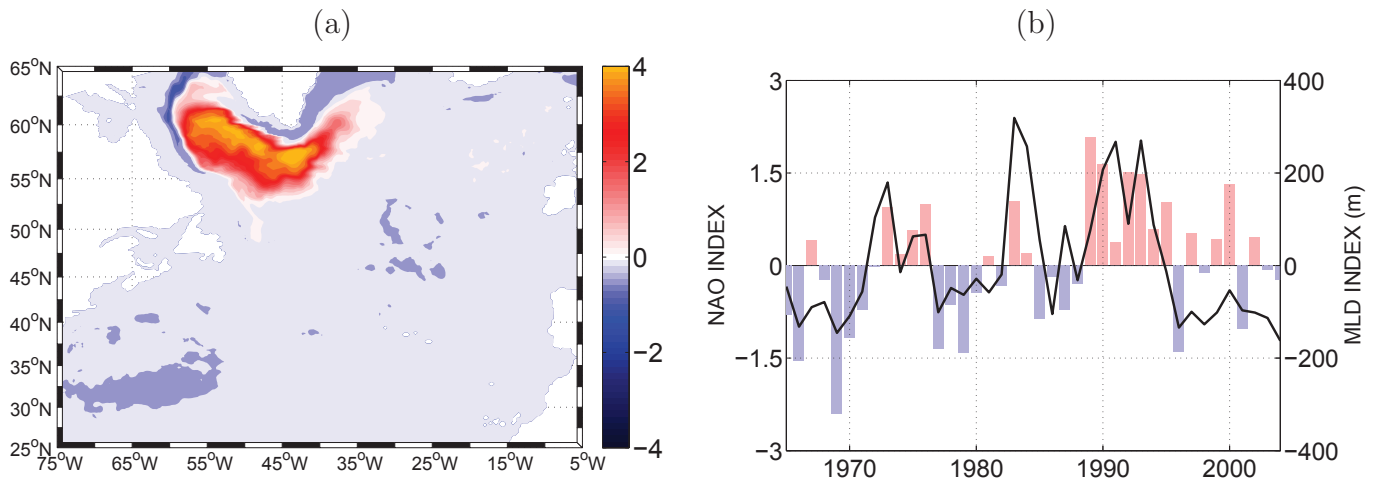


**Figure 2.9:** (a) Spatial pattern of the first EOF of winter mixed layer depth in ORCA025-G70 (unitless). (b) The associated principal component (m), along with the normalized NAO index (bars).

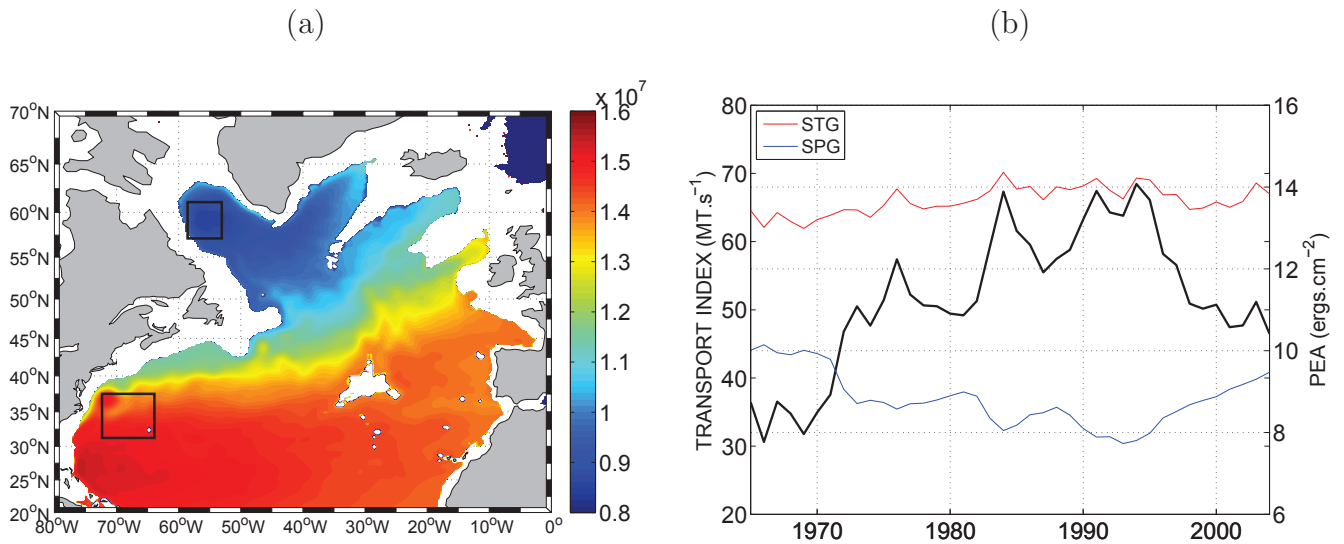


**Figure 2.10:** (a) Mean horizontal field of potential energy integrated over the 0-2000m layer ( $ergs.cm^{-2}$ ). (b) Timeseries of APE in the subtropical (red) and subpolar (blue) boxes shown in (a). The resulting intergyre baroclinic index is shown in black ( $MT.s^{-1}$ ).

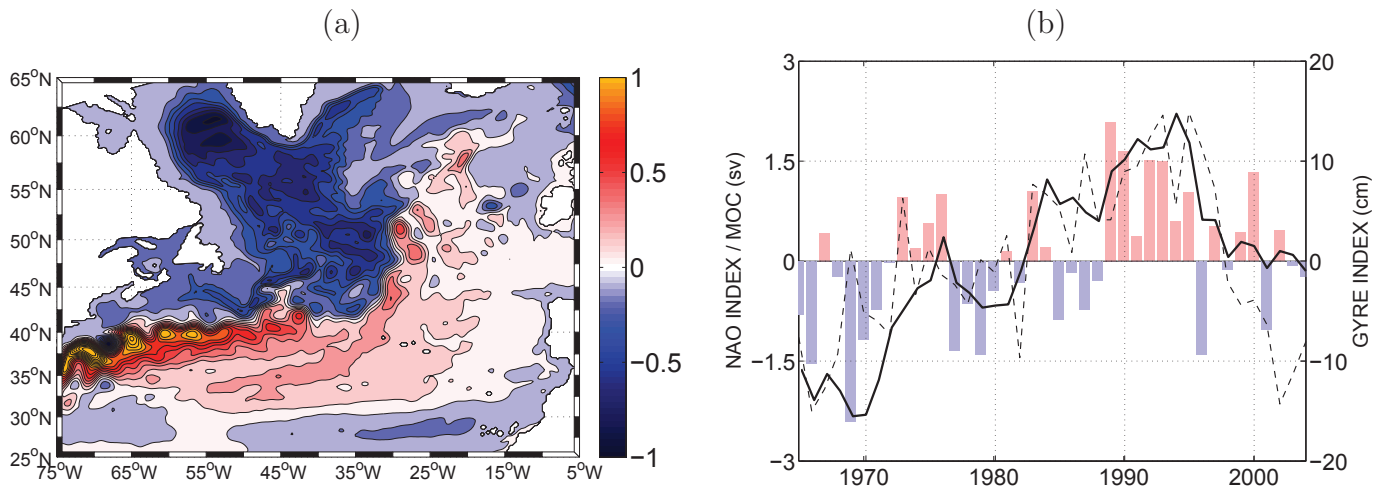


**Figure 2.11:** (a) Spatial pattern of the first EOF of sea-surface height in the North Atlantic from ORCA025-G70 (unitless). (b) The associated principal component (cm, thick black), the  $MOC_z$  anomalies at  $45^\circ N$  (Sv, thin dashed) and the normalized NAO index (bars).

structure, which explains 18% of the total variance, bears strong resemblances with that obtained from altimetry measurements, with two main poles of variability located in the subpolar gyre and in the intergyre region. The phase and amplitude of the associated principal component shows a consistent weakening of the subpolar gyre since the mid-1990's and a concomitant cyclonic anomalous circulation in the Gulf Stream/intergyre region. On longer timescales, the ORCA025-G70 reproduces earlier modeling results, with the 1990's gyre index decline preceded by a longer-term positive trend from the mid-1960s (Hátún *et al.*, 2005; Böning *et al.*, 2006). Note however that the structure of this mode in ORCA025-G70 is more zonal than the one found in observations, possibly due to the erroneous path of the NAC in the western basin. Comparison of Figure 2.10 and Figure 2.11 suggests that SSH stands as a satisfactorily proxy for stratification changes within the upper oceanic field, well below the wind-driven layer. Also shown in Figure 2.11b is a timeseries of  $MOC_z$  anomalies at  $45^\circ N$ , that is the exit of the subpolar gyre (thin dashed line). It agrees with similar diagnosis from various hindcast simulations and matches particularly well the decadal SSH gyre index, suggesting the potential of sea level variability for monitoring the low-frequency fluctuations of the MOC.

As was discussed in Chapter 1, several studies showed that fluctuations in the NAO were

accompanied by lateral shifts of the subpolar front, which are often used as a proxy for hydrographic changes in the eastern subpolar gyre (e.g. *Bersh*, 2002). Here, we follow *de Boisséson et al.* (2012) and define the subpolar front position from the longitude at which the 8°C isotherm intersects the 200m isobath (note that similar results are obtained with a surface definition of the front). Its anomalous displacements at 58°N in ORCA025-G70 are compared with the corresponding timeseries from WOD09 in Figure 2.12. Both index are similar on decadal timescales and depict a westward shift of the subpolar front during the early 1960's followed by a gradual eastward extension of cold subsurface waters until the mid-1990's and a sharp westward retreat between 1995 and the 2000's. The latter change is further illustrated in Figure 2.12, which shows the averaged position of the front for the period [1985 - 1995] and [1996 - 2004] in ORCA025-G70 and WOA09. This westward retreat is often associated in the literature with the concomitant sharp drop in the NAO index and associated contraction of the subpolar gyre that may have favoured the northward penetration of warm subtropical waters toward the Nordic Seas. Yet, the extent to which subsurface displacements of isotherm/isohaline reflect lateral shifts of velocity fronts in the eastern SPG is unclear and has not been observationally evidenced. In ORCA025-G70, *De Boisséson* (2010) showed that the substantial hydrographic changes post 1995 (see Figure 1.23a) were not accompanied by horizontal displacements of the main NAC branches in the Iceland and West European basins. This will be further discussed in the following chapters.

## Conclusion

A short evaluation of the ORCA025-G70 simulation in the northern North Atlantic has been carried out. Overall, the model is able to fairly reproduce the mean large-scale circulation (surface currents,  $MOC_z$ ,  $MOC_\sigma$ ,  $\psi_{BT}$ , meridional heat transport, mixed layer depth), despite some weaknesses that are common to such eddy-permitting simulations. Amongst them, the unrealistic Gulf Stream separation off Cape Hatteras and the too southerly path of the NAC in the western North Atlantic should be kept in mind for the following analysis. The two main branches of the NAC in the vicinity of the MAR are consistently simulated, and the more

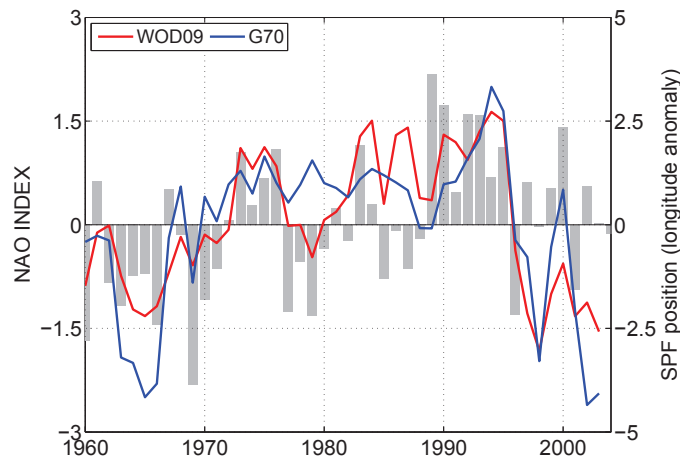


**Figure 2.12:** Anomalies in the longitudinal position of the subpolar front ( $8^{\circ}\text{C}$  at  $200\text{m}$ ) in ORCA025-G70 (blue) and WOD09 (red), along with the normalized NAO index (bars).

complex current systems of the eastern subpolar gyre are well-represented. In particular, the mean full-depth temperature, salinity and velocity fields along the A25-Ovide section are in good agreement with observational estimates.

The simulated interannual/decadal variability in ORCA025-G70 is also in line with observational proxy of the large-scale circulation in the North Atlantic. Long-term changes in the upper density field and associated anomalous patterns of circulation are satisfactorily reproduced in the model: the periods of intense convection in the Labrador Sea (early 1970's, mid-1980's and early 1990's) (*Yashayaev et al.*, 2007), the gradual intensification of the NAC from the late 1960's until the mid-1990's (*Curry and McCartney*, 2001), the slowing subpolar gyre circulation in the 1990's and early 2000's (*Häkkinen and Rhines*, 2004), and the lateral shift of the subpolar front in the eastern subpolar gyre (*Bersh*, 2002). The model evaluation will continue in the following Chapter 3 and Chapter 4.

### 2.2.3 The Lagrangian analysis tool: ARIANE

The Lagrangian analysis tool ARIANE was extensively used in this study. Its algorithm, based on an off-line volume-preserving scheme, is described in *Blanke and Raynaud* (1997) and *Blanke et al.* (1999). Its main purpose is to calculate trajectories of numerical particles within a three-

dimensional and time-dependent velocity field of an OGCM. For such calculation, the velocity field is assumed to be constant over successive periods equal to the available sampling (monthly averaged velocity field of the ORCA025-G70 simulation will be used). The resulting trajectories are interpreted as the pathways followed by small volume-conservative water parcels advected within the model velocity field from a given initial section to several final sections.

The particles are distributed along the initial section according to the archived Eulerian velocity field at each time step: particles are more numerous in regions where the incoming transport is the largest. In addition, the number of particles within each velocity grid cell was calculated in the present study so that the individual transport attributed to each particle does not exceed 0.5 mSv (we checked that the use of a smaller value, for improved accuracy, leads to very similar results). The sum of all particle transports in each grid cell amounts to the corresponding incoming Eulerian transport. Here, the accuracy in the computation of the volume transfer between the initial and final sections is estimated as 0.1 Sv. Along their paths, particles will change their hydrographic properties according to the local Eulerian fields of the ocean model. Between two successive positions, the temperature and salinity of each particle therefore evolve according to the parameterized thermodynamics of the model. Supplementary information about ARIANE can be found at <http://stockage.univ-brest.fr/grima/Ariane/>.

# Chapter 3

## Decadal variability of the $\text{MOC}_\sigma$ across the A25-Ovide section

This chapter is based on an article submitted to *Journal of Geophysical Research*.

---

### Abstract

*Decadal changes of the Meridional Overturning Circulation (MOC) at the A25-Ovide section between Portugal and Greenland are investigated in a numerical simulation forced by atmospheric reanalysis data for the period 1965-2004. The intensity, composition and structure of the upper MOC limb are assessed using a Lagrangian analysis tool. Its mean transport is fed by water masses of two distinct origins: the subtropics and the Labrador Sea. Two vertical overturning cells are consequently identified: a subtropical cell connecting low and high latitudes (12 Sv) and a cell internal to the subpolar gyre (4 Sv). The decadal MOC variability is associated with synchronized transport changes of the subtropical and subpolar inflow within the North Atlantic Current (NAC). The varying strength of the MOC is further related to changes in the upper horizontal transport distribution. When the MOC is in a strong phase (early 1990's), the northern branch of the NAC in the Iceland Basin is strong while the southern branch at the Rockall*

*Trough entrance is relatively weak. The inverse situation holds for a persistent weak MOC state (1970's). Contrary to the conclusions of earlier studies, variability in the strength and shape of the subpolar gyre does not stand as the main driver of the changing NAC structure, which is largely induced by the horizontal variability of the subtropical inflow. Additionally, the recently shown intrusion of subtropical waters into the Northeastern Atlantic (late 1960's, early 1980's and 2000's) are shown to primarily occur during periods of weak MOC circulation at A25-Ovide.*

---

### 3.1 Introduction

The quantification and understanding of long-term changes in the redistribution of heat between low and high latitude regions stand as a major challenge in climate research. In the North Atlantic Ocean, this meridional heat transport is mainly carried out by the Meridional Overturning Circulation (MOC): a vertical circulation cell depicting a northward transport of light waters within its upper limb and a return flow of relatively dense waters at depth. The present study focuses on the MOC variability at the A25-Ovide section joining Cape Farewell (Greenland) and Portugal, and particularly emphasizes decadal changes in the strength, composition and structure of the warm water transport carried out by the North Atlantic Current (NAC).

From a dynamical point of view, two prominent and permanent pathways of the NAC east of the Mid-Atlantic Ridge (MAR) are usually described in the literature: a northern branch, often referred to as the subpolar front, which flows from the Charlie Gibbs Fracture Zone (CGFZ) into the Iceland basin as part of the cyclonic subpolar gyre circulation, a southern branch that flows within the Rockall Trough and that preferentially crosses the Iceland-Scotland Ridge to feed the Nordic Seas (*Bower et al.*, 2002; *Brambilla and Talley*, 2006; *Bower and von Appen*,

2007). A significant fraction of those surface waters is progressively transformed through air-sea interactions into intermediate and deep water masses during their cyclonic journey around the Iceland and Irminger basins (*Brambilla and Talley, 2008; Brambilla et al., 2008*), and eventually meets the denser overflow waters along the Greenland continental slope to form the deep limb of the MOC (*Lherminier et al., 2010; Sarafanov et al., 2012*). Variability in the overflow intensity was found to be relatively small on decadal timescales (*Nilsen et al., 2003; Olsen et al., 2008*), suggesting that the MOC variability on such timescales reflects the varying rate of light-to-dense water mass conversion south of the Greenland-Scotland sills.

Observational evidence of interannual to decadal changes in the strength and structure of the MOC in the Northeastern subpolar Atlantic ocean is mainly provided by the analysis of hydrographic sections. The Ovide project was particularly aimed to describe the circulation and the water masses in the eastern subpolar gyre, through the analysis of repeat hydrographic surveys between Portugal and Greenland in the 2000's (the A25-Ovide line, see Figure 3.1) (*Lherminier et al., 2007, 2010; Daniault et al., 2011a,b; Gourcuff et al., 2011*). Similar investigations were also carried out at 60°N during the 2000's (*Sarafanov et al., 2012*) and across the A1E section between Greenland and Ireland during the 1990's (*Bersh, 2002*). Yet, while those efforts have largely contributed to the current understanding of the MOC structure in this particular region, investigating the decadal oceanic variability from such spatially and temporally sparse measurements is difficult.

The knowledge of global air-sea fluxes of heat, freshwater and momentum over the last decades has enabled the MOC variability to be addressed through Ocean General Circulation Models (OGCMs) experiments. Those tools have provided crucial information about the North Atlantic MOC and heat transport variability, particularly with regards to its spatial coherence (e.g. *Marsh et al., 2005; Bingham et al., 2007; Böning et al., 2006; Zhang, 2010*) and its response to idealized or observed atmospheric conditions. This response was particularly linked to the dominant mode of atmospheric variability known as the North Atlantic Oscillation (NAO) (*Hurrell, 1995*), which exerts a strong influence on the spatio-temporal distribution of buoyancy and mechanical fluxes at the air-sea interface (e.g. *Häkkinen, 1999; Eden and Willebrand, 2001;*

*Eden and Jung*, 2001; *Gulev et al.*, 2003; *Böning et al.*, 2006; *Deshayes and Frankignoul*, 2008; *Biastoch et al.*, 2008). Yet, relatively few studies focused on the local MOC variability in the eastern subpolar gyre. *Marsh et al.* (2005) briefly analysed the MOC and heat transport variability at A25 in an eddy-permitting model, and related it to similar analysis performed at two other hydrographic sections (AR7W and A5-RAPID). *Treguier et al.* (2006) focused on the MOC variability across the A25-Ovide line in the  $\frac{1}{6}^\circ$  Clipper model. The link between the MOC and the large-scale gyre circulation on relatively long timescales is however still missing.

The upper MOC limb in the eastern subpolar gyre is primarily composed of subtropical waters from the Gulf Stream, but is also linked to the cyclonic subpolar gyre circulation through the eastward extension of the Labrador Current that joins the NAC past Newfoundland (e.g. *Rosby*, 1996; *Bower et al.*, 2002; *Reverdin et al.*, 2003). *Schmitz and McCartney* (1993) showed, from a wide range of observations, a NAC of 20 Sv that includes a 7 Sv ( $1 \text{ Sv} = 10^6 \text{ m}^3\text{s}^{-1}$ ) component from the Labrador Sea. In a high-resolution model of the North Atlantic, *Böning et al.* (1996) partitioned the NAC transport within the upper 1000 m depth into a subtropical (14.1 Sv) and a subpolar (7.8 Sv) contribution. The respective signatures of both gyres on the decadal NAC variability were first addressed by *Hátún et al.* (2005). Using a salinity criterion to extract the respective inflow of subtropical and subpolar waters in the NAC, they found opposite decadal changes in the volume transport of both source waters. Those changes were correlated with the buoyancy-driven intensity of the subpolar gyre, as depicted in the so-called "gyre index" (*Häkkinen and Rhines*, 2004). The weakening and westward retreat of the subpolar gyre and the subsequent increased transport of subtropical waters toward the Nordic Seas was particularly invoked to explain the sharp warming and salinization of the eastern subpolar gyre in the late 1990s and early 2000s (*Bersh et al.*, 2007; *Holliday*, 2003; *Thierry et al.*, 2008; *Robson*, 2010; *Häkkinen et al.*, 2011a; *Yeager et al.*, 2012). A causal relationship between the subpolar gyre dynamics and hydrographic changes in the North Eastern Atlantic was recently dismissed by *Herbaut and Houssais* (2009). The authors rather proposed the setup of a NAO-related wind-driven anomalous circulation in the intergyre region as a potential driving mechanism (*Marshall et al.*, 2001; *Eden and Willebrand*, 2001). In addition, *Häkkinen*

*et al.* (2011a) recently showed episodes of increased penetration of Gulf Stream waters toward the eastern subpolar gyre (late 1960's, around 1980 and early 2000's), presumably driven by wind-stress variability. The link with the MOC variability in mid-high latitude regions remains obscure though.

The present study aims to investigate the spatio-temporal variability of the upper MOC limb across the A25-Ovide section for the period 1965-2004. We will combine a global eddy-permitting simulation with a Lagrangian analysis tool to address the following points: (a) provide a description of the mean structure and composition of the upper MOC limb in the eastern subpolar gyre (ESPG) and relate its decadal variability to subpolar and subtropical transport changes, (b) investigate associated changes in the horizontal structure of the NAC, (c) examine the link between the MOC variability and the spatial extent of subtropical water masses in the ESPG. The ESPG refers hereafter to the region bounded by the A25-Ovide section and the Greenland-Scotland sills (and hence encompasses part of the intergyre region). The study domain and the different sections discussed in the text are shown in Figure 3.1. Section 3.2 describes the mean (1965-2004) structure and composition of the upper MOC limb across A25-Ovide. Its decadal variability is assessed in Section 3.3 and 3.4, and the link with the NAO is briefly discussed in Section 3.5. Section 3.6 summarizes the results.

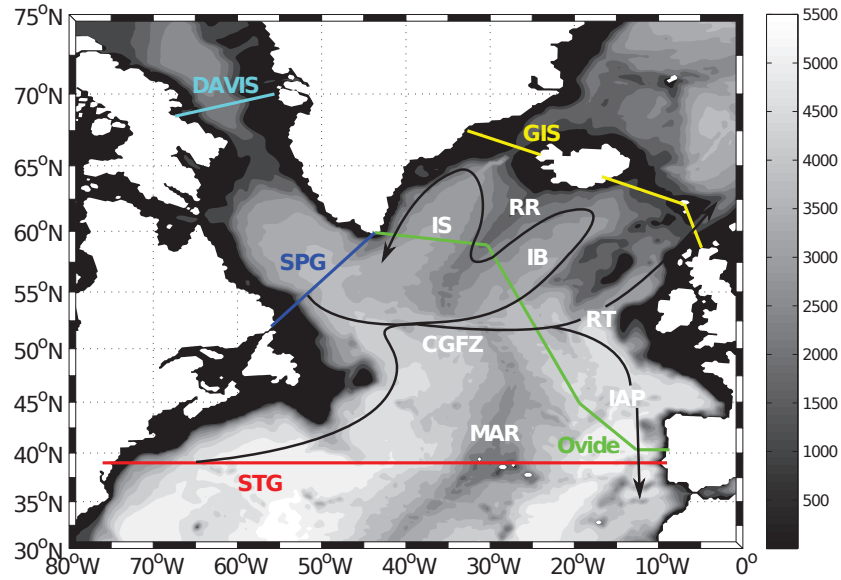


**Figure 3.1:** Bathymetry of the northern North Atlantic (in m) and positions of the sections discussed in the text: the A25-Ovide section (green), the STG transect (red), the SPG transect (blue), the Davis Strait section (cyan) and the GIS section (yellow). The main basins and topographic features mentioned in the text are labelled as: IS (Irminger Sea), IB (Iceland Basin), RT (Rockall Trough), IAP (Iberian Abyssal Plain), MAR (Mid-Atlantic Ridge), CGFZ (Charlie Gibbs Fracture Zone), RR (Reykjanes Ridge). The black lines stand for a simplified view of the main pathways of the North Atlantic Current

### 3.2 The mean MOC<sub>σ</sub> across the A25-Ovide section: spatial structure and composition

We here focus on the mean structure of the MOC at A25-Ovide. An Eulerian description of the vertical and horizontal shape of both MOC limbs is presented first and compared with available observational estimates. Lagrangian experiments are then used to detail the mean composition of the upper MOC limb.

### 3.2.1 The Eulerian view

The A25-Ovide hydrographic section was occupied during summer every other year between 2002 and 2010, and the subsequent analysis of the circulation represents a benchmark to validate the mean current structure simulated in ORCA025-G70. Here, the method used to compute the MOC transport follows that of *Lherminier et al.* (2010). Potential density referenced to 1000m ( $\sigma_1$ ) is used instead of depth as a vertical coordinate to avoid a compensation effect, which would result from the East Greenland Irminger Current transporting cold waters at the same depth as the warm and northward NAC. The plane-normal velocity field is hence integrated from Greenland to Portugal within discrete isopycnal layers, before being summed vertically from the ocean bottom to be consistent with *Lherminier et al.* (2010). The resulting overturning streamfunction is labelled as MOC <sub>$\sigma$</sub>  hereafter. The density surface associated with the maximum of MOC <sub>$\sigma$</sub>  (referred to as  $\sigma_{MOC}$  hereafter) delimits the upper and lower limbs of the overturning (referred to as MOC<sub>UPPER</sub> and MOC<sub>LOWER</sub> hereafter). Hence the MOC <sub>$\sigma$</sub>  intensity corresponds to the integrated transport of MOC<sub>LOWER</sub>, which slightly differs from the integrated transport of MOC<sub>UPPER</sub> due to a non-zero net transport across the section, which presumably occurs within the upper layers (about 1 Sv in *Lherminier et al.* (2010)).

The mean vertical structure of the simulated MOC <sub>$\sigma$</sub>  at A25-Ovide for the period 1965-2004 is plotted in Figure 3.2a (solid colored lines). In ORCA025-G70, the maximum value amounts to 16 Sv with a mean  $\sigma_{MOC}$  positioned at  $\sigma_1 = 32.09$ , which is in line with typical overturning estimates in the Northeastern Atlantic from eddy-permitting models (e.g. *Marsh et al.*, 2005; *Treguier et al.*, 2006) and observations (*Lherminier et al.*, 2010) ( $15 \pm 1$  Sv at  $\sigma_1 = 32.14$ , dashed line in Figure 3.2a). The maximum MOC <sub>$\sigma$</sub>  in ORCA025-G70 is slightly lighter and stronger than the observed one, possibly due to the different averaging periods considered (*Treguier et al.*, 2006) and/or model errors. The net transport across the section amounts to 1 Sv, which is consistent with recent estimates of the Arctic mass balance (*Maslowski et al.*, 2004; *Cuny et al.*, 2005; *Serreze et al.*, 2006). Also shown in Figure 3.2a is the mean vertical structure of the MOC <sub>$\sigma$</sub>  at the Greenland-Scotland sills as seen in ORCA025-G70. The transports of its lower

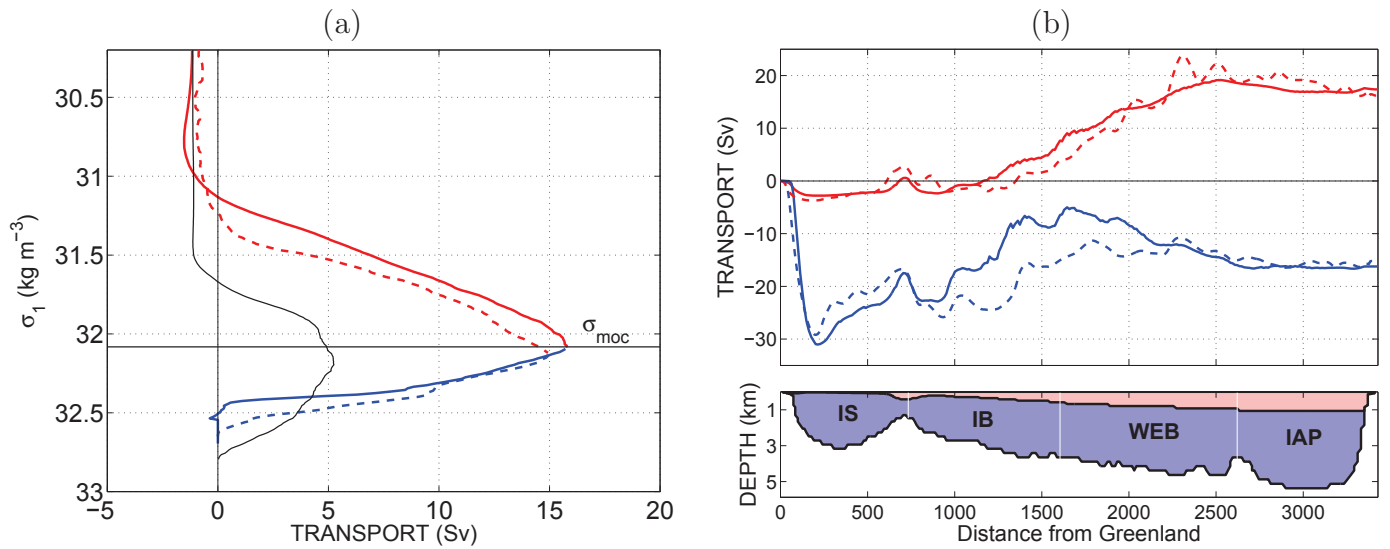


**Figure 3.2:** (a) Mean (1965-2004) vertical structure of the MOC<sub>σ</sub> at A25-Ovide (solid colored line). The mean velocity field has been integrated in density layers ( $0.01 \text{ kg m}^{-3}$  resolution) and accumulated from the bottom (the transport sign has been inverted for clarity, so that the MOC<sub>σ</sub> intensity stands as a positive variable). The horizontal line indicates the density of the MOC<sub>σ</sub> maximum that delimits the MOC<sub>σ</sub> upper (red) and lower (blue) limbs ( $\sigma_{MOC} = 32.09$ ). An observational estimate of the MOC<sub>σ</sub> vertical structure based on five hydrographic surveys (summer 2002, 2004, 2006, 2008 and 2010) is shown with a dashed line (Danialt, pers. com). The thin black line is the vertical structure of the MOC<sub>σ</sub> at the Greenland-Scotland sills, computed in the same manner as for the A25-Ovide section. (b) The upper panel shows the mean horizontal structure of the upper (red) and lower (blue) MOC<sub>σ</sub> limbs at A25-Ovide in ORCA025-G70 (solid lines) and observations (dashed lines). Transports have been accumulated from Greenland such that an increasing (decreasing) transport denotes a northward (southward) flow. The lower panel shows the coarse bathymetric features of the section and the two-dimensional position of  $\sigma_{MOC}$ . The four distinct basins discussed in the text are labelled as: IS (Irminger Sea), IB (Iceland Basin), WEB (West European Basin) and IAP (Iberian Abyssal Plain).

and upper branches are delimited by  $\sigma_1 = 32.2$  and respectively refer to the intensity of the deep overflows (5 Sv) and of the net Atlantic inflow towards the Nordic Seas (6 Sv). The overflows are equally partitioned between the Denmark Strait (2.5 Sv) and the Iceland-Scotland passage (2.5 Sv). The Atlantic inflow above the Iceland-Feroe sill and the Feroe-Scotland sill amounts to 2 Sv and 4 Sv, respectively. The model slightly underestimates the water mass exchanges between the Nordic Seas and the North Atlantic relative to observations. For instance, *Hansen and Østerhus* (2000) and *Østerhus et al.* (2005) estimated the mean overflow intensity at 6 Sv.

The bathymetry of the A25-Ovide section is shown in Figure 3.2b along with the mean horizontal structures of the simulated and observed MOC<sub>σ</sub> limbs. The model realistically reproduces the horizontal features of the observed MOC<sub>σ</sub> limbs. The upper limb (red lines)

presents a simple horizontal structure. It includes the lightest part of the southward flowing East Greenland Current (labelled as EGC hereafter, 3 Sv west of the 100 km) and the lightest part of the southward recirculation in the Iberian Abyssal Plain (labelled as REC hereafter, 3 Sv east of the 2500 km), which surround a strong northward transport in the Iceland Basin and West European Basin (23 Sv). This northward component of MOC<sub>UPPER</sub> is used as a proxy for the NAC transport hereafter. An anticyclonic recirculation occurs above Reykjanes Ridge, as shown in previous observational studies (*Bower et al.*, 2002; *Reverdin et al.*, 2003; *Flatau et al.*, 2003). The net transport of MOC<sub>UPPER</sub> is 17 Sv, out of which 6 Sv cross the Greenland-Scotland sills and reach the Nordic Seas (Figure 3.2a). This means that 11 Sv of Atlantic waters are converted into intermediate and deep water masses in the Irminger and Iceland basins before leaving the ESPG within MOC<sub>LOWER</sub>. These densified water masses merge with 5 Sv of deep overflow waters and 15 Sv of recirculating water from the Irminger and Iceland basins to form the narrow and intense boundary current along the Greenland continental slope (31 Sv). This quantitative picture of the basin wide volume transport and water mass transformation in the ESPG is in line with a recent estimate of the mean circulation between Cape Farewell and Iceland derived from hydrography and altimetry data (*Sarafanov et al.*, 2012).

### 3.2.2 The Lagrangian analysis

The use of the Lagrangian analysis tool will enable quantification of the transport of MOC<sub>UPPER</sub> according to the spatial origins of the involved water masses (subtropics and Labrador Sea). The experiments are performed offline within a domain bounded by the A25-Ovide section, a subpolar transect at the exit of the Labrador Sea (SPG section) and a subtropical transect at 39°N (STG section) (Figure 3.1). Every month between 1965 and 2003, about 300 000 numerical particles are initially positioned along A25-Ovide and above the time-dependent position of  $\sigma_{MOC}$ . Note that using a constant  $\sigma_{MOC}$  value ( $\sigma_1 = 32.09$ ) yields very similar results. The numerical particles are advected freely by the three-dimensional model velocity field (i.e. the density criterion is only applied along the A25-Ovide section), and their trajectories are

integrated until they leave the domain through one of the three defined sections (STG, SPG or A25-Ovide). To fully reproduce the transport of MOC<sub>UPPER</sub>, two different runs are needed: a temporal backward integration to quantify the northward (positive) flow across A25-Ovide (*EXP<sub>BACK</sub>*) and a temporal forward integration to quantify the southward (negative) flow (*EXP<sub>FOR</sub>*). The combined sum of the individual particle transports from both runs yields the total transport of MOC<sub>UPPER</sub> at A25-Ovide. Annual mean fields are then constructed from these monthly experiments. In *EXP<sub>BACK</sub>*, the integration is done during a 7-year period to ensure that a large majority of particles ultimately reach a final section (only 1% of the initial particles stay within the domain, on average). This maximum travel time is reduced to one year for the *EXP<sub>FOR</sub>* experiment due to the much smaller distances travelled by the forward particles (see below), which on average reach a final section within one year. Due to the forward integration, the year 2004 is not considered in the following Lagrangian study. Two particle classes are then identified. The "local" class comprises the particles that recirculate back towards A25-Ovide through local recirculations (around Reykjanes Ridge for instance) or as part of the mesoscale eddy field. As seen in Section 3.3.2, this class of particles has a null signature on the long-term average circulation but might be involved in the variability. The "remote" class comprises those particles that crossed either the STG or the SPG transects and thus refers to the large-scale oceanic flow. The "remote" versus "local" decomposition of the flow may be an original means to study eddy fluxes in higher resolution models. Here, we will only concentrate on the large-scale component of the circulation.

Four "remote" components are extracted and their respective mean horizontal streamfunctions are plotted in Figure 3.3. *EXP<sub>BACK</sub>* isolates the subtropical (Figure 3.3a, T<sub>STG</sub> hereafter) and subpolar (Figure 3.3b, T<sub>SPG</sub> hereafter) components of MOC<sub>UPPER</sub> from the Gulf Stream and the Labrador Current, respectively. Their respective mean transports amount to 15 Sv and 8 Sv and they jointly compose the NAC. This mean decomposition of the NAC transport is in line with the synthesized circulation scheme of *Schmitz and McCartney (1993)* and *Böning et al. (1996)*. *EXP<sub>FOR</sub>* quantifies the transport of the upper fraction of the East Greenland Current around Cape Farewell (Figure 3.3c, T<sub>EGC</sub> hereafter) and that of the southward recir-

culuation in the Iberian Abyssal Plain that feeds the eastern limb of the subtropical gyre (Figure 3.3d,  $T_{REC}$  hereafter). As already mentioned in the previous section, their mean transports amount to 3 Sv each.

The present Lagrangian experiments enable us to consider the horizontal distribution of the MOC<sub>UPPER</sub> components along A25-Ovide, as well as their respective hydrographic properties at A25-Ovide and in their source regions. Figure 3.4a shows the mean transport of the MOC<sub>UPPER</sub> components summed horizontally along the A25-Ovide line. The most important feature arising from this representation is the equal contribution of  $T_{STG}$  and  $T_{SPG}$  to the NAC transport north of 49°N. This suggests that the water masses originating from the subtropical and subpolar sections have mixed and share similar hydrographic properties at A25-Ovide. To further illustrate this point, the salinity signatures of the MOC<sub>UPPER</sub> components at the STG and SPG sections and at A25-Ovide are displayed in figures 3.4b and 3.4c, respectively. Due to the small distances travelled by the forward particles,  $T_{EGC}$  and  $T_{REC}$  do not significantly change their salinity signature between A25-Ovide and the SPG and STG sections, respectively. By contrast, the salinity content of  $T_{STG}$  ( $T_{SPG}$ ) has substantially decrease (increase) as the particles travelled from the STG (SPG) section to the A25-Ovide section. While  $T_{STG}$  and  $T_{SPG}$  have very distinct salinity signatures in their source regions ( $35 < S < 36.5$  and  $S < 35$ , respectively), they occupy the same salinity range at A25-Ovide ( $34.7 < S < 36$ ) and form a relatively homogenous water mass (a similar result is found when using temperature instead of salinity). This confirms the strong mixing of both source waters as they flow within the NAC from Flemish Cap to the ESPG.

While the subtropical contribution to MOC<sub>UPPER</sub> (15 Sv) originates in the Gulf Stream, the subpolar inflow from the Labrador Current (8 Sv) may have two distinct origins: the Arctic outflow via Davis Strait and the western boundary current exiting the Irminger Sea and flowing cyclonically around the Labrador Sea. According to Figure 3.3c, we already know that the latter comprises 3 Sv of EGC waters flowing above  $\sigma_{MOC}$  at A25-Ovide. To quantify the origin of the remaining 5 Sv, we conducted an additional Lagrangian experiment (using the outputs from *EXP<sub>BACK</sub>*) and decomposed  $T_{SPG}$  as the sum of three contributions: from Davis Strait

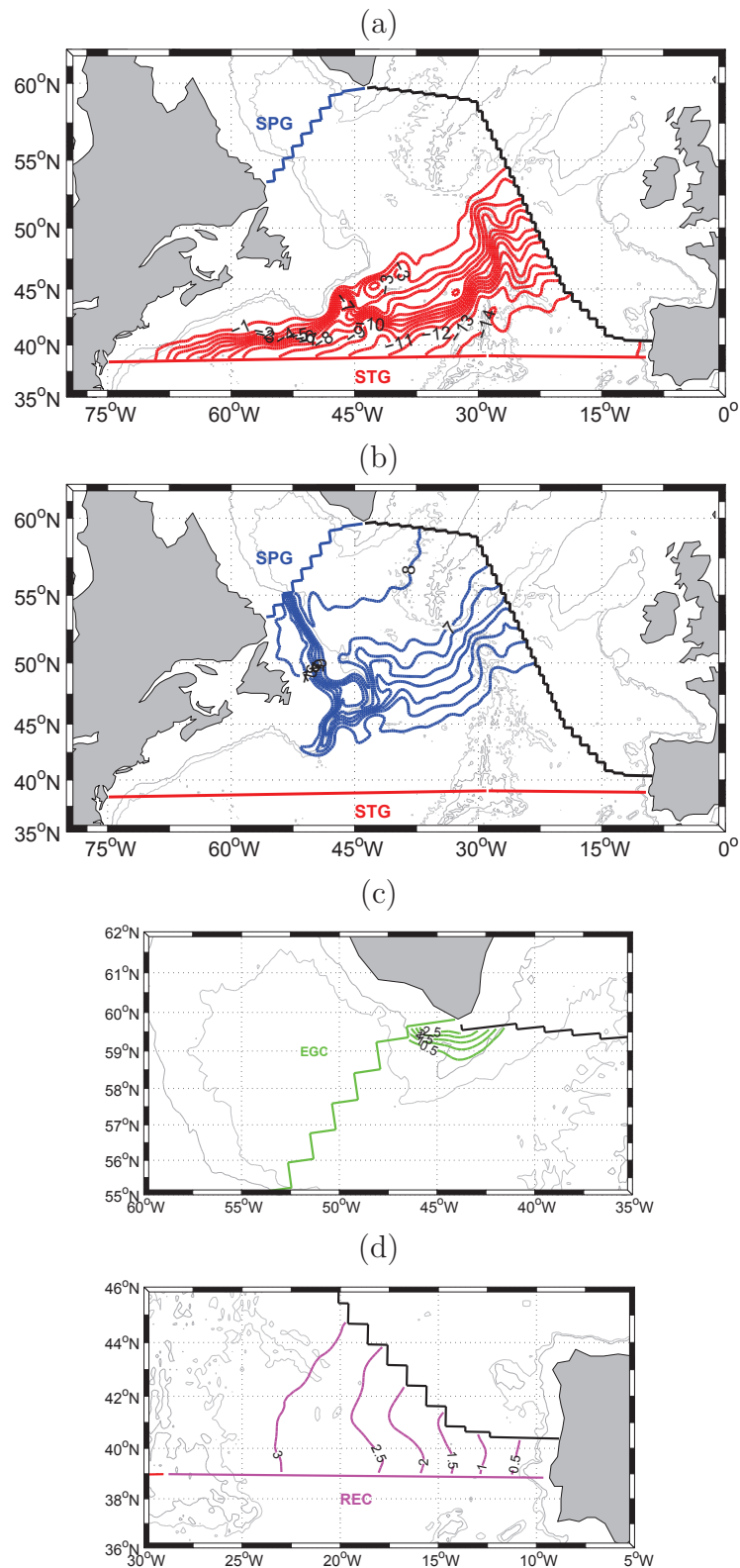


**Figure 3.3:** Mean (1965-2003) horizontal streamfunction ( $Sv$ ) of the four "remote" components contributing to the  $MOC_{UPPER}$  transport across A25-Ovide: (a) the subtropical transport ( $T_{STG}$ ), (b) the subpolar transport ( $T_{SPG}$ ), (c) the EGC transport ( $T_{EGC}$ ), and (d) the "Recirculation" transport ( $T_{REC}$ ). Contour interval is 1  $Sv$  in (a) and (b) and 0.5  $Sv$  in (c) and (d).

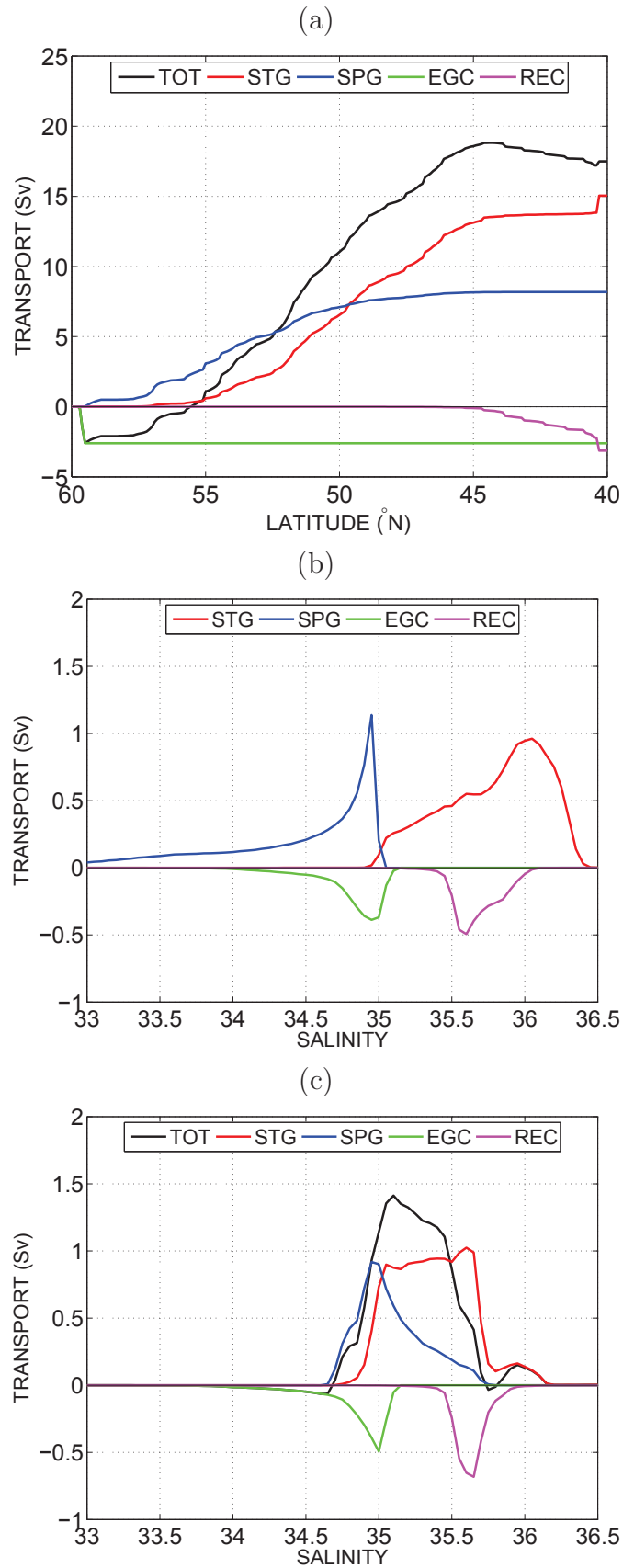


**Figure 3.4:** Mean (1965-2003) transport distributions (Sv) of the four "remote" components contributing to the MOC<sub>UPPER</sub> transport as a function of (a) latitude at A25-Ovide (accumulated from Greenland), (b) salinity measured at the STG and SPG sections and (c) salinity at A25-Ovide. In (b) and (c), the particle transports for each components were summed into  $\delta S = 0.125$  salinity bins.

( $T_{SPG}^{Davis}$ ), from the EGC above  $\sigma_{MOC}$  ( $T_{SPG}^{egc}$ ) and from the DWBC off Greenland below  $\sigma_{MOC}$  ( $T_{SPG}^{dwb}$ ). Figure 3.5 provides a quantification of the transports and a schematic of the upper and lower circulations deduced from the results previously described. The mean  $T_{SPG}^{Davis}$ ,  $T_{SPG}^{egc}$  and  $T_{SPG}^{dwb}$  amount to 1 Sv, 3 Sv and 4 Sv, respectively. Importantly, 4 Sv of the dense waters formed north of A25-Ovide and leaving the ESPG via MOC<sub>LOWER</sub> feed back into MOC<sub>UPPER</sub> via the Labrador Current instead of being exported toward the subtropics. The mean MOC <sub>$\sigma$</sub>  intensity at A25-Ovide (16 Sv) integrates two distinct patterns of circulation: an overturning cell connecting the western and eastern subpolar gyres (4 Sv) and a subtropical overturning connecting low and high latitude regions (12 Sv). The subpolar overturning implies a decrease in density of dense water masses in the northwestern Atlantic. To investigate in detail the involved mechanisms requires a complete study of air-sea interaction and mixing along the western margin of the subpolar gyre, which is beyond the scope of the present study. We can however infer from our Lagrangian results the spatial pattern of this dense-to-light conversion (Figure 3.6). Density changes along the mean streamfunction of  $T_{SPG}^{dwb}$  show an abrupt decrease in density in the vicinity of Flemish Cap, that is the region where the cold Labrador Current meets the warmer subtropical inflow from the Gulf Stream. Lateral mixing between the two source waters is likely important, as already noted from Figure 3.4b and 3.4c.

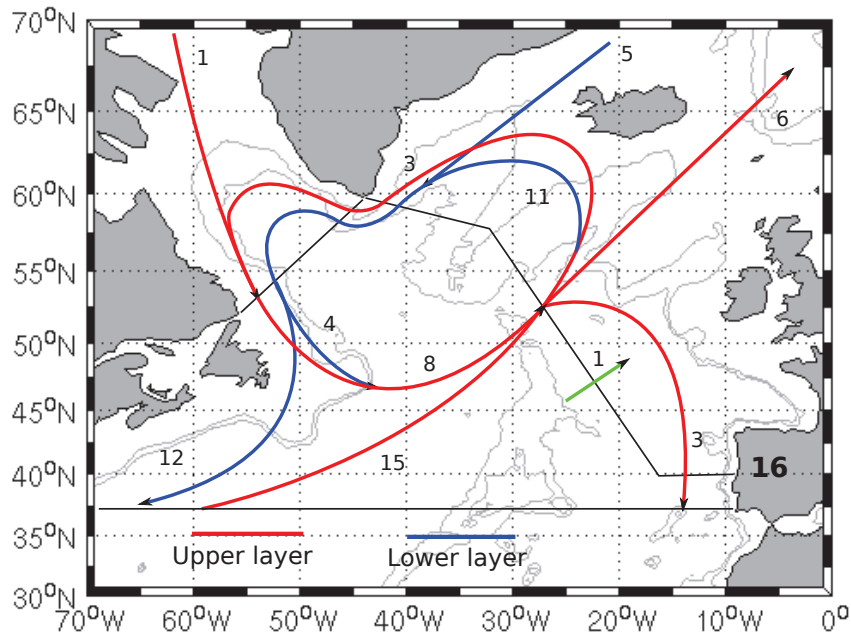


**Figure 3.5:** Schematic of the upper and lower circulation in the subpolar gyre deduced from Eulerian and Lagrangian diagnostics in ORCA025-G70. Red (blue) lines refer to the flow above (below) the mean  $\sigma_{MOC}$  value at A25-Ovide ( $\sigma_1 = 32.09$ ). The green arrow indicates the net transport across the section. Values are in Sv. The bold 16 Sv value indicates the mean MOC <sub>$\sigma$</sub>  intensity at A25-Ovide. The NAC advects 15 Sv of subtropical waters ( $T_{STG}$ ) and 8 Sv of subpolar waters ( $T_{SPG}$ ) within the upper MOC <sub>$\sigma$</sub>  limb at A25-Ovide. Out of these 23 Sv, 6 Sv recirculate within the upper limb via  $T_{REC}$  (3 Sv) and  $T_{EGC}$  (3 Sv), while 1 Sv is exported toward the Arctic Ocean. The remaining 16 Sv are densified in the Nordic Seas (5 Sv) and in the ESPG (11 Sv) and leave the region within the lower MOC <sub>$\sigma$</sub>  limb. A fraction (4 Sv) of these dense water masses decreases its density in the vicinity of Flemish Cape and feeds back into the upper MOC <sub>$\sigma$</sub>  limb at A25-Ovide, while the remaining 12 Sv are exported toward the subtropics.

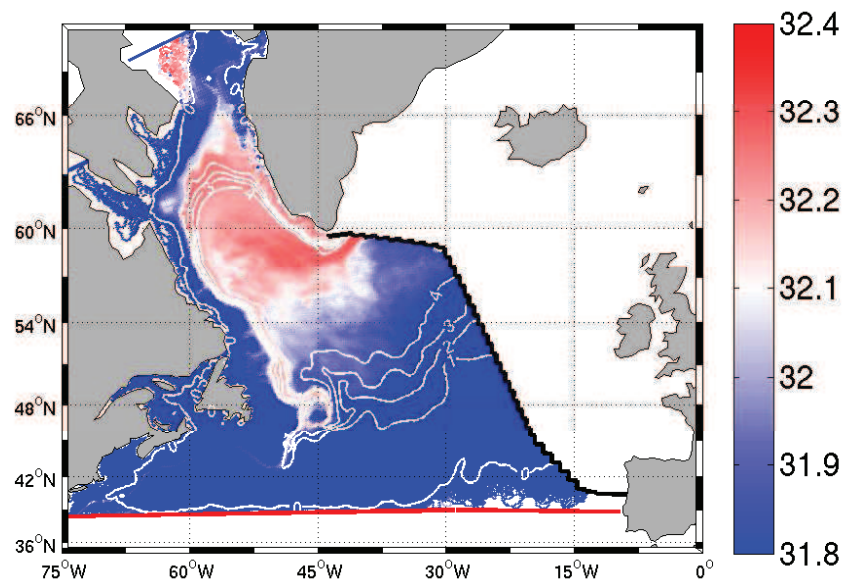


**Figure 3.6:** Mean (1965-2003) streamfunction ( $Sv$ ) of  $T_{SPG}^{dwb}$  (white lines, contour intervals of 1  $Sv$ ), superimposed on the associated mean particle density field ( $kg\ m^{-3}$ ). The colorbar is centered at  $\sigma_1 = 32.09$  that is the mean  $\sigma_{MOC}$  value at A25-Ovide.

### 3.3 Variability of MOC<sub>σ</sub>

We here focus on the interannual to decadal variability of the MOC<sub>σ</sub> at A25-Ovide for the period 1965-2004. The link between the strength of the MOC<sub>σ</sub> and the horizontal structure of its upper limb is investigated. An Eulerian analysis is presented first and is then complemented via the Lagrangian experiment results.

#### 3.3.1 The Eulerian view

Transport anomalies of the annual maximum MOC<sub>σ</sub> relative to the long-term mean (1965-2004) are presented in Figure 3.7. The decadal variability is characterized by three noticeable periods: a weakening of the circulation by 2.5 Sv between 1965 and 1974, a strong intensification by 4 Sv between 1974 and 1995, and a sharp decline of 3.6 Sv between 1995 and 2004. Although such low-frequency signal in the MOC<sub>σ</sub> strength cannot be easily detected in observations, it is consistent with the transport index proposed by *Curry and McCartney* (2001) that describes a gradual weakening of the NAC during the 1960s followed by a significant intensification between 1970 and up to 1996 and a rapid slow-down until 2003 (*Kieke et al.*, 2007). Those three major trends also appear in line with similar diagnosis performed in a wide range of OGCM experiments (e.g. *Marsh et al.*, 2005; *Bentsen et al.*, 2004; *Wunsch and Heimbach*, 2006; *Biastoch et al.*, 2008; *Huang et al.*, 2012). The decadal variability of the MOC<sub>σ</sub> evaluated across the Greenland-Scotland sills is relatively small (thin line in Figure 3.7), confirming that decadal changes of MOC<sub>σ</sub> at A25-Ovide reflect the changing rate of water mass transformation in the ESPG rather than transport changes originating in the Nordic Seas. This is either atmospherically-driven or internally-driven via entrainment downstream of the sills.

To investigate the link between the MOC<sub>σ</sub> variability and the changing horizontal structure of the NAC current system, we show in Figure 3.8a the difference in the cumulative horizontal transport of MOC<sub>UPPER</sub> between two distinct periods characterized by opposing MOC<sub>σ</sub> states (see gray shading in Figure 3.7): 1987-1997 (strong) minus 1968-1978 (weak). In this repre-

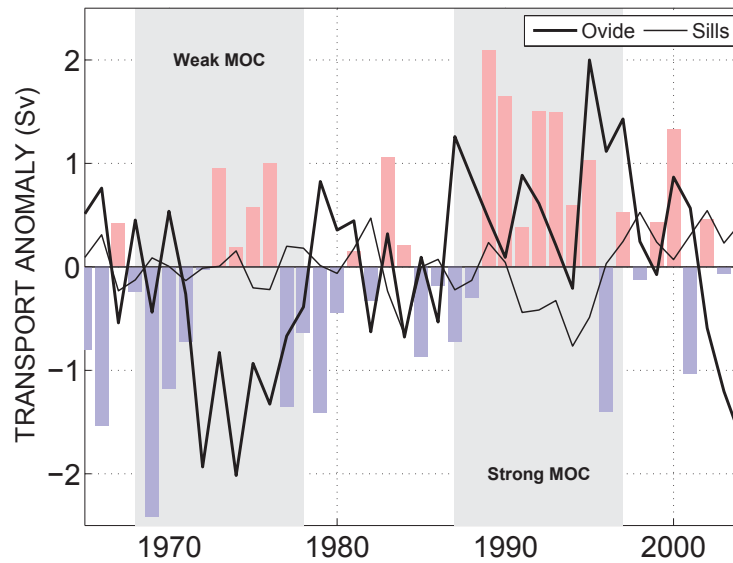


**Figure 3.7:** Annual transport anomalies of the MOC <sub>$\sigma$</sub>  across A25-Ovide (thick line) and across the Greenland-Scotland sills (thin line) relative to the mean of 1965-2004 (in Sv). The shaded areas denote two distinct periods respectively characterized by a weak (1968 - 1978) and a strong (1987 - 1997) MOC <sub>$\sigma$</sub>  state. The normalized winter NAO index is shown with bars (red: positive NAO years; blue: negative NAO years)

sensation, an upward (downward) slope within a given latitudinal range indicates a stronger (weaker) transport in 1987-1997 than in 1968-1978. Opposite latitudinal changes occurred on each side of 49°N between the two periods. Volume transports on each side of 49°N can be interpreted as the intensity of the northern and southern NAC branches that feed the Iceland basin and the Rockall Trough, respectively (*Lherminier et al.*, 2010). Note that 49°N is also a noticeable boundary for the mean composition of the NAC (see Figure 3.4a). Figure 3.8a implies that a strong MOC <sub>$\sigma$</sub>  state at A25-Ovide is associated with a relatively strong transport of the cold/fresh northern branch and a relatively weak transport of the warm/salty southern branch, and vice-versa for a weak MOC <sub>$\sigma$</sub>  state. Importantly, it is the respective intensities of the branches rather than a geographical shift in their positions that changes. In fact, the strongest velocity fronts in ORCA025-G70 keep a relatively fixed position over time (*De Boisséson*, 2010). In the following section, the variability signals previously described are assessed from a Lagrangian point of view, with a focus on changing transports associated with the subtropical and subpolar components of the NAC.

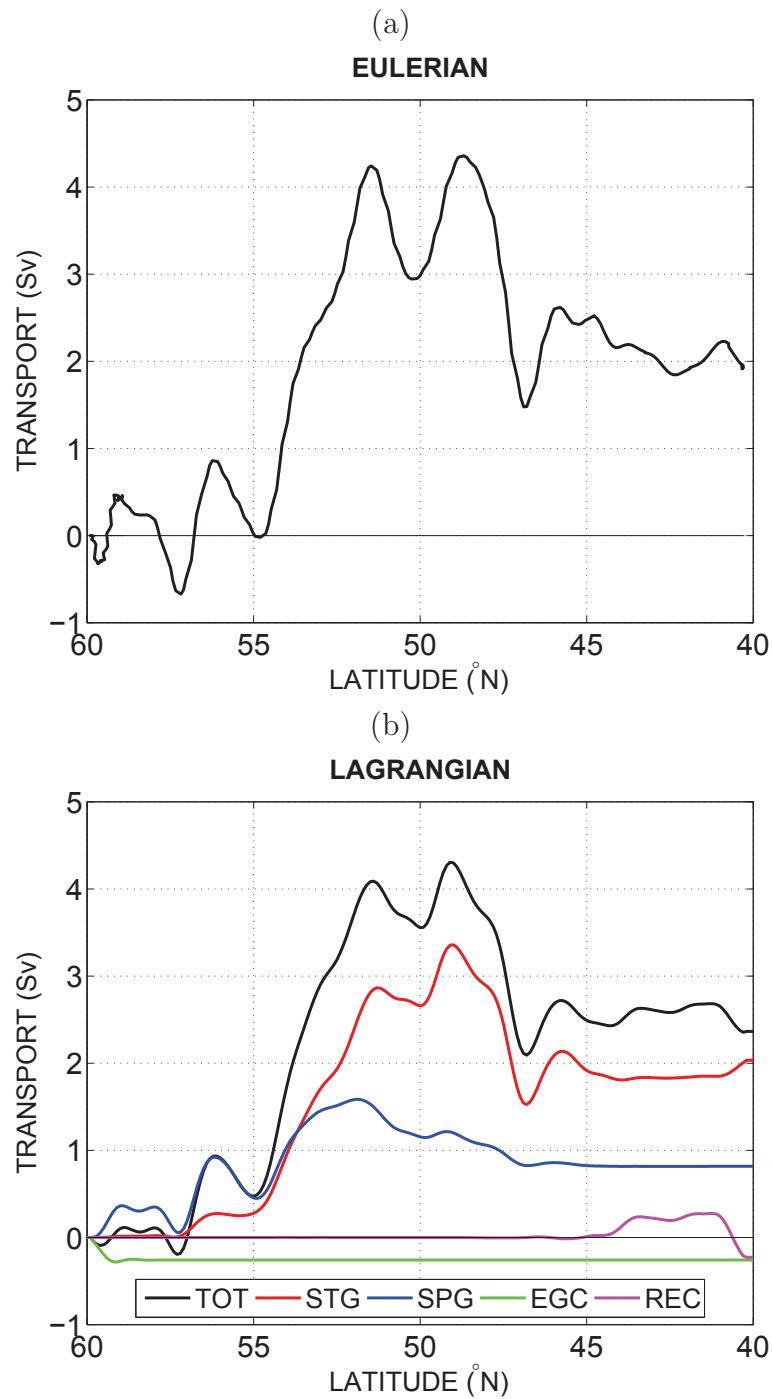


**Figure 3.8:** Changes in the latitudinal distribution of  $MOC_{UPPER}$  (in Sv) between the strong (1987-1997) and the weak (1968-1978)  $MOC_{\sigma}$  period depicted in Figure 3.7 for (a) the Eulerian calculation and (b) the Lagrangian reconstruction. The four remote components of  $MOC_{UPPER}$  are shown, as indicated in the legend. Transport anomalies have been summed from Greenland.

### 3.3.2 The Lagrangian analysis

The reconstructed anomalies of MOC<sub>UPPER</sub> in the Lagrangian framework agrees well with the Eulerian transport signal (Figure 3.9a). The small differences between the transports on interannual timescales result from the precision of the Lagrangian transport calculation (a small fraction of the numerical particles do not reach any final section within the allocated integration time). Note here that the transport index of MOC<sub>UPPER</sub> includes the contribution from the net transport variability, and is hence slightly different than the actual maximum MOC <sub>$\sigma$</sub>  signal described in Figure 3.7. Figure 3.9b displays the respective contributions of the "remote" and the "local" components of the circulation (see Section 3.2.2). Although both signals share a weak anti-correlation ( $r = -0.3$ ), most of the decadal signal is explained by the "remote" component, and hence the "local" contribution will be neglected hereafter.

Figure 3.10 shows the respective contributions of  $T_{STG}$ ,  $T_{SPG}$ ,  $T_{REC}$  and  $T_{EGC}$  to the total transport changes of MOC<sub>UPPER</sub>. The variability of the southward components of MOC<sub>UPPER</sub> ( $T_{REC}$  and  $T_{EGC}$ , Figures 3.10a and 3.10b, respectively) contains no substantial decadal signal. Their respective transport anomalies cannot be neglected on interannual timescales, though. A significant anti-correlation is found between  $T_{REC}$  and  $T_{STG}$  ( $r = -0.6$ ). This corroborates that the southward recirculation in the Iberian abyssal plain is closely related to the interannual variability of subtropical water transport carried out by the NAC, as proposed in recent observational and modeling studies (*Treguier et al.*, 2006; *Gourcuff*, 2008; *Lherminier et al.*, 2010). Interestingly, the two components of the NAC ( $T_{STG}$  and  $T_{SPG}$ , Figures 3.10c and 3.10d, respectively) exhibit similar decadal behaviours with an amplitude corresponding to  $\sim 25\%$  of their respective mean transports. Both components present a decreasing transport in the 1960-70s followed by a gradual intensification until the mid-1990s and a decline afterwards. The two components are strongly correlated on decadal timescales ( $r = 0.8$  when both signals are 10-year low-pass filtered). As a consequence, the proportion of subpolar and subtropical waters crossing the section within the NAC remains relatively constant on decadal timescales. In particular, the strong and weak MOC <sub>$\sigma$</sub>  phases of the 1990's and 1970's are characterized by

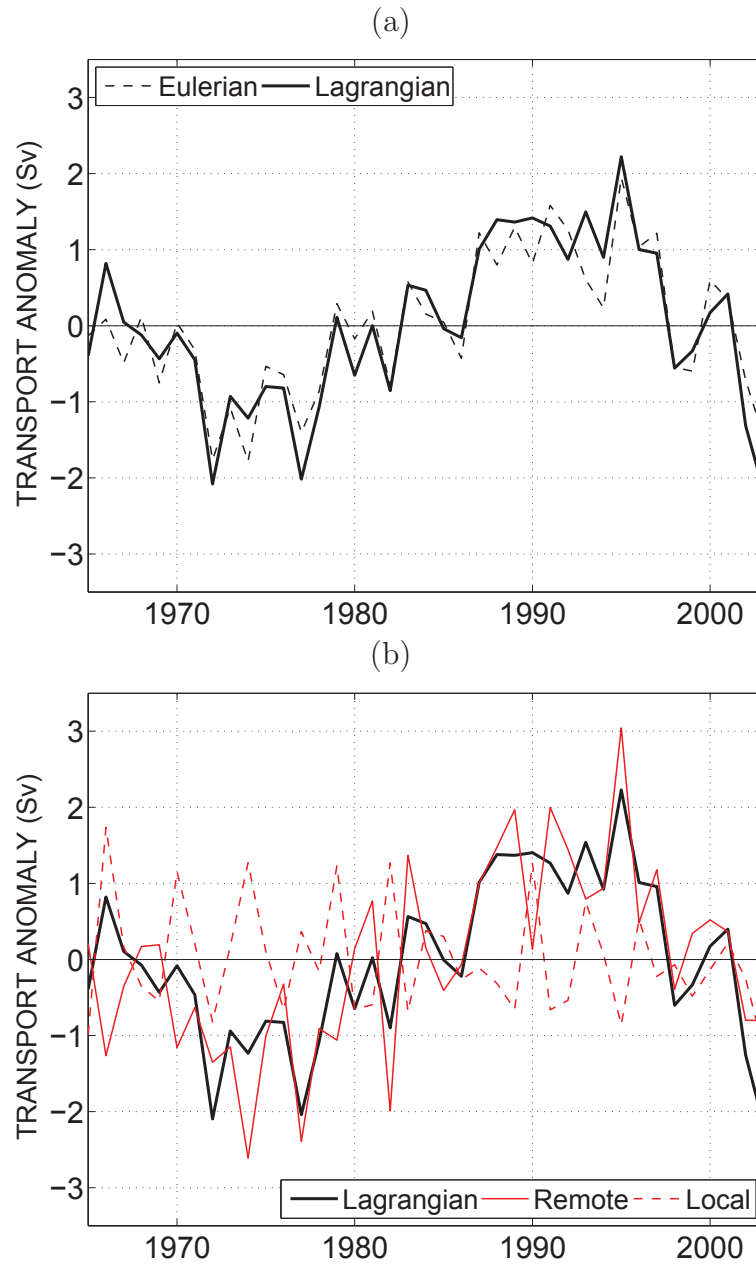


**Figure 3.9:** (a) Annual transport anomaly (Sv) of  $MOC_{UPPER}$  relative to the 1965–2003 period: Eulerian calculation (black line) and Lagrangian reconstruction (red line) including the “remote” and the “local” contributions. (b) Same as (a) but with the Lagrangian transport decomposed into its “remote” (solid red line) and “local” (dashed red line) parts.

the same proportion of subtropical (65 %) and subpolar (35%) waters within the NAC. Over the 1965-2004 time period, the  $\frac{T_{STG}}{T_{STG}+T_{SPG}}$  ratio fluctuates between 60% and 68% and those fluctuations show no correlation with the variability of the NAC (Figure 3.11).

As highlighted from the Eulerian diagnosis (Figure 3.8a), the difference between a weak and a strong MOC <sub>$\sigma$</sub>  state across the A25-Ovide section is characterized by opposed changes north and south of  $\sim 49^\circ\text{N}$ . In the Lagrangian experiments (Figure 3.8b), the transport changes on either sides of this latitudinal boundary are dominated by changes in the subtropical transport. Most importantly,  $T_{STG}$  accounts for about 70% of the total transport change between  $49^\circ\text{N}$  and  $58^\circ\text{N}$ , that is within the relatively cold and fresh Iceland Basin. The subpolar contribution cannot be neglected though, and dominates the transport changes north of  $55^\circ\text{N}$ .

In summary, the decadal variability of MOC<sub>UPPER</sub> is largely linked to the NAC variability ( $r = 0.86$ ), which reflects in-phase changes of the subtropical and subpolar transports. Additionally, the changing horizontal structure of the NAC transport between two persistent and opposed states of the MOC <sub>$\sigma$</sub>  is associated with opposite variability of its main branches, primarily induced by subtropical transport changes.

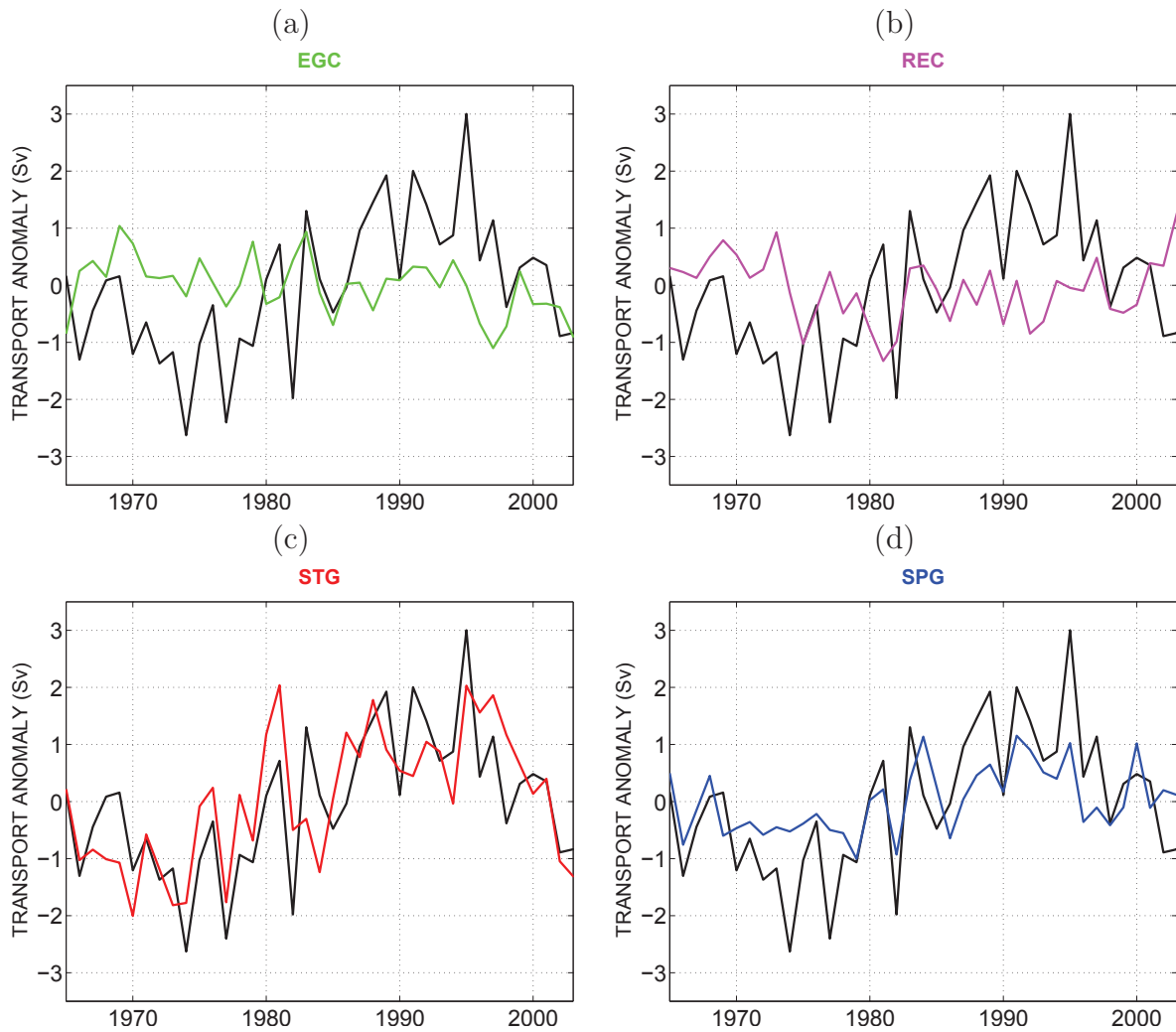


**Figure 3.10:** Annual transport anomaly (Sv) relative to the 1965-2003 period of the four MOC<sub>UPPER</sub> components (colored lines) superimposed on the total MOC<sub>UPPER</sub> transport anomaly (black). Positive anomalies for the  $T_{STG}$  and  $T_{SPG}$  ( $T_{EGC}$  and  $T_{REC}$ ) refer to an intensified (weakened) northward (southward) transport across A25-Ovide.

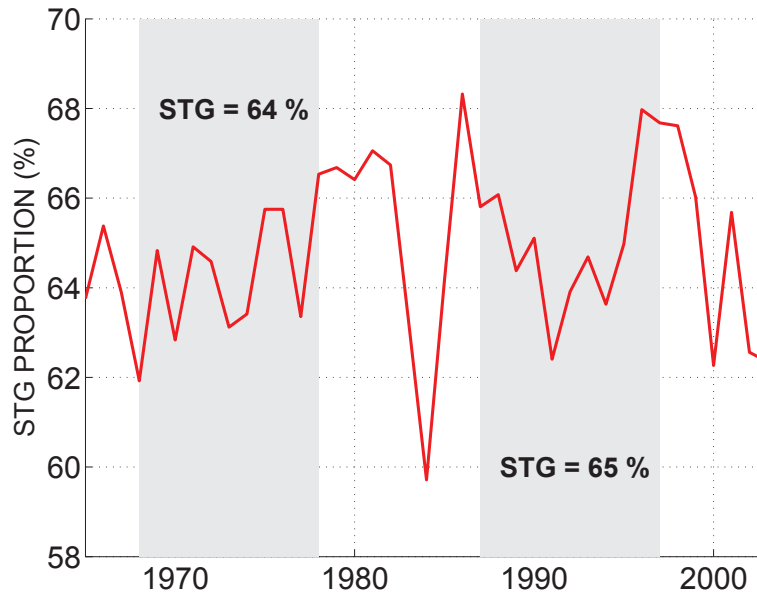


Figure 3.11: Annual anomalies (in %) of the  $\frac{T_{STG}}{T_{STG}+T_{SPG}}$  ratio at A25-Ovide.

### 3.4 On the link between the intensity and the spatial extent of the subtropical inflow

In a recent study based on numerical tracer experiments performed with the Simple Ocean Assimilation System (SODA), Häkkinen *et al.* (2011a) highlighted significant changes in the spatial extent of subtropical water masses in the northeastern Atlantic with potential effect on the salinity content of the ESPG. Three periods of increased connection between the Gulf Stream waters and the ESPG were observed: the late 1960's, the 1980's and the early 2000's. The authors suggested an impact of those penetration events on the composition of the upper MOC<sub>σ</sub> limb in mid-high latitude regions, but the link with the actual strength of the overturning cell remains obscure.

An additional set of Lagrangian experiments was conducted to relate our quantitative estimates of the subtropical contribution to the MOC<sub>σ</sub> variability at A25-Ovide (i.e.  $T_{STG}$ ) with a qualitative estimate of changes in the spatial extent of subtropical water masses. Each month between 1965 and 2004, artificial particles were distributed every 0.5° of longitude along the

STG transect at several depth levels between the surface and 1200m depth (a total number of 1560 particles were released each year at each depth level). The particles were then allowed to evolve freely within the model velocity field during 3 years. This particular advection time ensures that particles have enough time to reach the ESPG. We show in Figure 3.12a the resulting subtropical trajectories of particles released at the sea surface in 2001. One can note that a large majority of particles recirculated within the subtropical gyre south of 40°N while a relatively small proportion reached high latitude regions. This appears consistent with the very weak intergyre connections captured by observational surface drifters (*Brambilla and Talley, 2006; Häkkinen and Rhines, 2009*). To provide a temporally continuous quantification of intergyre exchanges within the upper water column, the number of numerical particles located east of the A25-Ovide line during each year was quantified. The resulting index is considered as a proxy for the northeastward extent of subtropical water masses, at each depth level (note that this index is not a volume transport index but a "penetration" index). It is displayed as a Hovmöller diagram in Figure 3.12b. The strongest intergyre connection occurs below the surface (at 300 m depth here) and relatively weak connection is seen at the surface. This is consistent with the recent study of *Burkholder and Lozier (2011)* who combined an eddy-resolving OGCM and artificial lagrangian floats to highlight the strong subsurface signature of intergyre exchanges in the North Atlantic. The three major periods of increased intrusion of subtropical waters towards the ESPG pointed out in SODA by *Häkkinen et al. (2011a)* are particularly well reproduced: the late 1960's, the 1980's and the early 2000's. Note also that relatively high values are observed around 1990. The (normalized) penetration index averaged within the 0-400m layer is compared in Figure 3.12c with the volume transport anomalies of T<sub>STG</sub> at A25-Ovide (see Figure 3.10c). Both timeseries, which can respectively be related to the northeastward extent and the strength of the subtropical contribution to the NAC/MOC<sub>UPPER</sub> transport, are anti-correlated ( $r = -0.55$ ). This is particularly evident during the well-documented period of the late 1990's-early 2000's: an intense weakening of the subtropical transport within the NAC occurred in concomitance with an enhanced intrusion of subtropical water in the ESPG. Investigating this causal relationship is beyond the scope of the present paper, and we here

simply conclude that the northeastward extent of subtropical water masses towards the ESPG describes an out-of-phase relationship with the actual subtropical volume transport variability, especially from 1985 onward.

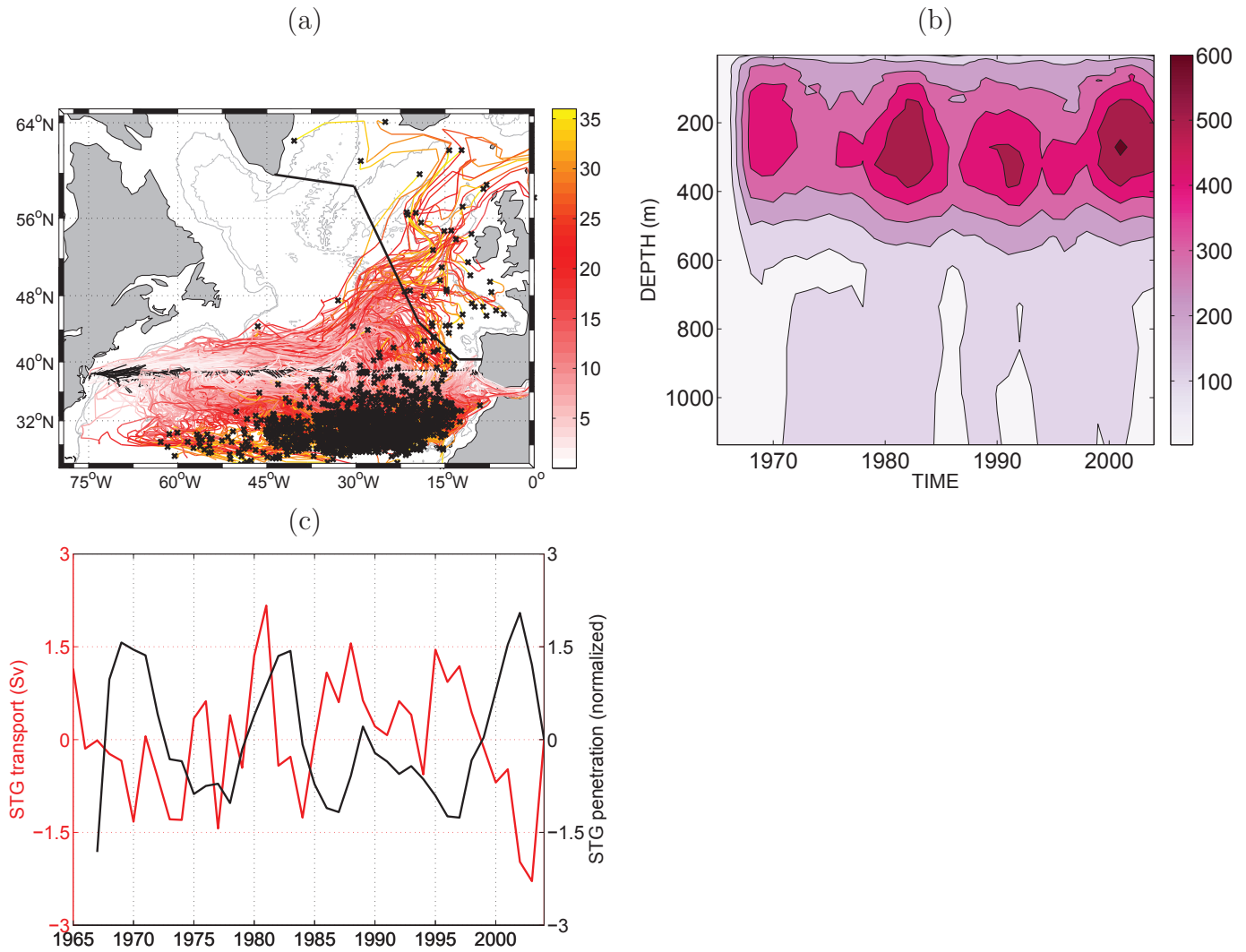


**Figure 3.12:** (a) Trajectories of 1560 numerical particles launched at the surface in 2001 along the STG transect and advected within the model velocity field during 3 years. Colors indicate the age of particles in month and black crosses indicate the particle final positions. (b) Hovmöller diagram of the normalized index of the northeastward penetration of subtropical waters in the ESPG. The index corresponds to the number of numerical particles located east of A25-Ovide during each year, as a function of launch depth from the STG line. (c) Same as (b) but average within the 0-400m layer (black line). The volume transport anomalies associated with the subtropical component of MOC<sub>UPPER</sub> ( $T_{STG}$ ) are shown in red. Both timeseries have been detrended.

### 3.5 Discussion

The described variability of the NAC/MOC <sub>$\sigma$</sub>  in ORCA025-G70 is globally consistent with the decadal NAO signal (see Figure 3.7). When considering the low-frequency part of both timeseries (10-year low-pass filtering), the NAO leads the MOC <sub>$\sigma$</sub>  at A25-Ovide by 4-5 years ( $r = 0.7$ ). Interestingly, the MOC <sub>$\sigma$</sub>  and NAC indexes at A25-Ovide show a clear correspondence with a baroclinic intergyre transport index computed from hydrographic data collected at Bermuda and at station *Bravo* in the Labrador Sea (*Curry and McCartney, 2001; Kieke et al., 2007*). This observational index of the NAC transport was shown to lag the NAO fluctuations by 2-3 years. The greater lag found at A25-Ovide in the model is consistent with the mean travel time needed by the numerical particles to reach the ESPG from the Labrador Sea or the subtropics (about 2 years). Moreover, *Curry and McCartney (2001)* showed that the subtropical and subpolar gyre intensities fluctuate in phase on decadal timescales, in good agreement with our Lagrangian results (see Figure 3.10).

Changes in the horizontal shape of the upper layer transport at A25-Ovide (see Figure 3.8) might reflect meridional shifts of the zero wind-stress curl line associated with the NAO low-frequency signal. Anomalous Ekman pumping is thought to create an anomalous gyre circulation at mid-latitudes, often referred to as the *intergyre gyre* (*Marshall et al., 2001*). It can be identified as the subtropical pole of variability in the gyre index spatial structure (see Figure 1.12 and Figure 2.11). During high NAO conditions, this intergyre gyre is anticyclonic, and tends to increase (decrease) the transport of the northern (southern) NAC branch. *Herbaut and Houssais (2009)* pointed out this wind-driven anomalous circulation as an important contributor to the changing structure of the NAC and associated changes in the salinity content of the ESPG. On the other hand, our "penetration" index, reflecting the northeastward intrusion of warm subtropical waters in the ESPG, shows no significant correlation with the NAO index at the 95% level. In fact, *Häkkinen et al. (2011a)* suggested that those episodes of increased intergyre connection in the northeastern Atlantic reflect a modulation of the climatological

wind stress curl field, which is only weakly correlated with the NAO index.

### 3.6 Conclusion

Decadal changes of the overturning circulation in the density space at A25-Ovide have been quantified in the ORCA025-G70 simulation (1965-2004). The mean structure and intensity of the MOC <sub>$\sigma$</sub>  were in line with observations and its variability was shown to sustain substantial decadal signals in good agreement with previous observational and modeling studies. A transport index of the upper MOC <sub>$\sigma$</sub>  limb across the A25-Ovide section was constructed from a set of Lagrangian experiments. The respective impacts of the subtropical and subpolar inflow variability on the strength and spatial structure of the NAC were of particular interest. The variability of the subtropical volume transport within the NAC was further compared to a qualitative index of the northward intrusion of subtropical water masses in the ESPG. Accordingly, we reach the following conclusions:

- *The time-averaged MOC <sub>$\sigma$</sub>  across A25-Ovide (16 Sv) can be decomposed into a subtropical cell connecting low and high latitude regions (12 Sv) and a cell internal to the subpolar gyre (4 Sv). The MOC <sub>$\sigma$</sub>  decadal variability is associated with an in-phase relationship between the subtropical and the subpolar components of the NAC.*

The NAC forms the main component of the upper MOC <sub>$\sigma$</sub>  limb in the ESPG. Its mean transport is composed of two-thirds of subtropical waters from the Gulf Stream (15 Sv) and one-third of subpolar water masses from the Labrador Current (8 Sv). Half of the subpolar contribution (4 Sv) is associated with a dense-to-light conversion of deep western boundary current waters. The Lagrangian experiments indicate that this decrease in density primarily occurs in the vicinity of Flemish Cap, where subpolar water masses meet the warm Gulf Stream waters. Strong lateral mixing was consistently observed in this particular region (e.g. Dutkiewicz *et al.*, 2001; Perez-Brunius *et al.*, 2004). Overall, the cyclonic subpolar gyre circulation contributes to a quarter of the mean MOC <sub>$\sigma$</sub>  at A25-Ovide (4 Sv out of 16 Sv). The remaining 12 Sv are

carried out by a subtropical meridional cell advecting Gulf Stream waters in its upper limb.

The maximum MOC <sub>$\sigma$</sub>  variability evaluated at A25-Ovide describes a strong positive trend between the mid 1970's and the mid 1990's followed by a rapid weakening until the mid 2000's, and presumably relates to NAO-related forcing. The transport changes in the upper limb are predominantly related to the intensity of the NAC, which reflects an in-phase relationship between its subtropical and subpolar components. This is in line with the study of *Curry and McCartney* (2001) that showed coherent changes in the strength of the subtropical and subpolar gyre on decadal timescales. The relative proportion of the basin wide subtropical and subpolar transports within the upper MOC <sub>$\sigma$</sub>  limb at A25-Ovide consequently shows no substantial decadal variations.

- *Decadal changes in the MOC <sub>$\sigma$</sub>  strength at A25-Ovide are associated with horizontal restructuring of the NAC transport.*

Opposed transport changes on each side of  $\sim 49^\circ\text{N}$  are noted. When the MOC <sub>$\sigma$</sub>  is in a strong phase (1990's), the cold water transport within the Iceland Basin associated with the northern NAC branch is strong while the warm water transport of the southern branch at the Rockall Trough entrance is relatively weak (the inverse is true for a weak MOC <sub>$\sigma$</sub>  phase as in the 1970's and 2000's). As shown through Lagrangian experiments, this spatial pattern of variability primarily reflects a redistribution of subtropical water masses within the NAC. This differs from the conclusion of *Hátún et al.* (2005) suggesting the subpolar gyre dynamics as the main driving mechanism behind the changing structure and composition of the NAC in the ESPG. This potential contradiction relies on the methods used to separate the subtropical and subpolar transport signatures within the NAC. We note here that the mean NAC transport north of  $49^\circ\text{N}$  is equally partitioned between waters of subpolar and subtropical origins ( $\sim 7$  Sv each), and that their respective signatures on the NAC variability cannot hence be extracted hydrographically.

- *Periods of expanded subtropical gyre generally occur during periods of weak subtropical*

*volume transport, and weak MOC <sub>$\sigma$</sub>  in the Northeastern Atlantic.*

Qualitative analysis of subtropical water trajectories enables us to continuously monitor the spatial extent of the subtropical gyre in the Northeastern Atlantic. The three periods of increased connection between Gulf Stream waters and the ESPG highlighted in *Häkkinen et al.* (2011a) were satisfactorily reproduced (late 1960's, around 1980 and early 2000's). The Lagrangian experiments enable us to link those penetration events with the intensity of the subtropical overturning cell. Both indices describe opposed behavior on interannual/decadal timescales, in agreement with the recent suggestion of *Chaudhuri et al.* (2011). A stronger (weaker) subtropical volume transport across A25-Ovide is generally associated with a weaker (stronger) northeastward intrusion of subtropical water masses in the ESPG.

The present description of the MOC <sub>$\sigma$</sub>  variability at A25-Ovide now needs to be considered in a heat/freshwater transport perspective. Heat transport was particularly shown to drive significant heat content changes on decadal timescales in the subpolar gyre (*Grist et al.*, 2010). A heat budget investigation within the ESPG performed in a similar Eulerian/Lagrangian framework is presented in the following chapter.

# Chapter 4

## Decadal heat content variability in the eastern Subpolar Gyre

---

### Abstract

*Historical and modern hydrographic data show substantial decadal variability in the heat content (HC) of the eastern subpolar gyre region. Those changes are here investigated in an eddy-permitting simulation (ORCA025-G70) forced by reanalysis products for the period 1965-2004. A heat budget calculation is performed within a box bounded by the A25-Ovide section and the Greenland-Scotland sills. The rate of change of HC results from the slight imbalance between the oceanic heat transport convergence and local air-sea heat fluxes. This imbalance is shown to be highly correlated with heat transport variability across the southern boundary ( $HT_{A25}$  hereafter).  $HT_{A25}$  basically describes a positive trend from relatively low values in the 1960's and early 1970's (causing a cooling of the domain) toward high values in the 1990s and early 2000s (causing a warming of the domain). This decadal signal is mainly induced by changes in the diapycnal component of the flow, which has a strong horizontal signature. The impact of temperature changes acting upon the mean oceanic circulation ( $\overline{V}\theta'$ ) dominates the long-*

term behavior of  $HT_{A25}$ , but this term is significantly damped by opposed changes induced by velocity anomalies ( $V'\bar{\theta}$ ). The total heat transport is then approximated using an index of the  $MOC_{\sigma}$  intensity and an index of the temperature difference between its two limbs. We show that both temperature and velocity anomalies are partly reflected in the heaves of isopycnals at A25-Ovide, which controls the depth and slope of the main pycnocline. A Lagrangian analysis of the thermally-driven heat transport shows that temperature anomalies along A25-Ovide are largely related to the varying proportions of cold subpolar waters and warm subtropical waters advected within the North Atlantic Current (NAC).

---

## 4.1 Introduction

Understand the mechanisms governing oceanic temperature and associated heat content (HC) variability has become an essential issue for better climatic prediction. While observational evidences from a wide range of *in situ* measurements show a global warming of the world's oceans since several decades (*Levitus et al.*, 2009), the associated patterns of HC changes highlight significant spatial disparities in the observed trends. Those inhomogeneity are particularly pronounced in the North Atlantic Ocean, where the subtropical and subpolar HC have evolved differently during the second half of the twentieth century: while the subtropical and tropical latitudes showed an overall heat gain, the subpolar region underwent a significant heat loss (*Lozier et al.*, 2008; *Zhai and Sheldon*, 2012). *Lozier et al.* (2008) estimated a heat loss in the whole subpolar gyre (51°N - 63°N) of  $-1.05 \pm 06 \cdot 10^{22}$  J between 1980-2000 and 1950-1970. The present Chapter focuses on the eastern Subpolar Gyre (SPG) region and aims to identify through the analysis of the ORCA025-G70 simulation, the principal processes responsible for the observed decadal signal during the 1965-2004 time span. The eastern SPG is chosen since

it encompasses regions where significant hydrographic changes were observed during recent decades: the Irminger Sea, the Iceland basin and the Rockall Trough (*Bersh, 2002; Holliday et al., 2008; Thierry et al., 2008*). These are key regions for the buoyancy-driven formation of intermediate and deep water masses that feed the lower limb of the Meridional Overturning Circulation (e.g. *Brambilla and Talley, 2008*) and any long-term modifications of the upper density field there may have significant climatic implications.

During the last five decades, the hydrographic content of the eastern SPG has undergone significant variability marked by a gradual cooling and freshening from the 1960's until the early 1990's followed by a sharp and intense warming and increase in salinity that prevails at least until 2007. Heat and freshwater exchanges at the air-sea interface were shown insufficient to explain this decadal signal and many studies have thus focused on the role played by changes in the advection of heat and freshwater by the large-scale oceanic circulation (e.g. *Bersh, 2002; Holliday, 2003; Thierry et al., 2008; Chaudhuri et al., 2011*).

The recent warming and increase in salinity of the eastern SPG in the late 1990's and early 2000's has received much attention, due notably to improved *in situ* data coverages and the advance of satellite measurements. It was shown to occur concomitantly with a buoyancy-driven weakening of the SPG circulation depicted in an altimetry-derived gyre index (*Häkkinen and Rhines, 2004*). *Bersh (2002)* showed using hydrographic data a concomitant westward shift of the subpolar front location along the A1E line joining Greenland and Scotland. The sharp switch of NAO conditions from a persistent positive phase in the early 1990's towards a strong negative episode in 1996 was widely invoked to explain those substantial changes of the SPG state. In hindcast numerical simulations, the weakening SPG of the 1990's was shown to be preceded by an intensification from the late 1960's (*Hátún et al., 2005; Böning et al., 2006*), which coincides with a positive trend in the NAO index and an observed cooling/freshening of the eastern SPG. *Marsh et al. (2008)* and *Grist et al. (2010)* confirmed the crucial role played by the gyre component of the heat transport in driving HC changes in the high latitude regions.

A closer look into the mechanisms associated with decadal HC changes in the eastern SPG was documented in the study of *Hátún et al. (2005)* based on a numerical hindcast simulation.

The SPG variability was presumed to control the respective inflows of cold/fresh subpolar waters and warm/salty subtropical waters toward the Nordic Seas. Using a salinity criterion to identify their respective signatures within the North Atlantic Current (NAC), *Hátún et al.* (2005) showed opposed transport variability of both source waters on decadal timescales that closely mimic the gyre index fluctuations. We saw in Chapter 1, however, that hydrographic criteria are not necessarily suitable to diagnose the respective transport variability of subtropical (i.e. from the Gulf Stream) and subpolar waters (i.e. from the Labrador Sea) in the eastern SPG. Consistently, *Chaudhuri et al.* (2011) also suggested that the transport of warm and salty waters toward the eastern SPG should be distinguished from the actual intergyre subtropical transport, which is stronger (weaker) during positive (negative) phases of the NAO. Using an ocean GCM forced by idealized atmospheric fields, *Herbaut and Houssais* (2009) excluded buoyancy-driven changes of the SPG circulation as a main driver of hydrographic changes in the eastern SPG. Instead, they pointed out the relevance of an anomalous circulation located over the climatological position of the Gulf Stream/NAC current system, referred to as the "intergyre gyre" (*Marshall et al.*, 2001; *Eden and Willebrand*, 2001). The latter is the second pole of variability described by the gyre index and was shown to result from largescale windstress curl anomaly related to the NAO.

Overall, the physical processes responsible for the substantial changes of the eastern SPG hydrographic properties are far from being totally understood. The main objective of this Chapter is to contribute to this understanding by providing a link between the regional circulation changes described in the aforementioned studies and the actual rate of change of HC in the eastern SPG. After briefly evaluating the ability of the ORCA025-G70 simulation to reproduce the observed heat content changes (Section 4.2), a heat budget calculation within a box bounded by the A25-Ovide section and the Greenland-Iceland-Scotland (GIS) sills (Figure 4.1) will be presented (Section 4.3). We particularly wish to emphasize the potential mechanisms linking the basin-wide heat transport variability and HC changes on decadal timescales. While HC variations in the Gulf Stream region are presumably related to the anomalous circulation acting upon the mean temperature field (*Eden and Jung*, 2001; *Jayne and Marotzke*, 2001),

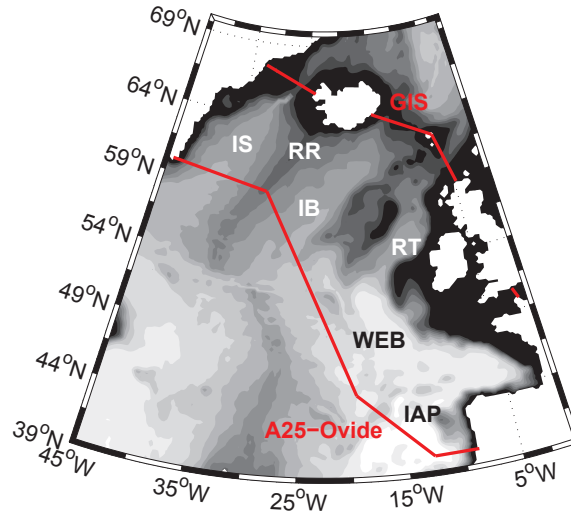


**Figure 4.1:** The study domain bounded by the A25-Ovide section and the Greenland-Iceland-Scotland (GIS) sills. The main basins and topographic features discussed in the text are labelled as: IS (Irminger Sea), IB (Iceland Basin), RT (Rockall Trough), WEB (West European Basin), IAP (Iberian Abyssal Plain), RR (Reykjanes Ridge).

the advection of temperature anomalies along the pathway of the NAC might be important in driving HC changes in the northeastern Atlantic, as suggested in observational and modeling studies (Sutton and Allen, 1997; Krahnemann *et al.*, 2000). Spatial and temporal decompositions of the full-depth heat transport across A25-Ovide will be proposed in Section 4.4. An approximation of  $HT_{A25}$  based on an index of the Meridional Overturning Circulation in the density plane ( $MOC_{\sigma}$ ) will be used to gain insights into the main mechanisms at play (Section 4.5). Finally, Lagrangian experiments (the  $EXP_{BACK}$  experiment described in Chapter 3) will be carried out to complement the Eulerian analysis (Section 4.6).

## 4.2 Validation of simulated heat content variability in the eastern SPG

As shown in Chapter 2, the ORCA025-G70 simulation is able to broadly reproduce the mean and anomalous dynamics and hydrographic features of the North Atlantic ocean seen in the

observational records. In addition, the consistency of the model temperature within our region of interest (the eastern SPG) was recently proven by *De Boisséson et al.* (2010). Through a seasonal heat budget calculation in the Iceland Basin's mixed layer, the authors highlighted the good agreement between ORCA025-G70 and the Argo database. Also, *de Boisséson et al.* (2012) showed that the simulated spatio-temporal characteristics of the subpolar mode water located over Reykjanes Ridge in ORCA025-G70 were consistent with observations. Here, the values of  $HC$  within the eastern SPG domain are calculated following equation 4.1,

$$HC(t) = \rho_0 C_p \int_x \int_y \int_z \theta(x, y, z, t) dx dy dz \quad (4.1)$$

where  $\rho_0$  is a reference density for seawater ( $\rho_0 = 1026 \text{ kg m}^{-3}$ ),  $C_p$  is the specific heat capacity ( $C_p = 3996 \text{ kg}^{-1} \text{ K}^{-1}$ ) and  $\theta$  is the three-dimensional potential temperature field. Annually-averaged anomalies of the simulated and observed (WOA09)  $HC$  within the 0-700m layer of the eastern SPG domain are compared in Figure 4.2. There is a very good agreement in the amplitude and phases of both timeseries ( $R = 0.9$ , significant at the 95% level<sup>1</sup>). Both signals describe a cooling ocean in the 1960's and 1970's followed by a period of relatively minor changes (1980's - early 1990's) and a sharp warming since the mid-1990's (this warming trend prevails until 2007 in WOA). Thus, the 1980's - early 1990's stands as a transition period between two significant switches in the eastern SPG hydrographic properties. The present study is particularly aimed to elucidate those changes and to propose potential driving mechanisms. The long-term change in  $HC$  between 1965 and 2004 for the 0-700m layer amounts to  $+2.2 \cdot 10^{21}$  J in WOA and  $0.2 \cdot 10^{21}$  J in ORCA025-G70, that is much weaker than the decadal variability (this long-term trend will not be studied in the present Chapter). Also shown in Figure 4.2 is the simulated  $HC$  change within the whole water column (thin blue line). The cooling in the 1960-1970's is slightly enhanced, possibly due to the adjustment of the deep water masses as no spin-up was performed for this simulation. Post 1980, the subsurface and full-depth signals are almost identical ( $R = 0.98$ ), meaning that much of the decadal changes in  $HC$  occurred

---

<sup>1</sup>All given correlation in the present chapter are calculated from detrended time series and are significant at the 95% level

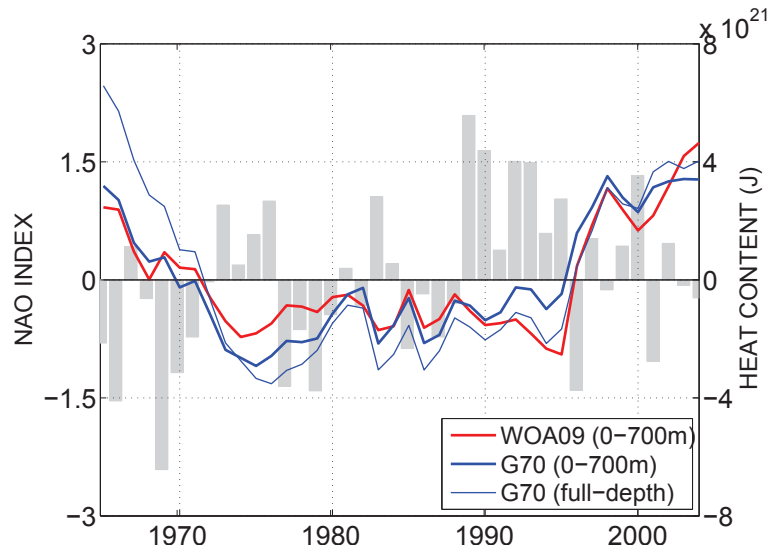


**Figure 4.2:** Heat content anomalies ( $J$ ) within the eastern SPG domain shown in Figure 4.1 and for the 0-500m layer for ORCA025-G70 (thick blue) and WOD09 (thick red). The full-depth anomalies in ORCA025-G70 are also shown (thin blue). The gray bars indicate the normalized NAO index.

within the upper few hundred meters.

### 4.3 Heat budget in the eastern SPG

Having established the ability of the ORCA025-G70 simulation to simulate observed changes in  $HC$  within the upper layers of the eastern SPG, we now investigate the mechanisms responsible for the substantial decadal signal shown in Figure 4.2. A first glimpse to the spatial features of  $HC$  variability is provided by a map of its standard deviation (Figure 4.3), which shows that the strongest changes in the 0-700m layer occurred in the Rockall Trough entrance, in the Iceland basin and in the eastern Irminger Sea. Those regions coincide with the main routes of the NAC branches, suggesting the crucial role of oceanic advection in generating those  $HC$  anomalies. Note that a very similar distribution was obtained using a 5-year low-pass filtered signal, indicating that the variance is mostly located on decadal timescales.

A full-depth annual heat budget calculation solving equation 4.2 within the eastern SPG domain is now presented. Since we are using monthly mean temperature fields, the change in

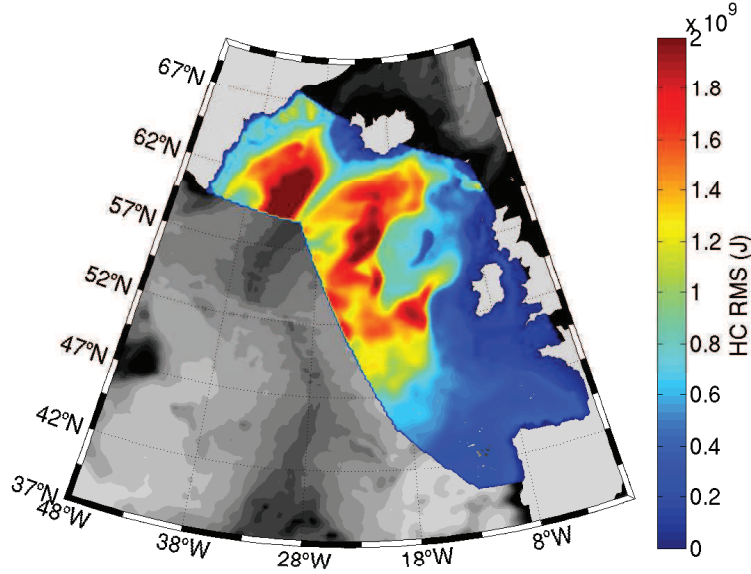


**Figure 4.3:** Map of heat content standard deviation ( $J$ ) for the 0-700m layer in ORCA025-G70 for the period 1965-2004 (annual mean fields).

$HC$  between the 1<sup>st</sup> January and 31<sup>st</sup> December of each year is computed using temperature values averaged for December and the following January. The annual rate of change of  $HC$  is balanced by the net surface heat flux and the net heat transport advection through the regional boundaries, averaged for the current year:

$$\underbrace{\frac{\partial HC}{\partial t}}_{\Delta HC} = \underbrace{\rho_0 C_p \int_x \int_z u(x, z, t) \theta(x, z, t) dx dz}_{OHT} + \underbrace{\int_x \int_y Q(x, z, t) dx dy}_{SHF} + residual \quad (4.2)$$

where  $u$  is the cross-sectional velocity field and  $Q$  is the surface heat flux, which includes the contributions from long/short wave radiations and sensible/latent heat fluxes. The term on the lhs of equation 4.2 is the heat content rate of change ( $\Delta HC$ ), the first term on the rhs is the oceanic heat transport convergence ( $OHT$ ) and the second term on the rhs is the net surface heat flux ( $SHF$ ). We have verified that heat content changes induced by vertical displacements of the sea-surface were negligible.

The long-term mean of  $\Delta HC$  is nearly zero (see black line in Figure 4.4a). The long-term mean  $SHF$  amounts to -0.16 PW (1 PW =  $10^{15}$  J s<sup>-1</sup>, negative sign indicates heat loss to the

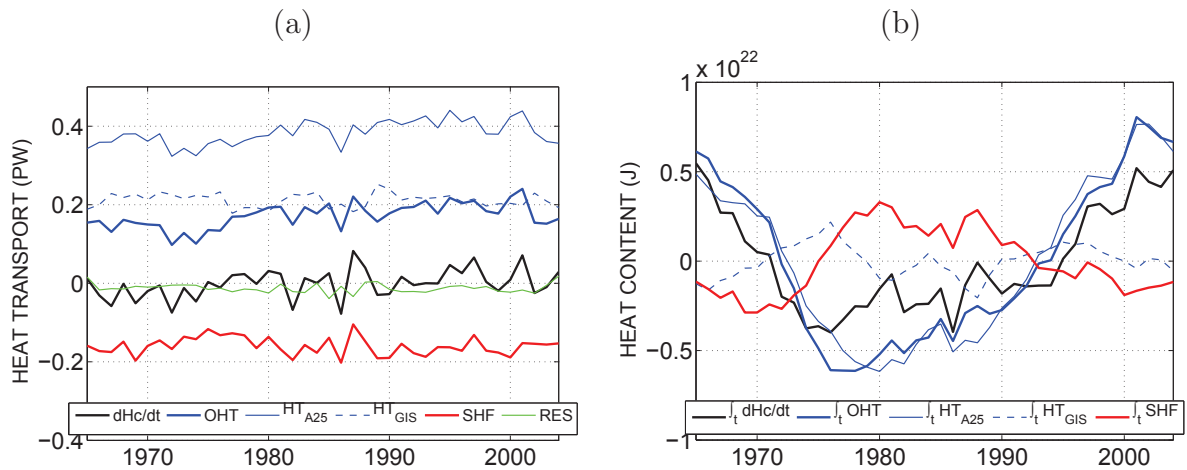


**Figure 4.4:** (a) Heat budget components (PW): heat content rate of change (black), air-sea heat flux (red, negative sign indicates a heat transfer from ocean to atmosphere) and heat transport convergence (blue). The latter is decomposed between the heat transport across the A25-Ovide section (thin blue) and across the Greenland-Iceland-Scotland sills (dashed blue). The green line stands for residual terms needed to close the budget. (b) Same as (a) but expressed as a heat content change (J). Heat flux anomalies are integrated in time from their initial (absolute) value of 1965.

atmosphere) with a standard deviation of 0.023 PW. The mean oceanic heat transports across the northern and southern boundary, referred to as  $HT_{GIS}$  and  $HT_{A25}$  hereafter, amount to  $0.21 \pm 0.017$  PW and  $0.38 \pm 0.031$  PW respectively, yielding an average  $OHT$  of  $0.17 \pm 0.03$  PW. Thus, a mean residual term of -0.01 PW has to be added to close the time-mean heat budget. This residual may partly account for diffusive isopycnal mixing across the domain boundaries, which cannot be directly estimated from the output fields of the model. In addition, the use of monthly fields may lead to numerical errors due to averaging of non-linear terms, although a similar residual was obtained with 5-days averaged fields (no figure shown). As shown below, the contribution of this residual to heat content changes is fairly small and remain relatively constant over years (see green line in Figure 4.4a).

Annually-averaged timeseries of  $SHF$  and  $OHT$  are then related to the year-to-year heat content change  $\Delta HC$  (Figure 4.4a). Positive (negative) values for  $\Delta HC$  depict a warming (cooling) relative to the previous year. Integrating over time the anomalous part of  $SHF$  and  $OHT$  (Figure 4.4b), enables to quantify their respective contributions to the long-term heat content signal revealed in Figure 4.2. The  $HC$  signal is largely related to changes in

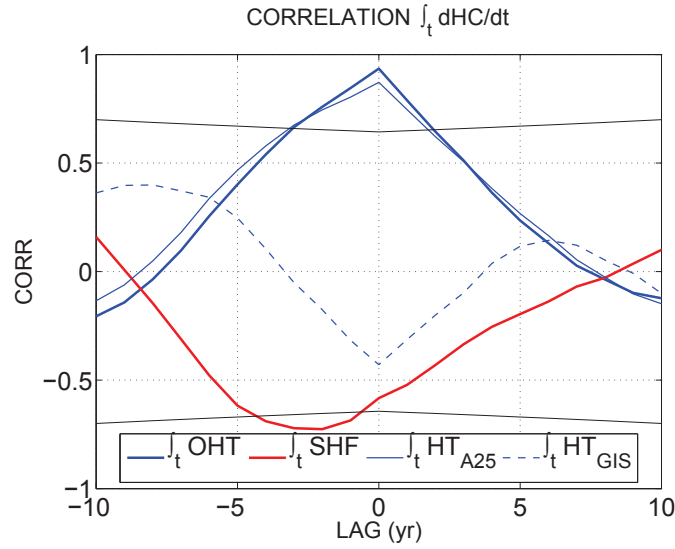


**Figure 4.5:** Lagged correlation between heat content annual anomalies and integrated air-sea heat fluxes (red), integrated heat transport convergence (blue), integrated heat transport across the A25-Ovide section (thin blue) and across the Greenland-Iceland-Scotland sills (thin dashed blue). Negative lags indicate that heat content anomalies lead the corresponding heat budget component. The thin black lines indicate the 95% confidence interval.

$\int_t OHT$  ( $R = 0.93$ , significant at the 95% level, Figure 4.5, blue line). The impacts of  $\int_t SHF$  changes are not negligible though and tend to damp the  $\int_t OHT$  contribution by  $\sim 40\%$ . Before 1980, negative  $OHT$  anomalies induced a cooling of  $1.13 \cdot 10^{22}$  J, while positive  $SHF$  anomalies induced a warming of  $0.44 \cdot 10^{22}$  J. After 1980, positive  $OHT$  anomalies warmed the domain by  $1.19 \cdot 10^{22}$  J while negative  $SHF$  anomalies led to a  $0.44 \cdot 10^{22}$  J cooling. The decadal variability in  $OHT$  is exclusively induced by anomalous heat transport across the A25-Ovide section ( $HT_{A25}$ ). Heat exchanges between the eastern SPG and the Nordic seas across the GIS section ( $HT_{GIS}$ ) is comparatively small and share no significant correlation with the  $HC$  signal. This is consistent with the weak decadal variability of the density-overturning across the sills reported in Chapter 1 (The  $HT_{GIS}$  contribution to  $OHT$  will be consequently ignored in the following analysis). Interestingly,  $\int_t SHF$  lags  $HC$  by 1-3 years ( $R = -0.7$ , significant at the 95% level, Figure 4.5, red line), suggesting that oceanic advection drives air-sea heat flux changes in the eastern SPG on decadal timescales (Figure 4.5): an increased advection of heat across the A25-Ovide section warms up the domain, thereby increasing the temperature

gradient at the air-sea interface and increasing the heat loss to the atmosphere.

Overall, the aforementioned features of the heat budget variability are in good agreement with a similar investigation performed by *Grist et al.* (2010) in the whole subpolar gyre and point changes in heat advection from the Atlantic basin as the main contributor of heat content variability in the northeastern Atlantic. We will concentrate in the following sections on the dynamical origins of  $HT_{A25}$  variability, through spatial and temporal decompositions of the total signal.

## 4.4 Full-depth heat transport variability at A25-Ovide

### 4.4.1 Spatial decomposition of $HT_{A25}$ : vertical and horizontal cell contributions

The full-depth heat transport across A25-Ovide in the  $(x, z)$  plane can be understood as the sum of three distinct contributions:

$$HT_{A25} = \underbrace{C_p \rho_0 \langle v \rangle \langle \theta \rangle \int_z L(z) dz}_{net} + \underbrace{C_p \rho_0 \int_z \bar{v} \bar{\theta} L(z) dz}_{vertical} + \underbrace{C_p \rho_0 \int_z \int_x v' \theta' dx dz}_{horizontal} \quad (4.3)$$

where  $\langle \dots \rangle$  indicates a two-dimensional average,  $\bar{\dots}$  indicates a zonal average and  $\dots'$  indicates the departure from the zonal average.  $L$  is the length of the section.

The first term in the rhs of equation 4.3 is the heat transport associated with the net volume transport across the section (i.e. the global mean velocity times the global mean temperature). In the North Atlantic, its variability should mainly depend on changes in the Arctic mass balance and associated water inflow through Bering Strait. The second and third terms respectively account for the contributions of the vertical and horizontal circulations. Referred to as the  $MOC_z$  and the Gyre component of the flow, they are often interpreted as measures of deep water formation and wind-driven circulations, respectively. We saw in Chapter 2 that this spatial decomposition depicts the vertical component as the main contributor to the

mean meridional heat transport in subtropical regions, whereas the cyclonic gyre circulation dominates in subpolar regions (see Figure 2.8).

The horizontal, vertical and net transport contributions to  $HT_{A25}$  anomalies are shown in Figure 4.6ab. They respectively accounts for 50% ( $0.19 \pm 0.05$  PW), 45% ( $0.17 \pm 0.04$  PW) and 5 % ( $0.02 \pm 0.02$  PW) of the long-term average signal. Thus, the total heat transport at A25-Ovide is carried out in almost equal amount by the horizontal gyre and the vertical  $MOC_z$  circulation cells. The heat transport variability associated with the net volume transport is relatively small on both interannual and decadal timescales and share no significant correlation with the total  $HT_{A25}$ . It is however inducing a slight warming in the early 1990's. On interannual timescales, the vertical and horizontal components are both significantly correlated at the 95% level with  $HT_{A25}$  ( $R = 0.6$  and  $R = 0.7$ , respectively). After removing the high-frequency signal with a 3 year low-pass filter, only the horizontal gyre contribution shows significant correlation with  $HT_{A25}$  ( $R = 0.7$ ), meaning that most of the low-frequency changes in  $HT_{A25}$  occur in the horizontal plane. This suggests that the decadal  $HT_{A25}$  variability is predominantly related to changes in the horizontal gyre circulation rather than changes associated with a net sinking of water ( $MOC_z$ ) that would result from deep convection processes.

While this spatial decomposition of  $HT_{A25}$  give insights into the oceanic pathways whereby heat is transported across A25-Ovide, the main oceanic processes that drive the associated variability are still missing. Separating the respective impacts of velocity and temperature changes may provide useful information about the origins of  $HT_{A25}$  variability. Whereas the impact of velocity anomalies has been show to dominate heat content changes in the subtropics and in the Gulf Stream region (*Eden and Jung, 2001; Jayne and Marotzke, 2001*), the advection of temperature anomaly along the NAC path is likely important for generating  $HC$  changes in the eastern subpolar region (*Krahmann et al., 2000*). This is evalutaed in the following section.

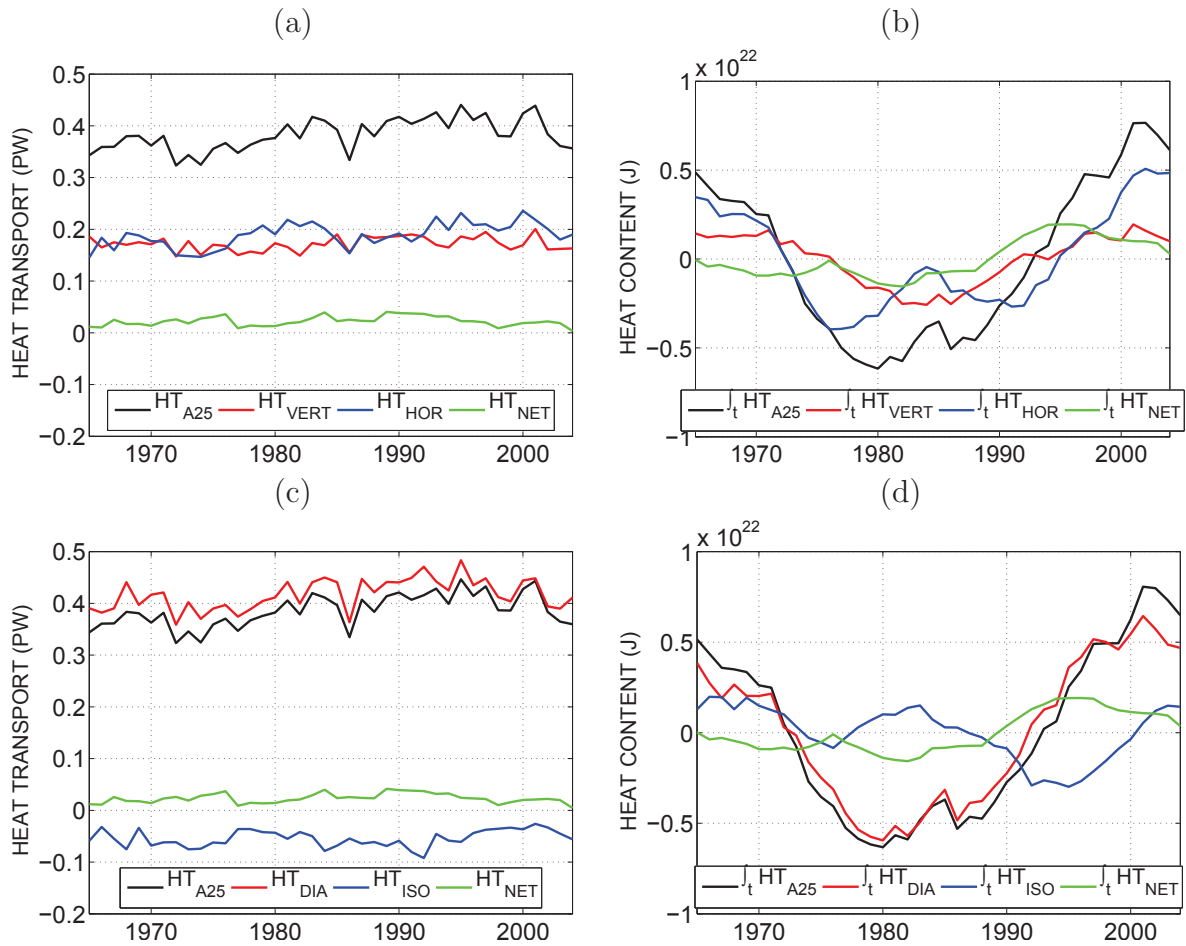


**Figure 4.6:** (a) Decomposition of the full-depth heat transport (PW) at A25-Ovide (black) in the depth framework into a vertical component (red), a horizontal component (blue) and a net contribution (green) following equation 4.3. (b) Same as (a) but expressed as a heat content change (J). Heat flux anomalies are integrated in time from their initial (absolute) value of 1965. (c) Decomposition of the full-depth heat transport (PW) at A25-Ovide (black) in the density framework into a diapycnal component (red), an isopycnal component (blue) and a net contribution (green). (d) Same as (c) but expressed as a heat content change (J).

### 4.4.2 Temporal decomposition of $HT_{A25}$ : temperature and velocity contributions

Heat transport changes are by definition induced by either velocity and temperature changes, or by correlated anomalies in both fields. By separating the two-dimensional velocity and temperature fields into a temporal mean and an anomalous part ( $v(x, z, t) = \bar{v}(x, z) + v'(x, z, t)$ ,  $\theta(x, z, t) = \bar{\theta}(x, z) + \theta'(x, z, t)$ ), one can hence identify three potential sources of variability for  $HT_{A25}$ :

- anomalous velocities acting upon the mean temperature field:

$$HT_v = C_p \rho_0 \int_z \int_x v' \bar{\theta} dx dz \quad (4.4)$$

- advection of temperature anomalies by the mean circulation:

$$HT_\theta = C_p \rho_0 \int_z \int_x \bar{v} \theta' dx dz \quad (4.5)$$

- correlation between velocity and temperature anomalies, referred to as the eddy transport:

$$HT_e = C_p \rho_0 \int_z \int_x v' \theta' dx dz \quad (4.6)$$

The signature of  $HT_e$  on the long-term average and variability of  $HT_{A25}$  is very small ( $HT_e = 0.006 \pm 0.008$  PW, green line in Figure 4.7). Although this might reflect the relatively low "eddy-permitting" resolution of the ORCA025-G70 simulation ( $\frac{1}{4}^\circ$ ), *Treguier et al.* (2006) also found small eddy heat fluxes at A25-Ovide using a higher resolution model ( $1/6^\circ$ ). In fact, eddies are presumed to carry heat away from the NAC stream rather than along it (i.e. they parallel the A25-Ovide section) (*Hall et al.*, 2004). Note that similar values were obtained using 5 days model outputs.

$HT_v$  and  $HT_\theta$  have zero long-term means and standard deviations of 0.037 PW and 0.055 PW (after a 3-year low-pass filtering), respectively. Their respective timeseries are shown in

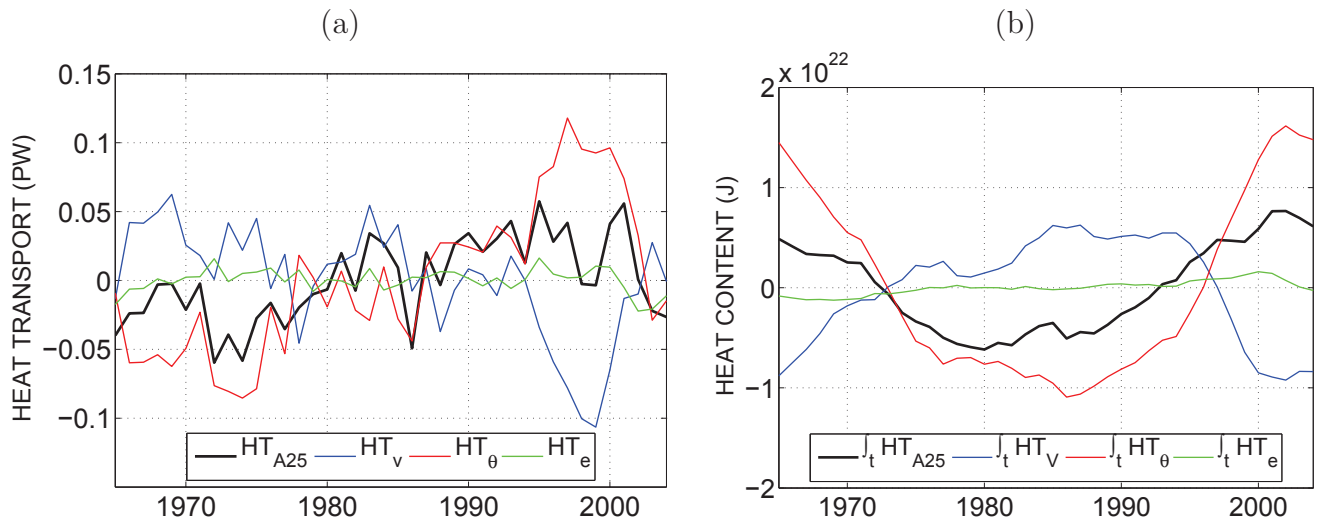


**Figure 4.7:** (a) Temporal decomposition of the full-depth heat transport (PW) at A25-Ovide (black) into a velocity component (blue), a temperature component (red) and an eddy component (green) following equations 4.4, 4.5 and 4.6 respectively. (b) Same as (a) but expressed as a heat content change (J). Heat flux anomalies are integrated in time from their initial (absolute) value of 1965.

Figure 4.7a, along with the total  $HT_{A25}$  signal. Surprisingly, the decadal behavior of  $HT_{A25}$  results from a strong opposition between those two components, slightly dominated in amplitude by the temperature contribution (see the integrated signals in Figure 4.7b). The contribution of velocity changes is characterized by strong positive anomalies in the late 1960's, mid-1970's and mid-1980's, followed by an episode of strong negative values in the late 1990's. This signal is consequently associated with a gradual warming between 1965 and 1985 ( $1.5 \cdot 10^{22}$  J) and a sharp cooling from 1995 to 2002 ( $-1.5 \cdot 10^{22}$  J) (Figure 4.7b). On the other hand,  $HT_{\theta}$  describes a positive trend from minimum negative values in the early 1970's to maximum positive values in the late 1990's. It is hence associated with a strong cooling between 1965 and 1985 and a warming thereafter ( $+ 2.5 \cdot 10^{22}$  J), which amplitude overcomes the opposed velocity-driven signal.  $HT_v$  and  $HT_{\theta}$  are highly anti-correlated on both interannual and decadal timescales ( $R = -0.75$  and  $R = -0.85$ , significant at the 95% level, respectively), which may suggest that velocity and temperature anomalies along A25-Ovide are governed in large part by the same dynamical mechanism. This will be discussed in Section 4.5.

Changes in the horizontal distribution of  $HT_{A25}$ ,  $HT_v$  and  $HT_\theta$  along A25-Ovide are shown as Hovmöller diagrams in Figure 4.8. The horizontal pattern of the total heat transport anomalies (Figure 4.8a) largely reflects changes in its velocity-driven component (i.e.  $HT_v$ ), which highlight striking latitudinal contrasts in the Iceland and West European basins prior and after the mid-1980's (Figure 4.8b). The period [1965-1985] shows relatively strong positive anomalies in  $HT_v$  along the southern portion of the West European Basin, with maximum values observed within the  $45^\circ\text{N} - 49^\circ\text{N}$  latitudinal range.  $HT_v$  is concomitantly negative in the southern Iceland Basin with minimum values reached around  $53^\circ\text{N}$ . Inversely, the period [1985-2004] is characterized by relatively weak (resp. strong)  $HT_v$  in the West European basin (resp. southern Iceland Basin). This horizontal distribution of the velocity-driven heat transport is consistent with opposed changes in the respective transport of the two main NAC branches on decadal timescales. In Chapter 3, we saw that the changing intensity of these branches were mainly induced by the subtropical component of the NAC (see Figure 3.8b), which preferentially fed the northern (resp. southern) branch in the 1990's (resp. 1970's). As discussed in Section 4.6, this may in turn affect the temperature content of the NAC north of about  $49^\circ\text{N}$ , through mixing with the colder waters of subpolar origin.

Local anomalies of  $HT_\theta$  along A25-Ovide are five times weaker than  $HT_v$  anomalies but have greater spatial extents (Figure 4.8c) which makes their integrated contributions to the basin-integrated  $HT_{A25}$  as significant as  $HT_v$  contribution. Most notably,  $HT_\theta$  anomalies cover the whole latitudinal extent of the NAC in the Iceland and West European basins between  $45^\circ\text{N}$  and  $57^\circ\text{N}$ . These anomalies peak within the  $50^\circ\text{N} - 54^\circ\text{N}$  latitudinal range, which corresponds to the mean position of the northern NAC branch. As for the velocity-driven contribution, the mid-1980's marks a temporal boundary between two distinct temperature states of the NAC: a cold period in [1965-1985] and a warm period in [1985-2004].  $HT_\theta$  has also a strong signature in the Irminger sea ( $58^\circ\text{N} - 60^\circ\text{N}$ ). The cooling and warming observed east of Reykjanes Ridge seems to arrive in the Irminger Sea a few years later, where two warm periods (the 1970's and 2000's) encompass a colder period (the 1980's). One can thus assume a slow propagation of temperature anomalies along the mean cyclonic circulation, from the NAC to the East

Greenland Current, via the anticyclonic recirculation around the tip of Reykjanes Ridge (note that the sign of  $HT_\theta$  anomalies along the section depends on the mean flow direction: a negative  $HT_\theta$  within the southward-flowing boundary current off Greenland indicates a warming of the western Irminger Sea, for instance).

Changes in the vertical distribution of  $HT_{A25}$ ,  $HT_v$  and  $HT_\theta$  are similarly shown in Figure 4.9. In the vertical plane, the  $HT_v$  signal is predominant within the 0-500m layer (Figure 4.9b), but anomalies of smaller amplitudes are visible down to the ocean bottom and are characterized by a pronounced layered structure (0-1500m, 1500m-3500m, 3500m-5500m). This layered structure of velocity anomalies is primarily found east of Reykjanes Ridge, and may hence reflect large-scale restructuration of the stratification within the NAC.  $HT_\theta$  changes are also intensified at the surface and extend down to about 2000m depth (Figure 4.9c). The total  $HT_{A25}$  peaks around 500 m depth (Figure 4.9a) due to the strong compensation between its two components within the top surface layer.

Although investigating the link between the oceanic variability described here and changes in the atmospheric forcing is beyond the scope of the present Chapter, we show in Figure 4.10 how  $HT_{A25}$ ,  $HT_v$  and  $HT_\theta$  respectively correlates with the NAO index. Interestingly, there exists no significant correlation between the NAO and the total  $HT_{A25}$  signal, whereas both  $HT_\theta$  and  $HT_v$  lag the NAO index by 5-6 years ( $R_\theta = 0.67$  and  $R_V = -0.63$ , respectively). Thus, the decadal variability in  $HT_{A25}$  appears to result from an imbalance between two opposed and delayed responses of the largescale circulation to the NAO forcing. Furthermore, the spatial pattern of  $HT_v$  (Figure 4.8, middle) appears consistent with NAO-related shifts of the Gulf Stream/NAC system, often referred to as the "intergyre gyre" pattern (*Marshall et al.*, 2001; *Eden and Willebrand*, 2001; *Herbaut and Houssais*, 2009): following the positive trend of the NAO index from the late 1960's to the early 1990's, the zero wind-stress curl line shifts northward and an anomalous anticyclonic circulation develops over the climatological position of the NAC, thereby potentially increasing the NAC transport in the Iceland Basin while decreasing it in the West European Basin.

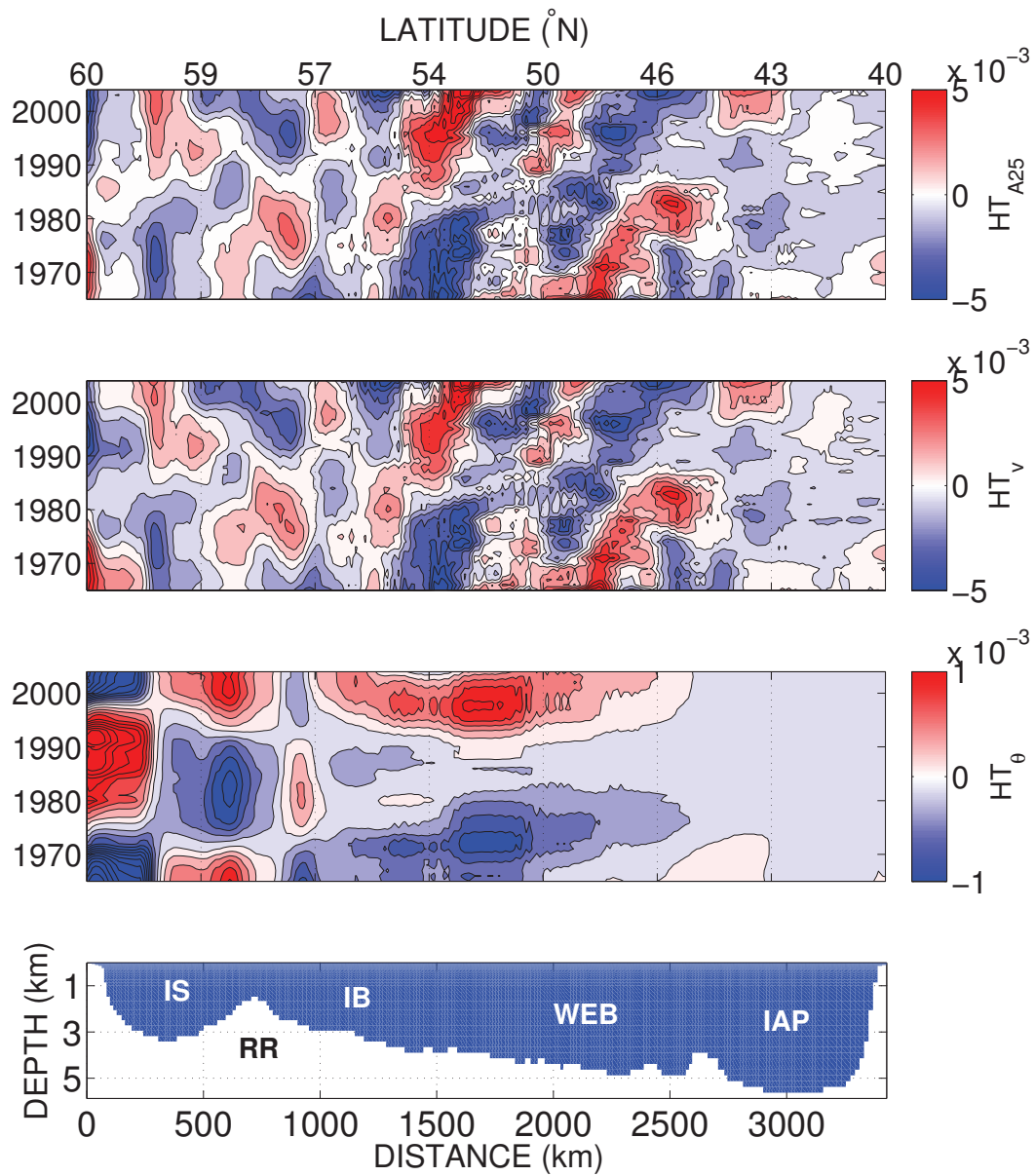


**Figure 4.8:** Time-distance diagrams of anomalies of (top) the full-depth heat transport, (middle) its velocity component and (bottom) its temperature component along A25-Ovide. Units are PW. The bathymetry along the section is shown in the bottommost panel, with labels RR (Reykjanes Ridge), IS (Irminger Sea), IB (Iceland Basin), WEB (West European Basin) and IAP (Iberian Abyssal Plain).

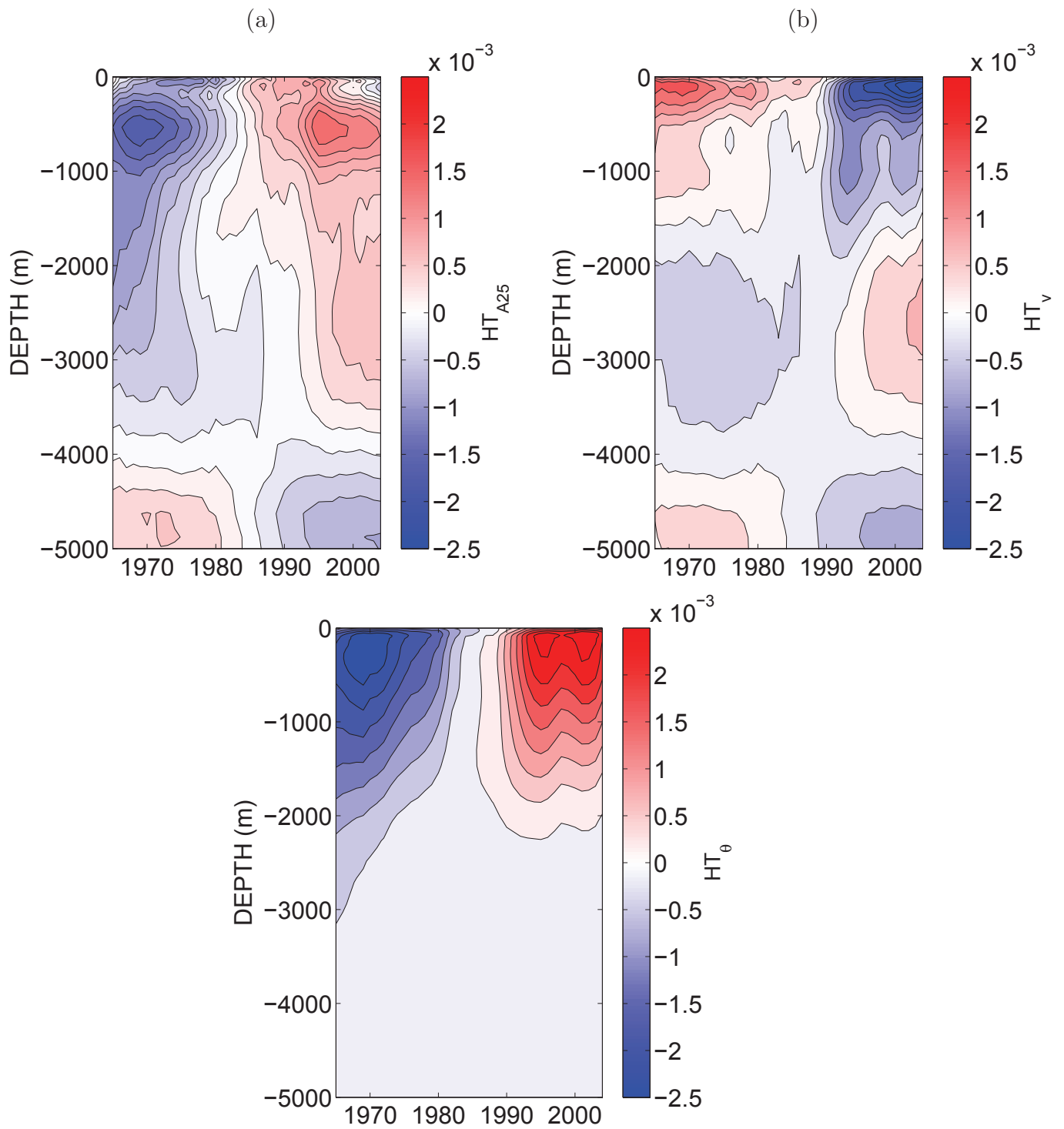
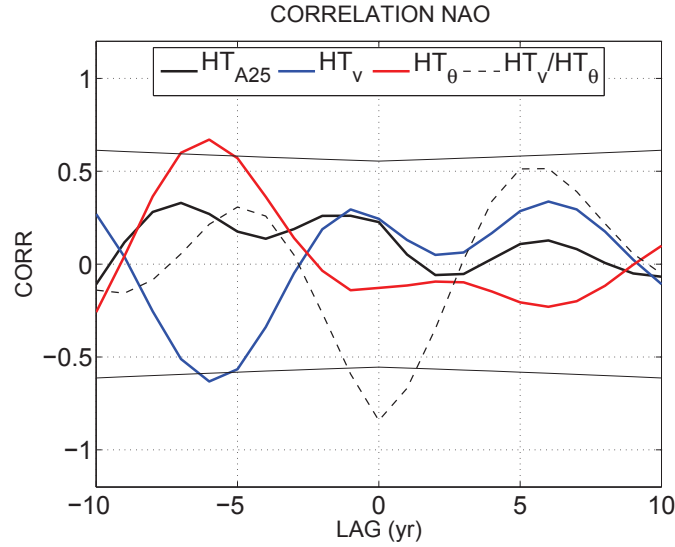


Figure 4.9: Same as Figure 4.8 but as a function of depth.



**Figure 4.10:** Lagged correlation between the normalized NAO index and  $HT_{A25}$  (black),  $HT_v$  (blue) and  $HT_\theta$  (red). All timeseries have been smoothed using a 3-year low-pass filter. The correlation between  $HT_v$  and  $HT_\theta$  is also shown (dashed). Negative lags indicate that the NAO leads the corresponding heat transport component. The thin black lines indicate the 95% confidence interval.

In summary, the mean full-depth heat transport at A25-Ovide is carried out in equal amount by the horizontal gyre and vertical overturning circulations. Both cells contribute significantly to its short-term variability, whereas the decadal signal is primarily associated with changes in the horizontal component. Interestingly, a temporal decomposition of  $HT_{A25}$  shows concomitant and opposed changes in its velocity- and thermally-driven components, both signals being significantly anti-correlated (see Figure 4.7). The spatial pattern of velocity and temperature anomalies within the NAC highlight two opposed circulation states prior and after the mid-1980's. During [1965-1985], the northern (southern) NAC branch was relatively weak (strong), while the current as a whole was relatively cold. The inverse situation holds during [1985-2004]. Both  $HT_v$  and  $HT_\theta$  are significantly correlated with the NAO index fluctuations, while the sum of both terms, that is  $HT_{A25}$ , is not.

Overall, the underlying mechanism behind  $HT_v$  and  $HT_\theta$  variations is still obscure. Most notably, the out-of-phased relationship linking both signals, which suggests a common driving mechanism, needs to be explained. Answers could be found in the origins of temperature

anomalies at A25-Ovide, which may be partitioned into two terms: changes in water mass properties on isopycnal surfaces (often referred to as "spiciness") and changes due to vertical movements of isopycnal surfaces (often referred to as "heaving"). In the following section, we infer some basic quantification of these respective contributions using an approximation of  $HT_{A25}$  based on an index of the  $MOC_\sigma$  (see Chapter 3).

## 4.5 On the link with the Meridional Overturning Circulation variability

When working in the density framework (instead of the depth framework), the second and third terms in equation 4.3 respectively relate to a diapycnal and an isopycnal mass flux. The diapycnal and isopycnal contributions to  $HT_{A25}$  anomalies are shown in Figure 4.6cd. The net volume transport contribution is by definition identical to that in the depth framework. The absolute heat transport is largely associated with the diapycnal component of the flow ( $0.42 \pm 0.05$  PW) which is slightly diminished by a negative isopycnal contribution ( $-0.06 \pm 0.03$  PW). The diapycnal component is also largely responsible for the interannual and decadal heat transport variability ( $R = 0.9$ , significant at the 95% level).

According to the close relationship between the total  $HT_{A25}$  variability and that of its diapycnal component, the total heat flux can be approximated using the  $MOC_\sigma$  intensity at A25-Ovide and the difference in temperature  $\Delta\theta$  between its upper and lower limbs. The computation of the  $MOC_\sigma$  is similar to that presented in Chapter 1, except that the vertical integration is performed from the ocean surface to include the contribution of the net volume transport across the section:

$$MOC_\sigma(t) = \int_x \int_{z=Z(\sigma_m(t))}^{z=0} v(x, z, t) dx dz \quad (4.7)$$

where  $Z(\sigma_m(t))$  is the depth of the maximum overturning ( $\sigma_m$ ) estimated in the density plane:

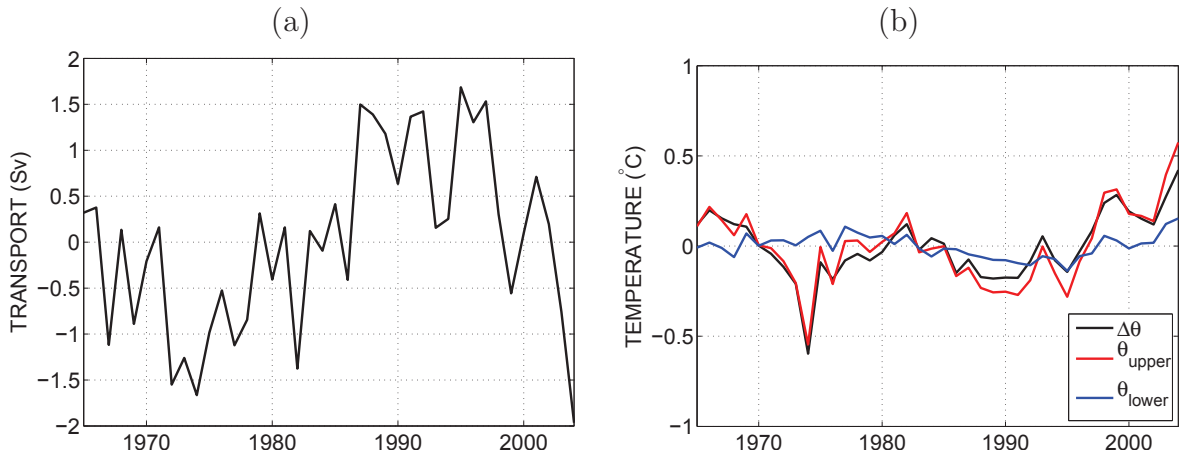


**Figure 4.11:** (a) Annual anomaly of  $MOC_{\sigma}$  (Sv, integration from the ocean surface) at A25-Ovide and (b) temperature anomaly ( $^{\circ}\text{C}$ ) of the (red) upper and (blue) lower  $MOC_{\sigma}$  limbs. The difference  $\Delta\theta$  between both temperature indexes is shown in black.

$$\int_x v(x, Z(\sigma_m(t)), t) dx = 0 \quad (4.8)$$

The mean 1965-2004  $MOC_{\sigma}$  and  $\Delta\theta$  are  $17 \pm 1$  Sv and  $7 \pm 0.2$   $^{\circ}\text{C}$ , respectively. Their associated timeseries are shown in Figure 4.11a and 4.11b, respectively. As already described in Chapter 3, the decadal  $MOC_{\sigma}$  signal at A25-Ovide is characterized by decreasing values in the 1960's and early 1970's, a gradual positive trend until the mid-1990's, and a strong decrease in transport until 2004. Most of the  $\Delta\theta$  variability is confined within the upper  $MOC_{\sigma}$  limb, which shows strong negative anomalies in the mid-1970's and around 1990 and strong positive anomalies in the late 1990's and early 2000's. Combining both signals yields an approximation of the total heat transport across the section, expressed as:

$$HT_{approx} = C_p \rho_0 MOC_{\sigma} \Delta\theta \quad (4.9)$$

$HT_{approx}$  fairly reproduces the actual  $HT_{A25}$  signal ( $R = 0.7$ , significant at the 95% level, Figure 4.12a). Following equation 4.9, its variability is related to changes in the intensity of the  $MOC_{\sigma}$  and/or changes in  $\Delta\theta$ . As the signal associated with the product of their respective anomalies is largely negligible (i.e.  $MOC'_{\sigma} \cdot \Delta\theta' \approx 0$ , not shown), the time-dependent part of

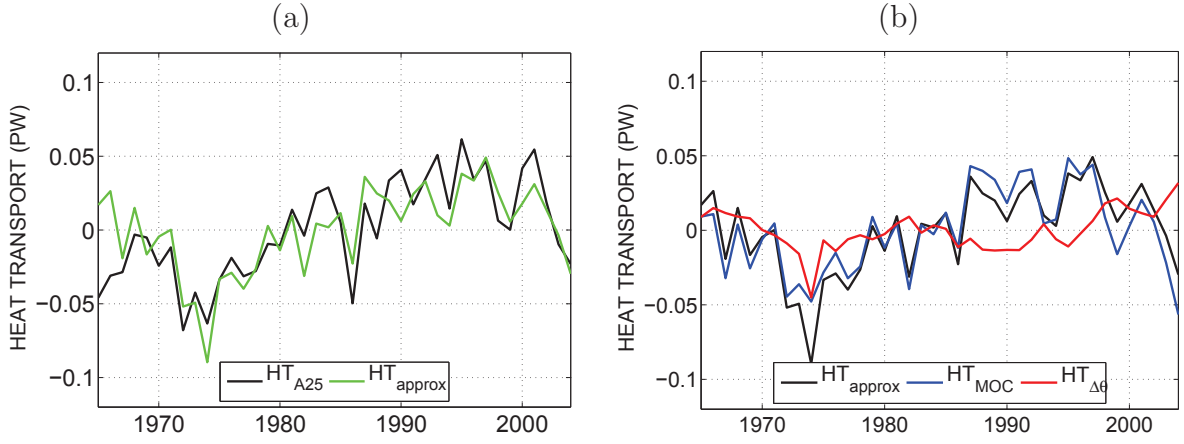


**Figure 4.12:** (a) Comparison of the actual heat transport anomalies at A25-Ovide (black) with the reconstructed signal (green) based on the  $MOC_\sigma$  and  $\Delta\theta$  index (see equation 4.9). Units are PW.

expression 4.9 can be expressed as:

$$HT_{approx} \approx \underbrace{C_p \rho_0 MOC'_\sigma \overline{\Delta\theta}}_{HT_{MOC_\sigma}} + \underbrace{C_p \rho_0 \overline{MOC_\sigma} \Delta\theta'}_{HT_{\Delta\theta}} \quad (4.10)$$

Both contributions are displayed in Figure 4.12b, showing that  $HT_{approx}$  is primarily impacted by the  $MOC_\sigma$  variability, with changes in  $\Delta\theta$  playing a secondary role. How does this reconcile with the respective contributions of  $HT_v$  and  $HT_\theta$  (see Figure 4.7), which show a strong impact of temperature anomalies on  $HT_{A25}$ ? By definition, the  $MOC_\sigma$  variability may arise through both velocity and density anomalies (i.e. changes in the respective volume of its limbs). The latter mechanisms, referred to as isopycnal heaving hereafter, can be simply understood as vertical movements of isopycnal surfaces past a depth horizon. In equation 4.7, isopycnal heaving is reflected in the varying depth of  $\sigma_m$  along the section, which determines the area over which the velocity field is integrated: deepening of  $\sigma_m$  in regions of mean northward (resp. southward) transport will increase (resp. decrease) the  $MOC_\sigma$  strength, while the inverse holds for a shallowing  $\sigma_m$ . Here, the term "heaving" also includes actual changes in the value of  $\sigma_m$ . We will see, however, that very similar results are produced using a constant  $\sigma_m$  and we hence keep the "heaving" appellation.

The time-average depth of  $\sigma_m$  along A25-Ovide, which mostly indicates the depth of the

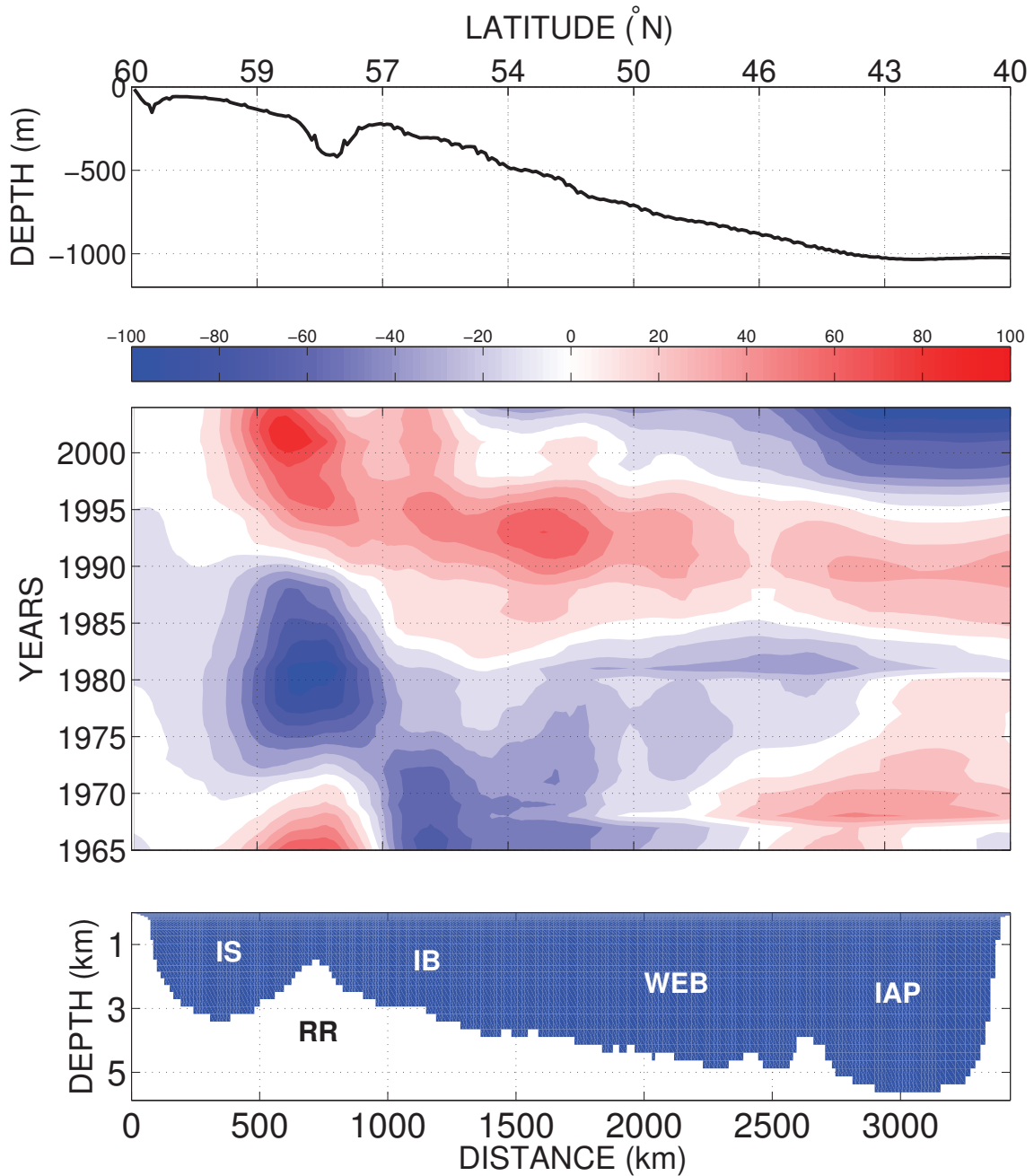


**Figure 4.13:** Top: Mean (1965-2004) depth of  $\sigma_m$  along A25-Ovide. Middle: Time-distance diagram of anomalies in the depth of  $\sigma_m$ . Positive (resp. negative) anomalies indicate a deepening (resp. shoaling) of  $\sigma_m$ . Units are m. Bottom: Bathymetry along A25-Ovide, with labels RR (Reykjanes Ridge), IS (Irminger Sea), IB (Iceland Basin), WEB (West European Basin) and IAP (Iberian Abyssal Plain).

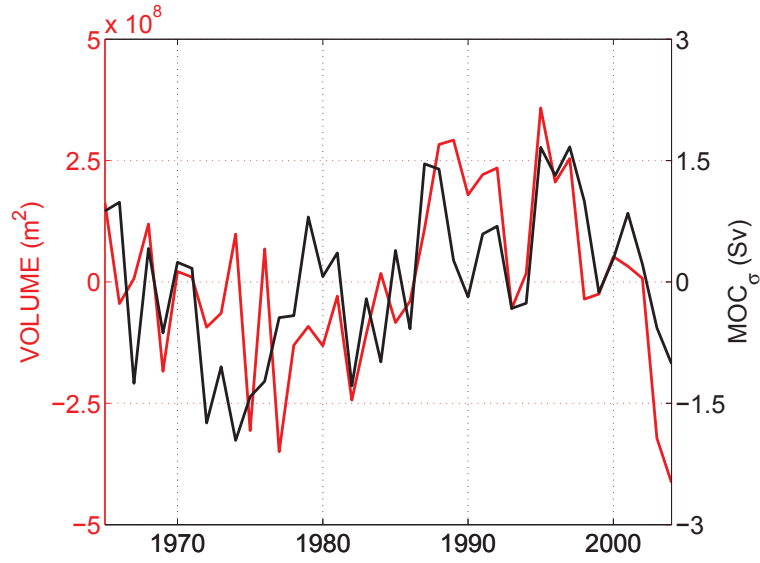


**Figure 4.14:** Volume anomalies of the upper  $MOC_{\sigma}$  limb (in  $m^2$ , red) along with the actual strength of the  $MOC_{\sigma}$  (in Sv, black).

main pycnocline, is shown in Figure 4.13 (top). It gradually increases from near zero off Greenland to about 1000 m off Portugal. Anomalous displacements of  $\sigma_m$  are displayed as a Hovmöller diagram in Figure 4.13 (middle). They are characterized by significant decadal fluctuations of  $\pm 100$  m along the whole section, except along the boundary region off Greenland. The deepening/shoaling of  $\sigma_m$  are particularly important in the vicinity of Reykjanes Ridge and within the Iceland basin, but significant anomalies are also observed in the Iberian abyssal plain. As shown in Figure 4.14, the associated volume (or area) anomalies of the upper  $MOC_{\sigma}$  limb is positively correlated with the actual strength of the overturning ( $R = 0.6$ , significant at the 95% level): a stronger  $MOC_{\sigma}$  is associated with an expanded upper limb, that is a deepening of  $\sigma_m$ . In order to establish a causal link between both indexes, one can rearrange equation 4.7 as the sum of four contributions:

$$MOC_{\sigma}^{Mean} = \int_x \int_{z=Z(\sigma_m)}^{z=0} \bar{v}(x, z) dx dz \quad (4.11)$$

$$MOC_{\sigma}^{Volume} = \int_x \int_{z=Z(\sigma_m)}^{z=Z(\sigma_m(t))} \bar{v}(x, z) dx dz \quad (4.12)$$

$$MOC_{\sigma}^{Velocity} = \int_x \int_{z=\overline{Z(\sigma_m)}}^{z=0} v'(x, z, t) dx dz \quad (4.13)$$

$$MOC_{\sigma}^{VelVol} = \int_x \int_{z=\overline{Z(\sigma_m)}}^{z=Z(\sigma_m(t))} v'(x, z, t) dx dz \quad (4.14)$$

where  $\overline{Z(\sigma_m)}$  refers to the mean depth of  $\sigma_m$  along A25-Ovide, estimated as  $\int_x \overline{v(x, \overline{Z(\sigma_m)})} dx = 0$ .

$MOC_{\sigma}^{Mean}$  is time-independent and is interpreted as the mean isopycnal transport across the mean isopycnal structure.  $MOC_{\sigma}^{Volume}$  is a measure of  $MOC_{\sigma}$  anomalies induced by isopycnal heaving and associated with changes in the volume of its upper and lower limbs.  $MOC_{\sigma}^{Velocity}$  refers to  $MOC_{\sigma}$  anomalies purely driven by velocity changes.  $MOC_{\sigma}^{VelVol}$  is the correlation between velocity anomalies and isopycnal heaving. Its contribution to the  $MOC_{\sigma}$  variability is relatively small and will be subsequently neglected. One can now substitute  $MOC_{\sigma}^{Volume}$  and  $MOC_{\sigma}^{Velocity}$  in the expression of  $HT_{MOC_{\sigma}}$  of equation 4.10, and extract three distinct contributions to the (approximated) heat transport variability:

$$HT_{approx} = C_p \rho_0 \left( \underbrace{MOC_{\sigma}^{Velocity} \overline{\Delta\theta}}_{Velocity} + \underbrace{\overbrace{MOC_{\sigma}^{Volume} \overline{\Delta\theta}}^{Heaving} + \overbrace{MOC_{\sigma} \Delta\theta'}^{Properties}}}_{Temperature} \right) \quad (4.15)$$

The first term on the rhs of equation 4.15 is a measure of heat transport changes purely driven by velocity anomalies and has to be compared with the original  $HT_v$  signal (Figure 4.16b). Both the second and third term on the rhs of equation 4.15 are measures of heat transport changes driven by temperature anomalies and the sum of both contributions should be compared with the original  $HT_{\theta}$  (Figure 4.16a). The former term relates to isopycnal heaving, while the latter reflects changes in the actual temperature difference between the  $MOC_{\sigma}$  limbs (i.e the spiciness component of  $HT_{\theta}$ ). The respective contribution of those three components of the total  $HT_{approx}$  are shown in Figure 4.15, along with three simple schematics illustrating

the corresponding mechanism involved.

The most striking result from this decomposition is the predominance of isopycnal heaving in driving the low-frequency variability of  $HT_{approx}$  (Figure 4.15a): a decreased heat transport in the late 1960's and early 1970's, a gradual intensification up to 1997 and a sharp decrease afterwards. This clearly demonstrates that a significant fraction of  $HT_{\theta}$ , i.e the temperature-driven component of the heat transport at A25-Ovide, is associated with large-scale restructurations of the vertical temperature/density field. We note that using a constant value for  $\sigma_m$  ( $\sigma_1 = 32.09$ ) yields a very similar signal (dashed line in Figure 4.15a). Temperature anomalies are also manifested in the "spice" or "property" component of  $HT_{approx}$  (Figure 4.15b) which depicts changes in the actual temperature difference between both  $MOC_{\sigma}$  limbs ( $\Delta\theta'$ ). As noted earlier, those temperature changes are exclusively restricted to the upper limb and notably led to strong negative (resp. positive) anomalies during the 1970's (resp. late 1990's early 2000's). The sum of  $HT_{heaving}$  and  $HT_{property}$  is significantly correlated with the actual temperature component  $HT_{\theta}$  ( $R = 0.83$ , Figure 4.16a).

The velocity component of  $HT_{approx}$  ( $HT_{approx}^{Velocity}$ , Figure 4.15c) is also very similar to the actual velocity component  $HT_v$  ( $R = 0.88$ , Figure 4.16b). The difference between both indexes arises from the use of the mean temperature field  $\overline{\theta(x, z)}$  in  $HT_v$ , instead of  $\overline{\Delta\theta}$  in  $HT_{approx}$  (compare equation 4.4 and equation 4.13). Therefore, there is an additional term in  $HT_v$  that is not considered in  $HT_{approx}$ : local velocity anomalies acting upon the mean horizontal temperature gradient along the section. As the difference between both indexes is characterized by enhanced  $HT_v$  anomalies in the late 1960-early 1970's and late 1990's, this term may particularly reflect the opposed variability of the northern and southern NAC branches revealed in Figure 4.8.

One can note from Figure 4.13 that heaves of  $\sigma_{MOC}$  are not uniform along the A25-Ovide section, most particularly during the 1960/70's and the late 1990's, that is the periods where strong  $HT_v$  anomalies are observed. Figure 4.17 shows a three-dimensional view of the anomalous depth of  $\sigma_{MOC}$  along the section. Significant large-scale changes in the slope of  $\sigma_{MOC}$  in the Iceland and West European Basin (between 1000 km and 3500 km) are observed during these

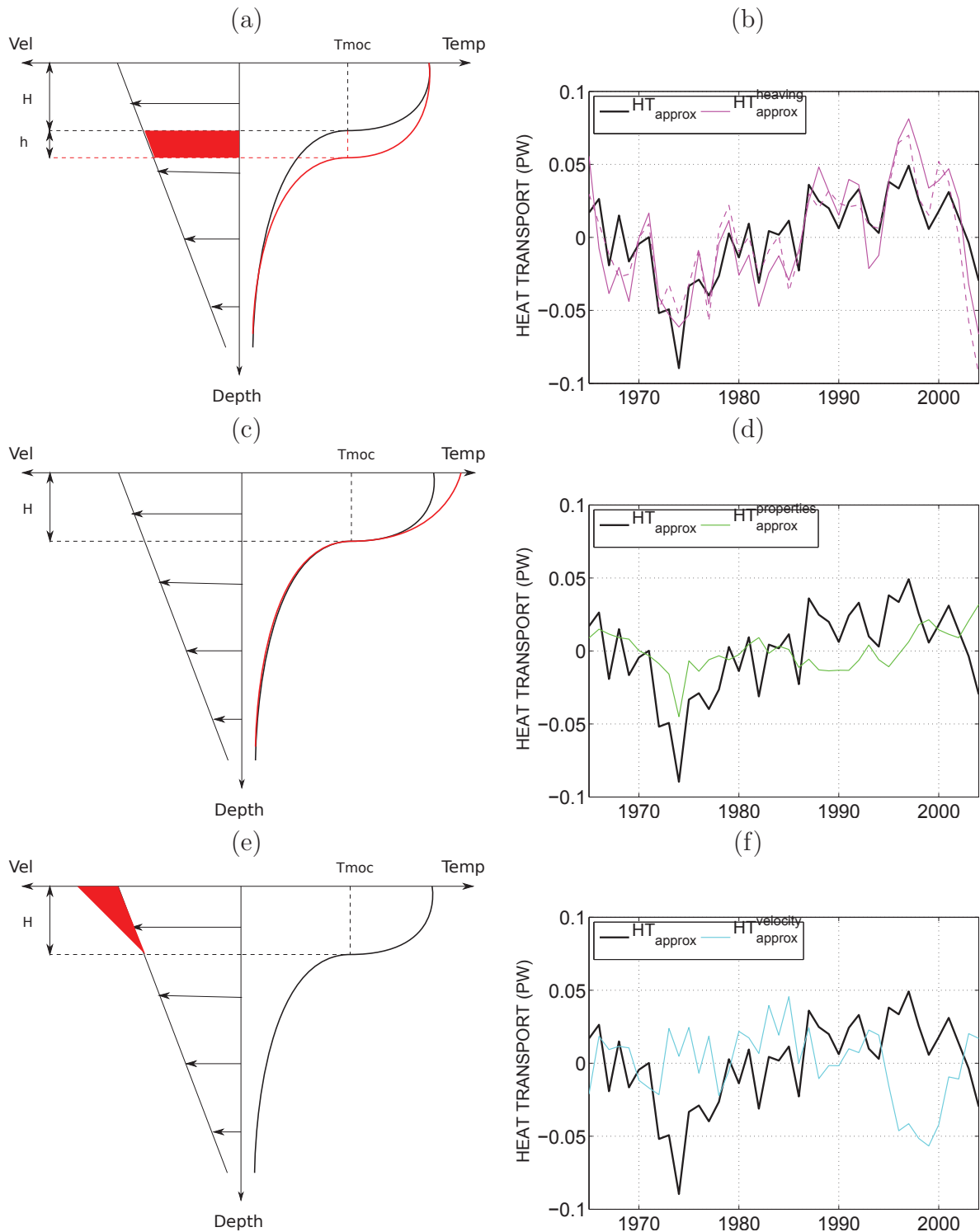


**Figure 4.15:** The three components of the approximated heat transport  $HT_{approx}$  (black line) following equation 4.15 at A25-Ovide: (a,b) heaving, (c,d) property and (e,f) velocity. The dashed line in (b) is the same signal computed using a constant  $\sigma_m$  value ( $\sigma_1 = 32.09$ ). The left panel schematizes the associated mechanisms for the case of an increased heat transport in the regions of mean northward flow (the NAC for instance). Temperature profiles are used (instead of density) for clarity.  $T_{MOC}$  is thus the analogous of  $\sigma_{MOC}$ . The red color indicates anomalies in the corresponding field (velocity or temperature).  $H$  and  $h$  are the mean and anomalous depth of the thermocline.

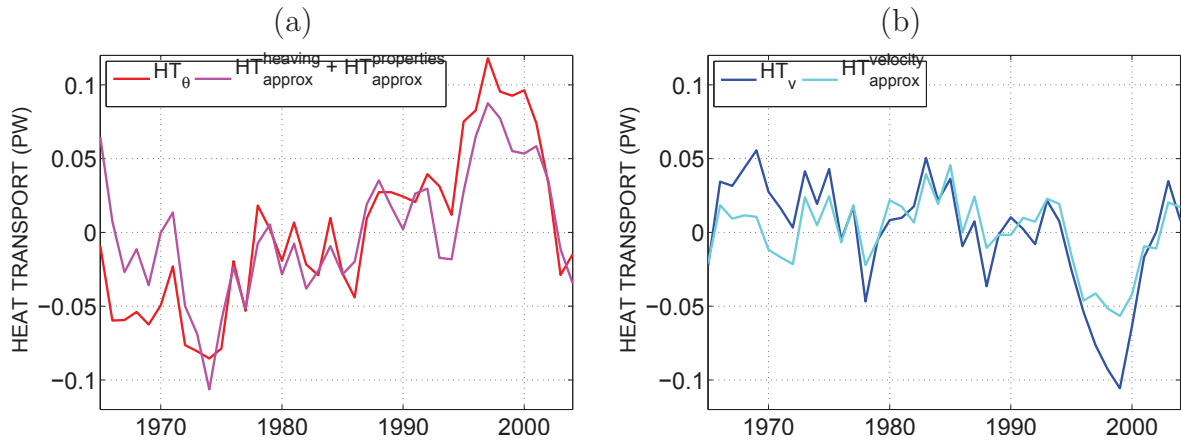


**Figure 4.16:** (a) Comparison of the actual  $HT_\theta$  signal (red, equation 4.5) with the reconstructed signal (magenta, sum of the second and third terms in equation 4.15). (b) Same as (a) but for the velocity-driven component  $HT_v$  (blue, equation 4.4) and its reconstruction (cyan, first term in equation 4.15).

two periods. To quantify this, anomalies in the depth of  $\sigma_m$  were spatially averaged within two regions: between Reykjanes ridge and  $50^\circ\text{N}$  and between  $50^\circ\text{N}$  and Portugal. The difference between both timeseries yields a largescale index of the pycnocline slope, which, through the thermal wind relationship, can be related to largescale changes in the velocity field. Interestingly, this index matches remarkably well the velocity-driven component of  $HT_{A25}$  (Figure 4.18), suggesting that large-scale heaving of isopycnals east of Reykjanes Ridge is also an important driver of velocity anomalies (note that a very similar index is obtained using the  $\theta = 6^\circ\text{C}$  isotherm instead of  $\sigma_{MOC}$ ). This may explain the anti-correlation found between  $HT_\theta$  and  $HT_v$ , firstly revealed in Figure 4.7.

In summary, decadal changes in heat transport across A25-Ovide primarily results from the varying depth of the main pycnocline east of Reykjanes ridge. Isopycnal heaving is captured by the temperature-driven component of  $HT_{A25}$  and is largely responsible for its low (resp. high) values simulated in the 1960-70's (resp. 1990's). This mechanism is also influencing the velocity-driven component of the heat transport through largescale changes in the pycnocline slope, which tend to damp the thermal contribution. This is particularly evident during the late 1990's - early 2000's period (see Figure 4.17): a deepening of  $\sigma_{MOC}$  within the Iceland Basin induces a

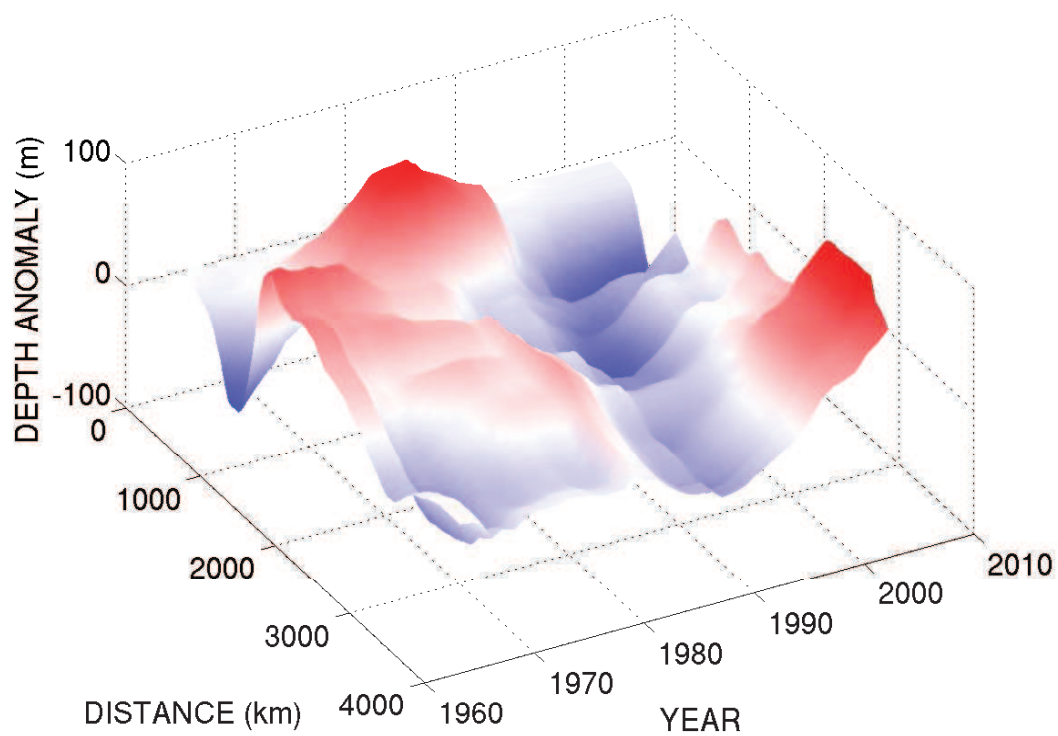


**Figure 4.17:** *Three-dimensional view (time, distance, depth anomaly) of the vertical displacements of  $\sigma_{MOC}$  (in m) along A25-Ovide.*

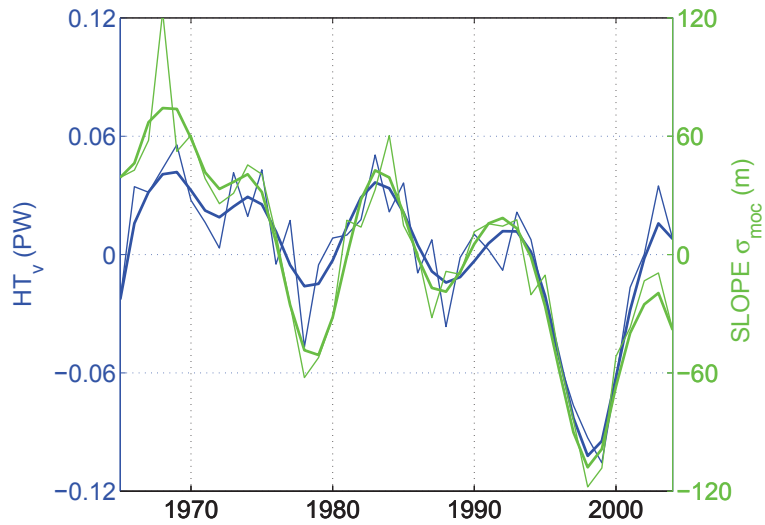


**Figure 4.18:** Comparison of the velocity component of the heat transport at A25-Ovide (blue, in PW) with an index of the pycnocline slope east of Reykjanes Ridge (green, in m). The latter is defined by the difference in the depth of  $\sigma_m$  averaged north and south of  $50^\circ\text{N}$ . The thin lines are annual values, the thick lines are 3-year low-pass filtered signals.

strong increase in the thermal component of  $\text{HT}_{A25}$ . This deepening occurs concomitantly with an elevation of  $\sigma_{MOC}$  in the Iberian Abyssal plain, which induces negative velocity anomalies through a decay of the pycnocline slope. This mechanism is presumably responsible for the anti-correlated fluctuations of  $\text{HT}_\theta$  and  $\text{HT}_v$ . Changes in water mass properties within the upper layers, as well as local velocity anomalies of the distinct NAC branches also contribute, to a lesser extent, to heat transport anomalies at A25-Ovide.

In Chapter 3, we showed the power of the Lagrangian approach to study volume transport changes at A25-Ovide. A decomposition of the NAC transport into a subtropical and a subpolar component enabled to link its changing structure with its changing composition. In the following section, we take advantage of the outputs from the *EXP<sub>BACK</sub>* experiment to complement the previous Eulerian diagnostics of heat transport variability at A25-Ovide. *ARIANE* gives access not only to the respective transport of subpolar and subtropical water masses between the initial and final sections, but also to their respective hydrographic properties in their source regions (namely the Labrador Sea and the subtropics). Thus, the particle tracking may provide crucial information about the origin of temperature anomalies advected from the western Atlantic toward the eastern SPG. We have so far highlighted the significant role of isopycnal

heaving in driving heat transport variability at A25-Ovide. Through a Lagrangian reconstruction of  $HT_\theta$ , we will attempt to answer the following question: Could isopycnal heaving at A25-Ovide be a consequence of a remote process?

## 4.6 A Lagrangian approach for investigating temperature and associated heat transport anomalies

### 4.6.1 Reconstructing the $HT_\theta$ signal in ARIANE

To investigate the origins of temperature anomalies along A25-Ovide, the thermally-driven heat transport  $HT_\theta$  is reconstructed using the Lagrangian analysis tool ARIANE. The analysis is restricted to the upper limb of the  $MOC_\sigma$  at A25-Ovide that contains most of the full-depth signal (see below). In addition, we assume that temperature anomalies are mostly linked with a large-scale signal propagating from the western Atlantic within the NAC. In other words, we assume that temperature anomalies advected by the upper East Greenland Current from the Nordic Seas are negligible. We thus only consider two main source waters in our reconstruction: a subtropical contribution from the Gulf Stream and a subpolar contribution from the Labrador Sea, which jointly compose the NAC. The methods used to compute the Lagrangian transport of the NAC in ARIANE was fully detailed in Chapter 3 and we will here simply highlight the basic steps of the  $HT_\theta$  reconstruction.

The Lagrangian experiments are performed within a domain bounded by the A25-Ovide section, a subpolar transect at the exit of the Labrador Sea (SPG section) and a subtropical transect at  $40^\circ\text{N}$  (STG section) (see Figure 3.1 in Chapter 3). Every month between 1965 and 2004, hundred thousands of numerical particles are initially positioned along A25-Ovide above  $\sigma_m$ . The particles are advected backward in time within the three-dimensional model velocity field (i.e. the density criterion is only applied along the A25-Ovide section) and their trajectories are integrated until they leave the domain through one of the three defined sections (STG, SPG and A25-Ovide). The hydrographic properties of a given particle are available in

both the initial and final sections. As described in Chapter 3, the mean NAC transport (23 Sv) is decomposed into a subtropical component from the Gulf Stream (15 Sv) and subpolar component from the Labrador Current (8 Sv). To reconstruct the two-dimensional temperature field at A25-Ovide, particles are grouped into bins collocated on the original model grid cell (see Figure 4.19). The mass transport  $U$  within each bin can be decomposed into a subtropical ( $U_{STG}$ ) and a subpolar ( $U_{SPG}$ ) contribution. The temperature within each bin is then estimated as:

$$\theta^{A25} = \%_{STG}\theta_{STG}^{A25} + \%_{SPG}\theta_{SPG}^{A25} \quad (4.16)$$

where  $\theta_{STG}^{A25}$  and  $\theta_{SPG}^{A25}$  are the temperature of subtropical and subpolar particles spatially averaged within a bin and  $\%_{STG} = \frac{U_{STG}}{U}$  refers to the proportion of the subtropical transport within a given bin. The total Lagrangian signal at A25-Ovide is simply given by:

$$HT_{\theta}^{Lag} = \int_x \int_z \overline{U}\theta'^{A25} dx dz. \quad (4.17)$$

where  $\overline{\quad}$  indicates a temporal average (1965-2004) and  $\dots'$  indicates the departure from this temporal average. The resulting timeseries is compared in Figure 4.20 with the corresponding Eulerian signal (dashed and thick solid lines, respectively). Both signals match fairly well ( $R = 0.95$ ) and  $HT_{\theta}^{Lag}$  can hence be used to identify the predominant mechanisms responsible for the variability of the Eulerian  $HT_{\theta}$  previously described (see red lines in Figure 4.7). Note also that  $HT_{\theta}$  computed within the upper  $MOC_{\sigma}$  limb contains most of the full-depth signal (thin solid line).

#### 4.6.2 Decomposition of $HT_{\theta}^{Lag}$

Along A25-Ovide, subtropical and subpolar particles within individual bins have by construction very similar properties (i.e.  $\theta_{STG}^{A25} \sim \theta_{SPG}^{A25}$  within each grid cell). This was showed in

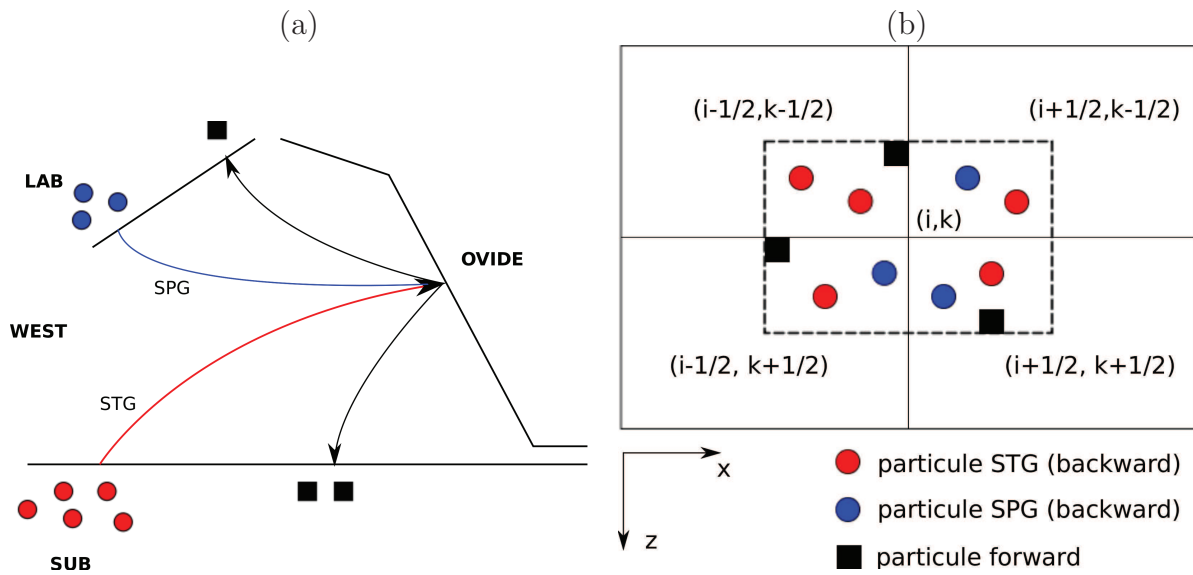


**Figure 4.19:** Schematic representation of the method used to reconstruct  $HT_\theta$  in ARIANE. The A25-Ovide section is divided into individual bins collocated on the original model grid cell. A large number of numerical particles are seeded along the section and advected backward and forward in time until they reach either the SPG or the STG transect. The transport within each bin is the algebraic sum of the individual particle transport present in the cell. Backward (resp. forward) particles are associated with a positive (resp. negative) transport. The time-averaged transport field along the section for the period 1965-2004 is then calculated. The temperature within each bin is estimated from the average temperature of subtropical and subpolar particles from the backward experiment (circles) and their relative proportion (see equation 4.16).

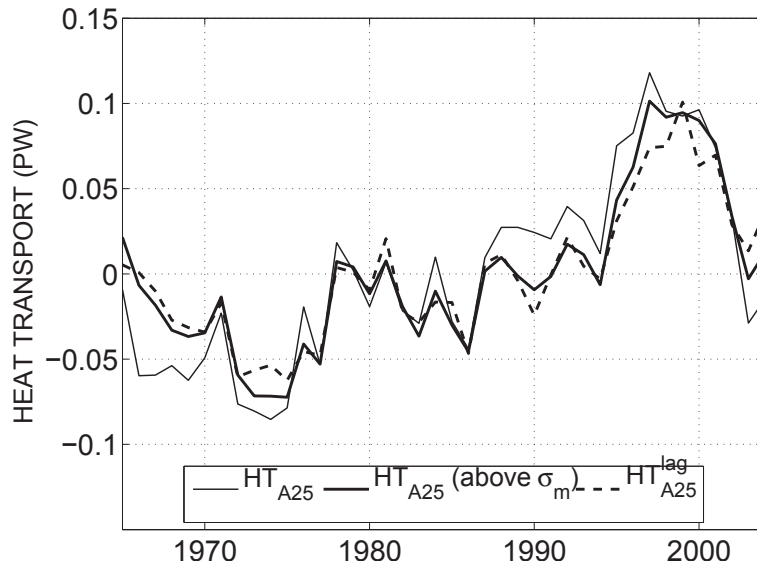


**Figure 4.20:** Comparison of the thermally-driven heat transport  $HT_\theta$  within the upper  $MOC_\sigma$  limb in the Eulerian (thick solid) and Lagrangian (thick dashed) framework. The full-depth Eulerian signal is shown with the thin black line.

Chapter 3 (Figure 3.4c) where we concluded that hydrographic criterion were not suitable to extract the subpolar and subtropical component of the NAC in the eastern subpolar gyre. Hence, the Lagrangian expression of  $\theta_{A25}$  as it stands in equation 4.16 contains little information about the origins of the anomalies (i.e. changes in  $\%_{STG}$  will have small impact on  $\theta^{A25}$ , and hence on  $HT_{\theta}^{Lag}$ ). We can however take advantage of the Lagrangian decomposition by using in equation 4.16 the particle temperatures in their source regions, namely the subtropics and the Labrador Sea:

$$\theta^{West} = \%_{STG}\theta_{STG}^{SUB} + \%_{SPG}\theta_{SPG}^{LAB} \quad (4.18)$$

Here, the respective properties of subtropical and subpolar water masses are very different (see Figure 3.4b in Chapter 3), and changes in  $\%_{STG}$  may lead to significant  $\theta^{West}$  anomalies. The difference between  $\theta^{A25}$  and  $\theta^{West}$  yields a measure of anomalous temperature changes along the water masses paths within the North Atlantic domain (i.e the region bounded by the A25, STG and SPG sections). In average, subtropical water masses are cooled by  $\sim 3.5^{\circ}\text{C}$  between  $40^{\circ}\text{N}$  and A25-Ovide, while subpolar water masses are warmed by  $\sim 6.5^{\circ}\text{C}$  between the Labrador sea and A25-Ovide (no figure shown). Any disturbance from this mean state will produce temperature anomalies within the NAC and hence impact  $HT_{\theta}$  at A25-Ovide. The resulting heat transport anomalies are here labelled as  $HT_{PATH}$ , following:

$$HT_{\theta}^{Lag} = HT^{West} + HT_{PATH} \quad (4.19)$$

where  $HT^{West}$  is the heat transport computed using  $\theta^{West}$  instead of  $\theta^{A25}$ . To a first approximation,  $HT_{PATH}$  anomalies can be interpreted as the impact of anomalous air-sea heat fluxes between the three sections. The heat transport signal is shown in Figure 4.21a, and the resulting heat content changes is shown in Figure 4.22a. The phase and amplitude of  $HT_{PATH}$  indicate that this mechanism is not the dominant source of  $HT_{\theta}$  variability at A25-Ovide. Its contribution is however not negligible and shows two episodes of relatively high positive anomalies (the late 1960's and early 1980's) embedded in a negative trend that sharply reversed since

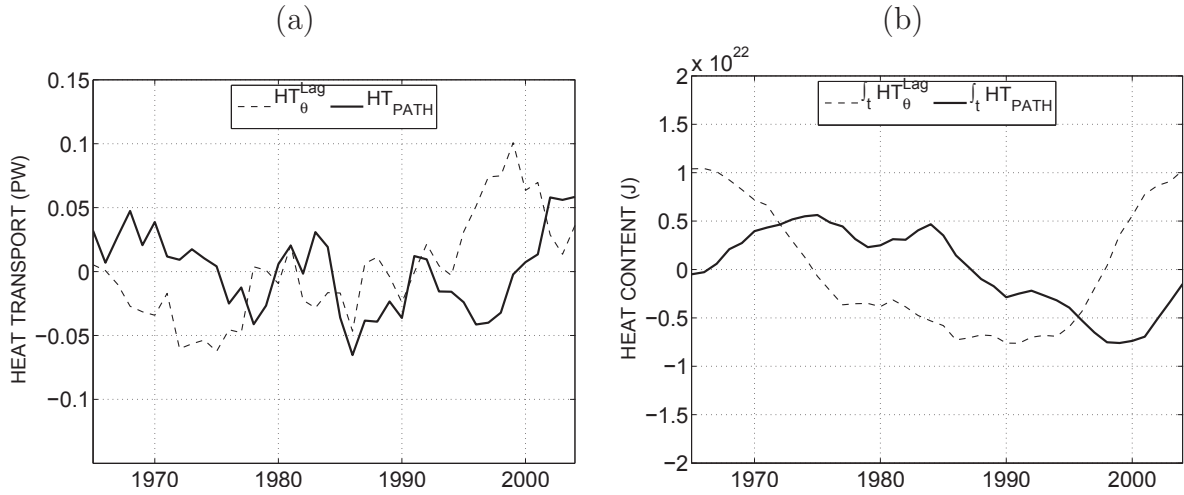


**Figure 4.21:** (a) Timeseries of  $HT_{\theta}^{Lag}$  (dashed) and  $HT_{PATH}$  (solid).  $HT_{PATH}$  is linked to the difference between  $\theta_{A25}$  and  $\theta_{West}$  and is interpreted as heat transport anomalies induced by anomalous air-sea heat fluxes between the STG/SPG transects and the A25-Ovide section. (b) same as (a) but expressed as a heat content change (J). Heat flux anomalies are integrated in time from their initial (absolute) value of 1965.

the mid-1990's. The associated heat content change describes a warming during the 1960's and early 1970's followed by a gradual cooling until the early 2000's (this will be further discussed below).

We can now focus on the origins of  $\theta^{West}$  anomalies and on their subsequent impacts on  $HT_{\theta}^{Lag}$ . The time-dependent temperature signal within each bin can be decomposed temporally as:

$$\theta^{West} = \underbrace{\left( \overline{\%_{STG}} \theta_{STG}^{SUB'} + \overline{\%_{SPG}} \theta_{SPG}^{LAB'} \right)}_{SOURCE} + \underbrace{\left( \%_{STG}' \overline{\theta_{STG}^{SUB}} + \%_{SPG}' \overline{\theta_{SPG}^{LAB}} \right)}_{PROP} \quad (4.20)$$

where the cross term  $\%'\theta'$  has been neglected. Hence, the total temperature-driven heat transport is decomposed as:

$$HT_{\theta}^{Lag} = HT_{SOURCE} + HT_{PROP} + HT_{PATH} \quad (4.21)$$

The first two terms on the right-hand side of 4.20 are measures of local temperature changes originating in the subtropics and the Labrador Sea, respectively. In average, subtropical particles at 40°N have a mean temperature of 14.6°C, while subpolar particles have a mean tem-

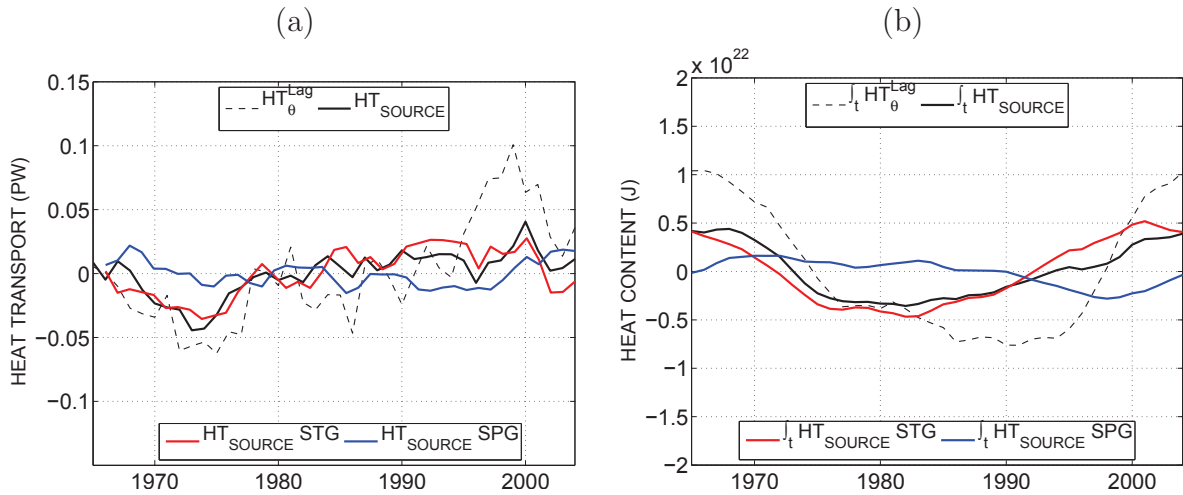


**Figure 4.22:** (a) Timeseries of  $HT_{\theta}^{Lag}$  (dashed) and  $HT_{SOURCE}$  (solid black), decomposed into a subtropical (red) and subpolar (blue) contribution.  $HT_{SOURCE}$  is linked to the formation of temperature anomalies at the STG and SPG transects. (b) same as (a) but expressed as a heat content change (J). Heat flux anomalies are integrated in time from their initial (absolute) value of 1965.

perature of  $2.9^{\circ}\text{C}$ . Any disturbance from this mean state will be captured in  $HT_{SOURCE}$ , the associated heat transport changes at A25-Ovide.  $HT_{SOURCE}$  can relate to either anomalous air-sea exchanges and/or anomalous mixing with adjacent water masses in both source regions. It is shown in Figure 4.22a and the resulting heat content signal is shown in Figure 4.22b (black lines).  $HT_{SOURCE}$  basically describes a positive trend between the early 1970's and late 1990's, mainly associated with a warming of subtropical water masses at  $40^{\circ}\text{N}$  (red line). A slight negative trend characterizes the temperature of subpolar water masses in the Labrador Sea (blue line). These signals are consistent with reduced (increased) heat loss to the atmosphere in subtropical (subpolar) regions following the concomitant positive trend in the NAO index. Both signals reversed in the late 1990's, in line with the pronounced NAO switch in the winter 1995/1996. The NAO index leads the subtropical ( $R = 0.45$ ) and subpolar ( $R = 0.55$ ) component of  $HT_{SOURCE}$  by 2-3 years, consistent with the mean travel time of the particles between their source regions and A25-Ovide. For instance, the negative  $HT_{SOURCE}$  anomaly found in 1974 at A25-Ovide is associated with a temperature anomaly formed in the subtropics a few year earlier. Overall,  $HT_{SOURCE}$  anomalies are not sufficient to explain the total  $HT_{\theta}^{Lag}$  at A25-Ovide, and most particularly the strong warming in the 1990-2000's.

The second contribution in 4.20 comes from changes in the relative proportion of subtropical and subpolar water masses transported by the NAC, given within each bin by the  $\%_{STG}$  ratio. Variations in  $\%_{STG}$  projects onto the very strong temperature contrast between subtropical and subpolar water masses in their source regions ( $\overline{\theta_{STG}^{SUB}} - \overline{\theta_{SPG}^{LAB}} = 11.7^\circ\text{C}$ ). Recall that we showed in Chapter 3 that the NAC transport was characterized by a relatively constant proportion of subtropical particles on decadal timescales (see Figure 3.11 in Chapter 3). When considering temperature changes, the term "constant" should be regarded with caution. In fact, it does not necessarily hold for local variations in  $\%_{STG}$ , which are now calculated within individual grid cell. For instance, a local anomaly in  $\%_{STG}$  of only 1% yields a temperature change in  $\theta_{West}$  of  $0.12^\circ\text{C}$ , which may significantly impact  $\text{HT}_\theta$ . We show in Figure 4.23 an Hovmöller diagram of  $\%_{STG}$  along A25-Ovide. Local anomalies of  $\pm 10\%$  are observed between  $50^\circ\text{N}$  and  $57^\circ\text{N}$ , that is where a substantial  $\text{HT}_\theta$  signal was shown to occur (see Figure 4.8c). As shown in Figure 4.24, the associated heat transport at A25-Ovide,  $\text{HT}_{PROP}$ , stands as the dominant source of  $\text{HT}_\theta$  decadal variability. It describes a strong positive trend from the late 1960's to the late 1990's, followed by a sharp weakening during the early 2000's, and is significantly correlated with the total  $\text{HT}_\theta$  signal ( $R = 0.5$ ). Thus, a significant fraction of the thermally-driven heat transport in the eastern SPG appears to be linked with changes in the relative proportion of the two main source waters that compose the NAC. In agreement with the lagged correlation found between the NAO and  $\text{HT}_\theta$  (see Figure 4.10),  $\text{HT}_{PROP}$  is also significantly correlated with the NAO fluctuations with a 5-year lag ( $R = 0.72$ ). Note that *Krahmann et al.* (2000) reported a similar travel time of temperature anomalies from Newfoundland to the eastern subpolar gyre.

In agreement with the relationship between heat transport and air-sea heat fluxes noted in Section 4.3 (the latter being driven by the former), an anti-correlation is found between  $\text{HT}_{PROP}$  and  $\text{HT}_{PATH}$  ( $R = -0.75$ , significant at the 95% level). The warming (resp. cooling) of the NAC waters induced by changes in the  $\%_{STG}$  ratio is presumably damped by increased (resp. decreased) heat loss to the atmosphere along their paths toward the eastern SPG.

In summary, the Lagrangian reconstruction of  $\text{HT}_\theta$  at A25-Ovide suggests that it is strongly impacted by changes in the relative proportion of subtropical and subpolar water masses ad-

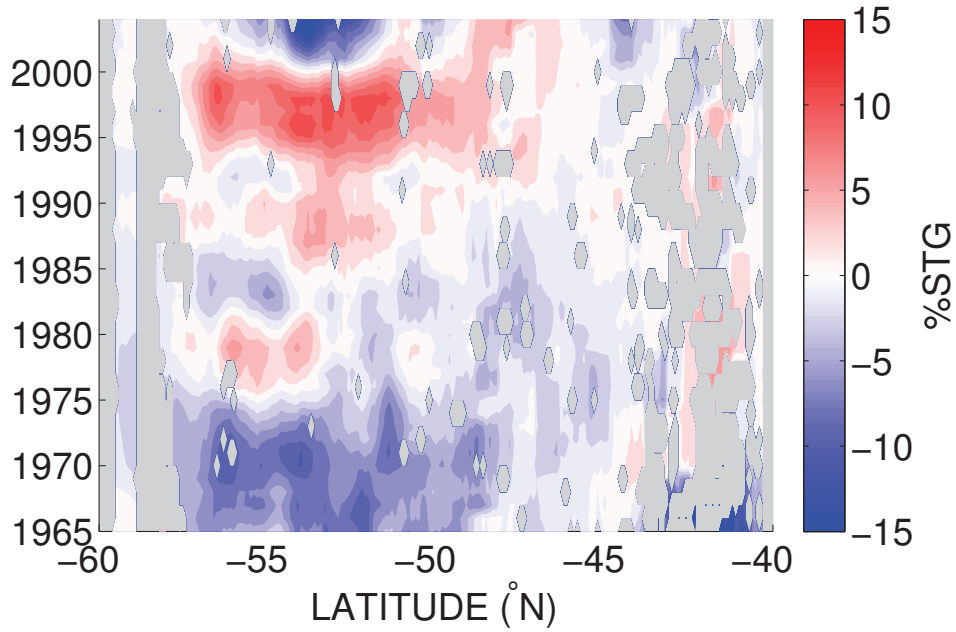


**Figure 4.23:** Time-latitude diagram of anomalies in the relative proportion of subtropical water masses along A25-Ovide (in %). The %<sub>STG</sub> ratio has been calculated within individual latitudinal bins (0.1°). Shading are associated with particles that are not including in the STG of SPG group of EXP<sub>BACK</sub> (i.e. the recirculation around Reykjanes Ridge, or the southward flow in the Iberian Abyssal Plain).

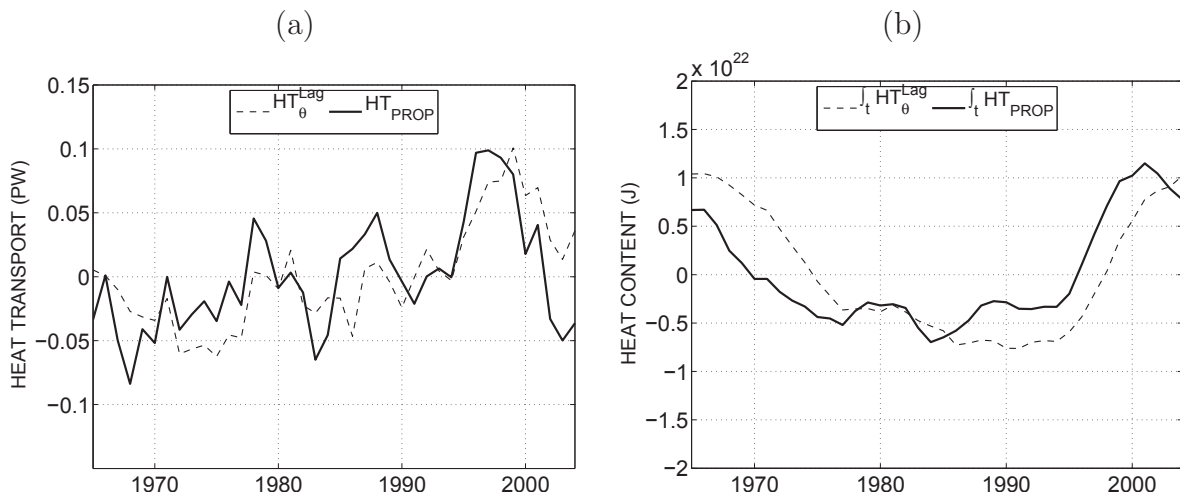


**Figure 4.24:** (a) Timeseries of  $HT_{\theta}^{Lag}$  (dashed) and  $HT_{PROP}$  (solid).  $HT_{PROP}$  is linked to changes in the relative proportion of subtropical and subpolar water masses advected across the A5-Ovide section. (b) same as (a) but expressed as a heat content change (J). Heat flux anomalies are integrated in time from their initial (absolute) value of 1965.

vedected witin the upper  $MOC_\sigma$  limb ( $HT_{PROP}$ ). In agreement with the results of Chapter 3, those changes are predominant north of about  $50^\circ\text{N}$ , that is within the northern NAC branch. They are accentuated by temperature anomalies advected from the Labrador Sea and the subtropics ( $HT_{SOURCE}$ ), and damped by anomalous air-sea heat fluxes along the water mass paths toward the eastern subpolar gyre ( $HT_{PATH}$ ). A causal relationship between the above mechanisms and the heaving of  $\sigma_{MOC}$  is a tentative one, but it would require additional investigations.

## 4.7 Conclusion

The low-frequency variability of the heat content in the eastern SPG region has been investigated in the ORCA025-G70 simulation for the period 1965-2004. The present simulation was shown to reproduce a consistent interannual-decadal signal close to observational estimates. The 40-year timeseries of heat content anomalies within a box bounded by the A25-Ovide section and the Greenland-Iceland-Scotland sills revealed two periods of significant changes within the upper few hundred meters of the water column: a strong cooling during the 1960 and early 1970's and a strong warming in the 1990 and early 2000's. A heat budget calculation within the considered domain points the oceanic heat transport variability across the A25-Ovide section as the main contributor to heat content decadal variations. The impact of air-sea heat fluxes is a delayed (2-3 years) damping of heat content trends, in response to the anomalous advection at A25-Ovide. Spatial and temporal decompositions of the heat transport at A25-Ovide were then performed and the Lagrangian analysis tool ARIANE was used to complement the Eulerian investigations. Accordingly, we list the following conclusions:

- *The low-frequency heat transport variability at A25-Ovide is primarily induced by changes in the horizontal gyre circulation. The total signal (mean and anomaly) is captured by the diapycnal component of the flow, which makes the  $MOC_\sigma$  a useful proxy for the full-depth heat transport.*

Due to the significant basin-wide sloping of isopycnal surfaces in mid-high latitude regions,

the meridional heat transport is carried out by both the vertical and horizontal circulation cells. This is verified across the A25-Ovide section where the subpolar gyre and the  $\text{MOC}_Z$  advect an almost equal amount of heat northeastward. While interannual heat transport variability is impacted by both components of the circulation, the horizontal gyre dominates on decadal timescales. A decomposition of the full-depth heat transport into isopycnal and diapycnal components shows that a significant fraction of the heat transport variability is associated with a diapycnal heat flux, reflecting the strong densification of surface waters during their cyclonic transit around the Iceland and Irminger basins. Consequently, The total heat transport variability is effectively captured by a  $\text{MOC}_\sigma$  index.

- *Heat transport variability at A25-Ovide results from an imbalance between opposed changes in its velocity and temperature components.*

The respective impacts of velocity anomalies acting upon the mean temperature field and the advection of temperature anomalies by the mean circulation have been quantified. Both signals are significantly anti-correlated on interannual and decadal timescales, suggesting a common driving mechanism. Their horizontal and vertical distributions along the section denote a transition between two distinct oceanic states: a cold and southerly NAC in [1965-1985] and a warm and northerly NAC in [1985-2004]. The trends in heat transport are mainly contained in the temperature component, which shows a strong and gradual intensification between the early 1970's and the late 1990's, evidenced within the North Atlantic Current core east of Reykjaneid Ridge.

- *Both temperature and velocity anomalies are partly reflected in the heaves of isopycnals at A25-Ovide*

The total heat transport signal has been approximated using an index of the Meridional Overturning Circulation in the density plane and an index of the temperature difference between its upper and lower limb. Although changes in the averaged temperature of the upper  $\text{MOC}_\sigma$  limb cannot be neglected, most of the variability is explained by the varying strength of the  $\text{MOC}_\sigma$ . In agreement with the temporal decomposition of  $\text{HT}_{A25}$ , its variability is mainly

”density-driven” and reflect changes in the volume of both limbs through vertical displacements of the main pycnocline. In fact, heaves of isopycnal surfaces affect in two opposite ways both components of the total heat transport: a deepening of the pycnocline north of the NAC core increases its thermal part, while inducing negative velocity anomalies through a decay of the pycnocline slope, and vice versa for a shallowing pycnocline.

- *A Lagrangian study of the origin of temperature anomalies at A25-Ovide shows the strong impact of changes in the relative proportion of warm subtropical waters and cold subpolar waters advected within the North Atlantic Current.*

The temperature component of the heat transport at A25-Ovide was satisfactorily reconstructed using a Lagrangian analysis tool, which gave access to additional information regarding the two main source waters feeding the upper  $\text{MOC}_\sigma$  limb: the subpolar contribution from the Labrador Sea and the subtropical one from the Gulf Stream. On decadal timescales, the predominant mechanism driving temperature anomalies is associated with changes in the relative proportions of both source waters within the NAC. The strong intensification of  $\text{HT}_\theta$  between the early 1970’s and the late 1990’s is concomitant with an increased proportion of subtropical waters within the northern NAC branch. Anomalous air-sea heat fluxes in the Labrador Sea and the subtropics, as well as along the water masses path toward the eastern subpolar gyre, also contribute to the formation of temperature anomalies within the NAC. Although our results suggest a causal link between the changing composition of the NAC revealed in ARIANE and vertical displacements of isopycnals at A25-Ovide, we are so far only able to demonstrate the concomitance of both signals. The role of local forcing mechanisms (Ekman pumping, internal wave propagation) in driving isopycnal heaving needs to be investigated.

# Chapter 5

## The mean 2002-2010 circulation state along the merged AR7W/A25-Ovide line

---

### Abstract

*Repeated hydrographic cruises carried out along the AR7W line in the Labrador Sea are combined with mean dynamic topography and altimetry data to compute a time-average full-depth summer circulation for 2002-2010. The resulting hydrographic and velocity fields are merged with concomitant estimates from the A25-Ovide section joining Portugal and Greenland, thereby providing a basin wide picture of the subpolar gyre state in the 2000's. The total Meridional Overturning Circulation (MOC) along the merged line reaches  $10.7 \pm 1.4$  in the depth ( $z$ ) space and  $18 \pm 1.8$  Sv in the density ( $\sigma$ ) space, reflecting substantial water mass transformation in the horizontal plane. The full-depth heat transport across the merged line is primarily carried out by the horizontal component of the flow, and is fully captured by the diapycnal circulation. Most of the  $MOC_z$ ,  $MOC_\sigma$  occurred east of Greenland, depicting a minor contribution of the Labrador Sea to the time-mean basin wide MOC. However, some preliminary results suggest significant changes in the overturning rates of the Labrador Sea during recent decades. A similar*

*combination of multi-year hydrographic data at AR7W and altimetry data for the 1990-1996 time span indeed indicates a decrease in the  $MOC_z$  (-1.6 Sv) and  $MOC_\sigma$  (-3 Sv) at AR7W between the two periods.*

---

## 5.1 Introduction

The Meridional Overturning Circulation (MOC) in the North Atlantic Ocean is a measure of the amount of waters that sink in high latitude regions, through buoyancy exchange with the atmosphere and internal oceanic processes. The bottom layers of its deep branch are fed by Denmark Strait Overflow Waters (DSOW) and Iceland-Scotland Overflow Waters (ISOW) from the Nordic Seas, which entrain thermocline waters as they cascade down the Greenland-Scotland sills. At intermediate levels, one finds the Labrador Sea Water (LSW), a nearly homogeneous body of relatively cold and fresh water formed in the Labrador and Irminger Seas during convecting events. These two deep water products join to form the so-called North Atlantic Deep Water (NADW), which exit the subpolar basins as a deep western boundary current that participate in the ventilation of the deep world ocean.

To describe and quantify the respective contribution of the different NADW constituents to the basin wide MOC is a challenging task. Observational estimates are mainly provided by ship-based full-depth hydrographic measurements at transoceanic sections, which reflect instantaneous snapshots of the circulation. Although these estimates provide crucial insights into the amplitude of the variability, they are too sparse in time to efficiently resolve the associated timescales. This was clearly illustrated by *Sarafanov et al.* (2012) who showed the high degree of spreading between available estimates of the full-depth deep western boundary current (DWBC) transport at Cap Farewell (Greenland). However, the knowledge of continuous mea-

measurements of the velocity field at a given reference level, combined with repeated hydrographic profiles over the whole water column may provide reliable estimates of the mean circulation along a given transoceanic section. These estimates may yield information regarding oceanic states associated with particular and persistent atmospheric conditions, and may serve as a robust benchmark for numerical model validation. Yet, time-averaged observational estimates of the basin-wide thermohaline circulation in the subpolar gyre are relatively rare. Using 10 non-winter occupations of the AR7W line (joining the Labrador coast and Cap Farewell) in the 1990's, and 5 years of PALACE float data at 700m depth, *Pickart and Spall (2007)* calculated a mean absolute velocity field and derived various volume and heat transport quantities. Interestingly, they found a relatively small overturning rate of only 2 Sv across the AR7W section, despite the large volume of LSW formed during the early 1990's (*Yashayaev et al., 2007*). Similarly, *Sarafanov et al. (2012)* provided a precise quantification of the mean circulation between Cap Farewell and Iceland during the 2000's, from altimetry data and repeated hydrographic measurements along 59.5°N. Their mean overturning estimate reaches  $16.5 \pm 2.2$  Sv, in line with the concomitant value deduced from inverse methods across the A25-Ovide ( $16 \pm 1$  Sv, see Chapter 3). In the present Chapter, we will attempt to answer the following questions:

**Can satellite altimetry be used to provide consistent estimates of the time-mean full-depth circulation in the Labrador Sea?** Following in many aspects the protocol of *Sarafanov et al. (2012)*, a time-average velocity section along the AR7W section for the 2002-2010 time span will be reconstructed based on a combination of three products:

- altimetry-derived sea-surface height anomaly (SLA)
- a mean dynamic topography (MDT) from assimilated model of the geoid
- a mean hydrographic field from repeated oceanic surveys.

After a brief presentation of the mean circulation pattern in the Labrador Sea (Section 5.2), the 2000's mean hydrography along AR7W will be described (Section 5.3). In Section 5.4, the

*thermal wind* relationship will be used to compute a mean velocity field along the transect and the basic features of the circulation will be assessed.

**What was the contribution of the Labrador Sea to the time-mean basin wide overturning during the 2000's?** The final objective of the present chapter is to answer this question by providing a mean quantitative picture of the full-depth circulation in the 2000's, along a transect comprising the AR7W and the A25-Ovide lines (Figure 5.1). This merged transect bounds to the south the main regions involved in the thermohaline circulation of the North Atlantic: the Labrador Sea, the eastern subpolar gyre and the Nordic Seas. Taking advantage of published estimations of volume exchanges across the Greenland-Scotland sills, we should be able to quantify the contributions of these three regions to the subpolar MOC and associated heat transport. Note that we only consider the time-averaged picture of the 2000's, leaving the study of year-to-year changes for future investigations. Based on the A25-Ovide fields presented in Chapter 1 (Figure 1.11), integrated volume and heat transport quantities across the merged AR7W/A25-Ovide transect will be presented in Section 5.5.

**Can we infer the presumed changes in the Labrador Sea overturning between the 1990's and the 2000's?** As shown in Chapter 1, a relationship between the intensity of the vertical and horizontal circulations in the subpolar gyre and fluctuations in the the North Atlantic Oscillation (NAO) is evident. As opposed to the 1990's where a persistent positive phase of the North Atlantic Oscillation (NAO) induced intense winds and associated oceanic heat loss over the whole subpolar gyre (*Häkkinen and Rhines, 2004*), the mean 2000's circulation pattern was established during a prolonged period of relatively weak/neutral atmospheric forcing (see NAO index on Figure 1.15). Importantly, the major changes in the subpolar gyre circulation that followed the NAO index drop in the winter 1995-96 (weakening of the upper circulation, reduced convection, intensification of the deep circulation) primarily occurred in the second half of the 1990's (*Häkkinen and Rhines, 2004; Bersh et al., 2007*). We thus expect substantial changes in the strength of the horizontal and vertical circulation in the Labrador

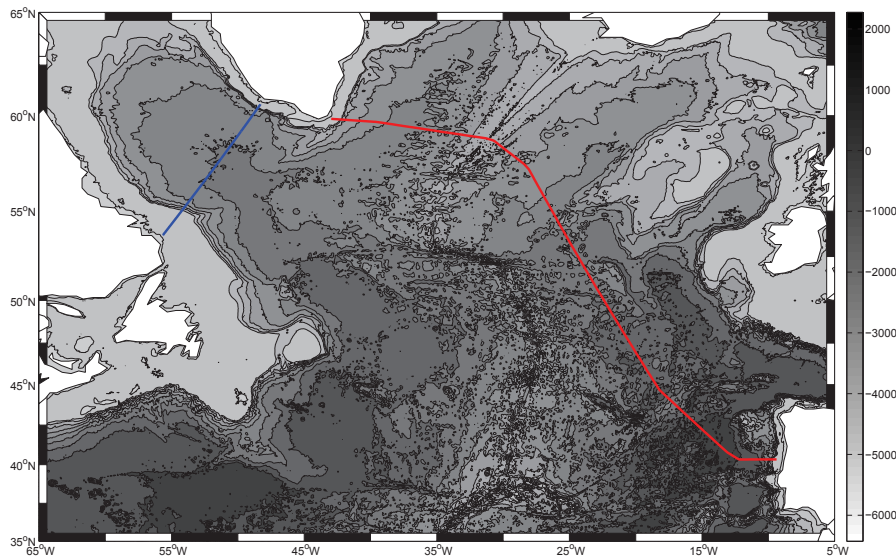


**Figure 5.1:** Positions of the nominal sections AR7W (blue) and A25-Ovide (red) used in the present study, superimposed on the bathymetry of the northern North Atlantic (in m).

Sea between the early 1990's and the 2000's time periods. Using the same "altimetry" methodology to compute an absolute velocity field at AR7W during the early and mid 1990's, we will document in Section 5.6 some preliminary results of a 1990's - 2000's inter-comparison. The main results of the whole analysis will be summarized in Section 5.7.

## 5.2 Schematic circulation in the Labrador Sea

Figure 5.2 shows a schematic view of the shallow and deep circulations in the Labrador Sea, aimed to introduce the main currents discussed hereafter. The overall circulation is characterized by an intense cyclonic boundary current encircling the basin and a relatively weaker flow in the interior. East of Greenland, the upper boundary current is usually divided into the cold East Greenland Current (EGC) above the shelfbreak and the warmer Irminger Current (IC) above the upper slope (*Pickart et al.*, 2005). A third constituent of the boundary current was documented by *Bacon et al.* (2002): the East Greenland Coastal Current above the Greenland plateau. Along the western Greenland margin, IC and EGC jointly form the so-called West

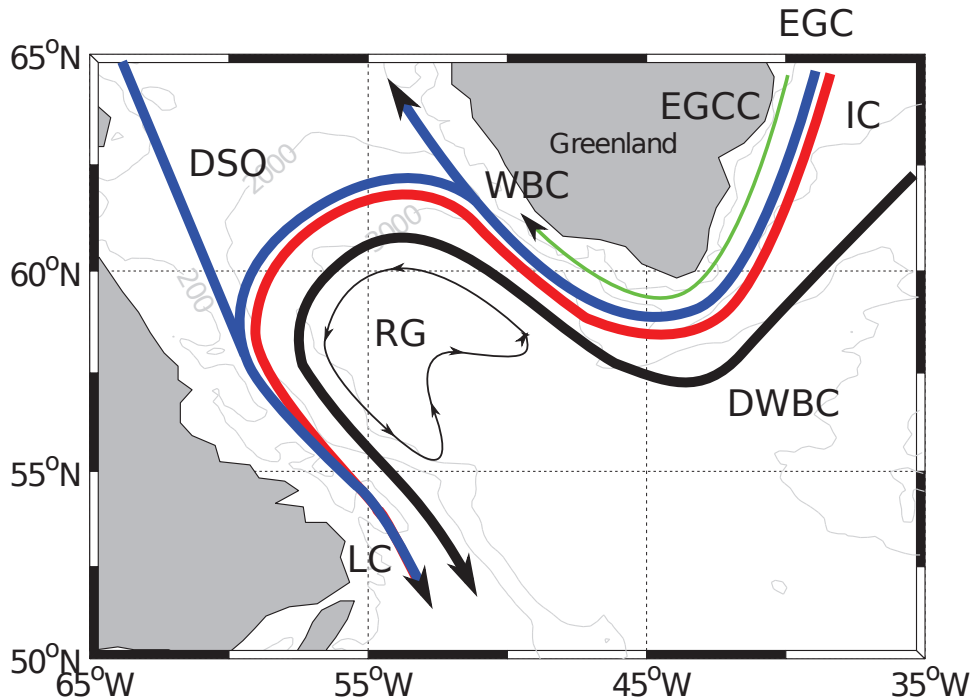


**Figure 5.2:** Schematic representation of the Labrador Sea circulation. Blue (resp. red) colors indicate relatively cold upper-layer currents comprising the East Greenland Current (EGC), Irminger Current (IC), West Greenland Current (WBC), Labrador Current (LC) and Davis Strait Outflow (DSO). The green arrow indicates the East Greenland Coastal Current (EGCC). The thick black arrow stands for the deep western boundary current (DWBC), while the thin black line indicate the anticyclonic recirculation gyre (RG) evidenced by Lavender *et al.* (2000). Inspired from Pickart and Spall (2007).

Greenland Current, which flows cyclonically around the basin and eventually meets the cold and fresh outflow from Davis Strait (DSO) before leaving the Labrador Sea off Canada as the Labrador Current (LC). As studied in Chapter 3, part of the LC will retroreflect into the eastward flowing North Atlantic Current near Flemish Cap. At deeper levels (at the base of the continental slope), a strong Deep Western Boundary Current (DWBC) primarily composed of overflow-derived dense waters from the Nordic Seas is observed. A weaker clockwise barotropic circulation is present in the basin interior (Lavender *et al.*, 2000).

### 5.3 Mean summer hydrography at AR7W in the 2000's

The method for estimating mean sections of hydrographic properties relies on a gridding-then-averaging procedure. Since the station positions slightly differ from one survey to the other,

	AR7W	OVIDE
2002	2 July - 8 July	10 June - 12 July
2004	20 May - 26 May	4 June - 7 July
2006	26 May - 30 May	21 May - 28 June
2008	23 May - 29 May	10 June - 10 July
2010	18 May - 24 May	8 June - 7 july

**Table 5.1:** Dates of AR7W and OVIDE cruises and associated numbers on hydrographic stations used in the study. A total number of 135 AR7W stations and 477 A25-Ovide stations were used to compute the average.

the full-depth hydrographic profiles from each cruises (the cruise dates are given in Table 5.1.) were interpolated onto a nominal and regular grid (7 km x 5 m) (blue line in Figure 5.1) The five gridded fields were then averaged to provide single sections of temperature, salinity and planetary potential vorticity along AR7W, respectively shown in Figure 5.3a, 5.3b and 5.3c.

Due to increased solar heating and freshwater exchanges with the adjacent shelfbreak, the surface layers are well-stratified at this time of the year. Cold and fresh waters ( $\theta = 0.5^{\circ}\text{C}$ ,  $S = 33.7$ ) are visible above the shelfbreak on the eastern side of the basin, while warm and salty Irminger waters advected within the WGC occupy the upper slope ( $\theta = 5^{\circ}\text{C}$ ,  $S = 34.95$ ). They become colder and fresher as they move along the periphery of the Labrador Sea via air-sea fluxes and mixing with the outflowing Arctic waters, and leave the basin within the LC ( $\theta = 3.9^{\circ}\text{C}$ ,  $S = 34.89$ ). The signature of the DSO waters is visible at the western boundary as a body of very fresh and cold waters confined above the Labrador shelf ( $\theta = -1^{\circ}\text{C}$ ,  $S = 33$ ). The weakly stratified water in the middle of the water column is the water mass known as the Labrador Sea Water (LSW), which stands as the densest mode water formed by deep convection in the subpolar basins. The LSW is most commonly defined from a static range of a given variable. Accordingly, *Kieke et al.* (2006) introduced the "classical" and "upper" classes of LSW from the density ranges 27.74-27.80 and 27.68-27.74  $\text{kg m}^{-3}$ , respectively. The "classical" class is typically associated with a relatively fresh, cold and dense LSW product (such as the early 1990's one), while the "upper" class typically refers to warmer and lighter LSW (such as the 2000's product). The reliability of this basic method for identifying a given LSW class was recently questioned by *Yashayaev et al.* (2007). The authors rather pointed out

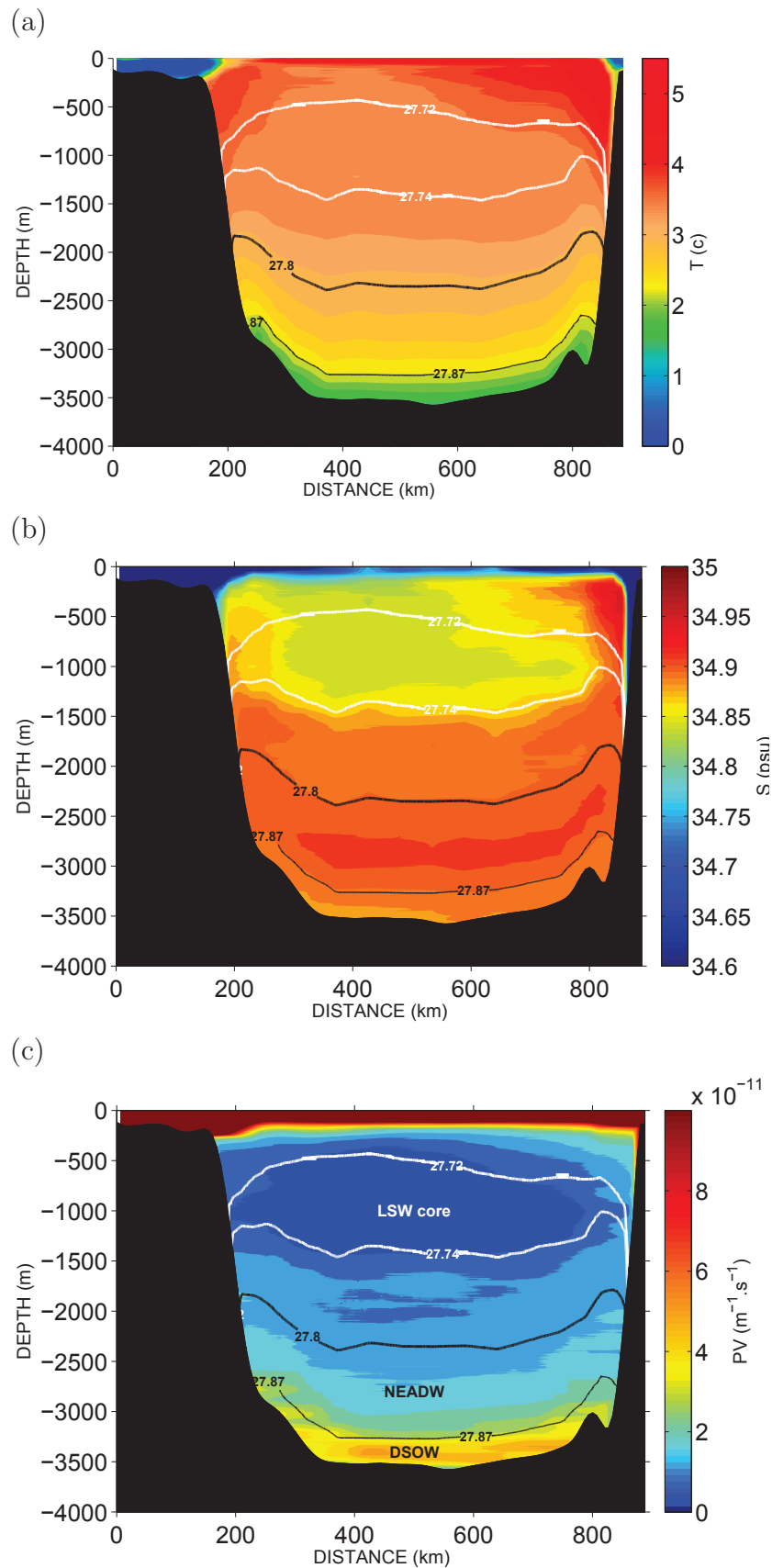


**Figure 5.3:** Mean summer section of (a) temperature ( $^{\circ}\text{C}$ ), (b) salinity and (c) potential vorticity ( $\text{m}^{-1}\text{s}^{-1}$ ) at AR7W computed from the 2002, 2004, 2006, 2008, and 2010 cruises. The white lines indicate the isopycnal surfaces  $\sigma_0 = 27.72$  and  $\sigma_0 = 27.74$ , i.e. the upper and lower bounds for the LSW core. The thick black line indicates the isopycnal surface  $\sigma_0 = 27.80$ , an upper bound for overflow-derived deep water masses.

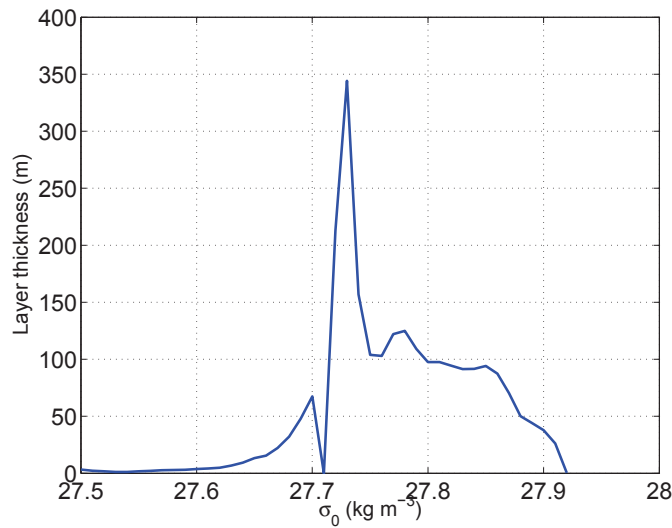


**Figure 5.4:** Basin-mean thickness (in m) of  $\Delta\sigma_0 = 0.01 \text{ kg m}^{-3}$  layers.

the relevance of volumetric approaches for defining and monitoring the dynamics and transformation of LSW. By computing the basin-mean thickness of individual isopycnal layers, one can effectively identify the LSW core. We follow their approach and compute the thickness of  $\Delta\sigma_0 = 0.01 \text{ kg m}^{-3}$  from the mean density field at AR7W (note that *Yashayaev et al. (2007)* used  $\sigma_2$  in their calculation). The resulting "volume" distribution (Figure 5.4) is characterized by a clear peak centered at  $\sigma_0 = 27.73$ . Hence, the isopycnal surfaces  $\sigma_0 = 27.72$  and  $\sigma_0 = 27.74$  are, in our case, a good proxy for the upper and lower bounds of the LSW core (see white contours on Figure 5.3). From this definition, the 2000's LSW core has an average temperature and salinity of  $3.5^\circ\text{C}$  and  $34.84$  and occupies the 500 - 1500m layer. Beneath the LSW are deep overflow waters advected from the eastern Atlantic. They are usually decomposed into a Northeastern Atlantic Deep Water contribution (NEADW) ( $27.80 < \sigma_0 < 27.87$ ,  $\theta = 2.9^\circ\text{C}$ ,  $S = 34.89$ ) and a Denmark Strait Overflow Water contribution ( $\sigma_0 > 27.87$ ,  $\theta = 2^\circ\text{C}$ ,  $S = 34.88$ ).

## 5.4 Mean summer velocity field across AR7W in the 2000's

### 5.4.1 Some basic theory for absolute velocity calculations

Most of the large scale oceanic flows satisfy the geostrophic equilibrium, meaning that they results from a balance between horizontal pressure gradients and the Coriolis force. Combining geostrophy with the hydrostatic relation (which relates the pressure at a given level to the weight of water above it) yields the so-called "thermal wind equation", which links vertical velocity shear to horizontal gradient in density,

$$\frac{\partial v}{\partial z} = -\frac{g}{f\rho_0} \frac{\partial \rho}{\partial x} \quad (5.1)$$

where  $u$  is the cross-sectional velocity,  $\rho$  is the density of seawater,  $g$  is the gravitational parameter,  $f$  is the Coriolis parameter,  $z$  is the vertical coordinate and  $y$  is the along-section coordinate. The vertical integration of the rhs of equation 5.1, which can be directly computed from observations of temperature, salinity and pressure, gives access to the relative (geostrophic) velocity, that is the velocity at a given pressure relative to a reference level. Hence, if the velocity is accurately known at any single level, the absolute velocity profile can be obtained. Historically, the assumption of a "level of no motion" at great depth has been frequently used for determining absolute velocity fields. More recently, the advance of satellite and drifting float measurements has provided new means to overcome the "reference level" issue. In the present study, the altimetry-derived sea-surface height  $\eta$  (in  $m$ ), which provides absolute geostrophic velocities at the sea-surface, will be used to reference the hydrographically-derived field of velocity shear. To that aim, we introduce the 'dynamic height' quantity defined as  $D = -\int_{p_1}^{p_2} \frac{1}{\rho} dp$  where  $p_1$  and  $p_2$  are two reference pressure levels and  $D$  is in unit of  $m^2 s^{-2}$ . It refers to the amount of work required to move a water parcel vertically from  $p_1$  to  $p_2$ . By vertically integrated equation 5.1, one can express the absolute velocity at level  $z$  between two stations

as:

$$v(z) = \frac{1}{f} \frac{\partial D}{\partial x} + \frac{g}{f} \frac{\partial \eta}{\partial x} = V_{relative} + V_{surface} \quad (5.2)$$

The first term on the rhs of equation 5.2 relates to relative velocity profiles computed from horizontal density gradient between two adjacent stations. The second term relates to the absolute surface geostrophic velocity computed from altimetry measurements. The algebraic sum of both terms at each depth level yields the absolute full-depth velocity profile.

### 5.4.2 Application to the AR7W section

We here apply the aforescribed method to compute a velocity section at AR7W for the 2002-2010 time span. Importantly, both terms in the rhs of equation 5.2 will be calculated using multiyear data composites, thereby filtering out a substantial fraction of high-frequency variability, including noise in the density structure and noise in the surface circulation. The datasets used (hydrographic data at AR7W, the MDT of *Rio and Hernandez* (2004) and SLA data from AVISO) have been previously described in chapter 2 (Tools and methods).

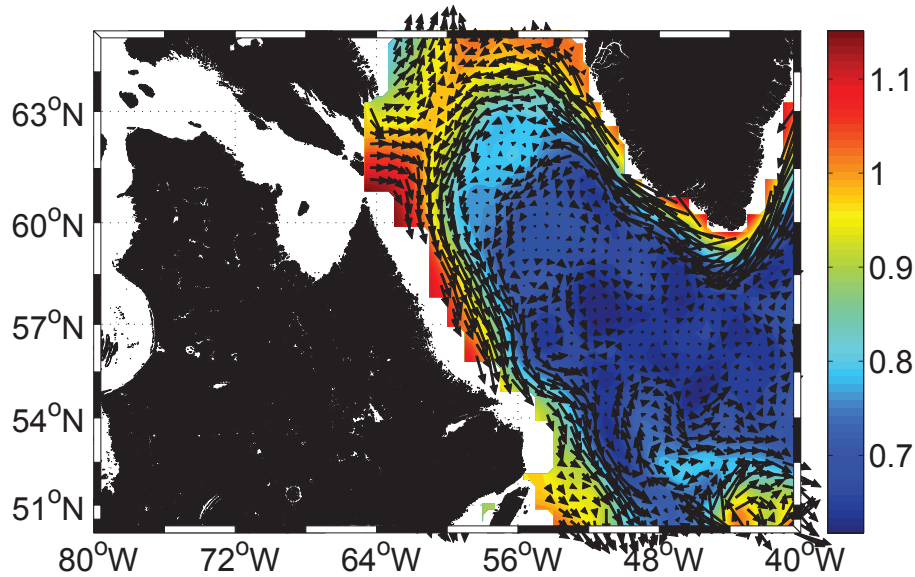
The first step in the reconstruction of a basin wide full-depth velocity field along AR7W is the determination of the 2002-2010 mean summer (May-June-July-September) absolute velocity at the sea-surface ( $U_{surface}$ ) (second term in the rhs of equation 5.2). Here,  $\eta$  is defined as the sum of sea-surface height anomalies (SLA) and mean dynamic topography (MDT). A map of the mean absolute dynamic height and associated geostrophic velocity field in the Labrador Sea is shown in Figure 5.5a, along with the corresponding horizontal profile of geostrophic currents interpolated along the AR7W nominal line (Figure 5.5b). The low-pressure center in the middle of the Labrador Sea is consistently associated with a strong cyclonic circulation along the continental boundaries of the basin. In the basin interior, one can note several cyclonic and anticyclonic recirculating cells. At AR7W, surface velocities reach  $0.3 \text{ m s}^{-1}$  and  $0.15 \text{ m s}^{-1}$  within the WGC and LC, respectively, while surface current are comparatively weak within the interior of the basin. Interestingly, the anticyclonic recirculation gyre highlighted

in *Lavender et al.* (2000) is not evident here. Note that the inshore portion of the southward flowing Labrador Current is not well-sampled by the altimeter. This might underestimate the volume transport of outflow from the Davis strait, which presumably occurs within this inshore shallow region.

As a second step, horizontal differences in dynamic height  $D$  for each pair of stations were computed and used in the *thermal wind* relation (first term in equation 5.2) to yield relative geostrophic velocity fields referenced to the sea-surface. As for the hydrographic property sections, the resulting two-dimensional velocity fields were interpolated onto the nominal grid and averaged altogether to provide a single estimate of the mean full-depth relative velocity (Figure 5.6a). According to equation 5.2, the absolute velocity section is obtained by summing up the relative velocity and the surface velocity (at each depth level). As the velocity profiles calculated between two adjacent stations extends down to their deepest common level, some approximations are needed to fill the so-called "bottom triangle". We follow the technique of *Bacon* (1998) and compute velocity in the triangles by imposing (1) constant  $v$  and (2) constant  $v$  shear below the deepest common level of adjacent stations, and by taking the average of (1) and (2) outcomes.

Although our mean velocity section is based on a composite of five individual sections, it may still be polluted by high-frequency noise. Some studies have indeed documented relatively high turbulent kinetic energy on both the eastern and western side of the basin, leading to energetic velocity fluctuations on short timescales (e.g. *Prater*, 2002; *Fischer et al.*, 2004). The absolute velocities for each of the five individual sections were obtained by referencing each section using the corresponding altimetry-derived surface geostrophic profile, and a section of the standard velocity error  $\epsilon$  was computed as  $\epsilon = \frac{\sigma}{\sqrt{N}}$ , where  $\sigma$  is the standard deviation of the velocity at each grid node and  $N$  the number of statistically independent sample (i.e. 5 here). This standard error contains the uncertainties that result from the bottom triangle approximation, as obtained from the two different techniques of velocity extrapolation presented above. That is,  $\sigma$  was calculated from the 10 velocity sections (5 from technique (1) and 5 from technique (2)), but keeping  $N = 5$  (*Sarafanov et al.*, 2012) (the same methodology is used for computing

(a)



(b)

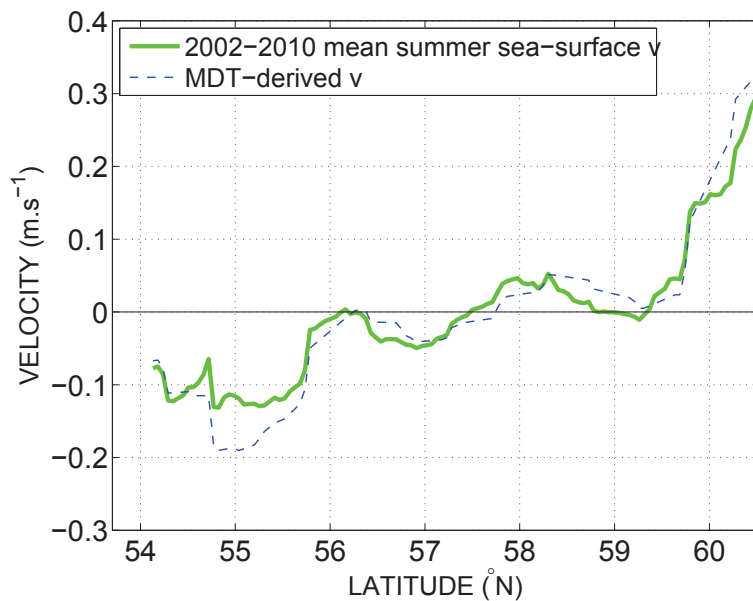


**Figure 5.5:** (a) Mean dynamic topography (m) and mean surface geostrophic currents in the Labrador sector, calculated from the Rio05 MDT. (b) The corresponding horizontal distribution of the mean absolute surface geostrophic currents across AR7W (green), obtained by summing the 2002-2010 mean summer altimetry-derived surface current anomalies to the MDT-derived absolute surface current (dashed blue).

errors on volume transport quantities in section 5.5).

The absolute velocity field is shown in Figure 5.6b with the associated standard errors displayed in Figure 5.6c (the individual velocity sections are provided in appendix C). The most striking feature is the overall barotropic nature of the circulation in the whole basin, illustrated by the strong differences between the relative and absolute velocity fields. Errors are relatively weak in the basin interior, but are important at the basin boundaries where they can reach  $8 \text{ cm s}^{-1}$  (large bottom triangles, high eddy kinetic energy). Vertical velocity profiles within the core of the western and eastern boundary currents are shown in Figure 5.9. As expected from the distribution of surface geostrophic currents, higher velocities are reached along the eastern boundary of the section (full-depth average of  $0.16 \text{ m.s}^{-1}$ ), as compared to the western margin (full-depth average of  $-0.11 \text{ m s}^{-1}$ ). The two profiles depict relatively strong velocities in the 0-1000m layer associated with the WGC and LC, as well as a bottom-intensified flow in the deep layers. Offshore of the boundary current stands a weak anticyclonic recirculation (at 300 km and 700 km), as evidenced by *Lavender et al.* (2000) using Lagrangian drifting floats. As shown in section 5.7, it is however much weaker than the 1990's one (*Pickart and Spall, 2007*). An additional barotropic cyclonic cell is consistently observed in the basin interior. A significant flow reversal induced by strong lateral density shear is visible adjacent to the eastern boundary. This flow reversal is not a persistent feature of the 2000's circulation and was only present in 2002 and 2008 (see individual sections in appendix C). Interestingly, *Pickart and Spall (2007)* also found a similar structure during the 1990's, associated with significant temporal variability. A similar but shallower flow reversal is also observed at the western margin, which was not present in earlier estimates of the western boundary circulation at the exit of the Labrador Sea (*Fischer et al., 2004*). Note, however, that both flow reversal at both ends of the section are associated with the highest uncertainties in the velocity estimates ( $\sim 0.08 \text{ m s}^{-1}$ ).

A two-dimensional transport field was constructed by simply multiplying the absolute velocity field at each grid point by the corresponding cell area. Figure 5.8 displays the transport values within binned within portions of five distinct layers, delimited by isopycnal surfaces along which the zonally-integrated transport is zero (not shown). The total net transport across the

section is -2.8 Sv, which is in line with recent observational estimates of the Arctic outflow through Davis Strait ( $-2.3 \pm 0.7$  Sv in 2004-05, *Curry et al.* (2011)). The net transport within the overflow layer ( $\sigma_0 > 27.8$ ) is consistently small (-0.6 Sv), as no water entering the Labrador Sea from Davis Strait is presumed to flow into that layer (*Pickart and Spall*, 2007). Note that the limited extent of altimetry data on the Labrador shelf may lead to a slight underestimation of the DSO transport, and thus of the net transport. The full-depth transport field is used in the following section to provide some estimates of the horizontal and vertical circulation in the Labrador Sea during the 2000's, and for subsequent association with the A25-Ovide section.

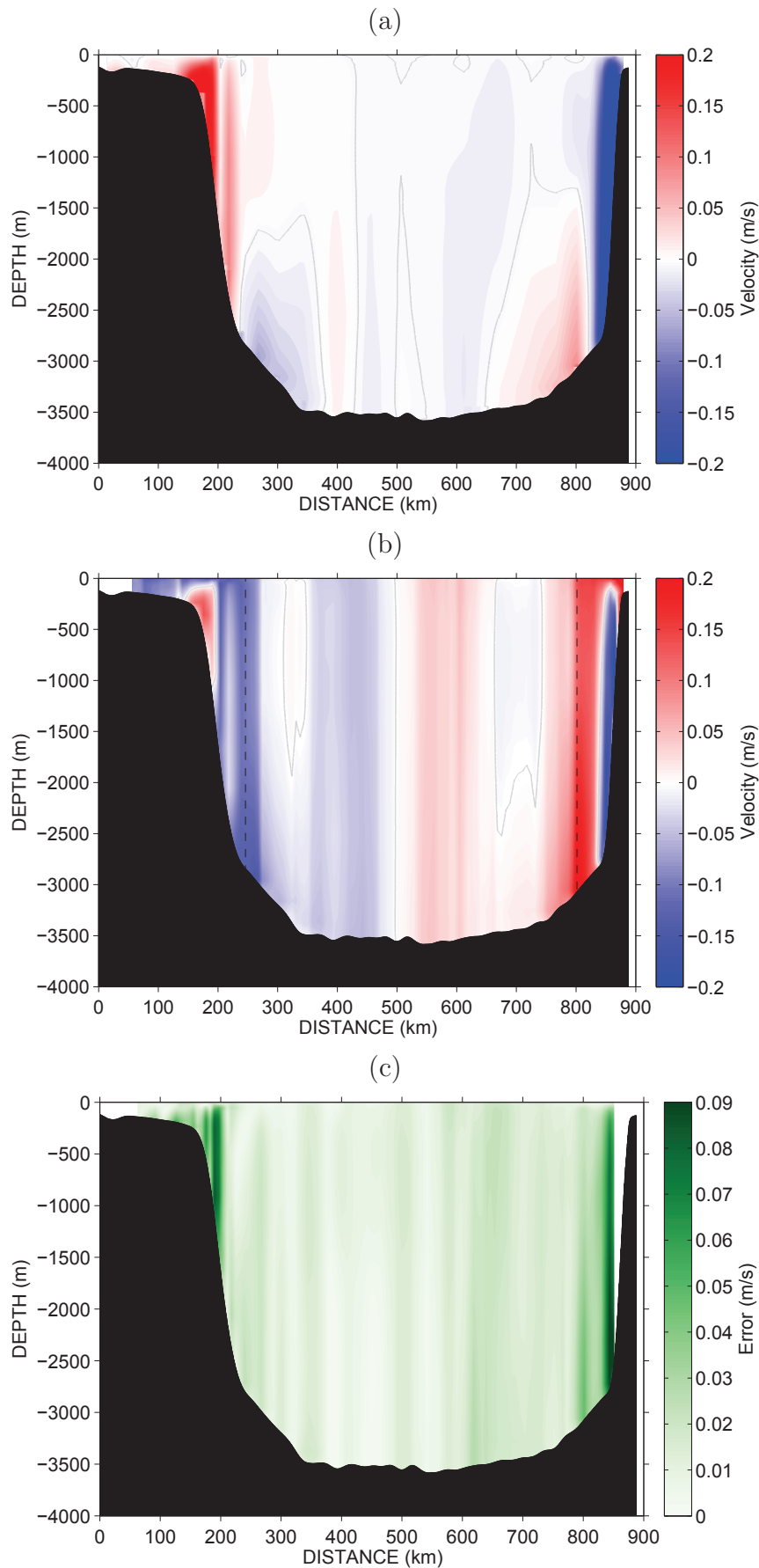


**Figure 5.6:** (a) Mean (2002-2010) summer relative velocity field referenced to the sea-surface at AR7W. (b) Mean (2002-2010) summer absolute velocity field at AR7W. (c) The associated velocity error. Units are  $\text{m s}^{-1}$ .

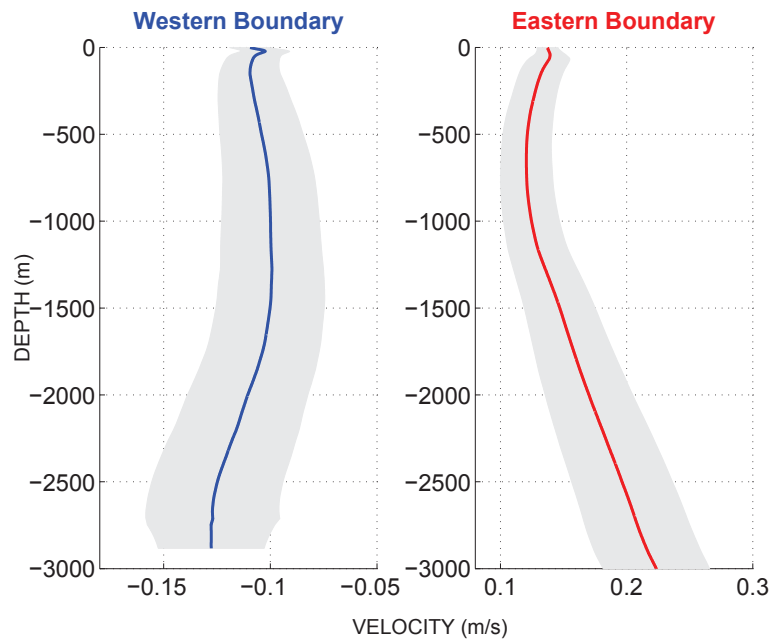


**Figure 5.7:** (a) Vertical velocity profiles ( $m s^{-1}$  in the (left) western and (right) eastern boundary current (note the different velocity scales). The gray shading indicates the associated errors. The profile position are indicated with dashed lines in Figure 5.6b.

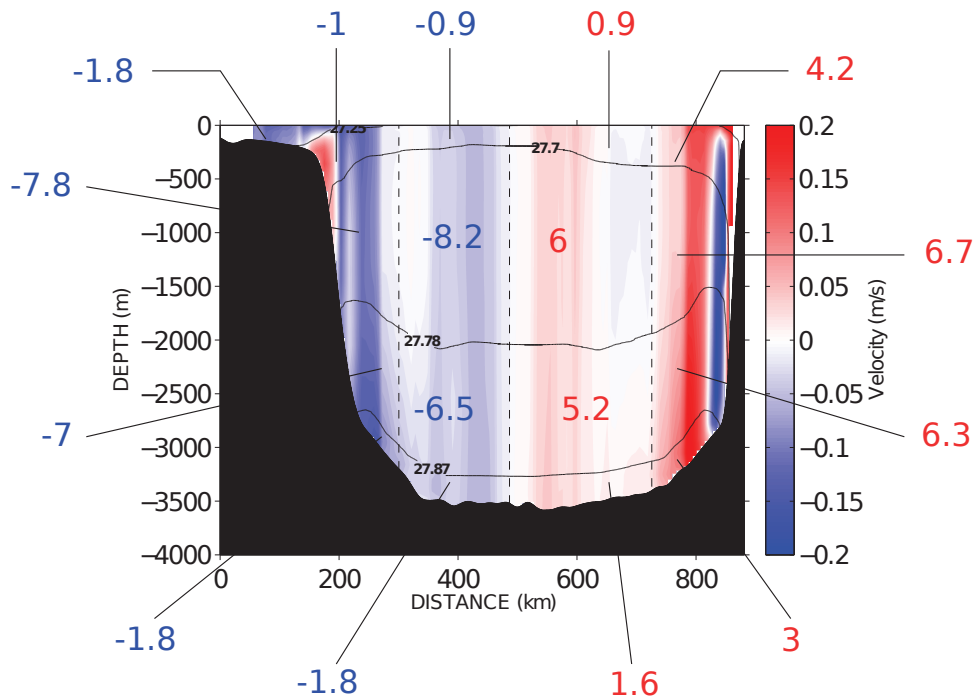


**Figure 5.8:** Spatial decomposition of the mean (2002-2010) summer absolute transport field at AR7W (values are in Sv). The black lines indicate the isopycnal surface  $\sigma_0 = 27.25$ ,  $\sigma_0 = 27.7$ ,  $\sigma_0 = 27.78$  and  $\sigma_0 = 27.87$ .

## 5.5 Merging the AR7W and A25-Ovide lines: the basin wide picture

In this section, we merge the mean temperature and velocity fields from the AR7W (Figure 5.3a and 5.6b) and A25-Ovide (Figure 1.11a and 1.11c in Chapter 1) sections to provide a basin wide mean state of the summer subpolar circulation during the 2000's. The mean and punctual merged sections of temperature, salinity and velocity are provided in appendix C. Here, we describe the structure and intensity of the horizontal and overturning cells, and quantify how they respectively contribute to the full-depth meridional heat transport. A detailed quantification of the more local components of the circulation at A25-Ovide will be separately provided by N.Daniault, and we hence mainly consider a brief overview of basin-wide integrated quantities.

### 5.5.1 Methodology applied to the Ovide data set

The Ovide cruises are concomitant with the AR7W ones (i.e. summer 2002, 2004, 2006, 2008 and 2010) and the method used for constructing mean fields of temperature and salinity is very similar to that presented above for the AR7W data set (gridding-then-averaging procedure, see red line in Figure 5.1). These fields have already been described in Chapter 1. The use of altimetric surface currents to reference the relative velocity field was, however, not conclusive (N. Daniault, personal communication). The main errors arised in the eastern portion of the section where the deepest stations were carried out (small errors in the surface current estimates reverberate over the whole water column). Instead of using surface geostrophic currents from altimetry as a reference tool, the absolute velocity field was obtained from inverse calculations. The thermal wind velocity field is combined with an *a priori* reference level velocity to provide a first guess estimate of the absolute velocity field. The following inversion consists of minimizing (in the least-squares sense) a set of constraints from independent transport estimates (i.e. ADCP measurements, conservation of mass and tracers). A detailed description of the method is provided in *Lherminier et al.* (2010) (note that I did not personally performed the inverse

calculations).

### 5.5.2 Volume transport

Figure 5.9 shows the horizontal structure of the barotropic transport cumulated from the Labrador coast along the merged AR7W/A25-Ovide line (thick black line). The barotropic transport in the Labrador Sea and in the western Irminger Sea is dominated by a prominent boundary current (36.7 Sv). Moving to the east, one can see the anticyclonic recirculation around the tip of Reykjanes ridge (13.7 Sv), a northeastward transport in the Iceland and West European Basin (40.9 Sv), and a southward recirculation in the Iberian abyssal plain (11.5 Sv). The net transport across the merged line amounts to -1.4 Sv (-2.8 Sv across AR7W and 1.4 Sv across A25-Ovide). As shown below, the isopycnal surface  $\sigma_1 = 32.17$  delimits the upper and lower limbs of the total  $\text{MOC}_\sigma$ . The transport structure within its upper limb (red line) is characterized by the northward flowing NAC, while the transport of the lower limb (blue line) is primarily carried out by the DWBC around Greenland and along the Labrador Coast. Note that Figure 5.9 does not include the Ekman transport contribution, which is largely negligible at AR7W ( $\sim 0.02$  Sv for 2002-2010) and relatively small at A25-Ovide ( $\sim -0.9$  Sv for 2002-2010).

We now focus on the shape and intensity of the zonally-integrated transport, and thereby quantify a mean state for the basin wide overturning circulation. We start by considering  $z$  as the vertical coordinate. An integration from the ocean bottom yields a maximum overturning of  $10.7 \pm 1.4$  Sv at 945 m depth across the merged section (Figure 5.10a). Here, this  $\text{MOC}_z$  estimate is representative of a net sinking or downwelling of surface waters, within the overflow from the Nordic Seas but also from entrainments of intermediate water into the DWBC. The respective contributions from the Labrador Sea and the eastern basin (Irminger, Iceland and Nordic Seas) to the total  $\text{MOC}_z$  are 2.5 Sv and 8.2 Sv, respectively. When considered individually, the  $\text{MOC}_z$  across the AR7W is slightly stronger and shallower ( $2.9 \pm 0.8$  Sv at 613 m depth), while the  $\text{MOC}_z$  at A25-Ovide reaches  $8.1 \pm 1.3$  Sv at 930 m. Overall, this

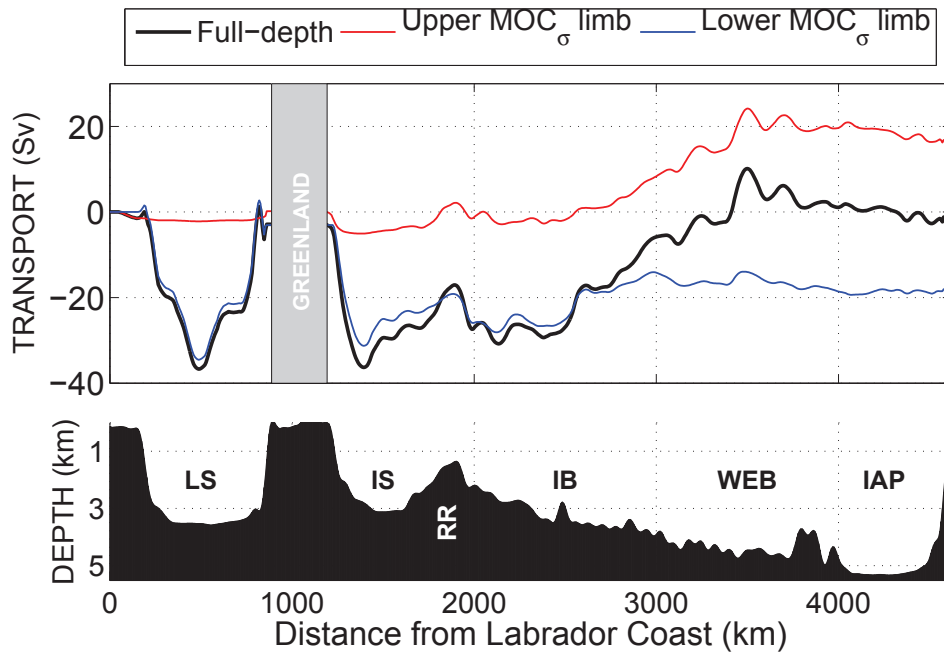


**Figure 5.9:** Full-depth integrated transport cumulated horizontally from the Labrador coast along the merged AR7W/A25-Ovide line (black). The red and blue lines show the transport distribution integrated within the upper and lower  $MOC_{\sigma}$  limbs ( $\sigma_{MOC} = 32.17$ ), respectively. The main basins and topographic features mentioned in the text are labelled as follows: LS (Labrador Sea), IS (Irminger Sea), IB (Iceland Basin), WEB (West European Basin), IAP (Iberian Abyssal Plain) and RR (Reykjanes Ridge).

decomposition shows that the global 2000's  $MOC_z$  in mid-high latitude regions is primarily associated with convection processes east of Greenland (77% of the total value).

As already discussed in the previous chapters, a  $MOC_z$  estimation in the subpolar region cannot be used as a proxy of the full water mass transformation. In the density ( $\sigma$ ) space, the total  $MOC_{\sigma}$  across the merged line amounts to  $18 \pm 1.8$  Sv with a mean  $\sigma_{MOC}$  value of  $\sigma_1 = 32.17$  (Figure 5.10b). This means that a significant fraction of the diapycnal mass flux in the whole subpolar gyre occurs in the horizontal plane ( $MOC_{\sigma} - MOC_z = 18 - 10.7 = 7.3$  Sv). The respective contributions from both sides of Greenland to the total  $MOC_{\sigma}$  are 3.1 Sv and 14.9 Sv, respectively. Taken individually, the respective  $MOC_{\sigma}$  across the AR7W and the A25-Ovide lines are  $4.7 \pm 1.3$  Sv ( $\sigma_{MOC} = 32.3$ ) and  $15.2 \pm 1.1$  Sv ( $\sigma_{MOC} = 32.14$ ). Interestingly, a deep overturning cell of 1 Sv within the overflow layer ( $\sigma_1 > 32.45$ ) is observed across AR7W, reflecting a dense-to-light conversion of overflow waters along their journey in the Labrador Sea (this deep overturning is also identifiable in the depth framework,

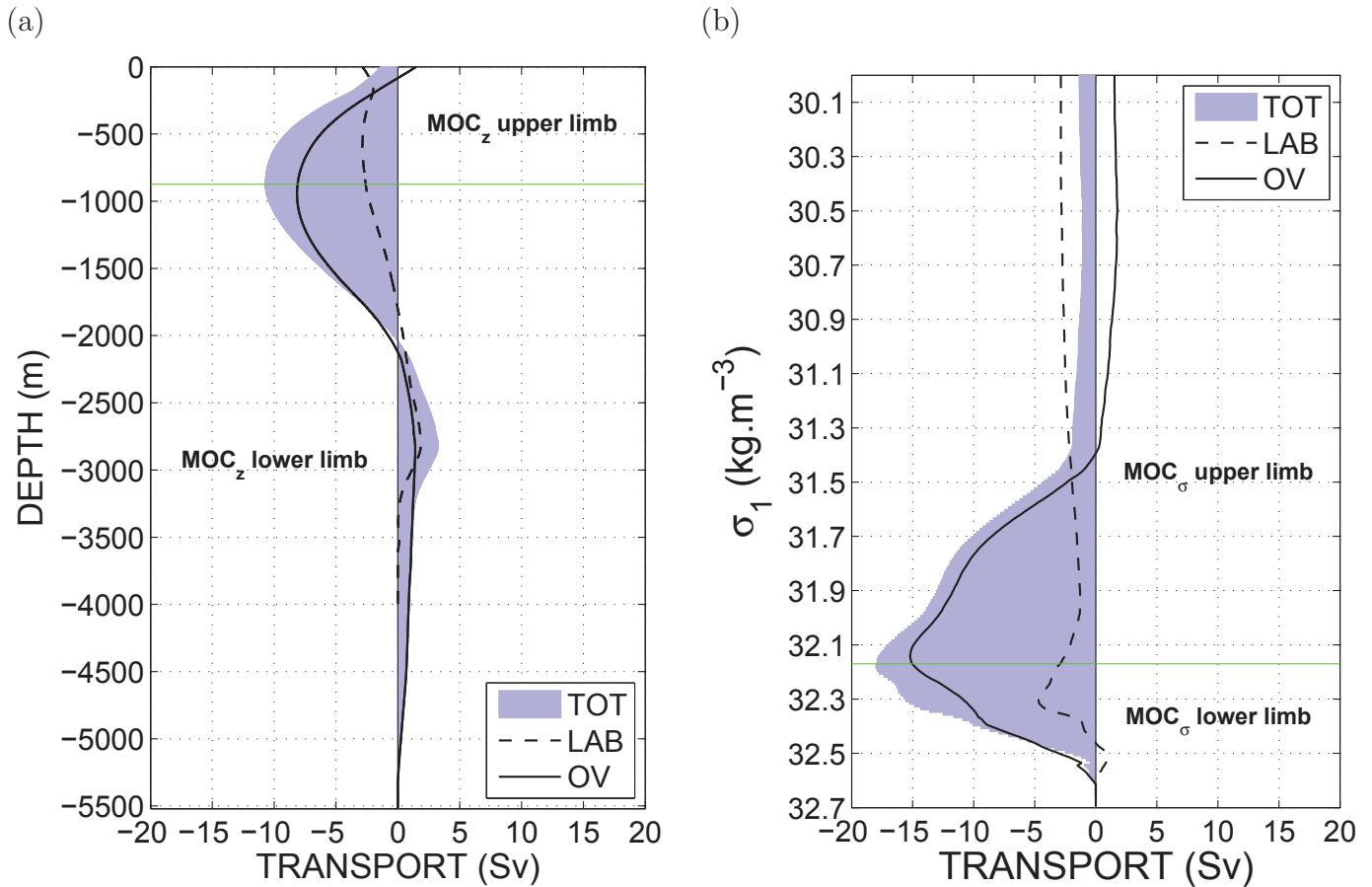


**Figure 5.10:** (a) Vertical structure of the zonally-integrated transport within  $\Delta z = 5$  m layers along the merged AR7W/A25-Ovide line (blue). The cumulated transport from the ocean bottom is shown. The same quantity computed for the individual AR7W and A25-Ovide sections is shown with a dashed and solid line, respectively. (b) Same as (a) but with  $\sigma_1$  as a vertical coordinate. In both (a) and (b), the horizontal green line indicate the vertical boundary between the upper and lower MOC limbs.

see Figure 5.10a). Overall, most of the total diapycnal mass flux associated with the formation of intermediate and dense water masses occurs east of Greenland (82% of the total value), with a presumed larger contribution from the eastern subpolar gyre, in agreement with *Sarafanov et al.* (2012).

### 5.5.3 Heat transport

By combining the mean transport and temperature fields, we here consider the magnitude of the full-depth heat transport in the subpolar gyre, and propose some common spatial decompositions of the time-mean flow contribution  $\overline{V\theta}$ . Using the five velocity/temperature fields individually, the eddy flux component of HT (i.e. the  $\overline{V'\theta'}$  term) across the merged line was estimated as 0.01 PW. Although this value should be regarded with caution due the shortness of our timeseries, its magnitude is in line with modeling results and consistent with the findings of *Hall et al.* (2004) and *Treguier et al.* (2006), who showed that eddies tend to transport heat across the mean path of the North Atlantic Current rather than along it.

As stated in chapter 4 (equation 4.3), the total HT can be partitioned into a vertical and horizontal component in the depth space, and an isopycnal and diapycnal component in the density space. These different components are quantified in Figure 5.11 for the merged section (black) and the individual AR7W (blue) and A25-Ovide (red) lines. As expected, the total HT (0.46 PW) is largely carried out in the eastern subpolar gyre (0.47 PW). It is only slightly diminished by a southward heat transport in the Labrador Sea (-0.01PW). In the depth space, the total HT is dominated by the lateral transport of the subpolar gyre (0.37 PW), while the vertical cell has a contribution of 0.14 PW. The contribution of the net volume transport amounts to -0.05 PW. In the density space, the total HT is largely associated with its diapycnal component (0.41 PW), as compared to the isopycnal contribution (0.1 PW) resulting from a temperature-salinity compensation (that is the water gets colder and fresher as it moves along the subpolar gyre boundary). Overall, the full-depth heat transport is mostly carried out east of Greenland across A25-Ovide, with relatively minor contribution from the Labrador Sea

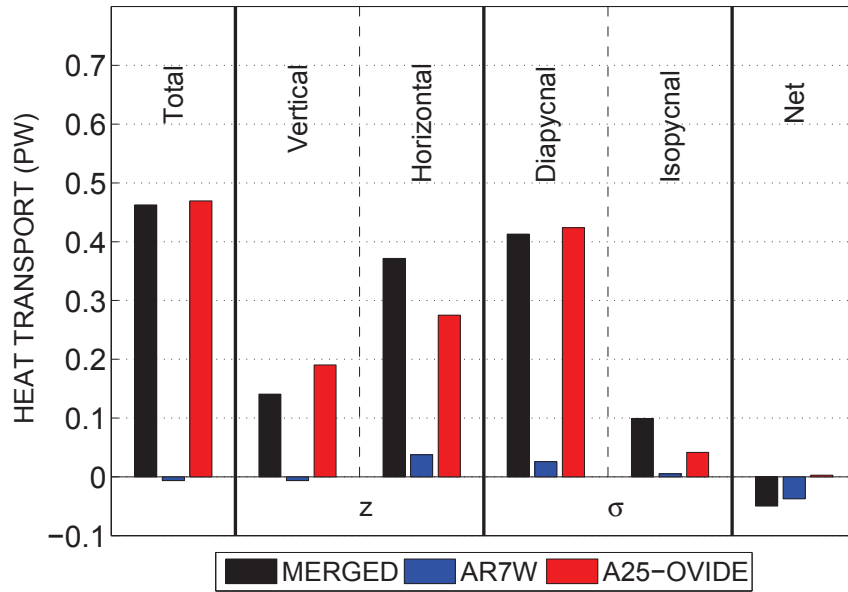


**Figure 5.11:** Decomposition of the total full-depth heat transport across the merged line (black), the AR7W line (blue) and the A25-Ovide line (red), decomposed into vertical, horizontal, isopycnal, diapycnal and net components following equation 4.3.

circulation. The Ekman component of HT for the 2002-2010 period was computed from the daily NCEP wind stress products and the averaged temperature of the 0-30 m layer. It is negligible across AR7W (0.001 PW) and relatively small at A25-Ovide (-0.05 PW).

## 5.6 A preliminary inter-comparison of the 1990's and 2000's circulation at AR7W

Applying the same gridding-then-averaging procedure for five AR7W cruises carried out in spring/summer during the early and mid-1990's (1990-92-93-94-96), and using a time-average surface geostrophic profile derived from altimetry data (1993-1996), an absolute velocity field was reconstructed. For easier comparison of both time periods, the two mean absolute velocity fields (1990's and 2000's) have been uniformly adjusted to obtain a net transport of -2 Sv across the section (the 1990's net transport is about 1 Sv northward). We note that the transport changes discussed below are not sensitive to the choice of this net transport value. This work is still at a preliminary stage, but some interesting results seem to emerge.

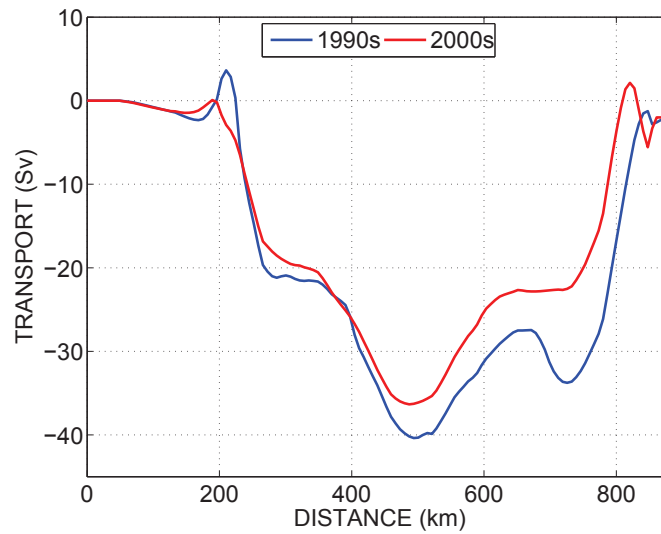


**Figure 5.12:** Horizontal structure of the vertically-integrated transport at AR7W (from the Labrador coast to Greenland) for the 1990's (blue) and the 2000's (red) mean velocity sections. Both velocity fields have been uniformly adjusted at each grid node to obtain a net transport of - 2 Sv across the section.

As expected from the results of many modeling studies (e.g. *Eden and Willebrand, 2001; Lu et al., 2007; Frankignoul et al., 2009*), the horizontal barotropic circulation was stronger in 1990's than in the 2000's (Figure 5.12). The difference between the maximums of the cumulated transports along the section for both periods amounts to 4 Sv. In agreement with the results of (*Pickart and Spall, 2007*), the anticyclonic recirculating gyre in the basin interior was stronger during the 1990's (most notably its eastern branch), whereas the (southward) flow reversal observed adjacent to the eastern boundary (see Figure 5.6b) was much weaker in the 1990's. Interestingly, our transport calculation reveals a strong (northward) flow reversal along the western boundary in the 1990's which was not present in the analysis of (*Pickart and Spall, 2007*). Note, however, that this peculiar feature is restricted to the upper few hundred meters, not entirely sampled by their float-derived reference velocity profile at 700m depth.

Of particular importance is the observed change in the overturning circulation between both periods, displayed in Figure 5.13. In the depth space, the  $MOC_z^{1990's}$  is stronger and deeper than the 2000's estimate: it amounts to 3.7 Sv at 1500m depth ( $MOC_z^{1990's} - MOC_z^{2000's} = 1.6$  Sv). In the density space, the mean  $MOC_\sigma^{1990's}$  is stronger and denser than for the 2000's time span: it reaches 7 Sv across  $\sigma_1 = 32.34$  ( $MOC_\sigma^{1990's} - MOC_\sigma^{2000's} = 3$  Sv). One can also note that

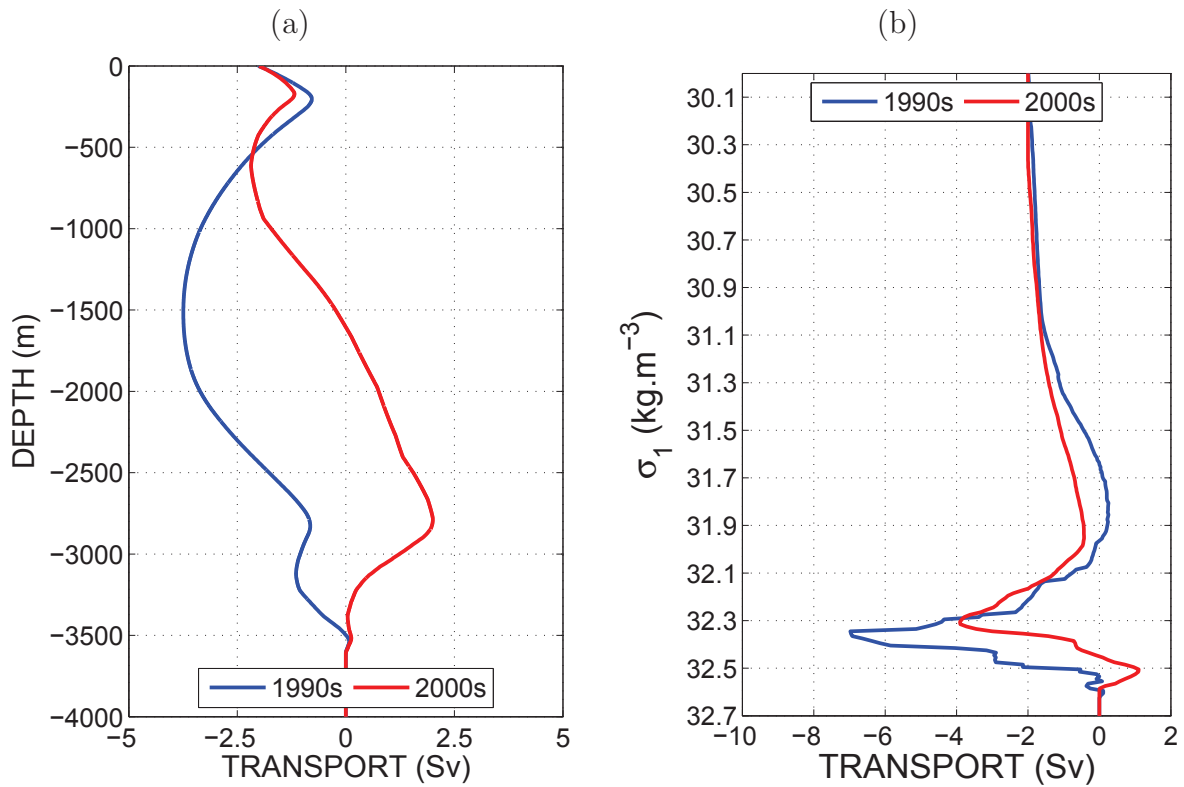


**Figure 5.13:** (a) Vertical structure of the zonally-integrated transport within  $\Delta z = 5$  m layers along AR7W from the 1990's (blue) and 2000's (red) mean velocity section. The cumulated transport from the ocean bottom is shown. (b) Same as (a) but with  $\sigma_1$  as a vertical coordinate. Both velocity fields have been adjusted uniformly adjusted at each grid node to obtain a net transport of - 2 Sv across the section.

the deep overturning ( $\sigma_1 > 32.45$ ) observed in the 2000's is not present in the 1990's estimate. Overall, these results are observational hints of an important contribution of the Labrador Sea to the basin wide MOC variability on decadal timescales, which is on the order of a few Sv in numerical model experiments (e.g. *Eden and Willebrand, 2001; Marsh et al., 2005; Böning et al., 2006*).

The  $\text{MOC}_z^{1990's}$  and  $\text{MOC}_\sigma^{1990's}$  intensities deduced from our "altimetry-derived" velocity field (3.7 Sv and 7 Sv, respectively) are curiously much stronger than the estimations of *Pickart and Spall (2007)* (1 Sv and 2 Sv, respectively). Many factors can be responsible for this potential contradiction. First, after adjusting uniformly our mean velocity field to obtain a zero mass balance (as in *Pickart and Spall (2007)*), the  $\text{MOC}_z^{1990's}$  and  $\text{MOC}_\sigma^{1990's}$  estimates decrease to 2.7 and 5 Sv, respectively. Second, we excluded the years 1997 from our computation,

that is when strong dynamic changes occurred in the subpolar gyre and most notably in the Labrador Sea (*Lu et al.*, 2007). Third, the reference velocity profiles used in both studies to derive absolute velocities do not cover the same temporal window. *Pickart and Spall* (2007) referenced their hydrographically-derived velocity field with float data at 700m depth spanning the period 1995-1999, that is a period of relatively weak atmospheric forcing in the Labrador Sea that led to a weakening of the subpolar gyre circulation (*Häkkinen and Rhines*, 2004). We here used a mean surface geostrophic profile for the 1993-1996 time span when the NAO index was relatively high and the gyre circulation in a relatively strong state. Due to the barotropic nature of the transport field at AR7W, these differences in the reference velocity profiles may explain a significant part of the maximum overturning spreading between both studies. More investigations are needed to complement these earlier findings and test their robustness against independent estimates (see perspectives in Chapter 6).

## 5.7 Conclusion

The 2000's mean hydrography and circulation along the AR7W transect in the Labrador Sea has been estimated from repeated hydrography sampling and altimetry-derived sea-surface height. Mean sections of temperature, salinity and density were computed from five oceanic surveys carried out in summer 2002, 2004, 2006, 2008 and 2010 by the *Bedford Institute of Oceanography*. The resulting *thermal wind* relative velocity field was adjusted with a time-averaged horizontal profile of surface geostrophic velocity computed from altimetry data (AVISO). A brief description of water mass characteristics and circulation of the Labrador sea was presented. The described circulation and hydrography were quantitatively consistent with previous studies. We then took advantage of concomitant oceanic surveys along the A25-Ovide transect to provide a basin wide picture of mean volume and heat transports in the subpolar gyre during the 2000's. Applying the same "altimetry" methodology for AR7W cruises carried out in the early and mid-1990's, some first results of transport changes between the two decades were described. Accordingly, we list the following conclusions:

- A basin wide mean Eulerian sinking ( $\text{MOC}_z$ ) of 10.7 Sv across 945 m was estimated along the merged AR7W/A25-Ovide line. It is primarily associated with downwelling east of Greenland (8.2 Sv), reinforcing some earlier suggestions that deep mixing in the Labrador Sea does not contribute significantly to the time-mean north Atlantic  $\text{MOC}_z$  (e.g. *Böning et al.*, 1996; *Pickart and Spall*, 2007).
- A basin wide mean transformation rate ( $\text{MOC}_\sigma$ ) of 18 Sv across  $\sigma_1 = 32.17$  was estimated along the merged line, meaning that a significant fraction of dense water production occurs in the horizontal plane. Again, a large part of the total diapycnal flux takes place in the eastern basin north of the A25-Ovide line.
- The total full-depth mean heat transport amounts to 0.46 PW, with a very minor contribution from the Labrador Sea sector. Its diapycnal component largely dominates its isopycnal counterpart, and is significantly induced by the horizontal gyre circulation (80 %) as compared to the vertical overturning cell. The eddy heat flux, as computed from our 5 snapshots, is found negligible compared to the time-mean flow contribution.
- Some preliminary analysis of a time-average absolute velocity section along AR7W during the early and mid 1990's reveal substantial changes in the horizontal and vertical circulation in recent decades. Most notably, the strength of the diapycnal overturning circulation has almost halved between the 1990's and the 2000's, in good agreement with modeling results that show a strong response of the subpolar North Atlantic to the sharp negative trend in the NAO index between the two periods.

The present analysis took benefits of multi-year data composites and the aforescribed results should be more suitable for numerical model validation than individual synoptic estimates. As already noted by *Sarafanov et al.* (2012), the combined use of repeated hydrographic surveys, Rio05 MDT and altimetry SLA seems to stand as a relatively simple and robust method to diagnose the mean full-depth circulation across a given

basin-wide section, without imposing any *a priori* constraints.

# Chapter 6

## Conclusion

The large-scale circulation of the North Atlantic Ocean is an important component of the global climatic system. Relatively warm and salty waters cool as they spread poleward through the subtropical and subpolar gyre within the North Atlantic Current (NAC), and eventually sink in localized regions of the subpolar gyre (Labrador Sea, Irminger Sea) and Nordic Seas (Greenland Sea, Norwegian Sea). The resulting dense water mass known as the North Atlantic Deep Water spread equatorward and ventilate the deep ocean on a global scale. On climate-relevant timescales, this Meridional Overturning Cell (MOC) is an important mechanism for the transfer of heat (HT) from low to high latitude regions, and the possibility of a substantial decline in the MOC intensity has consequently motivate several observational and modeling studies in recent years.

The spatio-temporal variability of the MOC occurs on a wide variety of timescales and via various physical processes, reflecting instantaneous and delayed responses of the ocean to the dominant modes of atmospheric variability. Due to the spatial and temporal sparsity of the observational record, global and regional models forced with observed reanalysis products have been alternatively used to quantify the MOC variability and investigate its causes. Through sensitivity experiments, many authors have shown the predominant role of the North Atlantic Oscillation (NAO) in driving the MOC fluctuations on interannual/decadal timescales. Those fluctuations were shown to be accompanied with substantial hydrographic changes in the North Atlantic, and most notably a sharp reversal of a freshening/cooling trend in the subpolar gyre since the mid-1990's.

During this PhD, we used one of these "realistic" simulation (the global eddy-permitting ORCA025-G70) to detail some aspects of the subpolar circulation variability and associated heat content changes during the last decades. Based on the literature review presented in Chapter 1, the model's ability to simulate a mean and anomalous large-scale circulation consistent with the available observational record was evaluated (Chapter 2). Despite some well-known slight deficiencies in simulating a consistent NAC path in the western Atlantic, the ORCA025-G70 simulation is able to fairly reproduce the mean current structure in the eastern basin, and most notably in the eastern subpolar gyre where the main NAC branches are satisfactorily represented. Furthermore, the patterns of interannual to decadal variability (dynamic and hydrography) over the whole North Atlantic are in good agreement with observational indexes of the upper circulation (e.g. *Curry and McCartney, 2001; Häkkinen and Rhines, 2004; Bersh, 2002; Thierry et al., 2008; De Boisséson et al., 2010; de Boisséson et al., 2012*), and in line with results from models of different configuration and resolution (e.g. *Marsh et al., 2005; Hátún et al., 2005; Böning et al., 2006; Biastoch et al., 2008*). Those conclusions gave credits to the analysis presented in the first part of the present manuscript (Chapter 3 and Chapter 4), which provided some complementary investigations on the MOC, HT and HC decadal variability in the eastern subpolar gyre. The A25-Ovide section joining Portugal and Greenland was used as a reference line to perform various Eulerian and Lagrangian diagnosis, with a particular fo-

cus on the NAC current system (horizontal structure, composition). In a third and somewhat independent part, an observational study was carried out to compute and analyze a full-depth velocity field along the AR7W/A25-Ovide line, joining the Labrador coast, Greenland and Portugal. Some characteristics of the basin wide MOC and HT were discussed. Also, we attempted to quantify the changes in the Labrador Sea MOC that presumably occurred since the preceding decade (*Eden and Willebrand, 2001; Marsh et al., 2005; Böning et al., 2006*). Below, we summarize the main results obtained from the modeling (Section 6.1) and observational (Section 6.2), and propose some clues for future related work.

## 6.1 Decadal variability in the eastern subpolar gyre: $\text{MOC}_\sigma$ , heat transport and heat content

### 6.1.1 Summary

In Chapter 3, we first described the mean characteristics of the  $\text{MOC}_\sigma$  across the A25-Ovide line. Density coordinates were used to better reflect water mass transformation processes occurring in high latitude regions. The mean intensity and structure of the  $\text{MOC}_\sigma$  in ORCA025-G70 agree particularly well with observational estimates (16 Sv of transformation across  $\sigma_1 = 32.1$ ). The major component of its upper limb is the NAC, which is fed by two distinct source waters: cold and fresh subpolar waters advected from the Labrador Sea by the Labrador Current, and warm and salty subtropical waters from the Gulf Stream. The Lagrangian analysis tool ARIANE provides an original way to dissociate their respective transports at A25-Ovide: 8 Sv and 15 Sv, respectively. It was shown that both source waters share similar hydrographic properties at A25-Ovide, and that their respective transport cannot be simply extracted from temperature and salinity criteria. About 70% (16 Sv) of these source waters are progressively transformed to higher density classes in the Nordic Seas (5Sv) and in the Iceland Basin and Irminger sea (11 Sv), before leaving the region via the deep western boundary current off Greenland. ARIANE enables to further elucidate the downstream pathways of the dense waters formed north of A25-

Ovide. It was shown that 4 Sv undergo a decrease in density near Flemish Cap and feed back into the eastward-flowing NAC. The remaining 12 Sv are advected equatorward and participate in the subtropical MOC. Hence the  $\text{MOC}_\sigma$  at A25-Ovide in ORCA025-G70 can be decomposed into a subpolar cell (25% of the total overturning) and a subtropical cell (75% of the total overturning).

The decadal  $\text{MOC}_\sigma$  signal simulated across the A25-Ovide section in ORCA025-G70 depicts a decreasing trend in the late 1960's and early 1970's, a gradual intensification until the mid-1990's, followed by a relatively sharp weakening until the end of the available timeseries (2004). This signal is consistent with observational proxy of the largescale circulation (e.g. *Curry and McCartney, 2001; Häkkinen and Rhines, 2004; Huck et al., 2008*) and appears robust across many hindcast simulations (e.g. *Bentsen et al., 2004; Marsh et al., 2005; Böning et al., 2006; Biastoch et al., 2008*). As already documented by others (e.g. *Curry and McCartney, 2001; Deshayes and Frankignoul, 2008*), it presumably reflects a time-integration of the NAO forcing.

The Lagrangian decomposition of the upper  $\text{MOC}_\sigma$  limb enabled to link its variability with the respective inflows of subtropical and subpolar waters within the NAC. It was shown that the decadal NAC variability is associated with synchronized transport changes of both source waters, which resulted in a relatively constant proportion of subtropical and subpolar water masses crossing the section above the main pycnocline. Two periods characterized by opposed  $\text{MOC}_\sigma$  states (weak in 1968-1978, strong in 1987-1997) were used to reveal associated changes in the horizontal structure of the NAC. During the strong  $\text{MOC}_\sigma$  phase, the northern (southern) NAC branch was found to be relatively strong (weak), while the inverse situation holds during the weak  $\text{MOC}_\sigma$  phase. According to the Lagrangian decomposition of the NAC, those changes are predominantly related to the subtropical inflow variability, suggesting potential hydrographic changes on a regional scale via mixing with the colder waters of subpolar origin. This conclusion somewhat contests previous suggestions that the buoyancy-driven subpolar gyre controls the changing structure and composition of the NAC (*Hátún et al., 2005*), and rather points out the wind-driven intergyre gyre circulation as a dominant actor (*Herbaut and Houssais, 2009*). Additionally, qualitative Lagrangian experiments revealed that periods of

expanded subtropical gyre (*Häkkinen et al.*, 2011a) generally occur during periods of weak subtropical volume transport and weak  $\text{MOC}_\sigma$  in the Northeastern Atlantic.

In Chapter 4, we investigated the origins of decadal heat content changes in the eastern subpolar gyre. Using the ORCA025-G70 simulation, regional heat budget was performed within a box bounded by the A25-Ovide section and the Greenland-Scotland sills. The model was shown to reproduce a HC signal for the 1965-2004 time span very close to observations: a strong cooling during the 1960-70's, a period of relatively minor changes in the 1980's, and a strong warming in the 1990-2000's. Those shifts in the hydrography of the eastern subpolar gyre were shown to be primarily induced by anomalous heat transport across A25-Ovide, with air-sea heat fluxes acting as a delayed, damping mechanism. While the time-averaged heat transport across A25-Ovide is carried out in almost equal amount by the horizontal and vertical circulation, its decadal variations are predominantly related to the gyre component of the circulation. A temporal decomposition of the full-depth heat transport revealed opposed impacts of the anomalous circulation acting upon the mean temperature field, and the advection of temperature anomalies by the mean circulation. The amplitude of the latter was shown to dominate on decadal timescales. A reconstruction of the heat transport signal based on a  $\text{MOC}_\sigma$  index helped in understanding this surprising anti-correlation: temperature anomalies are primarily associated with the heaves of isopycnal surfaces at A25-Ovide, which also impact the velocity-driven heat transport through large-scale changes in the pycnocline slope. By reconstructing the thermally-driven heat transport signal in ARIANE, we showed that temperature anomalies advected across A25-Ovide were significantly linked to the large scale gyre circulation, and most notably to the changing proportion of subtropical and subpolar water masses advected within the northern NAC branch, as firstly suggested in Chapter 3.

### 6.1.2 Related perspectives

As the aforedescribed results come from one simulation of a one model configuration, they should benefit from additional work to test their robustness in models of different resolution and

parametrizations, or forced with different atmospheric products. We note that some diagnosis ( $\text{MOC}_\sigma$  indexes, gyre index, Lagrangian decomposition of the NAC, ...) performed using the ORCA025-G85 simulation, which presents 75 vertical levels and is forced by more recent forcing fields, have yielded similar results. As the main deficiency of eddy-permitting model (such as ORCA025) for our purpose is the erroneous path of the NAC in the western Atlantic, it could be interesting to investigate similar questions in higher resolution simulations which were shown to considerably improve the upper ocean dynamics in this region. For instance, *Marzocchi et al.* (2012) showed that the new ORCA12 model configuration (75 vertical levels,  $\frac{1}{12}^\circ$  resolution) exhibits substantial improvements in the representation of boundary currents and mixed layers in the subpolar gyre. The performance of long interannual simulation with such global models in the near future will provide powerful tools to study the various and complex mechanisms that induce changes in the North Atlantic large scale circulation.

Chapter 3 and Chapter 4 could also be complemented through sensitivity experiments with idealized forcing fields (e.g. *Gulev et al.*, 2003; *Herbaut and Houssais*, 2009). Running our Lagrangian experiments on model simulations forced with climatological windstress (air-sea heat flux) and interannual air-sea heat flux (windstress) would inform us about the respective roles of these two forcings in driving the variability of the subtropical and subpolar gyre and their subsequent contributions to the NAC and MOC variability in the eastern subpolar gyre. While our results likely suggest a link between the decadal variability of the North Atlantic ocean (MOC, NAC structure, formation of temperature anomaly along the NAC path, etc) and the low-frequency NAO signal, the details of this atmospheric/oceanic interplay was not particularly assessed during the PhD. Interestingly, *Barrier et al.* (2012) recently highlighted the asymmetry of the horizontal oceanic response to changes in the NAO, with negative NAO phases controlling the meridional displacements of both gyres, and positive NAO phases leading to their intensification. Also, their study showed the important role of other weather regimes in driving anomalous circulation patterns in the North Atlantic. Amongst them, the Atlantic Ridge atmospheric mode (a positive phase of the East Atlantic Pattern, see *Häkkinen et al.* (2011a)) seems importantly involved in horizontal and vertical circulation changes (weakening gyres and

Ekman-induced MOC anomalies). Episodes of atmospheric blocking over the northern North Atlantic was also shown to influence the upper subpolar gyre circulation and hydrography (Häkkinen *et al.*, 2011b), as well as the MOC intensity through anomalous convection in the Labrador Sea (Barrier *et al.*, 2012). Investigating further the questions raised during this PhD in a "weather regime" perspective, instead of a "NAO only" perspective, is hence of potential interest.

As already shown in previous studies (Flatau *et al.*, 2003; Häkkinen and Rhines, 2004; Bower and von Appen, 2007; Häkkinen and Rhines, 2009), the continuous monitoring of the surface circulation by altimetry and drifting floats may provide crucial information about the subpolar gyre and NAC variability on interannual and decadal timescales. As these changes in the surface circulation may not be appropriate to study subsurface-intensified intergyre exchanges (Brambilla and Talley, 2006; Burkholder and Lozier, 2011), the increasing coverage of ARGO float measurements will provide an alternative means to study these questions. In particular, a Lagrangian tracking of ARGO floats in the subtropical and subpolar gyres could be used to investigate the changing structure and composition of the NAC current system seen in ORCA025-G70. Also, their hydrographic profiles in the vicinity of A25-Ovide may be used to observed and quantify the heave of isopycnal surfaces, which presumably stands as a key process in the  $MOC_{\sigma}$  and HT variability in the eastern subpolar gyre (Chapter 4).

## 6.2 The 2000's mean circulation along AR7W/A25-Ovide from observational datasets

### 6.2.1 Summary

In Chapter 5, we proposed an observational analysis of the 2000's time-average circulation in the subpolar gyre, based upon the computation of a mean hydrographic and velocity field along the merged AR7W and A25-Ovide line. The study started by a gross description of 2002-2010 mean hydrographic fields in the Labrador Sea, subsequently combined with altimetry-derived

surface geostrophic current to obtain an absolute full-depth velocity field along the section. Importantly, multi-year data composites of hydrographic profiles and altimetry data were used, thereby filtering out a substantial fraction of the high-frequency noise in both the density structure and the barotropic circulation. This technique, already employed by *Sarafanov et al.* (2012) at 60°N, seems to stand as a relatively simple and robust method to diagnose the mean full-depth circulation across a given basin-wide section, without imposing any *a priori* constraints.

We then took benefit of concomitant (2002-2010) mean absolute velocity and temperature fields at A25-Ovide to describe the basin-wide volume and heat fluxes across the merged line. The total Meridional Overturning Circulation (MOC) across AR7W/A25-Ovide reaches  $10.7 \pm 1.4$  in the depth ( $z$ ) space and  $18 \pm 1.8$  Sv in the density ( $\sigma$ ) space, reflecting substantial water mass transformation in the horizontal plane. The full-depth heat transport across the merged line is primarily carried out by the gyre component of the flow, and is fully captured by the diapycnal circulation. The eddy heat fluxes are presumably negligible in front of the time mean flow contribution.

Most of the  $MOC_z$  and  $MOC_\sigma$  occurred east of Greenland (77% and 82%, respectively), depicting a minor contribution of the Labrador Sea to the time-mean basin wide MOC and associated heat transport. Using the same "altimetry-hydrography" approach, a time-average full-depth circulation for the 1990-1996 time span at AR7W was estimated. Although the 1990's-2000's intercomparison is still at a preliminary stage, it already reveals substantial changes in the overturning rates in the Labrador between the two periods, with a decrease in the  $MOC_z$  and  $MOC_\sigma$  by 1.6 Sv and 3 Sv, respectively. These potential changes in the Labrador Sea MOC concur with the anomalous production of LSW: intense in the early 1990's and relatively weak in the early and mid-2000's (*Yashayaev et al.*, 2007).

## 6.2.2 Related perspectives

The aforescribed changes in the Labrador Sea circulation between the 1990's and the 2000's may suggest significant modification of the basin wide overturning circulation and associated heat transport in the North Atlantic ocean, which clearly motivate further hydrographic occupations of the AR7W line. The robustness of the hydrography-altimetry method in the Labrador Sea should, however, be further evaluated with independent data sets. Surface and subsurface profiling floats (e.g. ARGO) could be used as alternative tools for referencing the hydrography-derived relative velocity field. Applying inverse methods (as the one used for the A25-Ovide line) at AR7W could also give confidence in our results. Comparisons between our results and the upcoming study of *Hall et al.* based on LADCP analysis in the 2000's is of great interest.

As the A25-Ovide section was not continuously sampled during the 1990's, repeated hydrographic profiles carried out along the A1E section joining Greenland and Ireland (*Bersh, 2002*) could be alternatively used to provide a time-average picture of the full-depth circulation on both side of Greenland during that period. Subsequent comparison with our 2000's mean section should yield an original view of decadal changes in MOC and HT across the whole zonal extent of the subpolar gyre from the late 20<sup>th</sup> to the early 21<sup>st</sup> century.

---

Although there are no doubts that Atlantic waters undergo a vigorous meridional overturn, the three-dimensional pathways of the surface and deep limbs of the overturning are still poorly known, as are the dominant forcing mechanisms driving their spatio-temporal variability. While both observations and ocean models have revealed substantial changes in the MOC strength during the last few decades, these estimations are still associated with large uncertainties, and a direct influence of MOC changes on global and regional climate is largely uncertain. These are

reasons for further development of basin wide and full-depth monitoring arrays in the Atlantic sector. The continuous RAPID monitoring system at 26°N and the increasing measurements of ARGO drifting floats are important steps toward such achievement. Further development in ocean modeling (OGCM, assimilation systems, coupled climate models) is also crucial to reinforce our knowledge of the MOC dynamics and unravel its past variability on relatively long timescales for better climate predictability.

# Chapter 7

## Appendix

### 7.1 Appendix A: Alphabetic list of acronyms

AABW	Antarctic Bottom Water
ADT	Absolute Dynamic Topography
CGFZ	Charlie Gibbs Fracture Zone
DSOW	Denmark Strait Overflow Water
DWBC	Deep Western Boundary Current
ECMWF	European Centre for Medium-Range Weather Forecasts
ENACW	Eastern North Atlantic Central Water

$EXP_{BACK}$	The quantitative Lagrangian experiment used to describe the northward component of the $MOC_{UPPER}$ transport
$EXP_{FOR}$	The quantitative Lagrangian experiment used to describe the southward component of the $MOC_{UPPER}$ transport
GIS	Greenland-Iceland-Scotland sills
$HT_{A25}$	Heat transport intensity across A25-Ovide
$HT_{GIS}$	Heat transport intensity across the Greenland-Scotland sills
$HT_v$	Velocity-driven component of $HT_{A25}$
$HT_{approx}$	Approximation of $HT_{A25}$ from the intensity of the $MOC_{\sigma}$ and the temperature difference between its upper and lower limb
$HT_{\theta}$	Thermally-driven component of $HT_{A25}$
$HT_{\theta}^{Lag}$	Thermally-driven component of $HT_{A25}$ reconstructed in the Lagrangian framework
$HT_{VERT}$	Vertical component of the heat transport
$HT_{HOR}$	Horizontal component of the heat transport
$HT_{NET}$	Net component of the heat transport
$HT_{DIA}$	Diapycnal component of the heat transport
$HT_{ISO}$	Isopycnal component of the heat transport
IB	Iceland Basin
IC	Irminger Current
IS	Irminger Sea
ISOW	Iceland Scotland Overflow Water
LC	Labrador Current
LS	Labrador Sea
LWS	Labrador Sea Water
MAR	Mid-Atlantic Ridge
MDT	Mean Dynamic Topography

MHT	Meridional Heat Transport
$MOC_Z$	Meridional Overturning circulation in the depth space
$MOC_\sigma$	Meridional Overturning circulation in the density space
$MOC_{UPPER}$	Upper limb of $MOC_\sigma$
$MOC_{LOWER}$	Lower limb of $MOC_\sigma$
MW	Mediterranean Water
NAC	North Atlantic Current
NAO	North Atlantic Oscillation
NF	Newfoundland
$\psi_{BT}$	Barotropic Streamfunction
RR	Reykjanes Ridge
RT	Rockall Trough
SAIW	Subarctic Intermediate Water
SLA	Sea-level anomaly
SPG	Subpolar Gyre
SPMW	Subpolar Mode Water
SPF	Subpolar Front
STG	Subtropical Gyre
SSH	Sea-surface height
SST	Sea-surface temperature
$\sigma_{MOC}$	The isopycnal surface delimiting the upper and lower limbs of the $MOC_\sigma$
THC	Thermohaline Circulation (buoyancy-driven)
$T_{EGC}$	the East Greenland Current component of the upper $MOC_\sigma$ limb from the Lagrangian Experiment $EXP_{FOR}$
$T_{REC}$	Southward recirculation within the upper $MOC_\sigma$ limb in the Iberian Abyssal Plain, from the Lagrangian Experiment $EXP_{FOR}$

$T_{SPG}$	Subpolar transport component of the upper $MOC_{\sigma}$ limb from the Lagrangian Experiment $EXP_{BACK}$
$T_{STG}$	Subtropical transport component of the upper $MOC_{\sigma}$ limb from the Lagrangian Experiment $EXP_{BACK}$
$\theta_{A25}$	Two-dimensional binned temperature field at A25-Ovide deduced from the Lagrangian Experiment $EXP_{BACK}$
$\theta_{West}$	Two-dimensional binned temperature field "at A25-Ovide" deduced from the Lagrangian Experiment $EXP_{BACK}$ , using the particle temperature in the source regions (subtropics and Labrador Sea)
$U_{NET}$	The net (full-depth) transport across A25-Ovide
WOA09	World Ocean Atlas 2009
WGC	West Greenland Current

## 7.2 Appendix B: Merged fields of temperature, salinity and velocity along the AR7W/A25-Ovide line

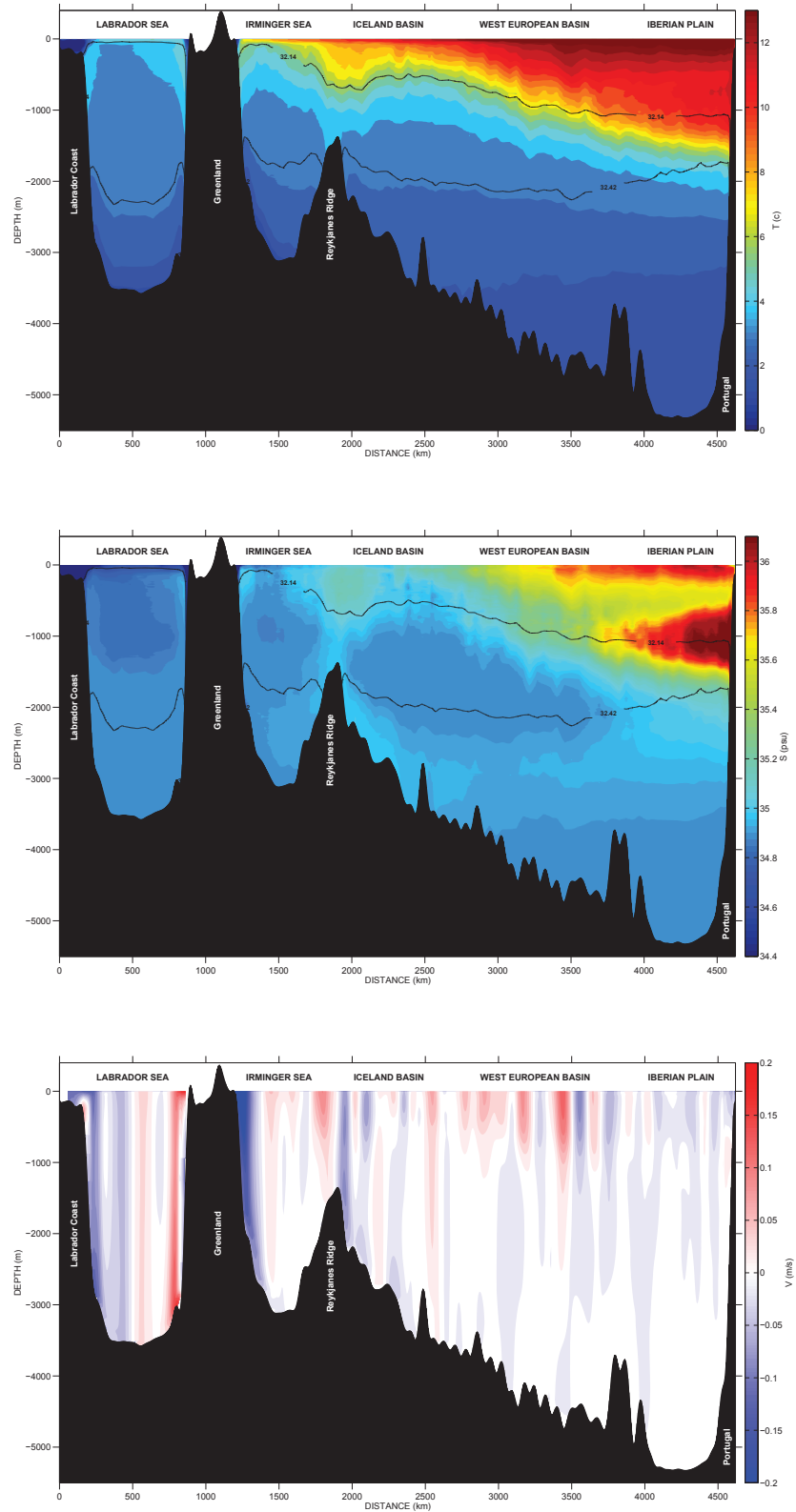


**Figure 7.1:** Mean summer sections of (top) temperature, (middle) salinity and (bottom) velocity along the merged AR7W/A25-Ovide for the 2002-2010 period. The isopycnal layer  $\sigma_1 = 32.14$ ,  $\sigma_1 = 32.42$  and  $\sigma_1 = 32.54$  are shown.

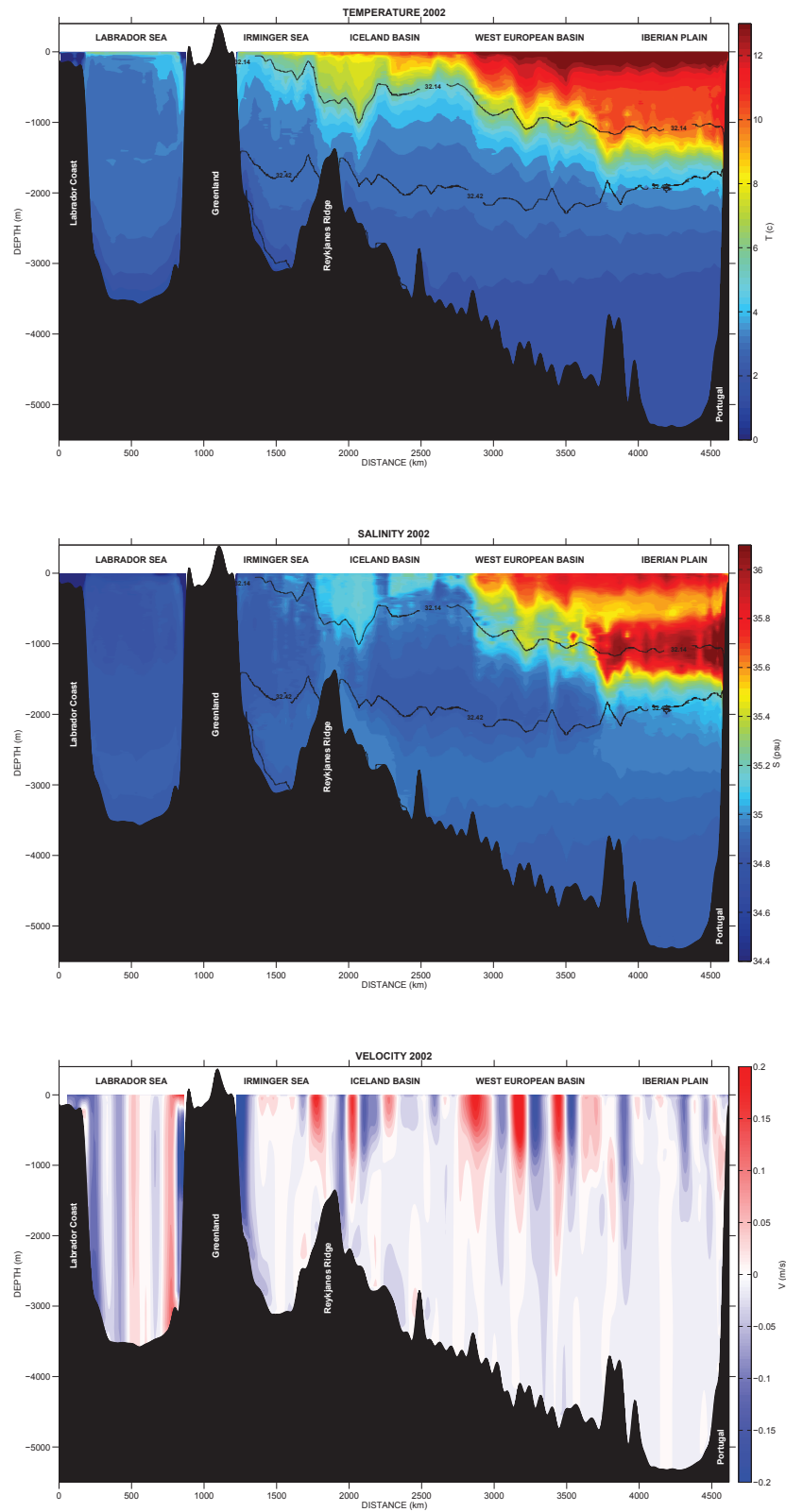


**Figure 7.2:** Sections of (top) temperature, (middle) salinity and (bottom) velocity along the merged AR7W/A25-Ovide line in summer 2002. The isopycnal layer  $\sigma_1 = 32.14$ ,  $\sigma_1 = 32.42$  and  $\sigma_1 = 32.54$  are shown.

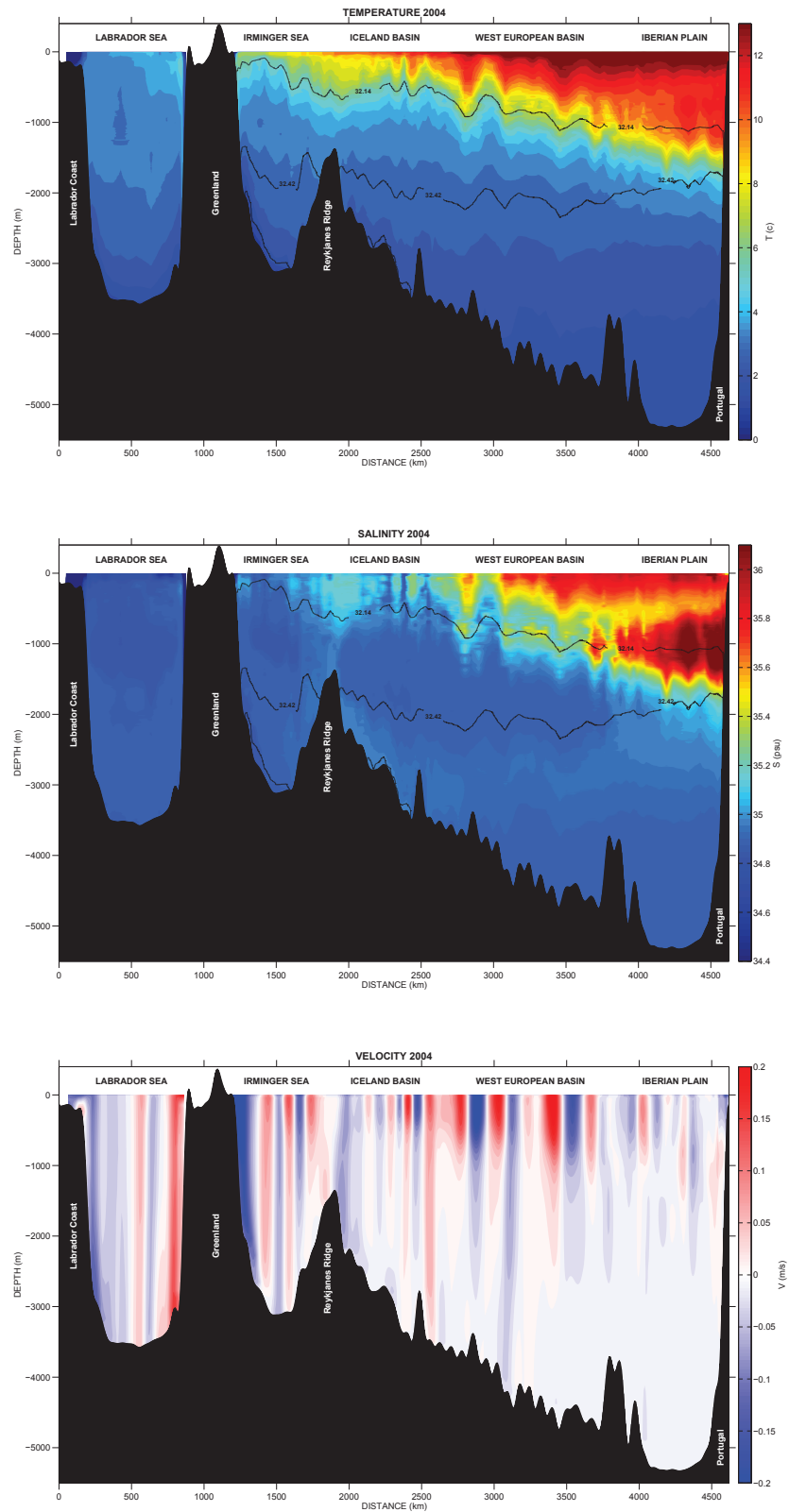


Figure 7.3: *idem* for 2004.

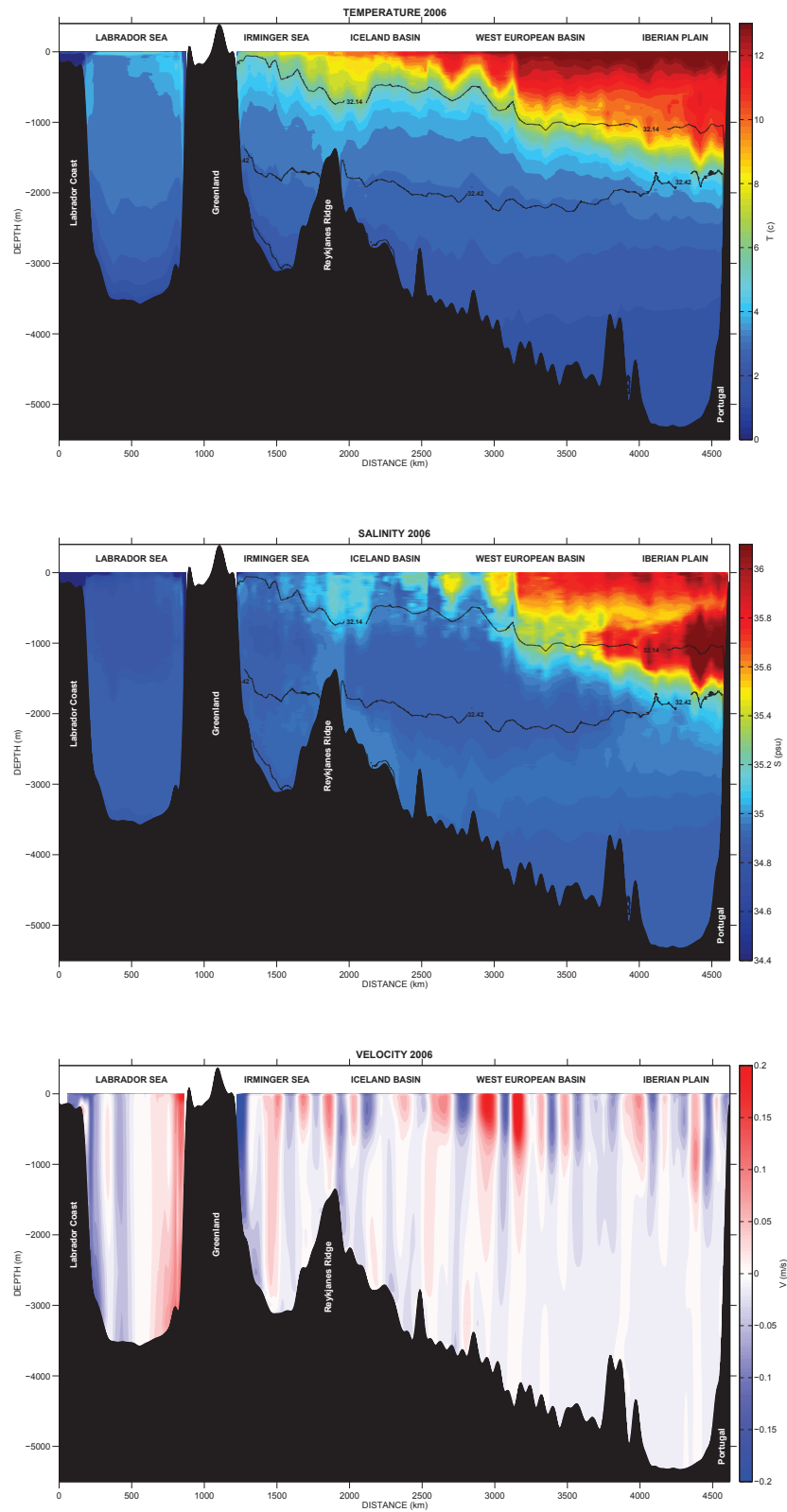


Figure 7.4: *idem* for 2006.

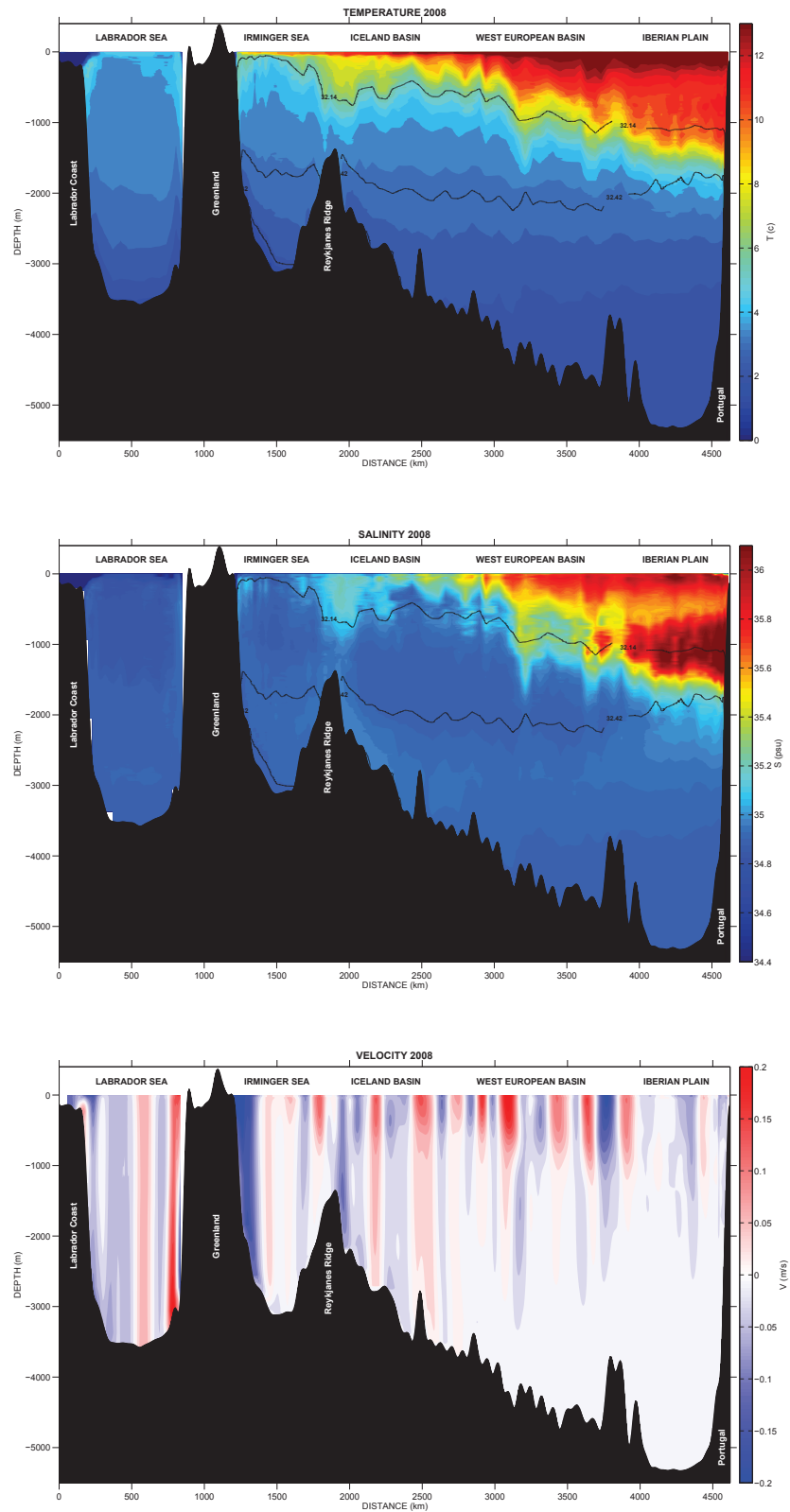


Figure 7.5: *idem* for 2008.

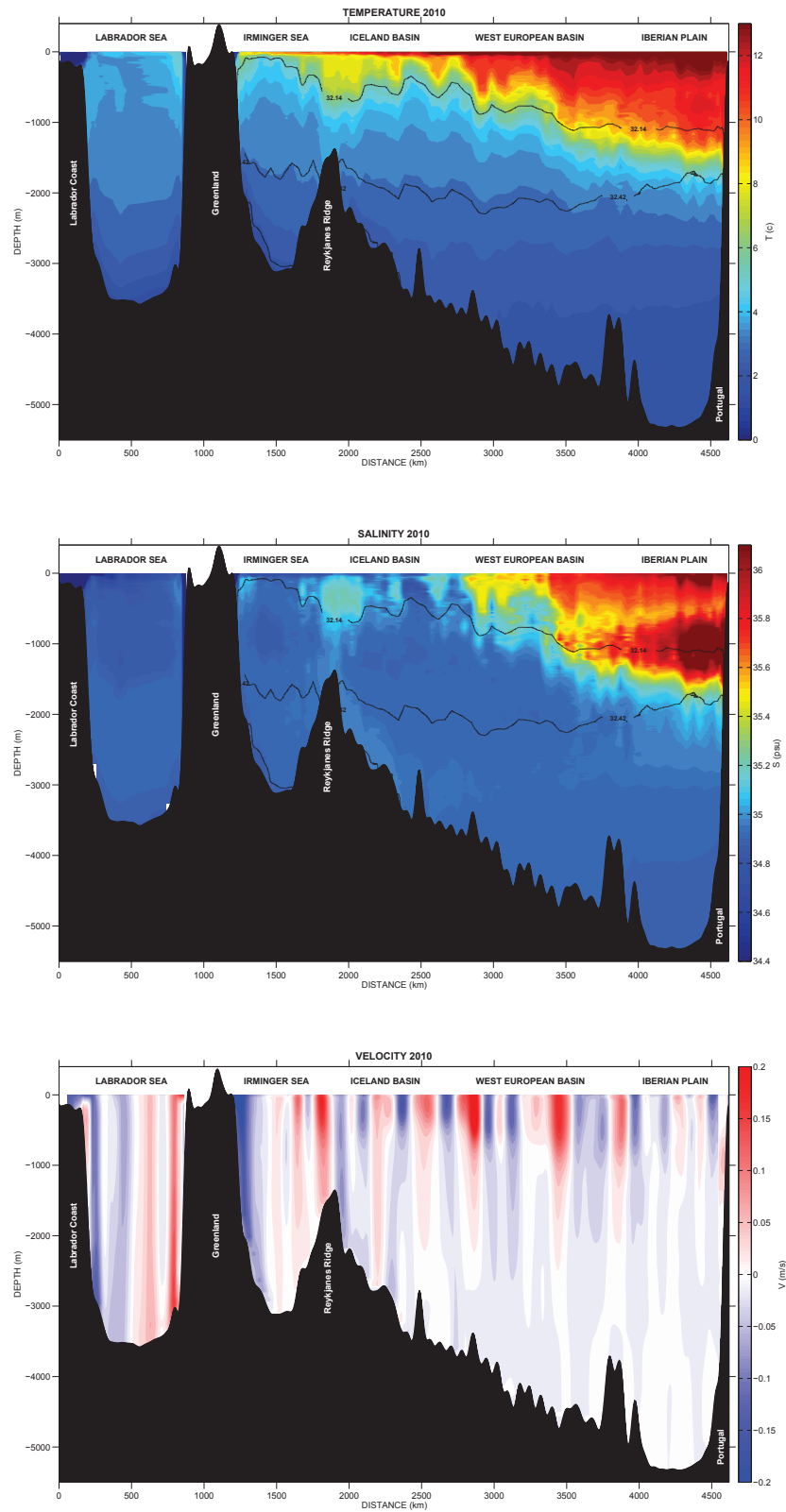


Figure 7.6: *idem* for 2010.

## 7.3 Appendix C: Chapter summaries in French

### 7.3.1 Chapitre 3: La variabilité décennale de la $MOC_{\sigma}$ à travers la section A25-Ovide

La variabilité décennale de la circulation méridienne de retournement (MOC) à travers la section A25-Ovide est étudiée à l'aide de la simulation numérique ORCA025-G70 pour la période 1965-2004. La pertinence de cette simulation pour une telle étude a été démontrée au Chapitre 2 via de nombreuses comparaisons avec les jeu de données disponibles et la littérature présentée au Chapitre 1. Malgré quelques déficiences du modèle dans le bassin Atlantique Ouest (Figure 2.2), la structure moyenne du système "Courant Nord Atlantique (NAC)" au dessus de la dorsale médio-Atlantique (MAR) et dans l'Est du gyre subpolaire (*Bower et al., 2002; Reverdin et al., 2003*), ainsi que les grands signaux de variabilité observés en Atlantique Nord (*Curry and McCartney, 2001; Bersh, 2002; Häkkinen and Rhines, 2004*) sont reproduits de façon cohérente dans ORCA025-G70 (Figures 2.10, 2.11 et 2.12).

La MOC à travers A25-Ovide est calculée en coordonnées densité ( $\sigma_1$ ), une méthode plus propice à l'évaluation des changements de transformation des masses d'eau dans les régions subpolaires. La structure moyenne de la  $MOC_{\sigma}$  à A25-Ovide dans ORCA025-G70 est très similaire à celle issue d'observations (*Lherminier et al., 2010*), avec un maximum de 16 Sv à  $\sigma_1 = 32.1$  (Figure 3.2a). Les structures horizontales de ses deux branches sont également cohérentes avec l'analyse de données (Figure 3.2b). On se focalise ici sur la branche haute ( $MOC_{UPPER}$ ), composée de la partie haute du courant Est Groenlandais (EGC, 3 Sv vers le Sud), du NAC (23 Sv vers le Nord) et d'une recirculation anticyclonique dans la plaine abyssal ibérique (REC, 3 Sv vers le sud). L'outil d'analyse Lagrangienne ARIANE permet de décomposer le transport du NAC en une composante subtropical ( $T_{STG}$ , 15 Sv) et une composante subpolaire ( $T_{SPG}$ , 8 Sv) (Figure 3.3ab). La distribution horizontale de  $T_{STG}$  et  $T_{SPG}$  le long de A25-Ovide indique qu'ils ne peuvent pas être simplement dissocier à l'aide de critères hydrographiques (*Hátún et al., 2005*). En fait,  $\sim 50\%$  des masses d'eau relativement froide et peu salée advectée dans

le bassin d'Islande proviennent des subtropiques (Figure 3.4a). Une décomposition détaillée de  $T_{SPG}$  permet de mettre en évidence deux cellules de retournement distinctes à A25-Ovide: une cellule subtropicale connectant les hautes et basses latitudes (12 Sv), et une cellule interne au gyre subpolaire (4 Sv). En d'autres termes, une fraction des eaux denses formée au nord de A25-Ovide et transportée vers le sud par le courant profond de bord ouest est réinjectée dans le NAC via des processus de mélange avec les eaux chaudes d'origine subtropicale aux alentours de Flemish Cap (Figure 3.5 et 3.6).

La variabilité décennale de la  $MOC_{\sigma}$  à A25-Ovide est caractérisée par un ralentissement jusqu'à la fin des années 60's (2.5 Sv) suivi d'une intensification graduelle (4 Sv) et d'un ralentissement abrupt entre 1995 et 2004 (3.6 Sv) (Figure 3.7). A l'aide d'ARIANE, on montre que ce signal de variabilité est associé à des changements synchronisés des apports subtropical et subpolaire dans le NAC (Figure 3.10).  $T_{STG}$  et  $T_{SPG}$  présentent en effet des comportements proches sur des échelles de temps décennales, et la proportion de masses d'eau subtropicale et subpolaire advectée par  $MOC_{UPPER}$  reste globalement constante ( $\sim 65/35$ , Figure 3.11). Les changements basse-fréquence de l'intensité de la  $MOC_{\sigma}$  à A25-Ovide sont ensuite reliés aux modifications de la structure horizontale du NAC. Lorsque la  $MOC_{\sigma}$  est dans une phase intense (1987-1997), la branche nord (sud) du NAC présente un transport relativement fort (faible) (Figure 3.8a). Inversement, lorsque la  $MOC_{\sigma}$  est dans une phase faible (1968-1978), le transport dans le bassin d'Islande (Rockall Trough) est relativement faible (fort). Contrairement aux suggestions de *Hátún et al.* (2005), nos expériences Lagrangiennes indiquent que la variabilité du gyre subpolaire ( $T_{SPG}$ ) n'est pas la cause principale de ces anomalies de transport sur le plan horizontal, qui sont en grande partie induites par la variabilité spatiale de  $T_{STG}$  (Figure 3.8b).

Des études récentes ont montré des changements importants dans la pénétration des masses d'eau subtropicales vers l'Est du gyre subpolaire (*Häkkinen and Rhines, 2009; Häkkinen et al., 2011a*). La fin des années 60's, le début des années 80's et le début des années 2000's furent en effet marqués par une avancé accentuée des masses d'eau "Gulf Stream" vers le Rockall Trough. Ici, cet index de "pénétration" des eaux subtropicales est reproduit de façon cohérente à l'aide

d'ARIANE, et comparé à l'index de transport  $T_{STG}$ . On montre que les épisodes de pénétration accentuée de masses d'eau subtropicales vers l'Atlantique nord-est sont généralement associés à des circulations de retournement faibles à travers A25-Ovide (Figure 3.12).

### 7.3.2 Chapitre 4: La variabilité décennale du contenu de chaleur dans l'Est du gyre subpolaire

La variabilité basse-fréquence du contenu de chaleur (HC) dans la partie Est du gyre subpolaire est étudiée dans la simulation ORCA025-G70 pour la période 1965-2004. La région d'étude est délimitée par la section A25-Ovide au sud et les seuils Groenland-Ecosse au nord, englobant ainsi la mer d'Irminger, le bassin d'Islande, le bassin Ouest Européen et la plaine abyssale Ibérique. La série temporelle des anomalies annuelles de HC calculées dans le modèle s'avère très proche du signal observé (WOA09) (Figure 4.2). Elle révèle deux périodes de changements significatifs dans les premières centaines de mètres de la colonne d'eau: un fort refroidissement pendant les 1960's et le début des années 1970's et un fort réchauffement pendant les 1990's et le début des années 2000's. Un bilan de chaleur dans notre domaine d'étude montre le rôle prédominant joué par le transport de chaleur à A25-Ovide ( $HT_{A25}$ ) dans la variabilité décennale de HC (Figure 4.3). L'impact des flux de chaleur air-mer s'illustre par une atténuation différée (2-3 ans) des grandes tendances observées. La suite de l'étude est consacrée à une description détaillée de  $HT_{A25}$ , via des décompositions spatiales et temporelles du signal et d'une analyse Lagrangienne de la variabilité.

Le transport de chaleur surface-fond moyen à travers A25-Ovide ( $\sim 0.4$  PW) est effectué dans des proportions similaires par la circulation verticale (i.e. la  $MOC_z$ ) et la circulation horizontale (i.e. les gyres) (Figure 4.6). Cependant, sa variabilité décennale qui décrit une tendance positive entre la fin des années 1960's et le milieu des années 1990's est principalement régie par la composante horizontal de la circulation. En outre, la variabilité du transport de chaleur total est globalement capturée par un index de la MOC en coordonnées densité. Les impacts respectifs des anomalies de vitesse se projetant sur le champ de température moyen

( $HT_\theta$ ), et de l'advection d'anomalies de température par la circulation moyenne ( $HT_v$ ) sont ensuite quantifiés. Curieusement, les anomalies de  $HT_{A25}$  résultent d'une forte opposition entre  $HT_\theta$  et  $HT_v$ , les deux signaux étant significativement anti-corrélés sur des échelles de temps inter-annuelle à décennale (Figure 4.7). Leurs distributions horizontales le long de A25-Ovide dénotent une transition entre deux états océanique distincts: un NAC relativement froid et sud en [1965-1985] et un NAC chaud et nord en [1985-2004] (Figure 4.8). Les deux signaux ( $HT_\theta$  et  $HT_v$ ) lag les fluctuations de l'index NAO de 5-6 années (Figure 4.10).

Afin d'appréhender d'avantage l'origine de la variabilité décrite par  $HT_\theta$  et  $HT_v$ , le transport de chaleur total est approximé via un index de la  $MOC_\sigma$  et un index de la différence de température entre ses deux branches. Ce dernier, qui décrit principalement des changements de température de la branche haute de la  $MOC_\sigma$ , joue un rôle relativement faible (mais non-négligeable) dans la variabilité de  $HT_{A25}$  qui est principalement régie par des changements d'intensité de la  $MOC_\sigma$  (Figure 4.12). En accord avec la précédente décomposition de  $HT_{A25}$  suggérant un impact important des anomalies de température advectées par la circulation moyenne sur la variabilité de  $HT_{A25}$ , la variabilité de la  $MOC_\sigma$  reflètent principalement des perturbations grande échelle de la stratification (i.e. des déplacements verticaux d'isopycnes). Le "heaving" des isopycnes à A25-Ovide affecte à la fois la composante "température" ( $HT_v$ ) et la composante "vitesse" ( $HT_\theta$ ) du transport de chaleur. Par exemple, un approfondissement de la pycnoline principale dans le bassin d'Islande produit des anomalies positives de  $HT_\theta$ , mais également des anomalies négatives de  $HT_v$  via une réduction de la pente de la pycnoline principale. Ce mécanisme est potentiellement à l'origine de l'anti-corrélation entre deux signaux préalablement révélée (Figure 4.15).

La composante température de  $HT_{A25}$  est reconstruite à l'aide de l'outil d'analyse Lagrangienne ARIANE (Figure 4.20), qui fournit des informations originales sur les propriétés hydrographiques des masses d'eau alimentant la branche haute de la  $MOC_\sigma$ : l'apport subpolaire en provenance de la mer du Labrador et l'apport subtropical en provenance du Gulf Stream. Sur des échelles de temps décennales, le mécanisme prédominant régissant la formation d'anomalies de température est associé à des changements de proportions de ces deux eaux sources dans le

NAC (Figure 4.24). Par exemple, la forte intensification de  $HT_\theta$  entre le début des années 70's et la fin des années 90's est concomitante à une augmentation de la proportion de masses d'eau subtropicales à l'intérieur de la branche nord du NAC (Figure 4.23). On note tout de même que la variabilité des flux air-mer dans les deux régions sources (Figure 4.22) et le long du trajet du NAC (Figure 4.21) contribue également à la formation d'anomalies de température, mais n'en est pas le principal responsable. Bien que nos résultats suggèrent un lien entre les changements de composition du NAC révélé par ARIANE et les déplacements verticaux d'isopycnes à A25-Ovide, nous ne pouvons actuellement que mentionner la concomitance de ces signaux.

### 7.3.3 Chapitre 5: La circulation moyenne observée le long de la section AR7W/A25-Ovide

Une circulation moyenne (2002-2010) surface-fond est estimée le long de la section AR7W en mer du Labrador suivant la méthode décrite par *Sarafanov et al.* (2012), qui consiste en une combinaison de mesures hydrographiques répétées et de mesures altimétriques de hauteurs de mer. Des sections moyennes de température, salinité et densité sont construites depuis cinq campagnes océanographiques menées par l'Institut Océanographique de Bedford en été 2002, 2004, 2006, 2008 et 2010 (Figure 5.3). Le champ de vitesse relatif calculé via la relation du vent thermique (Figure 5.6a) est ensuite ajusté avec un profil horizontal moyen de vitesses géostrophiques de surface obtenu depuis l'altimétrie satellitaire (AVISO) et la topographie dynamique moyenne de *Rio and Hernandez* (2004) (Figure 5.5). Le champ de vitesse absolu présente une structure principalement barotrope caractérisée par une circulation de bord cyclonique intense, des cellules de recirculation dans l'intérieur du bassin, ainsi que d'importants renversements de courants le long des bords Est et Ouest (Figure 5.6b). Le champ de vitesses absolues à AR7W est finalement combiné à un champ moyen (concomitant) de vitesse calculé par méthode inverse (*Lherminier et al.*, 2010) le long de la section A25-Ovide joignant le Groenland au Portugal, permettant ainsi une quantification de la MOC et du transport de chaleur moyen à l'échelle du bassin subpolaire pendant les 2000's.

Le maximum de la circulation de retournement moyenne calculée à travers la section commune AR7W/A25-Ovide est de  $10.7 \pm 1.4$  Sv en coordonnée profondeur ( $MOC_z$ ) et de  $18 \pm 1.8$  Sv en coordonnées densité ( $MOC_\sigma$ ) (Figure 5.10). Ceci montre qu'une fraction importante de la transformation des masses d'eau dans le gyre subpolaire s'effectue dans le plan horizontal. Le transport de chaleur total le long de la section commune s'élève à 0.46 PW (Figure 5.11). La composante diapycnale domine largement la composante isopycnale, et reflète une contribution importante de la circulation horizontale de gyre au dépend de la circulation verticale de retournement. La contribution des flux de chaleur tourbillonnaires est approximée via les cinq sections individuelles à 0.01 PW. Elle demeure donc largement négligeable devant la contribution de l'écoulement moyen, en accord avec des résultats issues de simulations numériques (*Treguier et al.*, 2006; *Pickart and Spall*, 2007).

Les circulations de retournement verticale ( $MOC_z$ ) et diapycnale ( $MOC_\sigma$ ) moyennes estimées à travers la section commune AR7W/A25-Ovide s'effectuent majoritairement à l'Est du Groenland (77% and 82%, respectivement), renforçant certaines suggestions d'une contribution faible de la mer du Labrador à la MOC totale moyenne en Atlantique Nord (e.g. *Böning et al.*, 1996; *Pickart and Spall*, 2007). Cependant, des résultats préliminaires suggèrent des changements importants de la circulation en mer du Labrador durant les dernières décennies. A travers une analyse similaire (hydrographie + altimétrie) portant sur des données récoltées le long de AR7W pendant les années 1990's, on peut en effet montrer un ralentissement de la  $MOC_z$  (-1.6 Sv) et de la  $MOC_\sigma$  (-3 Sv) entre les deux périodes (Figure 5.13), en cohérence avec la transition de l'index NAO d'une phase fortement positive (début des années 1990's) vers une phase relativement neutre (les années 2000's).

# Bibliography

- Bacon, S. (1998), Decadal variability in the outflow from the Nordic Seas to the deep Atlantic Ocean, *Nature*, *394*, 871–874, doi:10.1038/29736.
- Bacon, S., G. Reverdin, I. G. Rigor, and H. M. Snaith (2002), A freshwater jet on the east Greenland Shelf, *Journal of Geophysical Research*, *107*(3068), doi:10.1029/2001JC000935.
- Baehr, J., J. Hirschi, J.-O. Beismann, and J. Marotzke (2004), Monitoring the meridional overturning circulation in the North Atlantic: A model-based array design study, *Journal of Marine Research*, *62*(3), 283–312, doi:10.1357/0022240041446191.
- Barnier, B., G. Madec, T. Penduff, J.-M. Molines, A.-M. Tréguier, J. L. Sommer, A. Beckmann, A. Biastoch, C. Böning, J. Dengg, C. Derval, E. Durand, S. Gulev, E. Remy, C. Talandier, S. Theetten, M. Maltrud, J. McLean, and B. D. Cuevas (2006), Impact of partial steps and momentum advection schemes in a global ocean circulation model at eddy-permitting resolution, *Ocean Dynamics*, *56*, 543–567, doi:10.1007/s10236-006-0082-1.

- Barrier, N., A.-M. Treguier, J. Deshayes, and C. Cassou (2012), Response of North-Atlantic Ocean circulation to atmospheric weather regimes, *submitted to Journal of Physical Oceanography*.
- Belkin, I. M., and S. Levitus (1996), Temporal variability of the Subarctic Front near the Charlie-Gibbs Fracture Zone, *Journal of Geophysical Research*, *101*(C12), 28,317–28,324, doi:10.1029/96JC02794.
- Bentsen, M., H. Drange, T. Furevik, and T. Zhou (2004), Simulated variability of the Atlantic meridional overturning circulation, *Climate Dynamics*, *22*(6-7), 701–720, doi:10.1007/s00382-004-0397-x.
- Bersh, M. (2002), North Atlantic Oscillation-induced changes of the upper layer circulation in the northern North Atlantic Ocean, *Journal of Geophysical Research*, *107*(C10), 223–235, doi:10.1029/2001JC000901.
- Bersh, M., I. Yashayaev, and K. P. Koltermann (2007), Recent changes of the thermohaline circulation in the subpolar North Atlantic, *Ocean Dynamics*, *57*(3), 223–235, doi:10.1007/s10236-007-0104-7.
- Biastoch, A., C. W. Böning, and J. Getzlaff (2008), Causes of Interannual-Decadal Variability in the Meridional Overturning Circulation of the Midlatitude North Atlantic Ocean, *Journal of Climate*, *21*(24), 6599–6615, doi:10.1175/2008JCLI2404.1.
- Bingham, R. J., C. W. Hughes, V. Roussenov, and R. G. Williams (2007), Meridional coherence of the North Atlantic meridional overturning circulation, *Geophysical Research Letters*, *34*(L23606), doi:10.1029/2007GL031731.
- Blanke, B., and S. Raynaud (1997), Kinematics of the Pacific Equatorial Undercurrent: An Eulerian and Lagrangian Approach from GCM Results, *Journal of Physical Oceanography*, *27*(6), 1038–1053, doi:10.1175/1520-0485(1997)027<1038:KOTPEU>2.0.CO;2.

- Blanke, B., M. Arhan, G. Madec, and S. Roche (1999), Warm water paths in the equatorial Atlantic as diagnosed with a general circulation model, *Journal of Physical Oceanography*, *29*(11), 2753–2768, doi:10.1175/1520-0485(1999)029<2753:WWPITE>2.0.CO;2.
- Böning, C., M. Scheinert, J. Dengg, A. Biastoch, and A. Funk (2006), Decadal variability of subpolar gyre transport and its reverberation in the North Atlantic overturning, *Geophysical Research Letters*, *33*(L21S01), doi:10.1029/2006GL026906.
- Böning, C. W., F. O. Bryan, W. R. Holland, and R. Döscher (1996), Deep-water Formation and Meridional Overturning in a High-Resolution Model of the North Atlantic, *Journal of Physical Oceanography*, *26*(7), 1142–1164, doi:10.1175/1520-0485(1996)026<1142:DWFAMO>2.0.CO;2.
- Bower, A. S., and W.-J. von Appen (2007), Interannual variability in the Pathways of the North Atlantic Current over the Mid-Atlantic Ridge and the Impact of Topography, *Journal of Physical Oceanography*, *38*, 104–120, doi:10.1175/2007JPO3686.1.
- Bower, A. S., B. L. Cann, T. Rossby, W. Zenk, J. Gould, K. Speer, P. L. Richardson, M. D. Prater, and H. M. Zhang (2002), Directly measured mid-depth circulation in the northeastern North Atlantic Ocean, *Nature*, *419*, 603–607, doi:doi: 10.1038/nature01078.
- Brambilla, E., and L. D. Talley (2006), Surface drifter exchange between the North Atlantic subtropical and subpolar gyres, *Journal of Geophysical Research*, *111*(C07026), doi:10.1029/2005JC003146.
- Brambilla, E., and L. D. Talley (2008), Subpolar Mode Water in the northeastern Atlantic: 1. Averaged properties and mean circulation, *Journal of Geophysical Research*, *113*(C04025), doi:10.1029/2006JC004062.
- Brambilla, E., L. D. Talley, and P. E. Robbins (2008), Subpolar Mode Water in the northeastern Atlantic: 2. Origin and transformation, *Journal of Geophysical Research*, *113*(C04026), doi:10.1029/2006JC004063.

- Brodeau, L., B. Barnier, T. Penduff, A.-M. Tréguier, and S. Gulev (2009), An evaluation of ERA-40 and CORE atmospheric variables as drivers of global ocean models, *Ocean Modelling*, *31*, 88–104, doi:doi: 10.1016/j.ocemod.2009.10.005.
- Burkholder, K. C., and M. S. Lozier (2011), Subtropical to subpolar pathways in the North Atlantic: Deductions from lagrangian trajectories, *Journal of Geophysical Research*, *116*(C07017), doi:10.1029/2010JC006697.
- Chaudhuri, A. H., A. Gangopadhyay, and J. J. Bisagni (2011), Contrasting response of the eastern and western North Atlantic circulation to an episodic climate event, *Journal of Physical Oceanography*, *41*(9), 1630–1638, doi:10.1175/2011JPO4512.1.
- Cunningham, S. A., T. Kanzow, D. Rayner, M. O. Baringer, W. E. Johns, J. Marotzke, H. R. Longworth, E. M. Grant, J. J.-M. Hirschi, L. M. Beal, C. S. Meinen, and H. L. Bryden (2007), Temporal Variability of the Atlantic Meridional Overturning Circulation at 26.5°N, *Science*, *317*(5840), 935–938, doi:10.1126/science.1141304.
- Cuny, J., P. B. Rhines, and R. Kwok (2005), Davis Strait volume, freshwater and heat fluxes, *Deep-Sea Research I*, *52*(3), 519–542, doi:10.1016/j.dsr.2004.10.006.
- Curry, B., C. M. Lee, and B. Petrie (2011), Volume, Freshwater, and Heat Fluxes through Davis Strait, 2004-05, *Journal of Physical Oceanography*, *41*(3), 429–436, doi: 10.1175/2010JPO4536.1.
- Curry, R. G., and M. S. McCartney (2001), Ocean Gyre Circulation Changes Associated with the North Atlantic Oscillation, *Journal of Physical Oceanography*, *31*, 3374–3400, doi: 10.1175/1520-0485(2001)031;3374:OGCCAW;2.0.
- Daniault, N., P. Lherminier, and H. Mercier (2011a), Circulation and Transport at the southeast Tip of Greenland, *Journal of Physical Oceanography*, *41*(3), 437–457, doi: 10.1175/2010JPO4428.1.

- Daniault, N., H. Mercier, and P. Lherminier (2011b), The 1992-2009 transport variability of the East Greenland Current at 60 degrees N, *Geophysical Research Letters*, *38*(L07601), doi:10.1029/2011GL046863.
- De Boissésou, E. (2010), Les eaux modales du gyre subpolaire de l'Atlantique Nord: origine, formation, variabilité, Ph.D. thesis, Université de Bretagne Occidentale, <http://archimer.ifremer.fr/doc/2010/these-7469.pdf>.
- De Boissésou, E., V. Thierry, and H. Mercier (2010), Mixed layer heat budget in the Iceland Basin from Argo, *Journal of Geophysical Research*, *115*(C10055), doi:10.1029/2010JC006283.
- de Boissésou, E., V. Thierry, H. Mercier, G. Caniaux, and D. Desbruyères (2012), Origin, formation and variability of the Subpolar Mode Water observed over the Reykjanes Ridge, *Journal of Geophysical Research*.
- Deshayes, J., and C. Frankignoul (2008), Simulated Variability of the Circulation in the North Atlantic from 1953 to 2003, *Journal of Climate*, *21*(19), 4919–4933, doi: 10.1175/2008JCLI1882.1.
- Dutkiewicz, S., L. Rothstein, and T. Rossby (2001), Pathways of cross-frontal exchange in the North Atlantic Current, *Journal of Geophysical Research*, *106*(C11), 26,917–26,928, doi: 10.1029/1999JC000089.
- Eden, C., and T. Jung (2001), North Atlantic Interdecadal Variability: Oceanic Response to the North Atlantic Oscillation (1865-1997), *Journal of Climate*, *14*(5), 676–691, doi: 10.1175/1520-0442(2001)014<0676:NAIVOR>2.0.CO;2.
- Eden, C., and J. Willebrand (2001), Mechanism of Interannual to Decadal Variability of the North Atlantic Circulation, *Journal of Climate*, *14*(10), 2266–2280, doi:10.1175/1520-0442(2001)014<2266:MOITDV>2.0.CO;2.
- Fichelet, T., and M. A. M. Maqueda (1999), Modelling the influence of snow accumulation and

- snow-ice formation on the seasonal cycle of the Antarctic sea-ice cover, *Climate Dynamics*, *15*(4), 251–268, doi:10.1007/s003820050280.
- Fischer, J., F. A. Schott, and M. Dengler (2004), Boundary Circulation at the Exit of the Labrador Sea, *Journal of Physical Oceanography*, *34*(7), 1548–1570, doi:10.1175/1520-0485(2004)034<1548:BCATEO>2.0.CO;2.
- Flatau, M. K., L. Talley, and P. P. Niiler (2003), The North Atlantic Oscillation, Surface Current Velocity, and SST Changes in the Subpolar North Atlantic, *Journal of Climate*, *16*, 2355–2369, doi:10.1175/2787.1.
- Forget, G., H. Mercier, and B. Ferron (2008), Combining Argo profiles with a general circulation model in the North Atlantic. Part 2: Realistic transports and improved hydrography, between spring 2002 and spring 2003, *Ocean Science*, *20*(1), 17–34, doi:10.1016/j.ocemod.2007.06.002.
- Frankignoul, C., J. Deshayes, and R. Curry (2009), The role of salinity in the decadal variability of the North Atlantic meridional overturning circulation, *Climate Dynamics*, *33*(6), 777–793, doi:10.1007/s00382-008-0523-2.
- Fratantoni, D. M. (2001), North Atlantic surface circulation during the 1990’s observed with satellite-tracked drifters, *Journal of Geophysical Research*, *106*(C10), doi:10.1029/2000JC000730.
- Ganachaud, A., and C. Wunsch (2003), Large-Scale Ocean Heat and Freshwater Transport during the World Ocean Circulation Experiment, *Journal of Climate*, *16*, 696–705.
- Getzlaff, J., C. W. Böning, C. Eden, and A. Biastoch (2005), Signal propagation related to the North Atlantic overturning, *Geophysical Research Letters*, *32*(L09602), doi:10.1029/2004GL021002.
- Gourcuff, C. (2008), Etude de la variabilité de la circulation du Gyre Subpolaire de l’Atlantique nord à l’aide des données OVIDE et des mesures satellitaires., Ph.D. thesis, Université de Bretagne Occidentale, <http://archimer.ifremer.fr/doc/2008/these-6226.pdf>.

- Gourcuff, C., P. Lherminier, H. Mercier, and P.-Y. L. Traon (2011), Altimetry Combined with Hydrography for Ocean Transport Estimation, *Journal of Atmospheric and Oceanic Technology*, *28*, 1324–1337, doi:10.1175/2011JTECHO818.1.
- Gregory, J. M., K. W. Dixon, R. J. Stouffer, A. J. Weaver, E. Driesschaert, M. Erby, T. Fichelet, H. Hasumi, A. Hu, J. H. Hunglaus, I. V. Kamenkovich, A. Levermann, M. Montoya, S. Murakami, S. Nawrath, A. Oka, A. P. Sokolov, and R. B. Thorpe (2005), A model intercomparison of changes in the Atlantic thermohaline circulation in response to increasing atmospheric CO<sub>2</sub> concentration, *Geophysical Research Letters*, *32*(L12703), doi:10.1029/2005GL023209.
- Griffies, S. M., A. Biastoch, C. Böning, F. Bryan, G. Danabasoglu, E. P. Chassignet, M. H. England, R. Gerdes, H. Haak, R. W. Hallberg, W. Hazeleger, J. Junglaus, W. G. Large, G. Madec, A. Pirani, B. L. Samuels, M. Scheinert, A. S. Gupta, C. A. Severijns, H. L. Simmons, A.-M. Treguier, M. Winton, S. Yeager, and J. Yin (2009), Coordinated Ocean-ice Reference Experiments (COREs), *Ocean Modelling*, *26*(1-2), 1–46, doi:10.1016/j.ocemod.2008.08.007.
- Grist, J. P., S. A. Josey, R. Marsh, S. A. Good, A. C. Coward, B. A. de Cuevas, S. G. Alderson, A. L. New, and G. Madec (2010), The roles of surface heat flux and ocean heat transport convergence in determining Atlantic Ocean temperature variability, *Climate Dynamics*, *60*(4), 771–790, doi:10.1007/s10236-010-0292-4.
- Gulev, S. K., B. Barnier, H. Knochel, J.-M. Molines, and M. Cottet (2003), Water Mass Transformation in the North Atlantic and Its Impact on the Meridional Circulation: Insights from an Ocean Model Forced by NCEP-NCAR Reanalysis Surface Fluxes, *Journal of Climate*, *16*(19), 3085–3110, doi:10.1175/1520-0442(2003)016<3085:WMTITN>2.0.CO;2.
- Häkkinen, S. (1999), Variability of the simulated meridional heat transport in the North Atlantic for the period 1951-1993, *Journal of Geophysical Research*, *104*(C5), doi:10.1029/1999JC900034.

- Häkkinen, S., and P. B. Rhines (2004), Decline of the Subpolar North Atlantic Circulation During the 1990s., *Science*, *304*(5670), 555–559, doi:10.1126/science.1094917.
- Häkkinen, S., and P. B. Rhines (2009), Shifting Surface Current in the northern North Atlantic Ocean, *Journal of Geophysical Research*, *114*(C04005), doi:10.1029/2008JC004883.
- Häkkinen, S., P. B. Rhines, and D. L. Worthen (2011a), Warm and saline events embedded in the meridional circulation of the northern North Atlantic, *Journal of Geophysical Research*, *116*(C03006), doi:10.1029/2010JC006275.
- Häkkinen, S., P. B. Rhines, and D. L. Worthen (2011b), Atmospheric Blocking and Atlantic Multidecadal Ocean Variability, *Science*, *334*(6056), 655–659, doi:10.1126/science.1205683.
- Hall, N. M. J., B. Barnier, T. Penduff, and J. M. Molines (2004), Interannual variation of gulf stream heat transport in a high-resolution model forced by reanalysis data, *Climate Dynamics*, *23*(3-4), 341–351, doi:10.1007/s00382-004-0449-2.
- Hansen, B., and S. Østerhus (2000), North Atlantic - Nordic Seas exchanges, *Progress in Oceanography*, *45*(2), 109–208, doi:10.1016/S0079-6611(99)00052-X.
- Hansen, B., S. Osterhus, W. R. Turrell, S. Jonsson, H. Valdimarsson, H. Hátún, and S. M. Olsen (2008), The inflow of atlantic water, heat, and salt to the nordic seas across the greenland-scotland ridge, in *Arctic-Subarctic Ocean Fluxes: Defining the Role of the Northern Seas in Climate*, (Robert R. Dickson, Jens Meincke and Peter Rhines (eds) Springer Science + Business Media B. V.).
- Harvey, J. (1982), Theta-s relationship and water masses in the eastern north atlantic, *Deep Sea Research Part A*, *29*, doi:10.1016/0198-0149.
- Hátún, H., A. B. Sandø, H. Drange, B. Hansen, and H. Valdimarsson (2005), Influence of the Atlantic Subpolar Gyre on the Thermohaline Circulation, *Science*, *309*(5742), 1841–1844, doi:10.1126/science.1114777.

- Herbaut, C., and M.-N. Houssais (2009), Response of the eastern North Atlantic subpolar gyre to the North Atlantic Oscillation, *Geophysical Research Letters*, *36*(L17607), doi:10.1029/2009GL039090.
- Holliday, N. P. (2003), Air-sea interaction and circulation changes in the northeast Atlantic, *Journal of Geophysical Research*, *108*(3259), doi:10.1029/2002JC001344.
- Holliday, N. P., S. L. Hughes, S. Bacon, A. Beszczynska-Möller, B. Hansen, A. Lavín, H. Loeng, K. A. Mork, S. Osterhus, T. Sherwin, and W. Walczowski (2008), Reversal of the 1960s to 1990s freshening trend in the northeast North Atlantic and Nordic Seas, *Geophysical Research Letters*, *35*(L03614), doi:10.1029/2007GL032675.
- Huang, B., Y. Xue, A. Kumar, and D. W. Behringer (2012), AMOC variations in 1979-2008 simulated by NCEP operational ocean data assimilation system, *Climate Dynamics*, *38*(3-4), 513–525, doi:10.1007/s00382-011-1035-z.
- Huck, T., A. C. de Verdière, P. Estrade, and R. Schopp (2008), Low-frequency variations of the large-scale ocean circulation and heat transport in the North Atlantic from 1955-1998 in situ temperature and salinity data, *Geophysical Research Letters*, *35*(L23613), doi:10.1029/2008GL035635.
- Hurrell, J. W. (1995), Decadal trends in the North Atlantic Oscillation: Regional temperatures and precipitation, *Science*, *269*, 676–679, doi:10.1126/science.269.5224.676.
- Jayne, S. R., and J. Marotzke (2001), The dynamics of ocean heat transport variability, *Review of Geophysics*, *39*, 385–411.
- Jouanno, J., F. Marin, Y. du Penhoat, J.-M. Molines, and J. Sheinbaum (2011), Seasonal Modes of Surface Cooling in the Gulf of Guinea, *Journal of Physical Oceanography*, *41*, 1408–1416, doi:10.1175/JPO-D-11-031.1.
- Kieke, D., M. Rhein, L. Stramma, W. M. Smethie, D. A. LeBel, and W. Zenk (2006), Changes

- in the CFC Inventories and Formation Rates of Upper Labrador Sea Water, 1977-2001, *Journal of Physical Oceanography*, *36*, 64–86, doi:10.1175/JPO2814.1.
- Kieke, D., M. Rhein, L. Stramma, W. M. Smethie, J. L. Bullister, and D. A. LeBel (2007), Changes in the pool of Labrador Sea Water in the subpolar North Atlantic, *Geophysical Research Letters*, *34*(L06605), doi:10.1029/2006GL028959.
- Krahmann, G., M. Visbeck, and G. Reverdin (2000), Formation and Propagation of Temperature Anomalies along the North Atlantic Current, *Journal of Physical Oceanography*, *31*, 1287–1303, doi:10.1175/1520-0485(2001)031<1287:FAPOTA>2.0.CO;2.
- Krauss, W. (1995), Currents and mixing in the Irminger Sea and in the Iceland Basin, *Journal of Geophysical Research*, *100*(C6), doi:10.1029/95JC00423.
- Large, W., and S. Yeager (2004), Diurnal to decadal global forcing for ocean and sea-ice models: The datasets and flux climatologies, *Note ncar/tn*, Natl. Cent. for Atmos. Res., Boulder, Colo.
- Lavender, K. L., R. E. Davis, and W. B. Owens (2000), Mid-depth recirculation observed in the interior Labrador and Irminger seas by direct velocity measurements, *Nature*, *407*, 66–69, doi:10.1038/35024048.
- Levitus, S., T. P. Boyer, M. E. Conkright, T. O'Brien, J. Antonov, C. Stephens, L. Stathoplos, D. Johnson, and R. Gelfeld (1998), World Ocean Database 1998, *NOAA Atlas NESDIS*, *18*.
- Levitus, S., J. I. Antonov, T. P. Boyer, R. A. Locarnini, H. E. Garcia, and A. V. Mishonov (2009), Global ocean heat content 1955-2008 in light of recently revealed instrumentation problems, *Geophysical Research Letters*, *36*(L07608), doi:10.1029/2008GL037155.
- Lherminier, P., H. Mercier, C. Gourcuff, M. F. Alvarez, S. Bacon, and C. Kermabon (2007), Transport across the 2002 Greenland-Portugal section and comparison with 1997, *Journal of Geophysical Research*, *112*(C07003), doi:10.1029/2006JC003716.

- Lherminier, P., H. Mercier, T. Huck, C. Gourcuff, F. F. Perez, P. Morin, A. Sarafanov, and A. Falina (2010), The Atlantic Meridional Overturning Circulation and the Subpolar Gyre observed at the A25-OVIDE Section in June 2002 and 2004, *Deep-Sea Research I*, 57(11), 1374–1391, doi:10.1016/j.dsr.2010.07.009.
- Lique, C., A.-M. Treguier, B. Blanke, and N. Grima (2010), On the origins of water masses exported along both sides of Greenland: A Lagrangian model analysis, *Journal of Geophysical Research*, 115(C05019), doi:10.1029/2009JC005316.
- Lozier, M. S. (2010), Deconstructing the Conveyor Belt, *Science*, 328(5985), 1507–1511, doi:10.1126/science.1189250.
- Lozier, M. S., S. Leadbetter, R. G. Williams, V. Roussenov, M. S. C. Reed, and N. J. Moore (2008), The Spatial Pattern and Mechanisms of Heat-Content Change in the North Atlantic, *Science*, 319(5864), 800–803, doi:10.1126/science.1146436.
- Lu, Y., D. G. Wright, and I. Yashayaev (2007), Modelling hydrographic changes in the Labrador Sea over the past five decades, *Progress in Oceanography*, 73(3-4), 406–426, doi:10.1016/j.pocean.2007.02.007.
- Madec, G. (2008), NEMO Ocean engine, *Tech. rep.*, Institut Pierre-Simon Laplace.
- Marsh, R., B. D. Cuevas, A. C. Coward, and H. L. Bryden (2005), Thermohaline circulation at three key section in the North Atlantic over 1985-2002, *Geophysical Research Letters*, 32(L10604), doi:10.1029/2004GL022281.
- Marsh, R., S. A. Josey, B. A. de Cuevas, L. J. Redbourn, and G. D. Quartly (2008), Mechanisms for recent warming of the North Atlantic: Insights gained with an eddy-permitting model, *Journal of Geophysical Research*, 113(C04031), doi:10.1029/2007JC004096.
- Marshall, J., H. Johnson, and J. Goodman (2001), A study of the Interaction of the North Atlantic Oscillation with Ocean Circulation, *Journal of Physical Oceanography*, 14(7), 1399–1421, doi:10.1175/1520-0442.

- Marzocchi, A., J. J.-M. Hirschi, N. P. Holliday, S. A. Cunningham, A. T. Blaker, S. Masina, and A. C. Coward (2012), Establishment of the North Atlantic subpolar circulation in an eddy-resolving ocean model, *submitted to Ocean Modelling*.
- Maslowski, W., D. Marble, W. Walczowski, U. Schauer, J. L. Clement, and A. J. Semtner (2004), On climatological mass, heat and salt transports through the Barent Sea and Fram Strait from a pan-Arctic coupled ice-ocean model simulation, *Journal of Geophysical Research*, *109*(C03032), doi:10.1029/2001JC001039.
- Mauritzen, C., and S. Häkkinen (1999), On the relationship between dense water formation and the "Meridional Overturning Cell" in the North Atlantic Ocean, *Deep-Sea Research I*, *46*, 877–894.
- Molines, J. M., B. Barnier, T. Penduff, L. Brodeau, A. M. Treguier, S. Theeten, and G. Madec (2006), Definition of the interannual experiment ORCA025-G70, 1958-2004, *LEGI Report*.
- Niiler, P. P., N. A. Maximenko, and J. C. McWilliams (2003), Dynamically balanced absolute sea level of the global ocean derived from near-surface velocity observations, *Geophysical Research Letters*, *30*(2164), doi:10.1029/2003GL018628.
- Nilsen, J. E. Ø., Y. Gao, H. Drange, T. Furevik, and M. Bentsen (2003), Simulated North Atlantic-Nordic Seas water mass exchanges in an isopycnic coordinate OGCM, *Geophysical Research Letters*, *30*(1536), doi:10.1029/2002GL016597.
- Olsen, S. M., B. Hansen, D. Quadfasel, and S. Østerhus (2008), Observed and modelled stability of overflow across the Greenland-Scotland ridge, *Nature*, *455*, 519–522, doi:10.1038/nature07302.
- Østerhus, S., W. R. Turrell, S. Jonsson, and B. Hansen (2005), Measured volume, heat and salt fluxes from the Atlantic to the Arctic Mediterranean, *Geophysical Research Letters*, *32*(L07603), doi:10.1029/2004GL022188.

- Paillet, J., and H. Mercier (1997), An inverse model of the eastern North Atlantic general circulation and thermohaline ventilation, *Deep Sea Research*, *44*(8), 1293–1328, doi:10.1016/S0967-0637(97)00019-8.
- Perez-Brunius, P., T. Rossby, and R. Watts (2004), Absolute Transport of Mass and Temperature for the North-Atlantic Current Subpolar Front System, *Journal of Physical Oceanography*, *34*(8), 1870–1883, doi:10.1175/1520-0485(2004)034<1870:ATOMAT>2.0.CO;2.
- Pickart, R. S., and M. A. Spall (2007), Impact of Labrador Sea Convection on the North Atlantic Meridional Overturning Circulation, *Journal of Physical Oceanography*, *37*(9), 2207–2227, doi:10.1175/JPO3178.1.
- Pickart, R. S., F. Straneo, and G. W. K. Moore (2003a), Is Labrador Sea Water formed in the Irminger basin?, *Deep-Sea Research I*, *50*(1), 23–52, doi:10.1016/S0967-0637(02)00134-6.
- Pickart, S. R., M. A. Spall, M. H. Ribergaard, G. W. K. Moore, and R. F. Millif (2003b), Deep Convection in the Irminger Sea forced by Greenland tip jet, *Nature*, *424*, 152–156, doi:10.1038/nature01729.
- Pickart, S. R., D. J. Torres, and P. S. Fratantoni (2005), The East Greenland Spill Jet, *Journal of Physical Oceanography*, *35*(6), 1037–1053, doi:10.1175/JPO2734.1.
- Prater, M. D. (2002), Eddies in the Labrador Sea as observed by profiling RAFOS floats and remote sensing, *Journal of Physical Oceanography*, *32*(2), 411–427, doi:10.1175/1520-0485(2002)032<0411:EITLSA>2.0.CO;2.
- Price, J. F., and M. O. Baringer (1994), Outflow and deepwater production by marginal seas, *Progress in Oceanography*, *33*(3), doi:10.1016/0079-6611(94)90027-2.
- Rahmstorf, S. (1999), Shifting Seas in the greenhouse?, *Nature*, *399*, doi:doi: 10.1038/21066.
- Rattan, S., P. G. Myers, A.-M. Treguier, S. Theetten, A. Biastoch, and C. Böning (2010), Towards an understanding of Labrador Sea salinity drift in eddy-permitting simulations, *Ocean Modelling*, *35*(1-2), 77–88, doi:10.1016/j.ocemod.2010.06.007.

- Reverdin, G., P. P. Niiler, and H. Valdimarsson (2003), North Atlantic Ocean surface currents, *Journal of Geophysical Research*, *108*(3002), doi:10.1029/2001JC001020.
- Rhein, M., D. Kieke, and R. Steinfeldt (2007), Ventilation of the Upper Labrador Sea Water, 2003-2005., *Geophysical Research Letters*, *34*(L06603), doi:10.1029/2006GL028540.
- Rio, M.-H., and F. Hernandez (2004), A mean dynamic topography computed over the world ocean from altimetry, in situ measurements, and a geoid model, *Journal of Geophysical Research*, *109*(C12032), doi:10.1029/2003JC002226.
- Robson, J. I. (2010), Understanding the performance of a decadal prediction system, Ph.D. thesis, University of Reading, 223 pp.
- Rossby, T. (1996), The North Atlantic Current and surrounding waters: At the crossroads, *Review of Geophysics*, *34*(4), 463–481, doi:10.1029/96RG02214.
- Sarafanov, A., A. Falina, H. Mercier, A. Sokov, P. Lherminier, C. Gourcuff, S. Gladyshev, F. Gaillard, and N. Daniault (2012), Mean full-depth summer circulation and transports at the northern periphery of the Atlantic Ocean in the 2000s, *Journal of Geophysical Research*, *117*(C01014), doi:10.1029/2011JC007572.
- Schmitz, W. J. J., and M. S. McCartney (1993), On the North Atlantic Circulation, *Review of Geophysics*, *31*, 29–49, doi:doi: 10.1029/92RG02583.
- Schott, F., L. Stramma, and J. Fischer (1999), Interaction of the North Atlantic Current with the deep Charlie Gibbs Fracture Zone throughflow, *Geophysical Research Letters*, *26*(3), 369–372, doi:10.1029/1998GL900223.
- Schott, F. A., R. Zantopp, L. Stramma, M. Dengler, J. Fischer, and M. Wibaux (2004), Circulation and Deep-Water Export at the Western Exit of the Subpolar North Atlantic, *Journal of Physical Oceanography*, *34*, 817–843, doi:10.1175/1520-0485(2004)034<0817:CADEAT>2.0.CO;2.

- Schott, F. A., L. Stramma, B. S. Giese, and R. Zantopp (2009), Labrador Sea convection and subpolar North Atlantic Deep Water export in the SODA assimilation model, *Deep-Sea Research I*, *56*(6), 926–938, doi:10.1016/j.dsr.2009.01.001.
- Serreze, M. C., A. P. Barrett, A. G. Slater, R. A. Woodgate, K. Aagaard, R. B. Lammers, M. Steele, R. Moritz, M. Meredith, and C. M. Lee (2006), The large-scale freshwater cycle of the Arctic, *Journal of Geophysical Research*, *111*(C11010), doi:10.1029/2005JC003424.
- Smethie, W. M. J., and J. H. Swift (1989), The Tritium: Krypton-85 age of Denmark Strait overflow water and Gibbs Fracture Zone water just south of Denmark Strait, *Journal of Geophysical Research*, *94*(C6), doi:10.1029/JC094iC06p08265.
- Steele, M., R. Morley, and W. Ermold (2001), PHC: A global ocean hydrography with a high quality Arctic Ocean, *Journal of Climate*, *14*(9), 2079–2087, doi:10.1175/1520-0442(2001)014j2079:PAGOHWj2.0.CO;2.
- Sutton, R., and M. Allen (1997), Decadal predictability of North Atlantic sea surface temperature and climate, *Nature*, *388*, 563–567.
- Sy, A. (1988), Investigation of large-scale circulation in the central North Atlantic - The North Atlantic Current, the Azores Current, and the Mediterranean plume in the area of the Mid-Atlantic Ridge, *Deep Sea Research Part A*, *35*(3), 383–413, doi:10.1016/0198-0149(88)90017-9.
- Sy, A., U. Shcauer, and J. Meincke (1992), The North Atlantic Current and the associated hydrographic structure above and eastward of the Mid-Atlantic Ridge, *Deep Sea Research*, *39*(5), 825–853, doi:10.1016/0198-0149(92)90124-C.
- Talley, L. D., and M. S. McCartney (1982), Distribution and circulation of the Labrador Sea Water, *Journal of Physical Oceanography*, *12*, 1189–1205.
- The Labrador Sea Group (2008), The Labrador Sea deep convection experiment, *Tech. Rep. 79, 2033-2058*, Bull. Am. Meteorol. Soc.

- Thierry, V., E. D. Boisséson, and H. Mercier (2008), Interannual variability of the Subpolar Mode Water properties over the Reykjanes Ridge during 1990-2006, *Journal of Geophysical Research*, *113*(C04016), doi:10.1029/2007JC004443.
- Treguier, A., C. Gourcuff, P. Lherminier, H. Mercier, B. Barnier, G. Madec, J.-M. Molines, T. Penduff, L. Czeschel, and C. Böning (2006), Internal and forced variability along a section between Greenland and Portugal in the CLIPPER Atlantic model, *Ocean Dynamics*, *56*(5-6), 568–580, doi:10.1007/s10236-006-0069-y.
- Treguier, A. M., S. Theeten, E. P. Chassignet, T. Penduff, R. Smith, L. Talley, J. O. Beismann, and C. Böning (2005), The North Atlantic Subpolar Gyre in Four High-Resolution Models, *Journal of Physical Oceanography*, *35*, 757–774, doi:10.1175/JPO2720.1.
- Treguier, A.-M., M. H. England, S. R. Rintoul, G. Madec, J. L. Sommer, and J. M. Molines (2007), Southern Ocean overturning across streamlines in an eddy simulation of the Antarctic Circumpolar Current, *Ocean Science*, *3*, 491–507.
- Treguier, A.-M., J. Deshayes, C. Lique, R. Dussin, and J. Molines (2012), Eddy contributions to the meridional transport of salt in the North Atlantic, *Journal of Geophysical Research*, *117*, doi:doi: 10.1029/2012JC007927.
- Trenberth, K. E., and J. M. Caron (2001), Estimates of Meridional Atmosphere and Ocean Heat Transports, *Journal of Climate*, *14*, 3433–3443, doi:10.1175/1520-0442(2001)014;3433:EOMAAO;2.0.CO;2.
- Worthington, L. V. (1976), On the North Atlantic Circulation, *Johns Hopkins University Press*, *6*, 110pp.
- Wunsch, C. (2005), The total meridional heat flux and its oceanic and atmospheric partition, *Journal of Climate*, *18*, 4374–4380, doi:10.1175/JCLI3539.1.
- Wunsch, C., and P. Heimbach (2006), Estimated decadal changes in North Atlantic meridional

overturning circulation and heat fluxes 1993-2004, *Journal of Physical Oceanography*, *36*, 2012–2024, doi:10.1175/JPO2957.1.

Yashayaev, I., M. Bersh, and H. M. van Aken (2007), Spreading of the Labrador Sea Water to the Irminger and Iceland basins, *Geophysical Research Letters*, *34*(L10602), doi:10.1029/2006GL028999.

Yeager, S., G. Karspeck, G. Danabasoglu, J. Tribbia, and H. Teng (2012), A decadal prediction case study: Late 20th Century North Atlantic ocean heat content, *Journal of Climate*, *25*(15), 5173–5189, doi:10.1175/JCLI-D-11-00595.1.

Zhai, X., and L. Sheldon (2012), On the North Atlantic Ocean Heat Content Change between 1955-70 and 1980-95, *Journal of Climate*, *25*(10), 3619–3628, doi:10.1175/JCLI-D-11-00187.1.

Zhang, R. (2010), Latitudinal dependence of Atlantic meridional overturning circulation (AMOC) variations, *Geophysical Research Letters*, *37*(L16703), doi:10.1029/2010GL044474.